Bubble deformation and fragmentation in turbulence

Aliénor Rivière

PSL UNIVERSITÉ PARIS

THÈSE DE DOCTORAT

DE L'UNIVERSITÉ PSL

Préparée à l'École Supérieure de Physique et de Chimie Industrielles de la ville de Paris

Déformation et fragmentation de bulles en turbulence

Bubble deformation and fragmentation in turbulence

Soutenue par

Aliénor Rivière

Le 10 septembre 2024

École doctorale n°391

SMAER

Spécialité

Mécanique

Préparée au

Laboratoire de Physique et Mécanique des Milieux Hétérogènes

Composition du jury :

François PÉTRÉLIS DR, LPENS	*Président du jury* *Examinateur*
Aurore NASO DR, LMFA	*Rapportrice*
Frédéric RISSO DR, IMFT	*Rapporteur*
Stéphane POPINET DR, IJLR d'Alembert	*Examinateur*
Carlos MARTÍNEZ-BAZÁN Prof., U. de Grenade	*Examinateur*
Benjamin FAVIER CR, IRPHE	*Examinateur*
Laurent DUCHEMIN Prof., PMMH	*Directeur*
Stéphane PERRARD CR, PMMH	*Co-encadrant*
Christophe JOSSERAND DR, LadHyX	*Co-directeur* *(Invité)*

ESPCI PARIS | PSL

À mon père.
Parce que les bulles
c'est de la physique stylée.

Remerciements

Je remercie en premier lieu mes deux rapporteurs, Aurore Naso, et Frédéric Risso, ainsi que mes examinateurs, François Pétrélis, Carlos Martinez-Bazan, Stéphane Popinet et Benjamin Favier pour avoir accepté de juger mon travail et de faire le déplacement pour ma soutenance. Grâce à leurs questions précises et profondes, la discussion scientifique a été d'une grande richesse. Je les remercie également pour l'intérêt porté à mon travail et leurs retours positifs.

Mes remerciements vont ensuite, bien sûr, à mes trois encadrants qui, chacun à leur manière, ont largement contribué aux excellentes conditions de travail dans lesquelles j'ai réalisé cette thèse. Plus particulièrement, je tiens à remercier Stéphane Perrard qui a cru en moi dès le départ, acceptant d'encadrer une thèse de numérique. Rien n'aurait été possible sans son enthousiasme et son inventivité. Je remercie aussi chaleureusement Laurent Duchemin d'avoir supporté d'entendre le mot turbulence sans broncher chaque semaine pendant trois ans. Grâce à cet effort surhumain et ses multiples questions et remarques prétendument naïves, j'ai pu être assurée d'avoir une compréhension profonde de ce que j'observais. Enfin, Christophe Josserand a apporté du recul scientifique lors de nos réunions, permettant de garder une ligne directrice claire, et intéressante. Je pense que cette complémentarité de vision a été fructueuse et j'espère pouvoir travailler encore avec eux à l'avenir !

Je tiens aussi à remercier spécialement Luc Deike, qui non seulement m'a introduite dans le monde de la recherche et du numérique, mais aussi dans la communauté des bulles en turbulence. Son soutien inconditionnel, tant humain que scientifique, m'a été et m'est extrêmement précieux. I'de like also to thank the members, past and present, of his team : Baptiste Néel, Dan Ruth, Wouter Mostert (When I left Princeton, I thought : *When I grow up, I'd like to be Wouter.* I don't think I succeeded yet, but there's still some hope !), Jiarong Wu, Daniel Shaw, Palas Farsoyia, Megan Mazzatenta, Martin Erinin, Nicolo Scapin, Zehua Liu etc.. I really enjoyed being with you in Princeton. I am grateful for the insightful scientific discussions we had but also for the great times we had together. I hope we will continue to cross paths with each others in the future.

Au cours de cette thèse, j'ai eu la chance de discuter avec un grand nombre de personnes provenant de laboratoires différents. Je remercie particulièrement Maylis Landeau, Valentin Leroy, Stéphane Popinet et François Pétrélis pour les riches interactions que nous avons eues sur des sujets plus ou moins connexes à ma thèse, ainsi que les membres de mon comité Basile Gallet, Laurette Tuckerman et encore une fois Stéphane Popinet. Au laboratoire, je remercie tout particulièrement Sébastien Gomé sans qui ma première année au PMMH aurait été totalement

différente. Je lui suis particulièrement reconnaissante d'avoir découvert le monde de la transition à la turbulence et d'avoir pu travailler avec lui ainsi que Laurette Tuckerman et Dwight Barkley. Au cours de ces trois années, j'ai aussi pu voir la construction de notre groupe, les Turbots, du choix du nom jusqu'à sa croissance exponentielle (qui sature ?). Je remercie tous ses membres, Antonin Eddi, Philippe Bourrianne, Jishen Zhang, Baptiste Auvity, Sébastien Kuchly etc.. pour la bonne ambiance générale et pour m'avoir acceptée même si je ne faisais pas d'expérience ni de coin de table ni de milieu de table. Je souhaite de plus remercier l'équipe de non linéaire de l'ENS de m'avoir accueillie pendant un an en amont de ma thèse, pour leurs conseils ainsi que pour les riches discussions qui ont suivi ; pour n'en citer que quelques uns, François Pétrélis, Christophe Gissinger, Valentin Mouet, Gaurav Prabhudesai, Adrian Van Kan, Florentin Daniel, Marlon Vernet, Anxo Biasi etc... Je souhaite également remercier Zorana Zeravcic et Mathilde Reyssat avec qui j'ai eu la chance d'enseigner. Cela a été un réel plaisir de travailler avec elles pendant ces trois années. Je leur souhaite bien du courage pour gérer les prochaines inondations.

Je remercie tous les membres du PMMH, en particulier les lévitateurs, Xavier Mousset, Chloé Dupuis, Pierre-Ewen Lecoq ainsi que Gauthier Bertrand, Samantha Kucher et les membres passés et présents du bureau que je n'ai pas encore cités, Baptiste Lafoux, Joseph Vermeil, Hector Ignacio. De notoriété publique l'ambiance générale au laboratoire est excellente et c'est entre autre grâce à eux. Encore merci à Frédérique Auger et Claudette Barez pour leur soutien logistique infaillible au cours de ces trois années. Pour survivre pendant une thèse, mieux vaut être bien entouré. Je souhaite donc remercier spécialement mes ex-colocs, Guillaume Bermudez et Grégoire Le Lay, ainsi que mes amis, en particulier les musiciens d'Ossia, pour les heures passées ensemble en oubliant la thèse. Je suis aussi reconnaissante à ma famille, et en particulier à mes parents, de m'avoir toujours soutenue, bien que ne comprenant pas vraiment l'intérêt des bulles. Enfin, last but no least, ces dernières années auraient été totalement différentes si je n'avais pas eu Louis-Pierre Chaintron à mes côtés. Je lui en suis extrêmement reconnaissante tant pour son soutien que pour nos discussions scientifiques plus ou moins apaisées. J'espère que les années futures en seront encore remplies.

Résumé

La présence de bulles dans des écoulements contribuent à augmenter le mélange, ainsi que les échanges de matière et de chaleur entre les deux phases. Leur présence est ainsi primordiale dans un grand nombre de procédés industriels ainsi que dans des contextes environnementaux, caractérisés par des écoulements inertiels voire turbulents. Pour quantifier l'impact des bulles, il faut d'abord comprendre et modéliser leur distribution de taille, et son évolution temporelle. Dans des environements dilués, où l'évolution de la distribution est contrôlée par la fragmentation, la distribution présente deux lois de puissance séparées par une taille critique.

Dans un premier temps, nous nous intéressons à l'origine de la taille critique. Celle-ci correspond à la limite entre les bulles stables et instables, appelée échelle de Kolmogorov-Hinze. Les écoulements turbulents étant intrinsèquement caractérisés par de larges fluctuations, à la fois de pression et de vitesse, cette taille critique reste mal définie. Ici, nous proposons une nouvelle définition, probabiliste, de cette limite, qui inclue le temps de résidence des bulles dans les zones turbulentes. Pour cela, nous étudions numériquement la déformation d'une bulle, d'abord dans une géométrie d'écoulement modèle puis dans un écoulement turbulent homogène isotrope. Dans les deux cas, nous montrons que la dynamique de déformation peut être reproduite par une dynamique 1D sur le mode de déformation oblate-prolate. En extrapolant la dynamique obtenue dans le cas turbulent à des bulles qui cassent, nous quantifions la probabilité de fracture en un temps donné et en déduisons l'évolution de la taille critique au cours du temps.

Dans un second temps, nous nous intéressons à la génération de bulles sous l'échelle de Kolmogorov-Hinze. En effet, s'il y a un consensus sur l'origine de la distribution des bulles plus grandes que la taille critique, l'origine de la distribution pour les petites bulles restait à déterminer. Grâce à des simulations numériques directes, nous identifions que ces bulles proviennent de la rupture de filaments gazeux produits lors de la déformation de bulles plus grandes que l'échelle critique. Nous caractérisons ensuite la production et la fragmentation de ces filaments dans une géométrie d'écoulement modèle. Nous découvrons que la fragmentation de ligaments sous contrainte d'étirement conduit à une distribution de taille de bulles en loi de puissance qui coïncide avec la distribution sous l'échelle critique en turbulence.

Mots clés : bulle, turbulence, fragmentation, déformation, simulations numériques, modélisation

Abstract

Through their contributions to mixing, gas and heat transfers and aerosol production, bubbles play a central role in many industrial and environmental contexts, characterized by inertial flows, possibly turbulent. Understanding the physical processes controlling the bubble size distribution (BSD) and its temporal evolution, is key to quantify these exchanges. In dilute environments, in which breakup dominates, the BSD is characterized by two power laws separated by a critical size.

We first focus on the origin of this critical size. This size is known to be related to the Kolmogorov-Hinze scale, the size separating statistically stable, from unstable bubbles in turbulence. As a turbulent flow is characterized by large velocity and pressure fluctuations, this size is only defined in a statistical sense. We give here a new definition of this critical size, in terms of survival probability, which includes the residence time of bubbles within turbulent regions. To do so, we investigate numerically bubble deformations first in a model flow geometry and then in 3D homogeneous and isotropic turbulence (HIT). In both cases, we find that most of bubble deformation dynamics can be reproduced by a 1D model of the oblate-prolate mode. By extrapolating the deformation model obtained in turbulence to breaking bubbles, we deduce the probability of breaking and the evolution of the critical size in time.

We then investigate the generation of sub-Hinze bubbles. While there is a consensus for the origin of the power-law scaling for the super-Hinze BSD, the sub-Hinze BSD remained to be understood. By running DNS of bubbles in turbulence, we identify that sub-Hinze bubbles come from the fracture of gas filaments produced during the deformations of super-Hinze bubbles. We characterize filament production in a model flow configuration, as well as filament splitting. We find that filament breaking under stretching universally produces a power-law distribution, which coincides with the one obtained below breaking waves. This mechanism explains the origin of the sub-Hinze BSD.

Keywords : bubble, turbulence, breakup, deformation, numerical simulations, modeling

Contents

PREAMBLE

Chapter 1

Introduction

De tous temps les hommes ont été fascinés par les bulles.

A friend

Abstract

Through their contributions to mixing, heat and gas transfers, bubbles are fundamental in various industrial and environmental contexts, characterized by inertial flows. Understanding the physical mechanisms governing the bubble size distribution (BSD) in turbulent flows is then key when optimizing or quantifying physical processes driven by bubbles. In this thesis we aim at describing bubble breakups by means of numerical simulations of bubbles in both 3D homogeneous and isotropic turbulence and model flows. In this introduction, we recall the theoretical tools required to describe the evolution of the number of bubbles. We also identify one relevant flow topology around bubbles in turbulence, with the aim of finding a model geometry for bubble dynamics.

1 Bubble interactions with turbulence

1.1 Bubbles' contributions

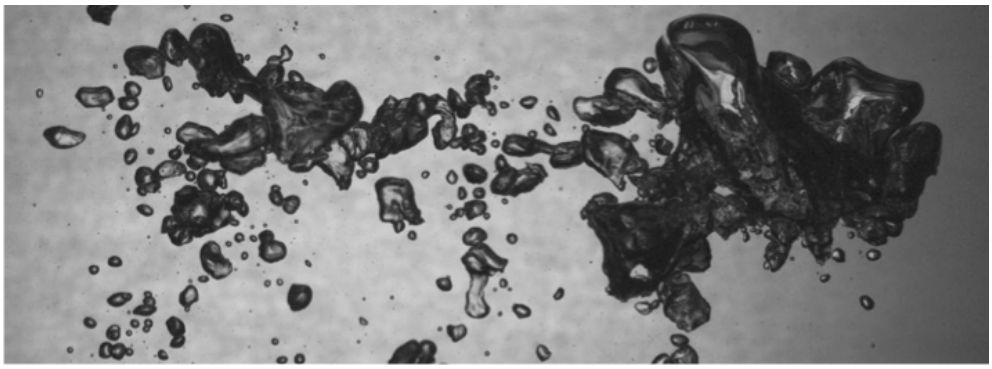

Figure 1.1 – Bubble fragmentation in a turbulent experiment. Picture from D. Ruth, S. Perrard and L. Deike.

The word *bubble* usually refers to two very different configurations: a spherical soap film in which a liquid separates two gas phases, or a pocket of gas immersed in a denser liquid. In this manuscript, we focus on the second configuration, illustrated on figure 1.1. As a moving object in a fluid with an interface, a bubble can contribute to various physical processes of fundamental and practical interests.

At the bubble interface, gas transfers take place. As a consequence, bubbles are widely used in industrial contexts to enhance chemical reactions between a gas and a liquid. A typical example is the bubble column reactor [83, 92, 105, 164]. In these reactors, bubbles are injected at the bottom of a liquid tank. While rising under the action of buoyancy, chemical reactions happen at their interface. In environmental contexts, such as oceans, rivers or waterfalls, bubbles contribute to gas transfers between the atmosphere and the liquid phase [12, 53, 57, 126, 216]. In particular, bubble induced gas transfer is the main pathway for low solubility gases [110], such as O_2, and is therefore essential to the life of the underwater biomass.

Bubbles not only contribute to mass transfer from the gas phase to the liquid phase, they can also induce a mass flux from the liquid to the gas phase. Indeed, when bursting at an interface, bubbles produce droplets through either jet drops or film drops [65, 207, 209]. When bursting happens at the ocean-atmosphere interface, these aerosols play a central role in the thermodynamics of the atmosphere : as condensation nuclei, they can initiate the formation of clouds [15, 16, 18].

As a last example, one can highlight the contribution of bubbles to mixing [164]. For instance, when rising under gravity, bubbles might produce a wake, which creates a local shear. In a cloud of bubbles, the wakes can interact which enhance agitation and possibly creates turbulence [164].

Bubbles are therefore involved in a variety of physical processes, some of them being illustrated on figure 1.2. As all these phenomenon are bubble-size dependent, when optimizing industrial processes or modeling a physical mechanism, one needs to know how many bubbles are present and what is their size, in other words, what is the bubble size distribution (BSD).

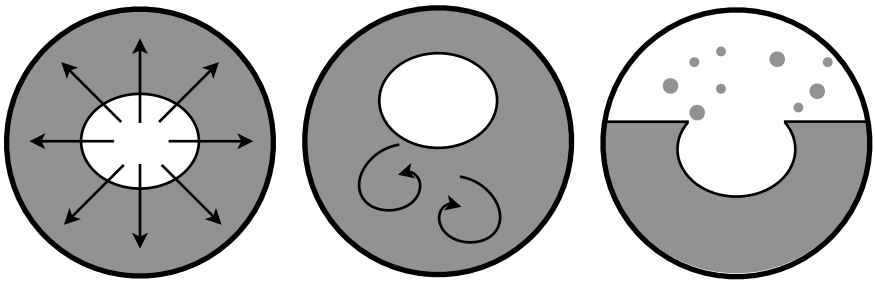

Figure 1.2 – Examples of three different physical processes involving bubbles.

This BSD evolves under the action of the external flow, as bubbles can, for instance, break or coalesce. One needs to identify how the BSD changes in time.

In general, one important parameter for bubble dynamics is the ratio between inertial forces and viscous forces at the bubble scale called the Reynolds number,

$$\mathrm{Re} = \frac{Ud}{\nu} \tag{1.1}$$

where U is a typical velocity scale, d the bubble volume equivalent diameter and ν, the kinematic viscosity of the liquid. In the situations described above, both in environmental and industrial conditions, one can estimate that the Reynolds number is large but finite. In bubble column reactors for instance, it varies from 1 to several hundreds depending on the regime. Consequently, the flow around bubbles is either fully turbulent [52, 53] or characterized by large velocity fluctuations heterogeneously distributed in space and time [164]. As an intermediate step, one could then model the external flow by a 3D isotropic and homogeneous turbulent flow and wonders how the BSD evolves in time.

In this thesis, we focus on the interaction between three dimensional turbulence and bubbles, in order to describe how bubbles break in a turbulent environment. Before introducing the BSD modelling, we recall a few ingredients of isotropic turbulence.

1.2 Statistical properties of 3D isotropic turbulence

Fluid turbulence is characterized by high fluctuations in both space and time, involving a large range of temporal and spatial scales. In this paragraph, we recall the main ingredients of three dimensional isotropic turbulence which will be useful all along the manuscript. We refer to Pope [142] for a more complete description of the statistical properties of 3D turbulence.

Let us consider a fully turbulent flow in a system of characteristic size L, and characteristic velocity U. The Reynolds number at the flow scale is $\mathrm{Re}_L = UL/\nu \gg 1$. One key feature, highlighted in particular by Kolmogorov [96], is the presence of eddies of any size. In the description given by Richardson and illustrated on figure 1.3, energy is continuously injected in the flow at a certain scale, called the integral length scale L_{int}, which sets the scale of the largest eddies in the system. Experimentally this scale is of the order of the object forcing

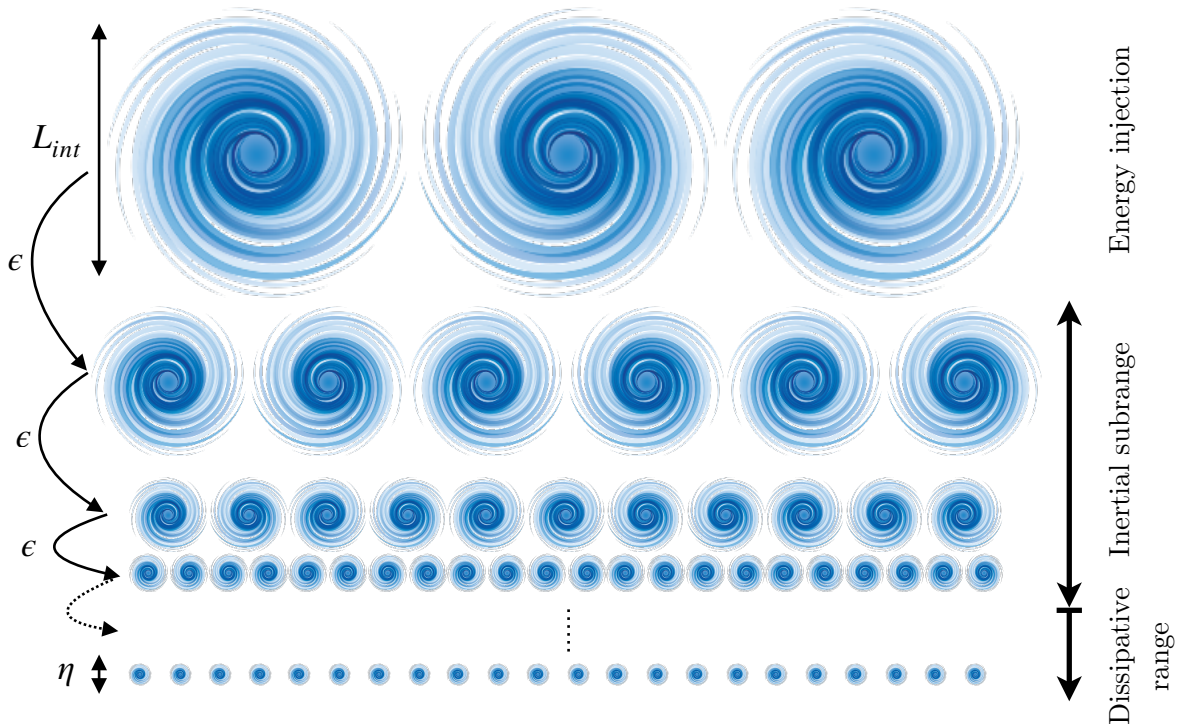

Figure 1.3 – Scheme of the Richardson-Kolmogorov cascade. Energy is injected at a large scale called the integral length scale L_{int}. This energy is then transferred to smaller scales, the inertial scales, with a rate ϵ, until energy is completely dissipated at a scale called the Kolmogorov length scale η.

the flow, for instance the blade dimensions of a propeller. These eddies are characterized by a velocity scale U_{int}, close to the root mean square velocity of the turbulent flow u_{rms}. The Reynolds number at the integral length scale is $\mathrm{Re}_{int} = L_{int}U_{int}/\nu \gg 1$. While the energy is continuously injected into these large structure, it is transferred to smaller scales through non linear interactions. These smaller eddies, in turn, transfer energy to smaller scales, until viscosity becomes important, at a scale ℓ_{DI}, and dissipates the energy. This is the Richardson-Kolmogorov turbulent cascade. The scales contained between L_{int} and ℓ_{DI} form the inertial sub-range, while smaller scales are called the dissipation range.

Since energy is dissipated at small scales and injected at large scales, the rate at which energy is dissipated ϵ is equal to the rate at which the largest eddies, of size L_{int}, transfer energy to smaller scales. One can estimate ϵ from the energy contained in eddies of size the integral scale which is of the order U_{int}^2. In addition, these eddies are associated with a timescale $t_{int} = L_{int}/U_{int}$. From dimensional arguments, we therefore obtain that the energy dissipation rate scales as $\epsilon = U_{int}^3/L_{int}$, in agreement with experimental observations [142].

In the inertial sub-range, ϵ alone controls the statistics of the flow. In particular, a quantity of interest for bubbles in turbulence is the averaged second order longitudinal velocity increments at scale r, $U(r)$, defined such that $U^2(r) = \langle \delta u(r)^2 \rangle$, with $\delta u(r) = u_L(\mathbf{x}, t) - u_L(\mathbf{x} + \mathbf{r}, t)$, where u_L is the velocity component along the direction of $\mathbf{x}$, and brackets denote ensemble averages. This velocity encodes speed variation along a line, in the direction of the line. It is

particularly relevant when investigating object deformations by a flow as it quantifies how fast two points situated on the object surface get closer or away from one another.In a homogeneous and isotropic turbulent flow, for r lying within the inertial range, $\langle \delta u(r)^2 \rangle$ relates to ϵ and r through $\langle \delta u(r)^2 \rangle = C(\epsilon r)^{2/3}$, where C is a numerical constant. Experimental measures reports values of C varying between 2 and 2.2 [142]. We choose $C = 2$ for consistency with Risso et al. [165]. Using this velocity scale we can then define a Reynolds number at scale r in 3D isotropic turbulence, which depends on ϵ and ν

$$\mathrm{Re}(r) = \frac{\langle \delta u(r)^2 \rangle^{1/2} r}{\nu} = \frac{\sqrt{2}\epsilon^{1/3} r^{4/3}}{\nu} \tag{1.2}$$

and is used to compare turbulent fluctuations between various flow geometries [179, 186]. From the energy dissipation rate, and the eddy scale r, within the energy cascade, one can also define a characteristic timescale within the turbulent cascade,

$$t_c(r) = \epsilon^{-1/3} r^{2/3}. \tag{1.3}$$

This timescale is called the eddy turnover time. It corresponds to the typical correlation time, or equivalently the rotation period of eddies of size r lying within the inertial range of scales. This timescale is central when discussing bubble deformations and breakup.

The scale at which energy is completely dissipated is called the Kolmogorov length scale η. It represents the smallest length scale of the flow. The Kolmogorov length scale is defined such that the Reynolds number at its scale is $\mathrm{Re}_\eta = 1$. From equation (1.2), we deduce the expression of the Kolmogorov length scale $\eta = (2)^{-3/8}(\nu^3/\epsilon)^{1/4}$.

The last relevant length scale is the Taylor micro-scale λ which sets the correlation length of velocity gradient. In homogeneous and isotropic turbulence, $\lambda = \sqrt{15\nu/\epsilon}\, u_{rms}$. The Taylor Reynolds number Re_λ, based on the Taylor micro-scale λ, characterizes the turbulent fluctuations

$$\mathrm{Re}_\lambda = \frac{u_{rms}\lambda}{\nu}. \tag{1.4}$$

In this manuscript, we will consider simulations of a homogeneous and isotropic turbulent flow described by Kolmogorov theory. We will also restrain ourselves to bubble sizes lying within the inertial range of the turbulent cascade, where inertia dominates over viscous effects.

2 Bubble size distributions

In order to quantify to contribution of bubbles to any physical mechanism one must know what is the bubble size distribution (BSD) and how it evolves in time. In this section, we first recall the theoretical framework modelling the evolution of the BSD in time, before highlighting some open questions related to bubble breakup.

2.1 Modelling the bubble size distribution

The bubble size distribution is described in terms of the number density of bubbles $\mathcal{N}(V, \mathbf{x}, t)$, defined such that $\mathcal{N}(V, \mathbf{x}, t)\mathrm{d}V\mathrm{d}^3\mathbf{x}$ is the number of bubbles with volume in the range $\mathrm{d}V$ about

V and in the spatial range $\mathrm{d}^3\mathbf{x}$ around $\mathbf{x}$, at time t. Note that another convention is to describe bubble size in terms of a volume-equivalent diameter d. The two approaches are equivalent provided we enforce $\mathcal{N}(V,\mathbf{x},t)\mathrm{d}V\mathrm{d}^3\mathbf{x} = \mathcal{N}(d,\mathbf{x},t)\mathrm{d}d\mathrm{d}^3\mathbf{x}$. In this section, we choose to describe bubbles size in terms of bubble volume V to alleviate notations (especially when describing coalescence and breakups) but we might use d in other chapters. The temporal evolution of the number density of bubbles at a given position $\mathbf{x}$ in time, is given by the conservation equation [87, 157, 215]

$$\partial_t\mathcal{N}(V,\mathbf{x},t) + \boldsymbol{\nabla}\cdot[\mathbf{u}(V,\mathbf{x},t)\mathcal{N}(V,\mathbf{x},t)] + \partial_V[R(V,\mathbf{x},t)\mathcal{N}(V,\mathbf{x},t)] = S[\mathcal{N}](V,\mathbf{x},t) \tag{1.5}$$

where, $\mathbf{u}$ is the mean velocity of bubbles of volume V at position $\mathbf{x}$ at time t, $R(V,\mathbf{x},t)$ is the rate of volume change and $S[\mathcal{N}](V,\mathbf{x},t)$ is a generic source term accounting for birth and death of bubbles of size V induced by coalescence and breakup and involves $\mathcal{N}$ itself. In words, the number density of bubbles of volume V at position $\mathbf{x}$, $\mathcal{N}$, evolves in time due to the advection of bubbles by the surrounding flow (second term of the left hand side, lhs), a continuous evolution of bubble volumes (third term), or physical processes inducing discrete volume changes (right hand size). This equation is also known as number density transport equation or the population balance equation (PBE) and is a generalization of Smoluchowski's coagulation equation [184]. For simplicity and to alleviate notations, we will consider here that the flow and the bubble distribution are homogeneous. From now on we therefore drop all the spatial dependency and remove the advection term $\boldsymbol{\nabla}\cdot[\mathbf{u}(V,\mathbf{x},t)\mathcal{N}(V,\mathbf{x},t)]$ from the PBE. Note however that the contribution of the advective term must be retained as soon as there is a mean flow, as is the case for instance in turbulent jet experiments (for instance [118, 199]). Let us first examine the physical origin of R and S.

The rate of change of bubble volume R originates from two main thermodynamic effects

- Gas compressibility.
- Phase change (dissolution).

These effects involve a single bubble continuously changing size. On the contrary, the source term S encompasses physical mechanisms involving at least two bubbles and generating fluxes between discrete sizes. The two main sources terms are

- Bubble coalescence, associated with a flux from small to large sizes.
- Bubble breakup, associated with a flux from large to small sizes.

To close the PBE, one needs to model each of these four contributions. We first examine the relevance of each term for the PBE of bubbles in turbulence and introduce the modeling strategies.

Gas compressibility: Volumetric oscillations are characterized by the Minnaert frequency, given by

$$f_M(d) = \frac{1}{\pi d}\sqrt{\frac{3\delta P_0}{\rho}} \tag{1.6}$$

where d is the bubble volume-equivalent diameter, δ the polytropic factor, P_0 the ambient pressure and ρ the liquid density. The typical turbulent timescale at size d is given by the eddy turnover time of eddies of size d, $t_c(d) = \epsilon^{-1/3} d^{2/3}$. The volumetric modes will be excited by turbulence, provided the two time scales are of the same order of magnitude, that is

$$f_M(d) t_c(d) = \frac{1}{\pi \epsilon^{1/3} d^{1/3}} \sqrt{\frac{3\delta P_0}{\rho}} \sim 1. \tag{1.7}$$

Let us estimate $f_M t_c$ for an air bubble (polytropic coefficient $\delta = 1.4$) in water (density $\rho = 1000\,\mathrm{kg.m^{-3}}$), at ambient pressure ($P_0 = 100\mathrm{kPa}$). Typical values of the energy dissipation rate range from 10^{-2}, for bubble induced turbulence [92], to 10 $\mathrm{m^2.s^{-3}}$, below breaking waves [52]. For bubbles of size ranging from 100 μm to 1 cm, we obtain

$$1 \ll 14 \leq f_M(d) t_c(d) \leq 530, \tag{1.8}$$

the smallest value of $f_M t_c$ being obtained for the largest bubble size and energy dissipation rate, therefore in a flow where we expect bubbles to be smaller than 1 cm. Hence in turbulence, turbulent timescales are always at least one order of magnitude larger than the period of bubble volumetric oscillations. The latter are never significantly excited by the flow. From now on, we thus neglect compressible effects for bubbles in turbulence.

Gas dissolution: Boussinesq [23] and Levich et al. [108] theoretically investigated the diffusive gas transfer of a bubble rising in a quiescent pure liquid, under the assumption of negligible volume variation. They showed that the gas transfer rate k_L depends on the gas diffusivity in the liquid $\mathcal{D}$, the bubble diameter d and the rising speed U_r through

$$k_L = \frac{2}{\sqrt{\pi}} \sqrt{\frac{U_r \mathcal{D}}{d}}. \tag{1.9}$$

In practice, gas dissolution also depends on the gas concentration in the liquid. The smaller the gas concentration, the faster the gas dissolution. Detsch [58] studied the dissolution of rising air bubbles in quiescent clear and sea water. For bubbles of size ranging from 100 μm to 1 mm he found that the bubble diameter decreases linearly in time. The rate of change of bubble diameter varies between 1 $\mu\mathrm{m.s^{-1}}$ for bubbles rising in clear water with an air saturation of 80%, and 4 $\mu\mathrm{m.s^{-1}}$ at 20% of saturation. Similar values were found in sea water. As a consequence, he measured that 200 μm bubbles dissolve after approximately 3.3 min in clear and sea water and 700 μm bubbles dissolve in about 15 min.

This picture can be modified in the presence of a turbulent surrounding flow as turbulence enhances mixing close to the bubble interface and can therefore enhance dissolution. Farsoiya et al. [68] studied numerically the dissolution of gas bubbles in a turbulent environment. They found that bubble radius shrinks linearly in time, as in the quiescent case. They showed that the decrease rate k_L, also called transfer rate, depends on turbulence intensity and follows $k_L = 0.65\,\mathrm{S_c}^{-1/2} (\epsilon\nu)^{1/4}$, where $\mathrm{S_c} = \nu/\mathcal{D}$ is the Schmidt number, the ratio between the liquid viscosity ν and the gas diffusivity in the liquid $\mathcal{D}$. This relation is measured in a clean liquid

(when no gas is initially dissolved into the liquid), whereas in both industrial and environmental contexts, a large quantity of gas is usually already present. Oceans, for instance, are known to be supersatured in O_2. The obtained value of the transfer rate will therefore be an upper bound for the real value obtained under realistic conditions. We can nevertheless estimate k_L for an air bubble in water. Air is mainly composed of nitrogen (N_2, 80%) and di-oxygen (O_2, 20%), whose Schmidt numbers in water are 240 and 440 respectively. For ϵ ranging from 10^{-2}, to 1 $m^2.s^{-3}$ we obtain that k_L ranges from 0.4 to 1 $mm.s^{-1}$ for N_2 and 0.3 to 1 $mm.s^{-1}$ for O_2. According to these transfer rates, a one millimeter bubble dissolves in more than 1 s. In a turbulent flow of energy dissipation rate ranging from 10^{-2}, to 1 $m^2.s^{-3}$, this dissolution time corresponds to 20 to 100 eddy turnover time at the scale of a 1 mm bubble.

Dissolution becomes important when considering long timescales and small bubbles, which do not break. In this thesis, we restrain ourselves to relatively short timescales, given by the eddy turnover time, so that we can neglect dissolution.

It follows from the two last sections that, when investigating BSD evolution on timescales given by turbulence, one can neglect both compressibility effects and dissolution. We then assume $R = 0$ in the PBE. We now discuss coalescence and breakups.

Coalescence: The flux associated with the coalescence of bubbles of size V_0 with bubbles of size $V - V_0$, creating a bubble of size V is generally written as [102, 111, 112, 174]

$$\Phi_c(V_0, V, t) = \lambda_c(V - V_0, V_0)h(V - V_0, V_0)\mathcal{N}(V - V_0, t)\mathcal{N}(V_0, \mathbf{x}, t) \tag{1.10}$$

where $\lambda_c(V_1, V_2)$ is the collision frequency of bubbles of size V_1 and V_2, and $h(V_1, V_2)$ is the collision efficiency which quantifies the number of collisions effectively leading to coalescence. The source terms associated with coalescence then are written as,

$$S_c[\mathcal{N}](V, t) = \frac{1}{2}\int_0^V \Phi_c(V_0, V, t)\mathrm{d}V_0 - \int_0^\infty \Phi_c(V, V_0 + V, t)\mathrm{d}V_0 = S_c^{\text{birth}} - S_c^{\text{death}}. \tag{1.11}$$

The first term is a birth term encoding the increase in number of bubbles of size V due to the coalescence of two smaller bubbles of size V_0 and $V - V_0$ respectively. The 1/2 factor avoids to double count each coalescence event. The second term is a death term, accounting for the coalescence of bubbles of size V with any other bubble. This death term is alternatively written as

$$S_c^{\text{death}} = \kappa_c(V)\mathcal{N}(V, t) \tag{1.12}$$

where $\kappa_c(V)$ is the coalescence rate of bubbles of size V with any other bubble and reads $\kappa_c(V) = \int_0^\infty \lambda_c(V, V_0)h(V, V_0)\mathcal{N}(V_0)\mathrm{d}V_0$.

We refer to Kolev [95] and Liao et al. [112] for reviews on coalescence models. For a coalescence to occur, two bubbles must interact. As a consequence, in all models, the coalescence frequency depends on the gas volume fraction: when volume fraction is low, the probability that two bubbles collide is low. Since coalescence is quadratic in the bubble size distribution (see the expression of the flux, equation (1.10)), coalescence is the dominant mechanism at large volume

fraction of air. This is typically the case in emulsions, or dense regimes in bubble columns. In these cases, the BSD reaches a stationary state resulting from the competition between breakup and coalescence.

Breakup: The flux Φ_b from size V_0 to V originating from the breakup of the bubble of size V_0 is written as [102, 111, 121],

$$\Phi_b(V_0, V, t) = m(V_0) f(V_0, V) \kappa_b(V_0) \mathcal{N}(V_0, t). \tag{1.13}$$

Here $m(V_0)$ is the average number of child bubbles produced by the breakage of bubbles of size V_0, $f(V_0, V)$ is the probability density to create a bubble of size V from a bubble of size V_0, also called the breakup kernel, and $\kappa_b(V_0)$ is the breakup frequency of bubbles of size V_0. Note that here, conversely to the coalescence flux, Φ_b depends linearly on $\mathcal{N}$. It follows from the expression of the flux that the source terms associated with bubble breakup can also be decomposed in terms of two integral quantities:

$$S_b[\mathcal{N}](V, t) = \int_V^\infty \Phi_b(V_0, V, t) \mathrm{d}V_0 - \frac{1}{m(V)} \int_0^V \Phi_b(V, V_0) \mathrm{d}V_0 = S_b^{\text{birth}} - S_b^{\text{death}}. \tag{1.14}$$

The first integral encodes the increase of the number of bubbles at size V due to the breakage of larger bubbles. The second term, is a death term, which represents the decrease of the number of bubbles of size V due to their own breakage. As before, this death term can be written in a simpler form, noticing that by definition, $\int_0^V f(V, V_0) \mathrm{d}V_0 = 1$,

$$S_b^{\text{death}} = \frac{1}{m(V)} \int_0^V m(V) f(V, V_0) \kappa_b(V) \mathcal{N}(V, t) \mathrm{d}V_0 = \kappa_b(V) \mathcal{N}(V, t). \tag{1.15}$$

At this point, we refer to the following reviews [102, 111, 121, 138] for the different modeling strategies of the breakup kernel and breakup rate. Starting from initially large bubbles, or potentially a single bubble, breakup is a central ingredient controlling the BSD. As breakup occurs on very short timescales, in dilute environments, it first creates a quasi stationary BSD, which eventually evolves due to dissolution, at longer time scales.

Conclusion: BSD in dilute medium In dilute environments, when neglecting the bubble volume change due to gas dissolution and compressibility, the PBE retains only terms related to bubble breakup

$$\partial_t \mathcal{N}(V, t) = \int_V^\infty \Phi_b(V_0, V, t) \mathrm{d}V_0 - \kappa_b(V) \mathcal{N}(V, t) \tag{1.16}$$

which holds in homogeneous settings. Breakup modeling is the subject of this thesis. We aim at identifying, from numerical data, the breakup rate κ_b and the different breaking mechanisms controlling the breakup kernel $f(V_0, V)$. The different modeling strategies for the breakup rate and the breakup kernel are reviewed in the introduction of parts I and II respectively (chapters 4 and 8). We start by reviewing some open questions related to bubble breakup.

2.2 Open questions in bubble breakup

In most applications, breakup cannot be neglected. The bubble size distribution will result from the competition between breakups and other physical mechanisms. There is one situation however where breakup alone controls the BSD: this is the case of dilute environment. This setting allows us to further investigate breakup processes.

2.2.1 Bubble size distribution in dilute regimes

In dilute environments, bubble breakup alone controls the bubble size distribution. Such a dilute environments in observed for instance below breaking waves. Indeed, when the wave overturns it entrains an air cavity which then fragments into multiple bubbles. The impact between the wave crest and the water surface creates an intense flow which develops, in one wave period, into a fully 3D flow [132]. At latter times, most of the wave energy has been dissipated but turbulent regions remain underwater, allowing an efficient bubble fragmentation. This phase, which lasts about two wave periods [132], is called the acoustic phase by Deane et al. [52]. Most of bubble fragmentation occur during this phase and the noise originating from volumetric oscillations is intense. After approximately two wave periods, energy is completely dissipated and only remains in the liquid a quiescent plume of bubbles rising to the surface. The whole process, from the wave breaking to the quiescent plume, lasts few seconds.

Figure 1.4, extracted from Deane et al. [52], shows the bubble size distribution measured below breaking waves, averaged during the acoustic phase. We observe two regimes, separated by a sharp limit for a critical bubble size $d_h \sim 1$ mm. For bubbles larger than a millimeter, the BSD exhibits a steep $d^{-10/3}$ scaling. On the contrary, for bubbles smaller than 1 mm the slope is shallower and follows $d^{-3/2}$. This shape of the bubble size distribution is preserved until the end of the acoustic phase, as shown by the upper curve of the inset plot, figure 1.4. At latter times, during the quiescent phase, (lower curve in inset), we still observe two power-law scalings for the bubble size distribution. However, the transition size as well as the exponents differ: the critical size decreases, and both exponents significantly increase. The BSD evolves due to differential rising speeds (larger bubbles rise faster) and dissolution. In open oceans, Deane et al. [52] reported similar BSD during the quiescent phase, namely two power-law regimes with a transition occurring around 1 mm in size.

To summarize, the BSD below breaking waves evolves following two steps:

1. The acoustic/active phase: Most of bubble fragmentation occurs during this period, creating a BSD characterized by two power-law scalings separated by a characteristic length scale.
2. The quiescent phase: The flow energy has been mostly dissipated. The BSD created during the active phase is the initial condition of this second phase. The BSD evolves due to preferential rising.

As the overall shape of the BSD during the quiescent phase completely originates from the aging of the BSD generated during the active phase, the key question is then to understand what controls the BSD in the fragmentation phase. In particular, we aim at identifying origin of the two power-law scalings and the critical transition size.

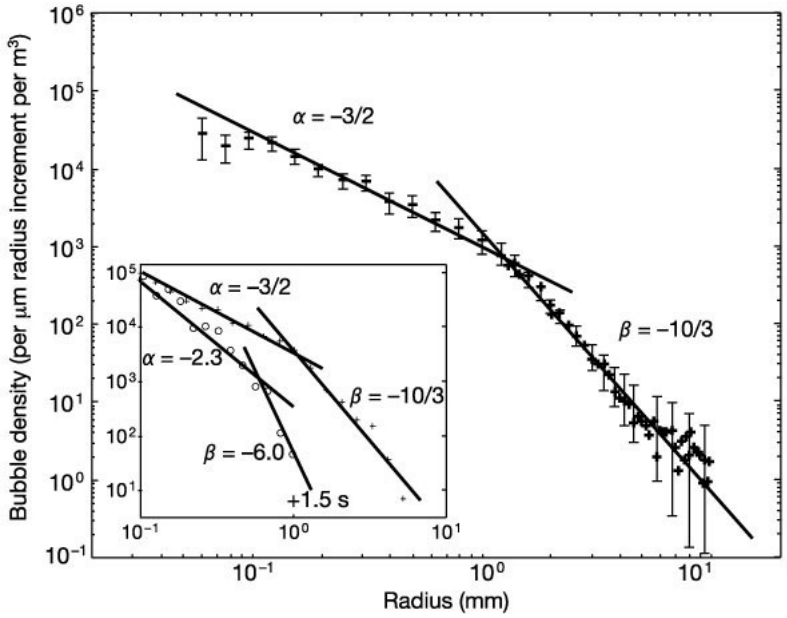

Figure 1.4 – Extracted from Deane et al. [52]. Bubble size distribution measured below breaking waves during the acoustic phase. The BSD exhibits two power-law scaling: $r^{-10/3}$ for $r > 1$ mm, and $r^{-3/2}$ for $r < 1$ mm. The inset compares the BSD at the beginning of the quiescent phase (crosses) and 1.5 s latter. Both slopes increase significantly between these two times.

2.2.2 Critical size - Kolmogorov and Hinze's original idea

As the Reynolds number at the bubble scale is large and the flow turbulent, Deane and Stokes suggested that the critical bubble size could result from the stability of bubbles in isotropic turbulence, as originally investigated by Kolmogorov and Hinze. In a turbulent environment, for bubble size lying within the inertial range of the turbulent cascade, Kolmogorov [97] and Hinze [84] suggested that breakup was primarily controlled by the interaction between the bubble and eddies of its size. The central idea is that a bubble is likely to break when the turbulent forcing due to pressure differences across the bubble, is strong enough to overcome the restoring capillary forces. The former has magnitude $\rho U^2 d^2$, while the latter is of order γd, where U a typical velocity scale and γ the surface tension between the gas and the liquid. The ratio between these two forces define the Weber number, $\mathrm{We} = \rho U^2 d/\gamma$. The typical velocity U scales as the mean-square longitudinal velocity increment $\langle \delta u^2(d) \rangle^{1/2}$ of the undisturbed flow, over a distance d. In homogeneous and isotropic turbulence, for d in the inertial range, the mean velocity increment is related to the average energy dissipation rate ϵ through $\langle \delta u^2(d) \rangle = 2(\epsilon d)^{2/3}$ [96]. This results in defining the Weber number in homogeneous and isotropic turbulence as

$$\mathrm{We} = \frac{2\rho\epsilon^{2/3} d^{5/3}}{\gamma}. \tag{1.17}$$

At low Weber number, capillary forces are strong enough to prevent breakup, while large Weber number bubbles can be easily broken. The limit between the two regimes sets the value of the critical Weber number We_c which is of order unity. This critical Weber number defines the critical bubble size d_h above which a bubble is likely to break through $\mathrm{We}_c = \mathrm{We}(d_h)$ [84, 165].

This critical size, called the Kolmogorov-Hinze scale, reads

$$d_h = \left(\frac{\mathrm{We}_c}{2}\right)^{3/5} \left(\frac{\gamma}{\rho}\right)^{3/5} \epsilon^{-2/5}. \tag{1.18}$$

Deane and Stokes noticed that the Kolmogorov-Hinze scale coincides with the critical size separating the two power-law regimes in the BSD (figure 1.4). They concluded that the critical size in the BSD separates bubbles into two categories: bubbles larger than d_h (super-Hinze bubbles) can still break and their distribution follows $\mathcal{N}(d) \propto d^{-10/3}$, while bubbles smaller than d_h (sub-Hinze bubbles) cannot break anymore and the BSD follows $\mathcal{N}(d) \propto d^{-3/2}$.

This explanation gives a physical argument of the origin of the critical size. However, it is not predictive. Indeed, experimentally-reported values of We_c varies between 0.5 and 8 [84, 118, 123, 165, 180, 199], corresponding to a numerical prefactor $(\mathrm{We}_c/2)^{3/5}$ varying between 0.4 and 2.3. Such variability has several origins: Due to turbulent fluctuations, the Kolmogorov-Hinze scale is a soft limit between breaking and non-breaking bubbles: any bubble can encounter a large enough pressure fluctuation which will break it. It follows that the breakup probability varies continuously with bubble Weber number from 0 (for very small bubbles, very low We) to 1 (for very large bubbles, very large We). It would be interesting to know how this probability evolves with We. In addition, another key quantity is the residence time of bubbles within the turbulent zone. Indeed, the survival probability depends on the time spent by the bubble within the turbulent zone. In experiments, this time corresponds to the observation time, which can be controlled by the bubble rising dynamics, advection speed, or the presence of non homogeneous regions for instance. Under breaking waves, it corresponds to the time during which turbulence is sustained. More generally, taking into account time in the analysis could give a hint to explain the variability of BSD shape. On the same line, turbulence is rarely homogeneous in natural environments, and one must quantify the time spent in each region to predict accurately bubble breakup. In this thesis we therefore propose to answer the following question:

Q1: How can we more properly define a critical Weber number in turbulence?

To answer this question, we will quantify the breakup probability depending on the physical parameters controlling the dynamics (namely, Weber and Reynolds number) as a function of time. To do so, in part I, we focus on bubble deformations and model the breakup probability.

2.2.3 Origin of the two power-law scalings

Qualitatively, the Kolmogorov-Hinze scale separates bubbles which are still likely to break ($d > d_h$), from bubbles which cannot break anymore. Both scalings should therefore be assessed independently.

The power-law scaling for the large bubble size can be recovered from dimensional analysis [52]. If we assume that the BSD originates from the fragmentation of bubbles, with average air injection rate Q (dimensions $\mathrm{m}^3.\mathrm{s}^{-1}$) due to turbulence only, characterized by its energy dissipation rate ϵ, (dimensions $\mathrm{m}^2.\mathrm{s}^{-3}$), by dimensional analysis the number density of bubbles

at scale d is written as

$$\mathcal{N}(d) \propto Q\epsilon^{-1/3}d^{-10/3} \tag{1.19}$$

where $\mathcal{N}$ is defined such that $\mathcal{N}(d)\mathrm{d}d$ is the number of bubbles of size d and is therefore of dimension m^{-1}. Physically, the BSD of super-Hinze bubbles is driven by a balance between air injection and bubble fragmentation, controlled by turbulence at scale d.

Up to now, there is no argument supporting the sub-Hinze bubble size distribution while these bubbles are of tremendous importance. Indeed, at the ocean-atmosphere interface, it has been showed that these small bubbles represent a large fraction of the surface of exchange. Their contribution to gas exchanges between the atmosphere and the oceans cannot be neglected. Additionally, when rising to the surface and bursting, they efficiently produce droplets, which play a central role in cloud formation. From dimensional considerations, another physical mechanism, which needs to be identified, must be taken into account in order to explain the $\mathcal{N} \propto d^{-3/2}$. We therefore ask the following question, which will be the subject of part II:

Q2: What physical mechanism produces the sub-Hinze bubbles and controls their BSD?

Answering this question has a general interest which goes beyond the oceanic context. Indeed, when other mechanisms are relevant, such as coalescence or dissolution, the BSD of small bubbles will result from a competition between the different physical processes.

3 From turbulence to model flows

In this thesis, together with the investigation of bubbles in turbulence, we propose to study bubble deformations and fragmentation in model configurations. These studies allow us to extract the dominant physical mechanism for bubble dynamics in more controlled flows. Building on the review from Meneveau [127] and references therein, we first describe the dominant local flow topologies in turbulence. Then, we identify the ones relevant for bubble deformations and breakup.

3.1 Main local flow topologies in single phase turbulence

The dynamics of a bubble, or more generally of a particle, is driven by the local velocity field $\mathbf{u}(\mathbf{x}, t)$. Depending on the local flow geometry, a large variety of displacement and deformations can be obtained. In this thesis, we want to identify the flow geometries driving bubble deformations and breakup. In general, one can characterize the local flow geometry around an arbitrary position $\mathbf{x_0}$ by linearizing the velocity field $\mathbf{u}(\mathbf{x}, t)$ around this point (provided the flow is not singular). The linear approximation of the velocity component u_i reads

$$u_i(\mathbf{x}, t) = u_i(\mathbf{x_0}, t) + A_{i,j}(\mathbf{x_0}, t)(x_j - x_{0j}) + ... \tag{1.20}$$

where $A_{i,j}$ are components of the velocity gradient tensor $\mathbf{A}$ defined by

$$A_{i,j} = \partial_{x_j} u_i. \tag{1.21}$$

Assuming the bubble moves with the local velocity $u_i(\mathbf{x_0}, t)$, $\mathbf{A}$ will drive deformations.

3.1.1 Strain rate and rotation rate tensor

A first natural decomposition of the velocity gradient tensor decomposes $\mathbf{A}$ into its symmetric $\mathbf{S}$ and antisymmetric $\mathbf{\Omega}$ parts. The symmetric tensor $\mathbf{S}$ is the strain rate tensor which encodes the stretching and compression directions of the velocity. As a real, symmetric tensor, it is diagonalizable in an orthogonal basis. In addition, as antisymmetric matrix are traceless $\mathrm{Tr}(\mathbf{\Omega}) = 0$. We deduce the expression of the trace of $\mathbf{S}$

$$\mathrm{Tr}(\mathbf{S}) = \mathrm{Tr}(\mathbf{A}) = \partial_{x_i} u_i. \tag{1.22}$$

Since we consider incompressible flows, $\mathbf{A}$ is also traceless which imposes that

$$\lambda_1 + \lambda_2 + \lambda_3 = 0 \tag{1.23}$$

where $\lambda_{i\in[1,3]}$ are the three real eigenvalues of $\mathbf{S}$. They are associated with three eigenvectors $\mathbf{e_1}$, $\mathbf{e_2}$ and $\mathbf{e_3}$. By convention, we assume $\lambda_1 > \lambda_2 > \lambda_3$. It follows from equation (1.23) that $\lambda_1 \geq 0$ and $\mathbf{e_1}$ represents the main stretching direction, $\lambda_3 \leq 0$ and $\mathbf{e_3}$ encodes the main compression direction. The last eigenvalue λ_2 can have both signs.

The antisymmetric part of $\mathbf{A}$, $\mathbf{\Omega}$ is the rotation rate tensor which encodes the direction and the intensity of the local vorticity $\omega = \boldsymbol{\nabla} \times \mathbf{u} = \omega \mathbf{e}_\omega$, where $\omega \geq 0$ is the vorticity intensity and $\mathbf{e}_\omega$ is the unit vector along the vorticity direction.

Bubbles might be affected by both vorticity and strain. Therefore, it is interesting to look at the relative orientation of vorticity with respect to the three directions $\mathbf{e_1}$, $\mathbf{e_2}$ and $\mathbf{e_3}$. This is done by measuring the probability density function of the angle between the two vectors, or equivalently the norm of the scalar product between the two unit vectors $|\mathbf{e}_\omega \cdot \mathbf{e_i}|$. When the norm is 1, the vectors are aligned, when it is zero, the two vectors are orthogonal to each others. Ashurst et al. [7] measured the probability density function (pdf) of these three norms in a DNS of isotropic turbulence. As reported on figure 1.5a (adapted from Meneveau [127]), they reported a preferential alignment between the intermediate eigenvector $\mathbf{e_2}$ and vorticity. On the contrary, $\mathbf{e_3}$ tends to be orthogonal to $\mathbf{e}_\omega$, and no preferential alignment is found with $\mathbf{e_1}$ (the pdf is flat). These results were latter confirmed by experimental investigations (see for instance [134, 195]).

This flow structure is valid around any arbitrary point in turbulence. Yet, as bubbles have a finite size, they are sensitive to coarse-grained velocity gradients at their scale. Masuk et al. [123] using Particle Image Velocimetry (PIV) measurements, investigated the flow structure around bubbles. They found that the flow alignments are preserved in the presence of a bubble and when coarse-graining at the bubble scale, suggesting that the flow structure is weakly affected by the presence of the bubble. In the next section, we identify the predominant flow topologies using orientation-invariant scalars of the velocity gradient tensor.

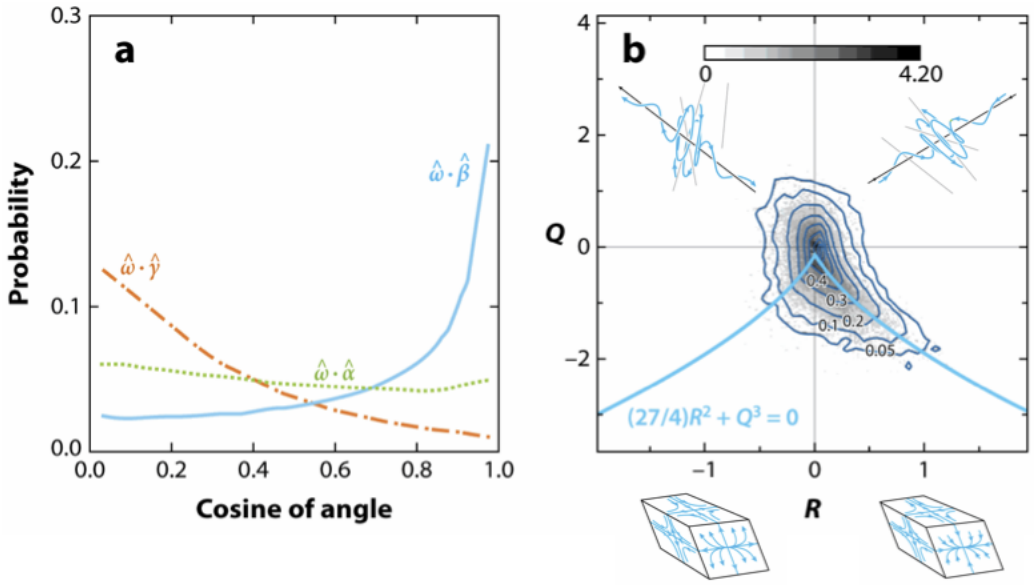

Figure 1.5 – Adapted from Meneveau [127]. a) Pdf of the norm of the scalar product between straining directions and vorticity direction. We have the following correspondence with the main text: $\hat{\alpha} = \mathbf{e_1}$, $\hat{\beta} = \mathbf{e_2}$, $\hat{\gamma} = \mathbf{e_3}$ and $\hat{\omega} = \mathbf{e}_\omega$. This subfigure is adapted by Meneveau from Ashurst et al. [7]. b) Joint pdf of R and Q measured by Gulitski et al. [80] in an atmospheric boundary layer at high Reynolds number. Schemes represent the main flow topology in each zone. The solid blue line separates vorticity free flows (below the line) from flows where vorticity is non zero (above the line).

3.1.2 Local flow topology - RQ plane

For this part, we mostly rely on the paper by Chong et al. [44] and Cantwell [29]. In the previous section, we described the flow field by decomposing velocity into stretching/compression and vorticity. These information can be summarized, for an incompressible flow, into two orientation-invariant scalars. As a 3x3 matrix, the eigenvalues of $\mathbf{A}$, are solution of the characteristic equation

$$\det[\mathbf{A} - \lambda\mathbf{I}] = 0, \tag{1.24}$$

where det is the determinant, and $\mathbf{I}$ the identity matrix. For a 3x3 matrix the characteristic equation rewrites

$$\lambda^3 + P\lambda^2 + Q\lambda + R = 0 \tag{1.25}$$

where

$$P = -\operatorname{Tr}[\mathbf{A}] \tag{1.26}$$

$$Q = \frac{1}{2}\left[\operatorname{Tr}[\mathbf{A}]^2 - \operatorname{Tr}\left[\mathbf{A}^2\right]\right] \tag{1.27}$$

$$R = -\det[\mathbf{A}] = \frac{1}{3}\left[-P^3 + 3PQ - \operatorname{Tr}\left[\mathbf{A}^3\right]\right] \tag{1.28}$$

where Tr is the trace. The three quantities (P, Q, R) fully characterize the flow structure. As $\mathbf{A}$ is traceless (the flow is incompressible), $P = 0$ and only two parameters remain $R = -\operatorname{Tr}[\mathbf{A}^2]/2$

and $Q = -\operatorname{Tr}[\mathbf{A}^3]/3$. Depending on the values of R and Q, the three eigenvalues of $\mathbf{A}$ can be either all real roots or a pair of complex conjugate roots and a real root. In the RQ-space, on the line separating these two domains, the three roots are real and two are equal. One can show that this line, separating real roots from complex roots, is solution of

$$D = \frac{27}{4}R^2 + Q^3 = 0 \tag{1.29}$$

where D is the discriminant of $\mathbf{A}$. For $D > 0$, $\mathbf{A}$ has complex eigenvalues , there is vorticity in the flow, while for $D < 0$ the three eigenvalues are real [29], $\mathbf{A}$ is symmetric. Figure 1.5b shows the R-Q plane with the prevalent flow geometry in each region. The blue line indicates the separation given by equation (1.29), which we call separatrix. One can distinguish four regions corresponding to four flow topologies:

- Below the separatrix and $R \leq 0$: There are three real eigenvalues, two of them being negative: the flow stretches along one direction $\mathbf{e_1}$ and compresses along the two other directions (bottom left scheme).
- Below the separatrix and $R \geq 0$: There are three real eigenvalues two of them being positive: the flow is compressing along one direction $\mathbf{e_3}$ and stretches along the two other directions (bottom right scheme).
- Above the separatrix and $R \leq 0$: Two eigenvalues are complex conjugates. The flow consists of a spiraling around one stretching direction, focusing on some plane (top left scheme).
- Above the separatrix and $R \geq 0$: Two eigenvalues are complex conjugate. The flow consists of a spiraling along a compression direction, expanding in the other directions (top right scheme).

On the separatrix, the three eigenvalues are real and two of them are equal. These geometries correspond to axi-symmetric straining flows, either stretching ($R \leq 0$) or compressing ($R \geq 0$) along the axis of symmetry.

All these flow topologies are not equally represented in a turbulent flow. Cantwell [30] was the first to measure the joint pdf of R and Q, in a direct numerical simulation. He showed that the pdf has a very peculiar shape, being skewed toward the right branch of the separatrix, defined by $Q = -3/2^{2/3}R^{2/3}$, called the Vieillefosse tail in reference to his analytical work [203, 204]. This flow feature has been recovered both numerically and experimentally by several authors [45, 80, 139, 194] (subset of references given in [127]). An example of this joint pdf is given on figure 1.5b, also adapted from Meneveau [127]. The figure shows the experimental joint pdf from Gulitski et al. [80], measured in an atmospheric boundary layer at high Reynolds number. While the upper part ($Q > 0$) is mostly symmetric with respect to $R = 0$, the probability is larger in the lower right quadrant.

The flow topology at a bubble scale r can be obtained by coarse-graining the velocity gradient tensor over a region of scale r [40, 137]. This coarse-grained tensor, $\mathbf{A}'$, is defined by

$$A'_{ij} = \frac{1}{\Gamma}\int_{\Gamma} A_{ij}\mathrm{d}^3x \tag{1.30}$$

where Γ is a volume of characteristic size r. As before, we can define the same corresponding invariants R' and Q'. Figure 1.6, adapted from Naso et al. [137] shows the evolution of the RQ

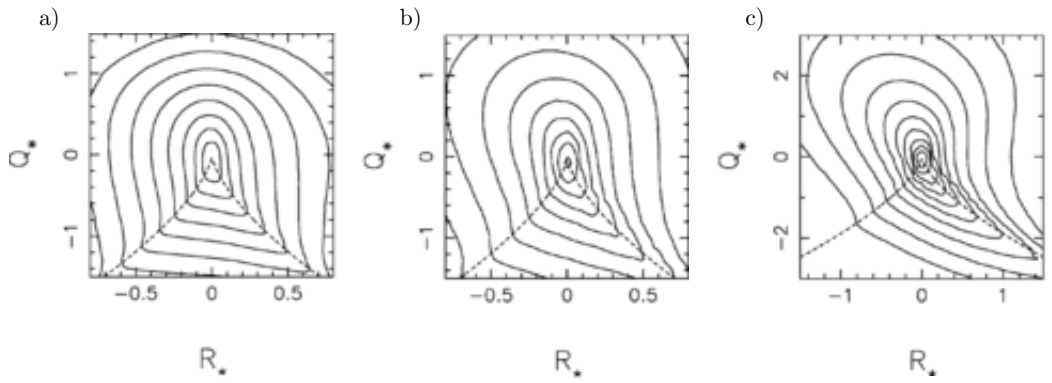

Figure 1.6 – Adapted with permission from Naso et al. [137]. Isocontours of the joint pdf of R and Q plane for the coarse-grained velocity gradient tensor in a DNS of isotropic turbulence. The velocity gradient tensor is coarse-grained at the scale a) $r = L_{int}$ (injection scale), b) $r = L_{int}/8$ (inertial range) c) $r = 2\eta$ (viscous range). Isocontours are spaced logarithmically and separated by factors of e.

plane, for the coarse-grained velocity tensor, as a function of r, measured in a DNS of isotropic turbulence at $\mathrm{Re}_\lambda = 130$, with $L_{int}/\eta \sim 100$. The two axis show the normalized values of R' and Q' respectively, defined by $R_\star = R'/\langle \mathrm{Tr}\left[(\mathbf{S}')^2\right]^{3/2}\rangle$ and $Q_\star = Q'/\langle \mathrm{Tr}\left[(\mathbf{S}')^2\right]\rangle$ respectively, where $\mathbf{S}'$ is the symmetric part of $\mathbf{A}'$. At the integral scale, (figure 1.6a, $r = L_{int}$), the joint pdf is nearly symmetric with respect to $R_\star = 0$. This symmetry is lost for scales within the inertial range (figure 1.6b, $r = L_{int}/8$), for $Q_\star < 0$. As for the local velocity gradient tensor, the probability is larger on the right branch of the separatrix. Two directions of stretching are more likely than two directions of compression. This effect is much more pronounced in the dissipative range, for $r \approx \eta$ (figure 1.6c).

We conclude that, for bubble sizes lying within the inertial range of turbulence, vorticity is combined with two directions of stretching or compression with equal probability. In the absence of vorticity, flows with two stretching directions are more likely than flows with two compressing directions.

3.2 Relevant flow geometries for bubble breakup

In the previous section we have identified the main flow topologies around bubbles in turbulence when their size lies within the inertial range. Nevertheless, flow configurations are not equally efficient in deforming and breaking bubbles. As a consequence, only a few flow geometries might be relevant for bubble dynamics.

One way to assess the relative efficiency of local flows is to investigate the relative orientation between the bubble shape and the stretching, compressing and vorticity direction. In turbulence, bubbles tend to elongate in one preferential direction, before potentially breaking. Several examples are given on figure 1.7. This kind of deformations and breakup lies in the *cigar-shape* type identified by Hinze [84].

One can envision two flow geometries around these bubbles: either a stretching along the longest bubble axis or a vorticity dominated field, with a vorticity vector aligned with the bubble

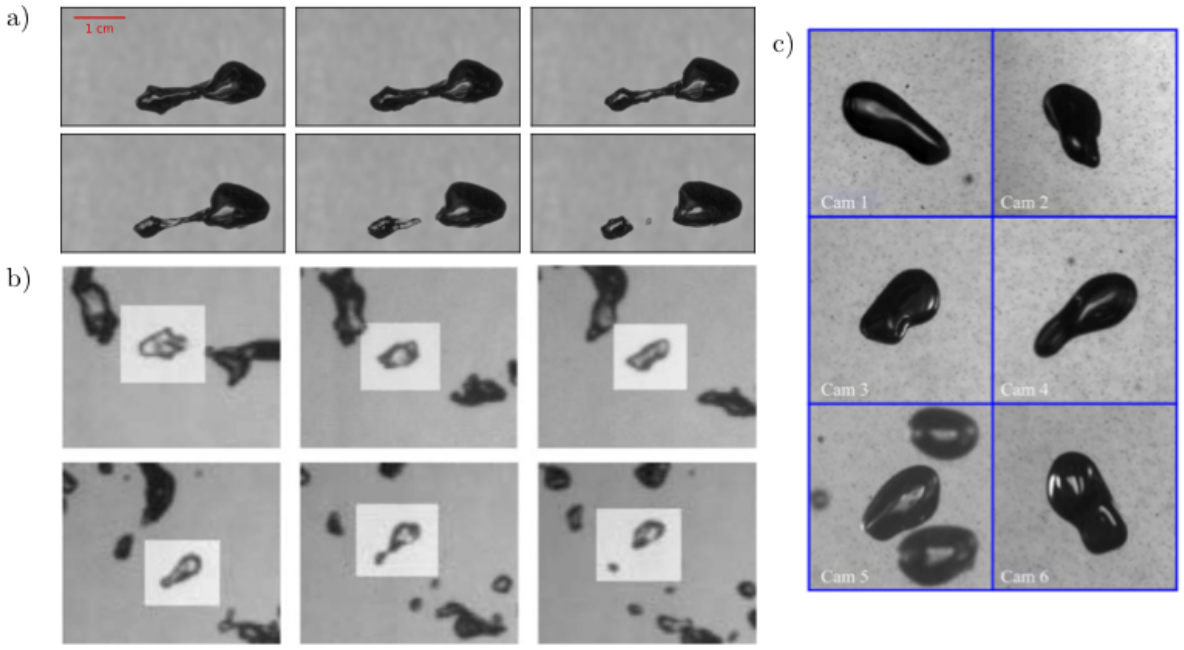

Figure 1.7 – Examples of bubble deformations and breakup in turbulence. a) Pictures taken by Daniel Ruth of a centimetric air bubbles in water, in isotropic turbulence. Evolution from left to right, top to bottom. b) Adapted from Rodríguez-Rodríguez et al. [170]. Deformations and breakup of a bubble of diameter 2.5 mm, at the centreline of a turbulent water jet. Temporal evolution from left to right, top to bottom. c) Adapted from Masuk et al. [123]. Six views of the same air bubble, taken by six high speed cameras, of a millimetric bubble, in a turbulent jet facility.

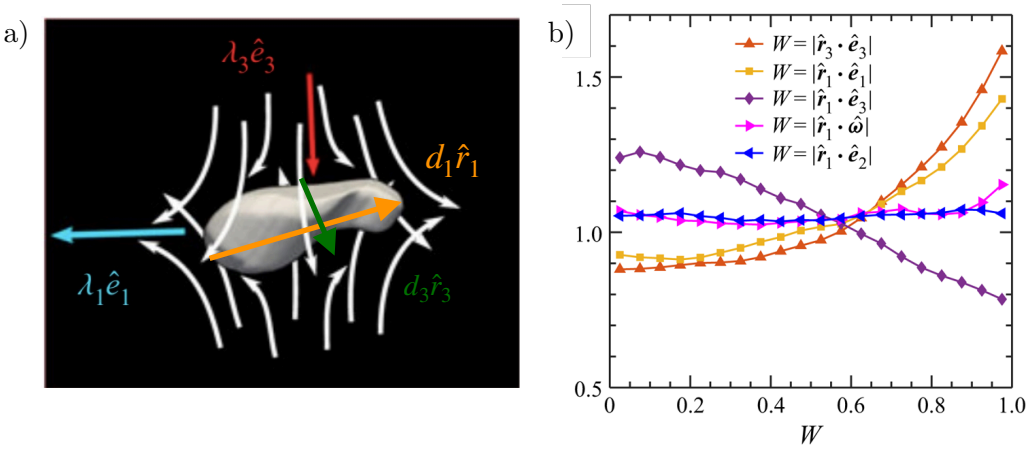

Figure 1.8 – Adapted from Masuk et al. [124]. a) Schematic representation of deformed bubble and coarse-grained flow surrounding it. The bubble longest axis defines $\mathbf{r_1}$. The shortest axis defines $\mathbf{r_3}$. b) Pdf of the relative orientation between bubble axes and the local strain and vorticity.

main axis. Masuk et al. [124] correlated the coarse-grained flow geometry with the bubble shape. In particular, they measured the relative orientation between the local strain and vorticity and the direction of the longest, $\mathbf{r_1}$, and shortest, $\mathbf{r_3}$, bubble axis, defined on figure 1.8a. These two vectors, $\mathbf{r_1}$ and $\mathbf{r_3}$ are defined by the furthest (resp. closest) interface point from the bubble center of mass, and are therefore not orthogonal. Figure 1.8b, adapted from [124], shows the pdf of the relative orientation between the bubble and its surrounding flow (therefore coarse-grained at the bubble scale). It clearly appears that the main bubble axis $\mathbf{r_1}$ aligns with the principal straining direction (maximum at $\mathbf{r_1}\cdot\mathbf{e_3}=1$), while being preferentially orthogonal to the main compressing direction (maximum at $\mathbf{r_1}\cdot\mathbf{e_1}=0$). Strikingly, no preferential alignment is found with the vorticity direction. The shortest bubble axis, on its side, aligns with the principal compressing direction. These results suggest that the most relevant flow geometries lie in the lower left quadrant of the RQ plane, below the separatrix, which surprisingly correspond to the most unlikely flows. In this region, vorticity is unimportant and one finds two directions of compression and one direction of stretching. In addition, as noticed by Rodríguez-Rodríguez and co-authors [162, 170], the breakup dynamics is fast compared to the other time scales thus we can reasonably assume that the flow is axi-symmetric.

We conclude that, as a first approximation, it is not necessary to include vorticity in the study. One of the most relevant model flow geometry for bubble deformations and breakup is therefore the uniaxial straining flow.

4 Outline of the manuscript

In this thesis, we aim at answering the two identified questions: *Q1* How can we more properly define a critical Weber number in turbulence? *Q2* What physical mechanism produces the sub-Hinze bubbles and controls their BSD? To do so, we propose to analyse numerically bubble deformations and breakup in both a model flow (the uniaxial straining flow) and DNS

of isotropic turbulence.

Part I is devoted to *Q1*, namely, defining the probability for a bubble to break depending on the main control parameters. To do so, we first describe bubble deformation and breakup in the model geometry (chapter 5). Then, we extend our study to bubble deformations in turbulence (chapter 6). Along the line, we will define a breakup rate, κ_b, for the population balance equation (chapter 7).

Part II addresses *Q2* and focuses on the sub-Hinze bubble generation. We first identify the origin of sub-Hinze bubbles in turbulence (chapter 9). Then, we describe more precisely their production in the more controlled situation of a uniaxial straining flow (chapter 10). Doing so, we obtain elements to constrain the expression of the breakup kernel $f(V_0, V)$ of the population model equation.

Before addressing the two main questions, we first describe in details the two numerical set-up used in this thesis (chapter 2), and the theoretical tools (chapter 3).

Chapter 2

Numerical configurations: Principle and convergence study [1]

On top we find the experimentalists, then the numericists and at the very bottom people doing machine learning.

A chairman

Abstract

In this chapter we present the numerical solver that we use, the *Basilisk* Flow solver and its specific features. Then we introduce the two numerical set-ups studied in this thesis. The first one is the uniaxial straining flow configuration used in chapters 5 and 10. The second one is a direct numerical simulation of a bubble in a turbulent flow, investigated in chapters 6, 7 and 9.

Contents

1. Some of the results in this chapter have been published in Rivière et al. [167] and Perrard et al. [141].

1 Basilisk flow solver: A brief overview

In this thesis, bubble dynamics and breakup are investigated by means of numerical simulations using the flow solver *Basilisk* (http://basilisk.fr). In this section, we recall the numerical methods implemented in *Basilisk*.

1.1 General considerations

Basilisk [86] is a free open source software written in C, first developed by S. Popinet, and then collaboratively by other authors to solve partial differential equations [2, 143, 144]. Several solvers are implemented, using the finite volume implementation, including the Navier-Stokes solver, that we use in this work. The interface between the gas and the liquid is represented using a sharp Volume-Of-Fluid implementation (VOF) [143], coupled with a robust implementation of height functions based interface curvature computation [144]. The accuracy of the solver has been largely demonstrated in complex multiphase flows, including wave breaking [56, 132], splashing [116, 190], bubble bursting [16] or liquid rim fragmentation [4].

In practice, the interface is tracked using the volume fraction $C(\mathbf{x}, t)$ of liquid in each cell of the computational domain, with $C = 1$ in the liquid, $C = 0$ in the gas, and $0 < C < 1$ in interfacial cells. The liquid density and dynamic viscosity are ρ and μ respectively (and $\nu = \mu/\rho$ the liquid kinematic viscosity). We define the gas-liquid density and viscosity ratios ρ_R and μ_R respectively, so that the gas density and viscosity read $\rho.\rho_R$ and $\mu.\mu_R$. The density and dynamic viscosity in each cell then write $\rho(C) = \rho(C + \rho_R(1 - C))$ and $\mu(C) = \mu(C + \mu_R(1 - C))$. Both fluids are incompressible. We denote by γ the surface tension coefficient between the two phases, κ the local curvature and $\mathbf{n}$ the interface normal. We solve the one-fluid formulation of the Navier-Stokes equations, with variable density and viscosity

$$\rho(C)\left[\partial_t \mathbf{u} + \mathbf{u}\cdot\boldsymbol{\nabla}\mathbf{u}\right] = -\boldsymbol{\nabla}P + \boldsymbol{\nabla}\cdot\left[2\mu(C)\mathbf{D}\right] + \gamma\kappa\delta_S\mathbf{n} + \mathbf{f} \tag{2.1}$$

$$\partial_t\rho(C) + \boldsymbol{\nabla}\cdot\left[\rho(C)\mathbf{u}\right] = 0 \tag{2.2}$$

$$\boldsymbol{\nabla}\cdot\mathbf{u} = 0 \tag{2.3}$$

where $\mathbf{D} = (\boldsymbol{\nabla}\mathbf{u} + \boldsymbol{\nabla}\mathbf{u}^T)/2$ is the deformation tensor, δ_S is a Dirac function which concentrates the surface tension force at the interface [144], and $\mathbf{f}$ is a possible volumetric force whose expression varies among chapters.

1.2 Adaptive mesh refinement

Basilisk is based on an adaptive quad-octree grid, allowing to save computational time while resolving all the important length scales of each problem [143–145]. The grid adaptation algorithm is explained in great details in Van Hooft et al. [197]. Refinement is controlled by two parameters: the maximum refinement level Le and the criterion used to refine. The maximum refinement sets the minimum grid size as $\Delta = L/2^{Le}$, where L is the box size. The refinement criterion can be seen as the maximum error tolerated when refining/coarsening the grid. In both simulations presented in this thesis, we evaluate the error on both the velocity field and

the curvature of the interface. This choice allows us to minimize the error on the surrounding flow field as well as on the interfacial forces. Note that when the criterion is too restrictive, we obtain a regular grid of size the minimum grid size while a too coarse criterion does not allow any grid refinement. In practice, to test the numerical convergence of our simulations, we fix the refinement criteria and vary the maximum level Le.

1.3 Numerical parameters shared among chapters

While the numerical set-up varies between chapters, some parameters will be shared among them.

The force is $\mathbf{f} = \mathbf{0}$ in the stagnation point flow (chapters 5 and 10), while it is $\mathbf{f}(\mathbf{x}, t) = CA\mathbf{u}(\mathbf{x}, t)$, with A a constant, in the turbulence case (chapters 6, 7, 9), to maintain homogeneous and isotropic turbulence in the liquid phase [172]. In all chapters we have $\rho_R = 850$, the water-air density ratio. In turbulent simulations, chapters 6, 7 and 9, we use $\mu_R = 25$, close to the water-air ratio of 55. This choice eases the numerical computation, as it thickens the viscous boundary layer, which usually scales as $\sqrt{\nu}$. The boundary layers are therefore easier to resolve numerically. For consistency with these chapters, the value $\mu_R = 25$ is also used in the stagnation point simulation in chapter 5. However, we use the value $\mu_R = 55$ in chapter 10, for a better description of satellite bubbles generation.

2 A model flow configuration: the uniaxial straining flow

We have seen that one of the most relevant geometry for bubble deformations and breakup in turbulence is the uniaxial straining flow. In this section, we present the numerical configuration and verify numerical convergence for the single and the two phase simulation.

2.1 Physical setting

In a homogeneous and isotropic turbulent flow, bubbles are submitted to various flow configurations and intensities. As emphasized in the previous chapter, the uniaxial straining flow is among the most relevant flow geometries for bubble deformations and breakup, as schematized on figure 2.1. In this work, we aim at mimicking bubble deformations induced by this flow geometry, for bubbles of size close to the stability threshold, the Kolmogorov-Hinze scale d_h.

We first estimate the value of the Reynolds number at the Kolmogorov-Hinze scale. We recall that in homogeneous and isotropic turbulent flow, for a bubble size lying within the inertial range of the turbulent cascade, the Reynolds number at the bubble scale is written as

$$\mathrm{Re}_t = \frac{\langle \delta u(d)^2 \rangle^{1/2} d}{\nu} = \frac{\sqrt{2}\epsilon^{1/3} d^{4/3}}{\nu}. \tag{2.4}$$

In the oceans for instance, below breaking waves, $\epsilon \approx 1$ m^2.s^{-3} and the Kolmogorov-Hinze scale lies between 500 μm to 1 mm [52]. It follows that the Reynolds number at the Kolmogorov-Hinze scale ranges from 50 to 150. We therefore focus on Reynolds number varying between 10 and 800.

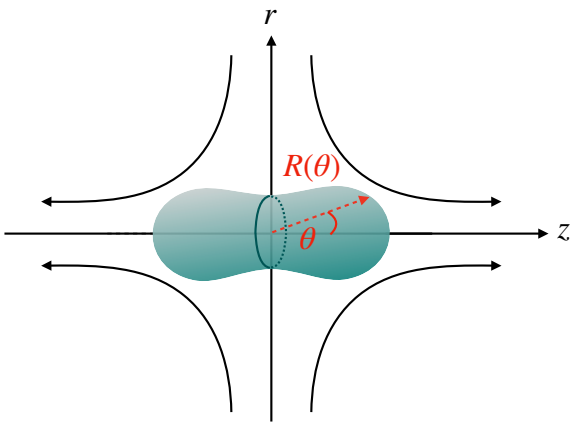

Figure 2.1 – Scheme of a bubble (in blue) is a uniaxial straining flow. The horizontal z-axis is the axis of symmetry. The vertical r-axis denotes the radial direction. Arrows qualitatively illustrate the direction of the surrounding flow.

In the following, we build a numerical experiment imitating bubble deformations induced by straining regions. In chapter 5 we investigate the deformation and breakup dynamics of a bubble in a uniaxial straining flow. In chapter 10 we focus on the generation of satellite bubbles. Let us first explain the principle of the numerical simulations, before testing the numerical convergence of each step in sections 2.2 and 2.3.

We solve the axi-symmetric Navier-Stokes equations in a cylindrical domain of size $L = 10R_0$ ($R_0 = d/2$), with left-right symmetry, ie $z \in [0, L]$ and $r \in [0, L]$ (schematized on figure 2.2). Imposing left-right symmetry allows us to maintain the bubble at the center of the stagnation point flow and therefore to focus on bubble deformations. We first create a uniaxial (axi-symmetric) straining flow whose velocity field is written as,

$$\mathbf{u}(r, z) = Ez\mathbf{e_z} - \frac{1}{2}Er\mathbf{e_r} \tag{2.5}$$

where $E \geq 0$ is the typical shear amplitude, $\mathbf{e_z}$ and $\mathbf{e_r}$ are unit vectors of the axi-symmetric coordinate system (z, r) (defined on figure 2.1). The velocity field is associated with the following pressure field,

$$P(r, z) = -\frac{1}{8}\rho E^2 r^2 - \frac{1}{2}\rho E^2 z^2 + P_0 \tag{2.6}$$

where P_0 is a constant. Both the velocity field and the pressure field are bi-polar.

We then inject a spherical bubble of diameter d, radius $R_0 = d/2$, at the center of the stagnation point flow and let the bubble evolve. Physically, this numerical experiment corresponds to a bubble quickly transported or suddenly submitted to a new straining region. Gas-liquid density ratio is $\rho_R = 850$, close to the air-water ratio. As discussed earlier, gas-liquid dynamic viscosity ratio is $\mu_R = 25$ in chapter 5 and 55 in chapter 10, close to the air-water ratio. Both phases are assumed incompressible, immiscible and non condensible.

Bubble dynamics is controlled by two dimensionless numbers. The first relevant dimensionless number is the Weber number which compares inertia and capillary forces at the bubble

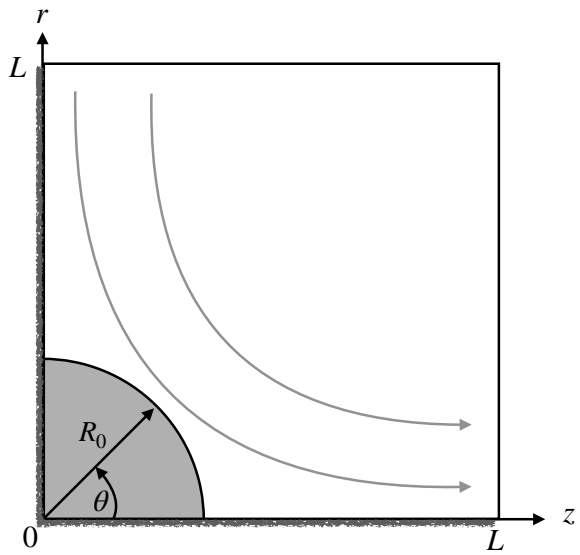

Figure 2.2 – Numerical domain (not at scale). The bottom axis (z-axis) is the axis of symmetry. The vertical (r-axis) is the radial direction. The initially spherical bubble is schematized by the grey region of radius R_0. Grey errors schematize the direction of the flow.

scale. It is based on the characteristic velocity $U = Ed$ at the bubble scale,

$$\mathrm{We} = \frac{\rho U^2 d}{\gamma} = \frac{\rho E^2 d^3}{\gamma}. \tag{2.7}$$

At low Weber number, bubbles are mainly rigid and do not break while they break at large enough Weber number. The second relevant parameter is the Reynolds number

$$\mathrm{Re} = \frac{Ud}{\nu} = \frac{Ed^2}{\nu}, \tag{2.8}$$

which compares inertia and viscous force. To make the analogy with turbulent configurations, we vary Re in an intermediate range, between 10 and 800. Note that one could use alternatively one of these two dimensionless number the Ohnesorge number $\mathrm{Oh} = \sqrt{\mathrm{We}}/\,\mathrm{Re} = \nu\sqrt{\rho/(d\gamma)}$ which thus, does not include the straining rate but only the material and geometrical properties of the bubble. While the Ohnesorge number plays an important role in the final stage of a fluid breakup [26, 64], it is more relevant in our configuration to use dimensionless numbers that involve the inertia of the flow.

The next two sections detail the numerical configuration and the choice of numerical parameters. We fist check numerical convergence for the single phase simulation, before investigating grid independence for bubble deformations and breakup.

2.2 Flow creation

We first run single phase simulations to obtain a uniaxial straining flow at a given Reynolds number. We call these single phase simulations, precursors. To create the uniaxial straining flow, we use Dirichlet boundary conditions for the velocity field at $r = L$ (inflow) and Neumann condition at $z = L$ (outflow), and conversely for the pressure. Starting from a fluid at rest,

the velocity field converges in a typical time $1/E$, to the straining flow. To vary the Reynolds number, we vary the numerical value of E, which changes the boundary conditions. Another relevant choice is to change the value of ν while keeping E constant.

We test the numerical convergence for the precursor simulations by comparing the total kinetic energy in the box in the absence of a bubble to the predicted value when varying the maximum level of refinement Le. Given the theoretical velocity field in a stagnation point flow we get the theoretical density of kinetic energy

$$K_{th} = \frac{1}{\pi L^3}\int_0^L \mathrm{d}x \int_0^L \mathrm{d}y \frac{1}{2}\rho \mathbf{u}^2 = \frac{11}{48}E^2L^2. \tag{2.9}$$

We denote K the experimental density of kinetic energy in the precursor simulations. The mismatch between K and K_{th} defines the error

$$\text{error} = 100.\frac{|K - K_{th}|}{K_{th}}. \tag{2.10}$$

Figure 2.3a shows an example of the typical temporal evolution of the density of kinetic energy for three maximum levels of refinement Le, at Reynolds $\mathrm{Re} = 200$. The kinetic energy starts from 0 and quickly reaches a plateau after a typical time $t \sim 1/|E|$. The plateau value depends on the maximum level of refinement Le and converges to K_{th} as Le increases. The error is less than 1% as soon as $Le > 7$. Figure 2.3b displays the error for the six different values of Re ranging from 10 to 800, as a function of Le. As soon as $Le \geq 7$, the error is less than 1%. In what follows, we fix the level of refinement to $Le = 9$, which fixes the minimum grid size Δ to $L/2^9$. If the grid were of constant cell size Δ, the number of points would be 512^2.

Note that, as the theoretical velocity field (equation 2.5) is independent of the viscosity we should, in theory, be able to run a single precursor simulation with an arbitrary value of ν. Then, we would change Re by changing ν. However, we do observe differences between precursor simulations when changing Re (figure 2.3b). Therefore, we preferred to run one precursor simulation per value of the Reynolds number.

2.3 Bubble's injection

For each Reynolds number precursor simulation, we extract a snapshot of the stationary state. Then, we inject a spherical, or ellipsoidal, bubble of volume equivalent radius $R_0 = L/10$ at the stagnation point ($r = z = 0$, see figure 2.2), by changing locally density and viscosity. The boundary conditions at the bubble interface are initially not fulfilled, nevertheless the code adapts in a few time steps to restore a solution. This time corresponds to a much shorter time than all physical time scales considered here, namely the bubble breakup time and period of oscillations. In addition, this bubble injection method has been successfully used to study bubble dynamics in other flows [141, 167]. During this second phase, to maintain the stagnation point flow we do not change the boundary conditions compared to the precursors simulations.

We test numerical convergence separately for chapters 5 and 10. Indeed, studying bubble deformations and breakup (chapter 5) involve resolving numerically the bubble period and the bubble scale. These time and length scales are much larger than the ones associated with satellite

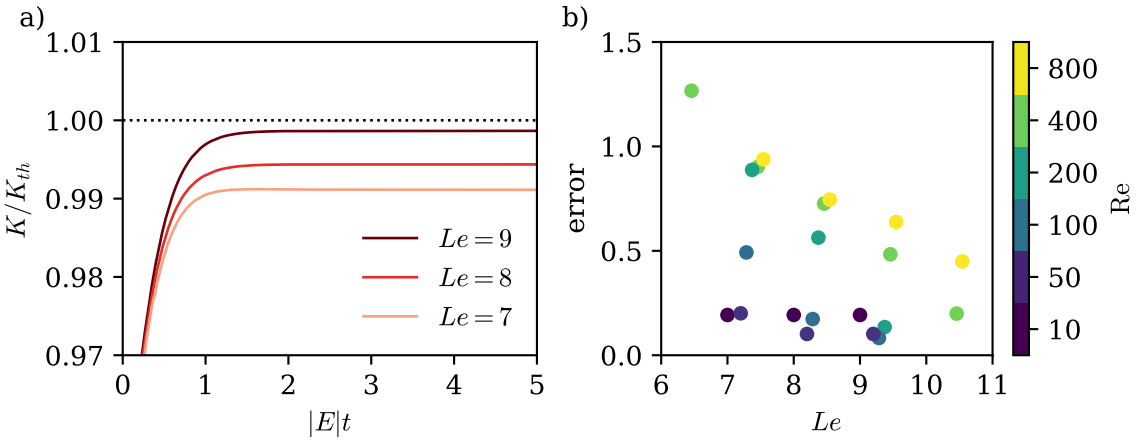

Figure 2.3 – a) Typical temporal evolution of the kinetic energy for different maximum levels of refinement at Re = 200. A stationary state is reached after approximately $1/|E|$, with an error smaller than 1% for all Le on the total kinetic energy. b) Error (in %), defined in equation (2.10), as a function of the maximum level Le and for all the Reynolds numbers. Points corresponding to different Re have been horizontally shifted for readability reasons. As soon as $Le \geq 7$ the relative error is less than 1%.

bubble generation (chapter 10). Therefore, it is easier to guaranty numerical convergence for the bubble dynamics than for the satellite bubble generation and we use a different numerical resolution for the two problems.

Numerical convergence test for bubble dynamics: In chapter 5 we investigate bubble deformations and breakup. We therefore test numerical convergence on a metric quantifying bubble deformations, together with bubble dimensionless lifetime ET. We follow bubble deformations by computing the amplitude of the second Rayleigh mode x_2, encoding oblate-prolate oscillations

$$x_2 = \frac{1}{2}\sqrt{\frac{5}{\pi}}\int_0^{\pi/2} \frac{R(\theta)}{R_0}(3\cos(\theta)^2 - 1)\sin(\theta)\mathrm{d}\theta \tag{2.11}$$

with the angle θ and the local radius $R(\theta)$ defined on figure 2.1. Figure 2.4a shows the temporal evolution of the amplitude of the oblate prolate mode x_2 as a function of the dimensionless time for $Le \in [9, 10, 11]$ for a breaking bubble at We = 8 and Re = 400. Before $0.5ET$, the three evolutions are linear in time and indistinguishible. However, as time grows, we observe a second linear regime and the slope differs for level $Le = 9$, compared to the other levels of refinement. The end of each curve corresponds to the breakup time ET, also reported on figure 2.4b as a function of Le. We observe a significant variation of 3.7% between level 9 and level 10. Conversely, the bubble lifetime only differs from 0.05% between level 10 and 11. We conclude that, as soon as $Le \geq 10$, bubble deformations and lifetime are grid converged. If the grid were of constant cell size, Δ, the number of points would be 1024^2 corresponding to 102.4 points per bubble equivalent radius.

Numerical convergence test of satellite bubbles: Bubbles do not break on the axis of symmetry in the uniaxial straining flow. Besides, they pinch-off at a position which depends

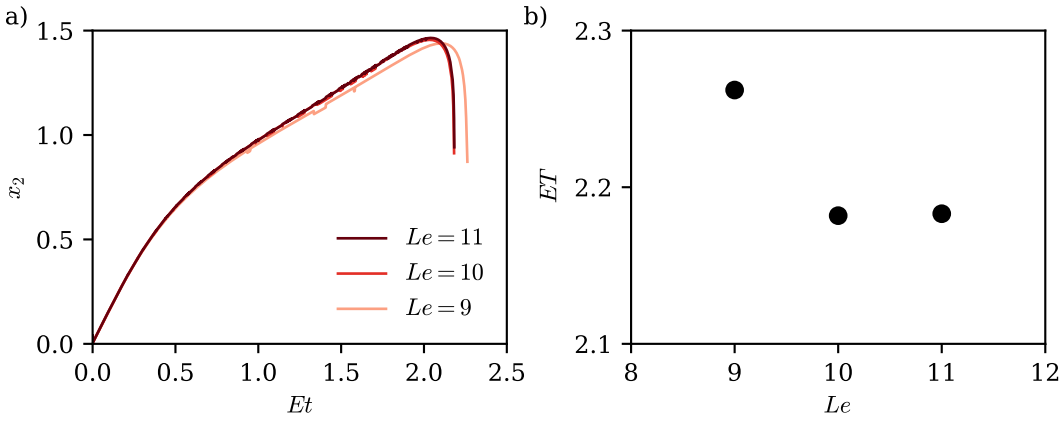

Figure 2.4 – a) Evolution of the amplitude of the second Rayleigh mode x_2 as a function of time at We = 8 and Re = 400. b) Evolution of the bubble lifetime at Re = 400 and We = 8 the maximum level of refinement Le.

on both the Reynolds and the Weber number. By convention, we call filament the volume encapsulated in the first satellite bubble. Indeed the first pinch-off can be followed by several others, which will break this satellite bubble into smaller pieces instead of the largest one. In the study reported in chapter 10, we want to resolve numerically the generation of satellite bubbles and in particular, the evolution of their volume with the two controlling parameters. We verify numerical convergence by following the evolution of the filament volume as a function of the refinement level Le. Figure 2.5a shows an example of the evolution of the filament volume V_f divided by the parent volume $V_0 = 4/3\pi R_0^3$, as a function of Le, for We = 400 and Re = 200. The filament volume is orders of magnitude smaller than the parent bubble volume. Therefore, the minimum grid size must be largely decreased compared to the previous case. The relative difference between level 12 and 13 is 63%, while it is 14% between level 13 and 14, corresponding to a relative difference in bubble equivalent radius of 18% and 4.5% respectively. Note that levels 12, 13 and 14 correspond to a resolution 19.2, 32.7 and 62 points per filament volume-equivalent radius respectively (and 409.6, 819.2, 1638.4 points per initial bubble radius respectively). The simulation at Re = 200 and We = 400 is actually one of the most challenging numerically, as can be seen on figure 2.5b, which represents the evolution of the filament volume with We and Re. The Reynolds number is color-coded, while symbols represent the level of refinement. As soon at $V_f/V_0 \geq 2e-4$, we do not observe any quantitative difference between points at level 12 and 13. These cases correspond to large We, and Reynolds number lower than 100. As cases at level 13 are time consuming, by default, we run all simulations at level 12. Level 13 is used when $V_f/V_0 \leq 10^{-4}$.

2.4 Table of the physical and numerical parameters

We summarize in table 2.1 the definition of the controlling parameters as well as the numerical values used in chapter 5 and 10.

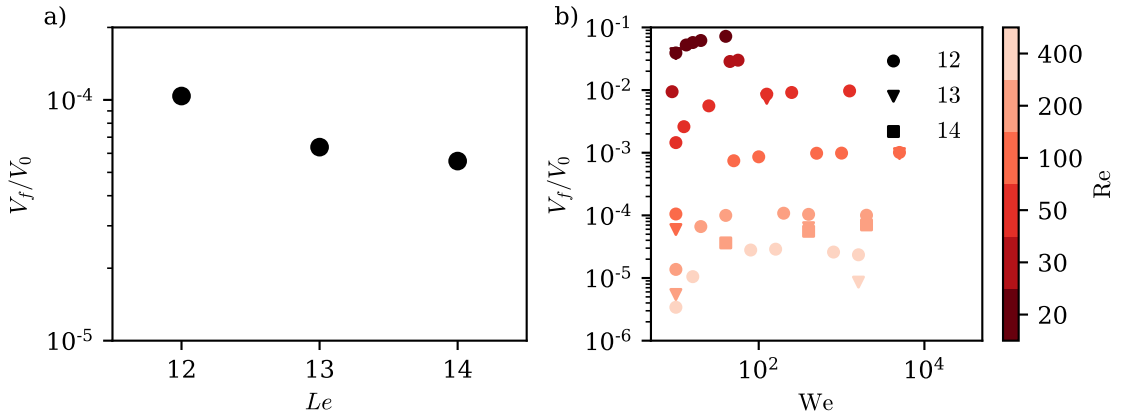

Figure 2.5 – a) Evolution of the filament volume as a function of Le, for a case at We = 400 and Re = 200. b) Evolution of the filament volume as a function of the Weber number. The Reynolds number is color-coded, while symbols encode the level of refinement.

Chapter	5	10
We	$\rho E^2 d^3/\gamma$	-
Re	Ed^2/ν	-
R_0/L	1/10	-
μ_R	25	55
ρ_R	850	-
R_0/Δ	102.4	$\geq$ 409.6

Table 2.1 – Summary of the physical and numerical values used along this thesis. A dash "-" denotes that the definition or value is shared among chapters.

3 Single bubble in HIT

Together with the simplified geometry, we run direct numerical simulations of a single bubble in homogeneous, isotropic and statistically stationary turbulent flow. In this section, we describe the numerical set-up.

3.1 Physical setting

We consider an initially spherical gas bubble, of diameter d, immersed in a homogeneous and isotropic turbulent flow. For bubble size lying within the inertial range of the turbulent cascade, where the flow is scale invariant, bubble dynamics is primarily controlled by the Weber number $\mathrm{We} = \rho U^2 d/\gamma$, where U is a characteristic velocity, which balances inertial and capillary forces. According to Kolmogorov and Hinze [84, 97], bubbles are primarily deformed by eddies of bubble size, so that U is the average longitudinal velocity increment at the bubble scale, $U^2 = \langle \delta u(d)^2 \rangle$, with $\delta u(d) = u_L(\mathbf{r}, t) - u_L(\mathbf{r} + \mathbf{d}, t)$, where u_L is the velocity component along the direction of $\mathbf{d}$. In a homogeneous and isotropic turbulent flow, for d lying within the inertial range, $\langle \delta u(d)^2 \rangle$ relates to ϵ, the energy dissipation rate and d through $\langle \delta u(d)^2 \rangle = C(\epsilon d)^{2/3}$, where C is a numerical constant. Experimental measures reports values of C varying between 2 and 2.2 [142]. We choose $C = 2$ for consistency with Risso et al. [165]. Eventually, the

Weber number of bubbles of size lying within the inertial range of a homogeneous and isotropic turbulent flow is written as,

$$\mathrm{We} = \frac{2\rho\epsilon^{2/3}d^{5/3}}{\gamma}. \tag{2.12}$$

Low Weber number bubbles do not break, while large bubbles can be easily deformed and break. Viscous effects are quantified by the Reynolds number at the bubble scale $\mathrm{Re}(d) = Ud/\nu$. Similarly, for bubbles within the inertial range of turbulence, the Reynolds number is written as

$$\mathrm{Re} = \frac{\sqrt{2}\epsilon^{1/3}d^{4/3}}{\nu}. \tag{2.13}$$

As for the uniaxial straining flow, the numerical simulation is performed in two steps. We first create a statistically stationary turbulent flow in a square periodic box of size L^3. We call these single phase simulation precursor simulations. Then we inject a spherical bubble at the center of the simulation, while maintaining turbulence. As turbulence is intrinsically fluctuating, for every turbulent state and Weber number, we perform several simulations starting from different statistically equivalent turbulent flow configurations. To do so, we use several initial flow snapshots separated by at least one eddy turnover time or at the bubble scale $t_c(d)$ to ensure statistical independence. In chapter 6 and 7, snapshots are separated by at least $6t_c(d)$. In chapters 6, 7 and 9, we use $\rho_R = 850$ and $\mu_R = 25$.

3.2 Single phase simulation

We create a homogeneous and isotropic turbulent flow by solving the 3D single phase Navier-Stokes equation, with an additional linear forcing,

$$\mathbf{f}(\mathbf{x}, t) = CA\mathbf{u}(\mathbf{x}, t), \tag{2.14}$$

following the method introduced by Rosales and Meneveau in 2005 [172]. Such an approach has been used previously by several authors in various multiphase flow contexts such as the interaction between turbulence and a fixed solid sphere [136], a rising bubble in turbulence [193] or evaporation and mixing in two phase turbulent flows [62]. The numerical constant A controls the turbulence intensity. We set its value to 0.1. The velocity field is multiplied by the liquid volume fraction C to ensure forcing in the liquid phase only. Note that in the single phase simulation $C = 1$ everywhere. A linear forcing induces a mean flow which grows in time. Therefore, to prevent divergence of the kinetic energy, at each time step, we remove the average velocity at every point in space. This procedure ensures to have a homogeneous and isotropic turbulent flow. This method has been previously implemented and provided as an example on the *Basilisk* website. Starting from an isotropic "ABC" flow the velocity field converges to a turbulent state after a transient.

Turbulence statistics: We monitor the temporal evolution of the flow by following several statistical quantities associated with the turbulent state: the density of kinetic energy K, the dissipation rate ϵ, and the Taylor Reynolds number Re_λ. The density of kinetic energy, which

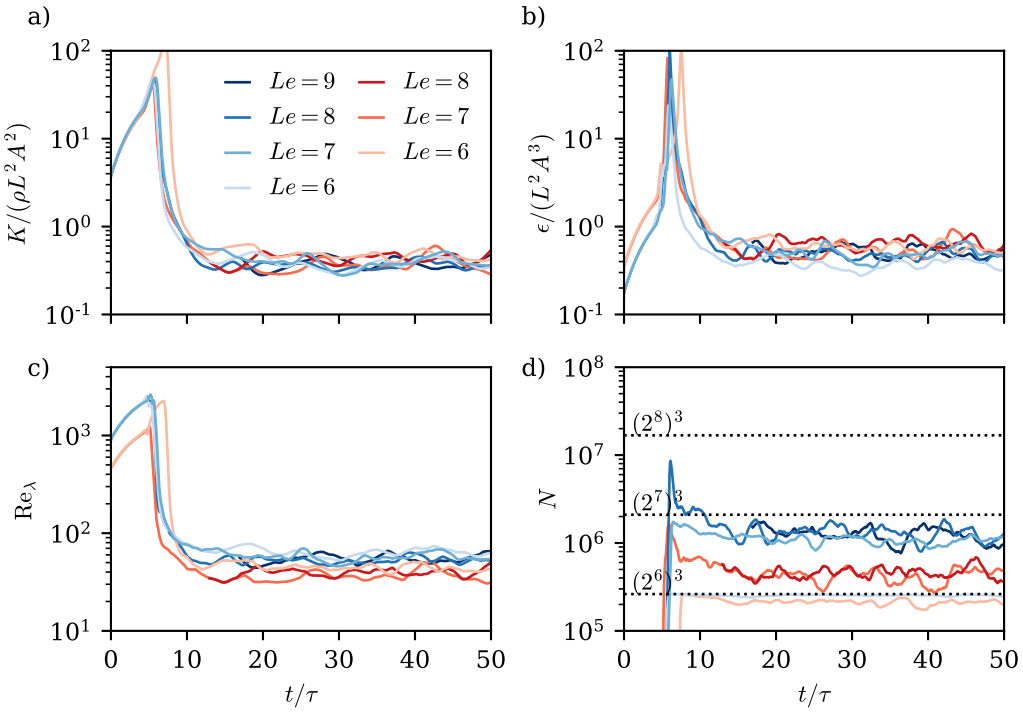

Figure 2.6 – Temporal evolution of turbulent statistics in precursor simulations as a function time in units of the eddy turnover time at the integral length scale τ. Data corresponding to $\mathrm{Re}_\lambda = 55$ are in blue shades, while $\mathrm{Re}_\lambda = 38$ correspond to red shades. a) Density of kinetic energy, b) energy dissipation rate, c) Taylor Reynolds number, c) Number of grid points. Black dotted lines denotes the number of grid points for an equivalent regular grid.

quantifies velocity fluctuations in the flow, is defined as

$$K = \frac{1}{2V}\int \rho \mathbf{u}^2(\mathbf{x}, t)\mathrm{d}^3x = \frac{3}{2}\rho u_{rms}^2, \tag{2.15}$$

where u_{rms} is the root mean square of the velocity and the factor 3 comes from the flow isotropy. The mean energy dissipation rate per unit mass quantifies the rate of energy exchange between scales. It is defined through

$$\epsilon = \frac{\nu}{V}\int (\partial_i u_j + \partial_j u_i)^2 \mathrm{d}^3x. \tag{2.16}$$

Finally, the Taylor Reynolds number quantifies the flow fluctuations. It is based on the correlation length of velocity gradients, the Taylor micro-scale, $\lambda = \sqrt{15\nu/\epsilon}\, u_{rms}$ in homogeneous and isotropic turbulence [142]. The Taylor Reynolds number is then defined by

$$\mathrm{Re}_\lambda = \frac{u_{rms}\lambda}{\nu}. \tag{2.17}$$

Note that $A = \epsilon/(3u_{rms}^2)$ [172]. Therefore, prescribing the value of A to a constant imposes a constant eddy turnover time at the integral scale $\tau = u_{rms}^2/\epsilon$. We change the value of Re_λ by changing the value of the kinematic viscosity ν. Decreasing ν decreases the Taylor micro-scale, as well as the Kolmogorov length scale $\eta = \nu^{3/4}/\epsilon^{1/4}$, below which viscous effects become important. Therefore, the two values of Re_λ might need two different refinement levels.

Figure 2.6 shows the temporal evolution of K, ϵ and Re_λ as a function of time for different maximum levels of refinement. Blue and red range of colors correspond to two different numerical values of the liquid kinematic viscosity leading to two different stationary values of Re_λ. Time is made dimensionless using the eddy turnover time $\tau = u_{rms}^2/\epsilon$ averaged over the statistically stationary period. After 10τ, every flow converges to a statistically stationary state. Blue curves correspond to $\mathrm{Re}_\lambda \approx 55$, while red curves correspond to $\mathrm{Re}_\lambda = 38$. Note that for some simulations (for instance $\mathrm{Re}_\lambda = 55$, $Le = 9$) we use as flow initial conditions a flow snapshot at a lowest resolution instead of starting from an ABC flow. This procedure saves computational time and avoids flow divergence that might happen during the inertial kinetic energy growth at the beginning of the simulation. As we have fixed to value of A to 0.1 in all simulations, the statistically stationary values of both ϵ and K are the same in all simulations, even when ν varies. We do not observe significant differences between different levels of refinement for each Re_λ, except at $\mathrm{Re}_\lambda = 55$ and $Le = 6$. For this configuration the average density of kinetic energy is smaller than at larger resolution. This effect can be understood by looking at the total number of points N in the simulation, as a function of time reported on figure 2.6d. We observe that the number of grid points increases until it reaches its stationary value at the instant when the density of kinetic energy and dissipation rate are maximum. At $\mathrm{Re}_\lambda = 55$ and $Le = 6$, the number of grid points increases until it reaches $(2^6)^3$, corresponding to the number of grid points of a regular grid with grid size $(\Delta)^3$. Therefore, in this case, the maximum error that we prescribe is not respected. In all other cases, the number of grid points is well lower than the number of points in the equivalent regular grid. We note that more points are present in simulations at $\mathrm{Re}_\lambda = 55$, consistently with the existence of smaller scales in the flow. We conclude that the adaptive algorithm perform well as soon as $Le \geq 7$: we resolve the smaller scales in the flow while saving computational time.

To choose between levels of refinements greater that 7, we compute the number of grid points per Kolmogorov length. To resolve the dissipative scales we must have at least two points per Kolmogorov scales. An effective resolution at $Le = 8$, corresponds to 2 and 1.19 points per Kolmogorov length η at $\mathrm{Re}_\lambda = 38$ and 55 respectively. We therefore run precursor simulations at level 8 for $\mathrm{Re}_\lambda = 38$ and $Le = 9$ at $\mathrm{Re}_\lambda = 55$ (leading to 2.39 points per Kolmogorov length). Note that these resolutions correspond to 25.0 and 35.3 points per Taylor micro-scale at $\mathrm{Re}_\lambda = 38$ and 55 respectively (at $Le = 8$ and 9 respectively).

Structure functions: The turbulent state can be more precisely assessed by looking at the longitudinal $D_{LL}(r)$ and transverse $D_{NN}(r)$ structure functions, defined by

$$D_{LL}(r) = \frac{1}{3}\sum_i \langle (u_i(\mathbf{x},t) - u_i(\mathbf{x} + r\mathbf{e_i},t))^2 \rangle \tag{2.18}$$

$$D_{NN}(r) = \frac{1}{6}\sum_{i\neq j} \langle (u_i(\mathbf{x},t) - u_i(\mathbf{x} + r\mathbf{e_j},t))^2 \rangle \tag{2.19}$$

where $\mathbf{e_i}$ is the unit vector along the ith direction. In a homogeneous and isotropic turbulent flow, we expect $D_{LL}(r) = C_2(r\epsilon)^{2/3}$ and $D_{NN}(r) = 4/3 D_{LL}(r)$ with $C_2 \approx 2$ a universal numerical constant [142]. Figure 2.7a shows D_{LL} and D_{NN} compensated by their theoretical values as a

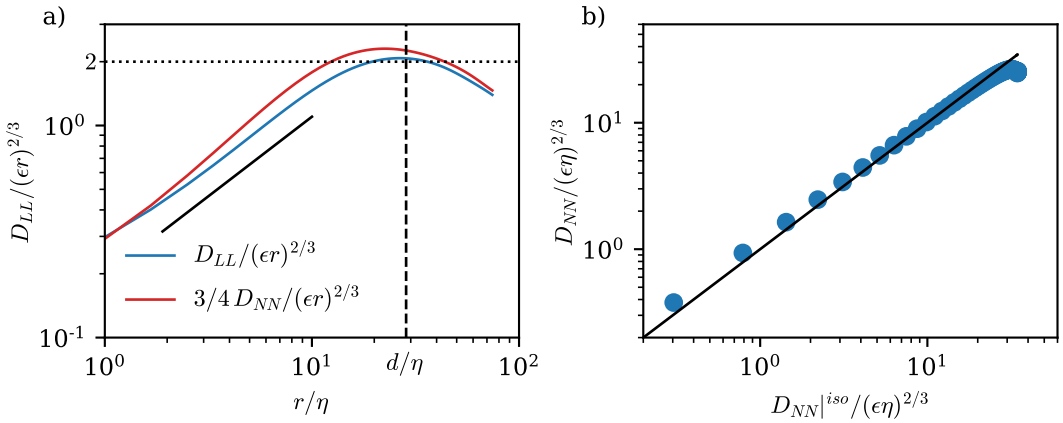

Figure 2.7 – Structure functions at $\mathrm{Re}_\lambda = 55$ a) Longitudinal and transverse structure functions normalized by their respective scaling in homogeneous and isotropic turbulence, as a function of r normalized by the Kolmogorov lengthscale η. The bubble size diameter (dashed line) lies within the inertial range of scales. The solid black line corresponds to $D_{LL} \propto r^2$, which holds for small values of r. b) Transverse scaling as a function of its isotropic expression $D_{NN}|^{iso}$. Both values are normalized by $(\epsilon\eta)^{2/3}$. The solid black line is the purely isotropic scaling.

function of r/η, for a precursor simulation at $\mathrm{Re}_\lambda = 55$ and $Le = 9$ (see [167] for the same plot at $\mathrm{Re}_\lambda = 38$). Although the inertial range is limited due to limited value of Re_λ, we do observe the Kolmogorov scaling and the relation between D_{LL} and D_{NN} is verified. In addition, the black dashed line shows that the bubble diameter lies within the inertial range of the turbulent cascade, where turbulence is reasonable.

Eventually, we use structure functions to verify flow homogeneity and isotropy. Indeed, in a homogeneous and isotropic flow, D_{NN} is uniquely determined by D_{LL} through [142]

$$D_{NN}|^{iso} = D_{LL} + \frac{r}{2}\partial_r D_{LL}. \tag{2.20}$$

This relation must hold also for limited values of Re_λ. Figure 2.7b shows D_{NN} as a function of $D_{NN}|^{iso}$, both normalized by $(\epsilon\eta)^{2/3}$, for $\mathrm{Re}_\lambda = 55$ (again, see [167], for $\mathrm{Re}_\lambda = 38$). The relation holds perfectly confirming the homogeneity and isotropy of the turbulent flow in the precursor simulations.

3.3 Two phase simulation

Similarly to the uniaxial straining flow, we output snapshots of the statistically stationary turbulent state and use these snapshots as flow initial condition. We inject a spherical bubble of diameter $d = 0.13L$, at the center of the numerical domain by changing the volume fraction C from 1 to 0. We also set the initial velocity inside the bubble to zero to guaranty that no breakup occur due to the initial inside flow. In practice, we tested several set of initial conditions and we find no dependency of bubble breakup in the initialization procedure. Indeed, the solver relaxes in a few time steps after initialization.

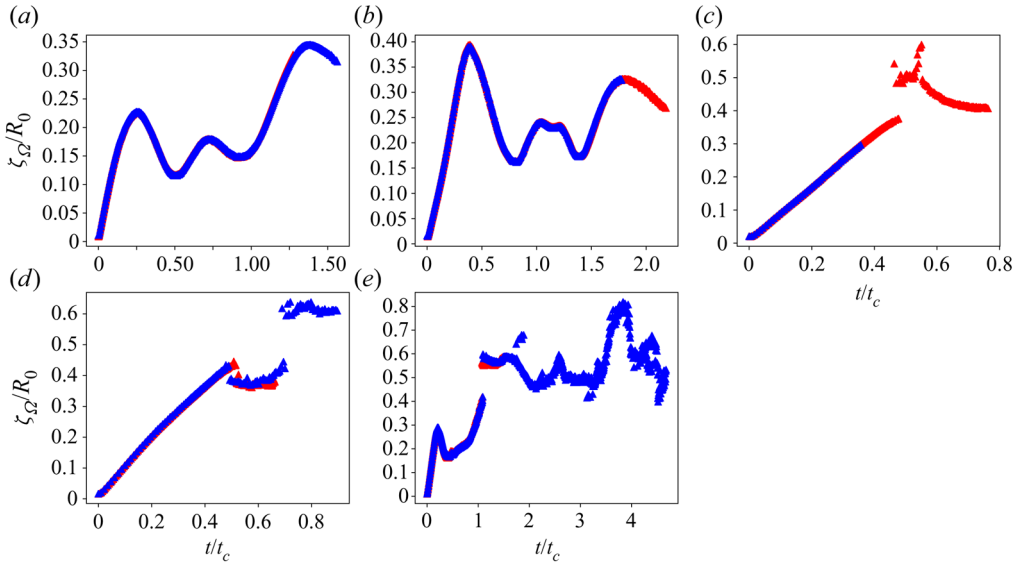

Figure 2.8 – Figure extracted from Perrard et al. [141]. Temporal evolution of the radius standard deviation ζ_Ω as a function of the dimensionless time t/t_c for fives Weber numbers $\mathrm{We} = 3, 6, 15, 30, 45$ (a to e) and $\mathrm{Re}_\lambda = 38$. We observe an excellent agreement between level 9 (blue) and level 10 (red) simulations at all We.

Numerical convergence test for bubble deformations: To quantify bubble deformations, we parameterize bubble surface by its local radius $R(\theta, \phi)$, in the comoving reference frame, where (θ, ϕ) are the usual polar and azimuthal angles of the spherical coordinate system. We test numerical convergence of bubble shapes by computing the bubble average surface deformation ζ_Ω as a function of time,

$$\zeta_\Omega = \frac{1}{4\pi} \int \left[R(\theta, \phi) - \bar{R} \right]^2 \mathrm{d}\Omega \tag{2.21}$$

where $\mathrm{d}\Omega = \sin(\theta)\mathrm{d}\theta\mathrm{d}\phi$ and $\bar{R} = 1/(4\pi) \int R(\theta, \phi)\mathrm{d}\Omega$. Figure 2.8 (extracted from [141]) shows five typical temporal evolution of ζ_Ω at $\mathrm{Re}_\lambda = 38$ for five different Weber number (3, 6, 15, 30 and 45), computed at level 9 (in blue) and level 10 (in red). Time is in units of the eddy turnover time at the bubble scale $t_c(d) = \epsilon^{-1/3} d^{2/3}$. We observe an excellent agreement between the two levels of refinement at all Weber number. We therefore fix the maximum level to 9. This choice corresponds to 68 points per bubble equivalent diameter and the equivalent number of points on a regular grid would be $(512)^3$.

Numerical convergence test for bubble breakup: An in-depth study of numerical convergence for bubble breakup can be found in Rivière et al. [167]. In this paragraph, we recall the main elements. As the breakup study (chapter 9) is performed at $\mathrm{Re}_\lambda = 38$, we focus on this value of Re_λ in this paragraph.

Since turbulence is a fluctuating state, we must verify that the statistics of breakup are grid converged instead of checking that each simulation is grid converged. Indeed, small differences lead to dramatic differences between cases in turbulence and changing Le for the same set of initial conditions can lead to dramatic differences in bubble breakup dynamics. To check grid convergence of breakup statistics, we run ensembles of simulations at $Le = 9$ and $Le = 10$.

We	3	3	6	6	15	15	30	30	45	45
Le	9	10	9	10	9	10	9	10	9	10
# runs	27	3	39	15	20	10	20	10	20	6

Table 2.2 – Number of runs per ensemble used in figure 2.9.

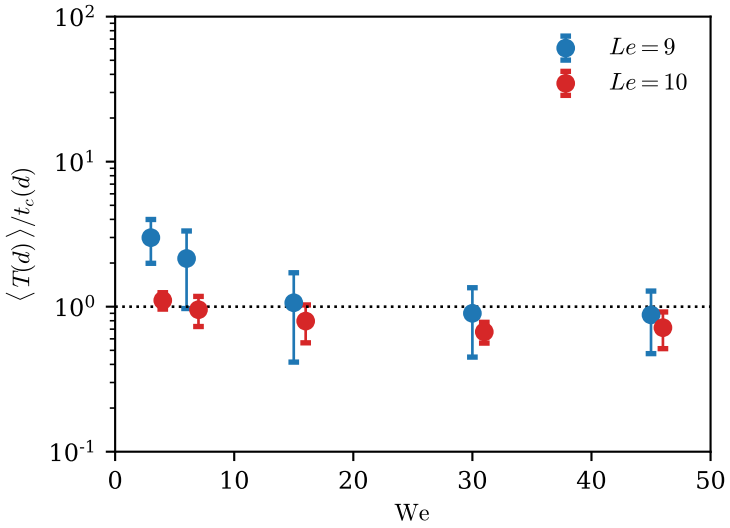

Figure 2.9 – Average dimensionless bubble lifetime $\langle T\rangle/t_c(d)$, in a turbulent flow at $\mathrm{Re}_\lambda = 38$, as a function of We at two refinements levels (9 and 10) for the first bubble breakup. Data at level 10 have been shifted to the right for readability reason. Errorbars encode the standard deviation.

We first check numerical convergence for the initial bubble lifetime T, as a function of We. Figure 2.9 shows the evolution of the ensemble averaged lifetime $\langle T\rangle$ of the initial bubble, in units of the eddy turnover time at the bubble scale $t_c(d)$ as a function of We, for the two levels of refinements $Le = 9$ and 10. Level 10 data are shifted to the right for readability reason. The error bars encode the standard deviation of the lifetime. The exact number of runs per ensemble used in this plot can be found in table 2.2. We find no significant differences between the two levels of refinements (within the errorbars), at all Weber number. As a consequence, we consider that bubble lifetime is converged at level 9. This level corresponds to 68 points per bubble equivalent diameter.

Similarly to the previous uniaxial straining flow, we want to resolve bubble fragmentation. Due to the large computational cost of each ensemble, increasing the resolution is not accessible. Instead, we adopt another strategy and look for the minimum number of grid points necessary for a bubble to be resolved, *ie* we look for the minimum bubble size resolved in our simulations. To do so we consider simpler numerical simulations: bubble breakup in a freely decaying turbulent flow. For these simulations, when we inject the bubble, we also stop forcing the flow, by setting $A = 0$. The Weber number is then defined at the initial instant, while the effective Weber number decreases as turbulence decays. The panel in figure 2.10a, (extracted from Rivière et al. [167]), shows an example of bubble deformations and breakup at $\mathrm{We} = 15$, $\mathrm{Re}_\lambda = 38$ and $Le = 9$. Colors indicate grid size at the interface, with warmer colors denoting smaller cell size.

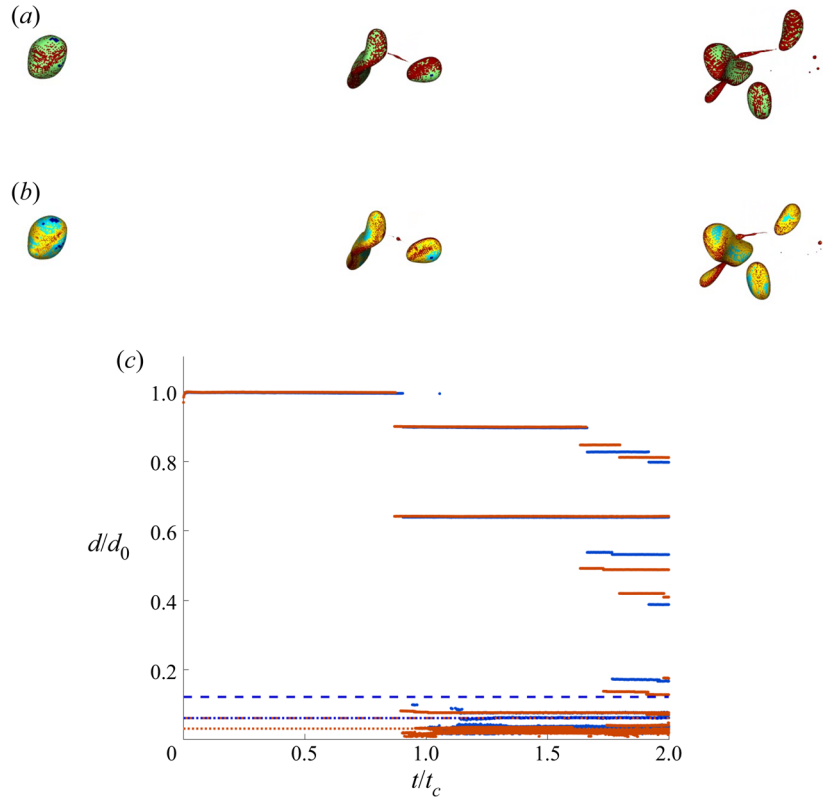

Figure 2.10 – Figure from W. Mostert, extracted from Rivière et al. [167]. a) Sequence of breakup for a bubble in a freely decaying turbulence. The initial bubble Weber number is 15, the initial Taylor Reynolds number is 38. The level of refinement is $Le = 9$. Colors indicate grid size on the bubble interface with warmer colors indicating smaller cell sizes. b) The same simulation at $Le = 10$. c) Evolution of the bubble equivalent diameters in the same simulations for $Le = 9$ (in blue) and $Le = 10$ (in red), as a function of time in units of $t_c(d_0)$. Dashed lines indicate the resolution of 8 grid points, 8Δ, at each level. Dotted line indicate 4Δ.

Note that more points are present in regions where curvature is higher as expected from the adaptive mesh refinement criterion. In spite of the flow decay, the bubble is initially largely deformed and breaks, creating two large bubbles and an elongated structure. As the largest child bubble is still very deformed, another sequence of breakups follows creating large bubbles, of size comparable to the initial bubble size, as well as tiny ones. The same sequence of breakups is recovered when increasing the resolution from level 9 to level 10, as illustrated on the panel b. Nevertheless we note some differences on the size of tiny bubbles. Note that these bubbles are resolved with only a few grid points and might therefore not be grid converged. This fact can be more properly assessed by computing the volume-equivalent diameter of every child bubble. Figure 2.10c shows the bubble volume-equivalent diameter of every bubble in the simulation, normalized by the initial bubble diameter d_0, as a function of time, in units of t_c. Level 9 data are in blue, while level 10 data are in red. Sizes above dashed lines are larger than 8Δ, while dotted lines indicate the 4Δ limit. For both levels, the initial bubble breaks at $t \approx t_c$ producing two large bubbles larger than $8\Delta_9$, with excellent quantitative agreement between the two resolutions.

The sequence of latter breakups is also very similar between the two resolutions. The number

and the size of child bubbles larger than 8Δ (at $Le = 9$) are close between the two levels of refinements. Figure 2.10 only shows an example for one initial turbulent snapshot but tests with several other initial configurations draw the same conclusions: the first breakup is always grid-converged, with lifetime differences smaller than 10%. This fact is consistent with our previous observations of statistical convergence of the first breakup in forced turbulence. The latter breakup sequence, in decaying turbulence, creates the same number of child bubbles for both resolutions (for child sizes larger than 8Δ at $Le = 9$). Their sizes agree within 10%. We are therefore confident that bubbles are size larger than 8 grid points at $Le = 9$ are statistically grid converged.

3.4 Table of the physical and numerical parameters

We summarize in table 2.3 the physical and numerical parameters used in the rest of this thesis.

Chapter	6 & 7	9
Re_λ	55	38
Re	124	62
d/L	0.13	-
d/λ	1.9	1.36
d/η	28.5	16.9
μ_R	25	-
ρ_R	850	-
d/Δ	68	-

Table 2.3 – Summary of the numerical and physical parameters used along chapters. The dash "-" indicates that the value does not change between chapters.

Chapter 3

Analytical tools

Many Russians worked on this subject.
What is your contribution?

A chairman

Abstract

In this chapter, we introduce two analytical tools which will be useful all along the manuscript. First, the spherical harmonics decomposition, which will be widely used in part I. Then we explain how we reconstruct family trees, knowing the position and volume of bubbles at each time step. The algorithm is used in part II.

Contents

1 Spherical harmonics decomposition

In part I, we aim at describing bubbles deformations to infer the likelihood of breakup. To quantify bubble deformations, we decompose bubble radius into the real spherical harmonics base. In this section, we detail a few characteristics of the spherical harmonics and the computation of the modes' amplitude in both the axi-symmetric and the 3D turbulent case.

1.1 General considerations

The (complex) spherical harmonics base $\{\tilde{Y}_\ell^m\}$ is an orthonormal base defined on the surface of a sphere. This base is therefore adapted for problems with spherical symmetries. The base is indexed by two integers: the principal number $\ell \geq 0$ and the secondary number $m \in [\![-\ell, \ell]\!]$. Each value of ℓ is associated with $2\ell + 1$ harmonics. Each harmonic depends on θ and ϕ, the usual colatitude and longitude of the spherical coordinate system. It can be expressed in terms of the associated Legendre polynomial P_ℓ^m

$$\tilde{Y}_\ell^m(\theta, \phi) = \sqrt{\frac{2\ell + 1}{4\pi} \frac{(\ell - m)!}{(\ell + m)!}} P_\ell^m(\cos\theta) e^{im\phi}. \tag{3.1}$$

From the complex base, one can define the real spherical harmonics base $\{Y_\ell^m\}$ through

$$Y_\ell^m = \begin{cases} \frac{i}{\sqrt{2}}(\tilde{Y}_\ell^m - (-1)^m \tilde{Y}_\ell^{-m}) & \text{if } m < 0 \\ \tilde{Y}_\ell^0 & \text{if } m = 0 \\ \frac{1}{\sqrt{2}}(\tilde{Y}_\ell^{-m} + (-1)^m \tilde{Y}_\ell^m) & \text{if } m > 0. \end{cases} \tag{3.2}$$

Figure 3.1 illustrates the shape of the first spherical harmonics (ℓ, m), for $\ell \in [\![0, 3]\!]$ and every m. Spherical harmonics on the same row share the same ℓ-value. Spherical harmonics on the same column share the same m-value. The $\ell = 0$ mode corresponds to radial oscillations. The three $\ell = 1$ modes correspond to translation along the three directions. For $\ell \geq 2$, the value of ℓ can be see qualitatively as the number of poles. The $\ell = 2$ modes correspond to oblate/prolate shapes. The $\ell = 3$ modes have a triangular shape etc... For a given ℓ, modes $-|m|$ and $|m|$ share the same shape up to a rotation and a change of sign.

In part I, we describe the bubble shape in a reference frame following the bubble. We decompose the local bubble radius $R(\theta, \phi)$ in the real spherical harmonics base,

$$R(\theta, \phi) = R_0 \left(1 + \sum_{\ell=2}^{\infty} \sum_{m=-\ell}^{\ell} x_{\ell,m}(t) Y_\ell^m(\theta, \phi)\right) \tag{3.3}$$

where R_0 is a constant, by incompressibility. We compute the amplitude of each mode amplitude $x_{\ell,m}$ in time through

$$x_{\ell,m} = \iint R(\theta, \phi) Y_\ell^m(\theta, \phi) \sin(\theta) \mathrm{d}\theta \mathrm{d}\phi \tag{3.4}$$

by orthonormality of the basis. We denote $\mathrm{d}\Omega = \sin(\theta)\mathrm{d}\theta\mathrm{d}\phi$ the solid angle.

Note that the three modes $\ell = 1$ are not present in the shape decomposition, equation (3.3). This absence comes out of the choice of the reference frame. This choice allows us to decouple

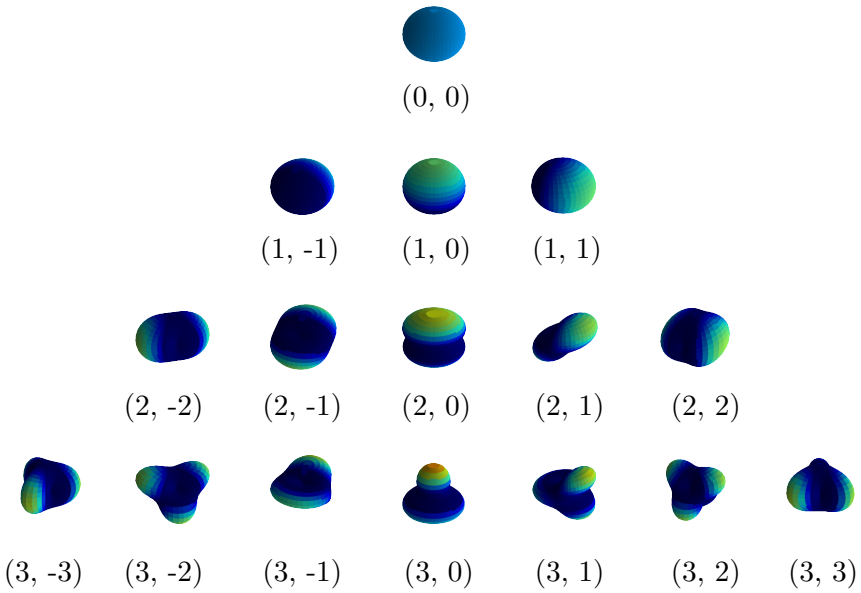

Figure 3.1 – Illustration of the shape of the real spherical harmonics for $\ell \in [\![0, 3]\!]$ and every m. Each line corresponds to a value of ℓ, while each column corresponds to a value of m. The amplitude of the deformations are exaggerated for clarity.

bubble deformations (modes $\ell \geq 2$), from bubble displacements (modes $\ell = 1$).

It is worth mentioning that all this description presumes that we can parameterize the local radius in terms of the two angles θ and ϕ. This assumption systematically falls down close to bubble breakup or when the bubble is dramatically deformed.

Caveats: Even though the real spherical harmonics base has been successfully used to describe bubble deformations both theoretically and experimentally, one shall remember that this decomposition is not intrinsic to the bubble shape. In particular, the value of each coefficient depends on the definition of the reference frame. More precisely:

- The decomposition depends on the choice of origin of the reference frame. Shifting the reference frame changes all the coefficients. To overcome this difficulty, in the computation of the spherical harmonics, we define the origin as the point which cancels the amplitude of the three modes $\ell = 1$. This choice ensures that the origin is defined define unambiguously at all times and that coefficients $x_{\ell,m}$ only describe bubble deformations.
- The decomposition is not invariant under rotation. A rotation of the reference frame (while keeping the origin fixed) changes the value of all coefficients such that $\ell \geq 1$. Nevertheless, rotating the reference frame redistributes energy of each mode (ℓ, m) over the modes sharing the same value of ℓ. The dimensionless energy contained in the modes ℓ, $\sum_m x_{\ell,m}^2$ for a given ℓ is invariant under rotation. In this work, we choose to keep the reference frame orientation constant. As a consequence, we cannot test the statistics associated with the different m-geometries. Other authors may have done a different choice. Roa et al. [169] rotated dynamically the reference frame in order to maximize, at each time step, the amplitude of the mode $(2, 0)$.

1.2 Local radius decomposition in the axi-symmetric case

In the model flow of the axi-symmetric straining flow, the decomposition only retains axi-symmetric modes, which correspond to $m = 0$. As we impose symmetry with respect to the $z = 0$ plane, we can choose $(r, z) = (0, 0)$ as the origin for the radius decomposition. This choice automatically enforces $x_{1,0} = 0$ without special treatment. In the real spherical harmonics base, the local radius, which now depends on θ only, can be written as

$$R(\theta) = R_0 \left(1 + \sum_{\ell=2}^{\infty} x_{\ell,0}(t) Y_\ell^0(\theta, 0) \right). \tag{3.5}$$

The spherical harmonics coefficients are computed using

$$x_{\ell,0} = 4\pi \int_0^{\pi/2} R(\theta) Y_\ell^0(\theta, 0) \sin\theta \mathrm{d}\theta. \tag{3.6}$$

The 2π prefactor comes from the ϕ-integration. The factor 2 from the integration between $\pi/2$ and π which gives the same value by symmetry with respect to the $z = 0$ plane. We compute the integral using a trapezoidal rule.

1.3 Local radius decomposition in 3D

We have developed and described the algorithm to compute the spherical harmonics decomposition in our previous work [141]. We recall here the method.

Discretization points are not spread uniformly on the surface of the bubble (see figure 3.2, left panel). In particular, more points are dynamically added to the regions of large curvature. To accurately compute the coefficients $x_{\ell,m}$ one has to precisely estimate the solid angle $\mathrm{d}\Omega$ associated with each point $\mathbf{r}_i$. This estimation is illustrated on figure 3.2. We first project all the interfacial points onto a unit sphere (center panel). Then, we compute the Voronoi diagram of the points on the sphere, using a function based on a robust Delaunay triangulation [32], already implemented in Python. The Voronoi diagram associates to each point a region containing all the points closest to this point than to any other points. The area of each polygon, computed using a shoelace formula, gives an estimate of $\mathrm{d}\Omega_i$. We found that the numerical error on the total solid angle $\sum_i \mathrm{d}\Omega_i$, which should sum up to 4π, is less than 0.1%. From them, we estimate the angular integral of any function $f(\mathbf{r})$, defined on the bubble surface, using

$$\iint \mathrm{d}\Omega f(\mathbf{r}) = \sum_i f(\mathbf{r}_i) \mathrm{d}\Omega_i. \tag{3.7}$$

The right panel of figure 3.2 illustrates the projection of the Voronoi diagram onto the initial bubble shape. As expected from the adaptive algorithm of *Basilisk*, regions of larger curvatures are characterized by smaller surfaces.

To validate the computation procedure, we first checked the orthonormality of the spherical harmonics, for $\ell \in [0, 10]$, all m using a set of 900 points, typical of the number of points in the DNS, randomly distributed on a unit sphere. We found a typical error of 0.1 % for $\ell < 5$, which increases for larger values of ℓ. We then tested, the accuracy of the computation on synthetic

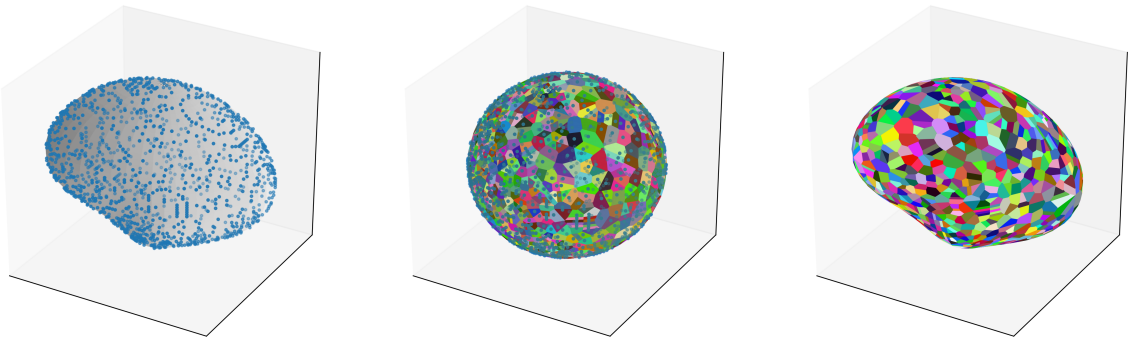

Figure 3.2 – Extracted from our previous work [141]. Illustration of the computation of the local solid angles using a Voronoi diagram. Left: A deformed bubbles. Blue points are interfacial points. Center: Projection of the surface onto a sphere of radius 1. The colored area are the Voronoi surfaces associated with each point. Right: Projection of the Voronoi diagram onto the initial bubble shape.

shapes, using again a set of 900 points randomly distributed. We found that the relative error is about 0.5 % of the largest non-zero harmonic coefficient for $\ell \leq 5$. In practice, an accurate estimate of the coefficients is obtained for $\ell \leq 5$. Note that, in order to minimize the error, we first compute the coefficient associated with Y_0^0, $x_{0,0}$. We then subtract its contribution, computing the other coefficients using $R(\theta) - R_0 x_{0,0} Y_0^0$.

As highlighted earlier the decomposition depends on the origin of the frame of reference and we define the center as the point for which the three harmonics $\ell = 1$ vanish. For DNS data, the position of this point is found recursively as follows: At each time step, we start from an initial guess. From this center, we compute the Voronoi diagram and the solid angles associated with each point. Using these solid angles, we then compute the value of the three harmonics $\ell = 1$, while moving the center position. As each harmonic $\ell = 1$ presents a symmetry of revolution, each of them depends on one coordinate of the center position. We therefore perform three, one dimensional gradient descents, one for each value of m, which gives us a new guess for the position of the center. From this new center, we compute the new solid angles value and start the whole process again. The recursion stops when the center displacement between two steps is less than $2.5.10^{-6} R_0$. This condition ensures that $|x_{1,m}| < 4.10^{-6}$ for all values of m.

2 Family trees in turbulence

In part II, we investigate bubble fragmentation. In particular, we aim at identifying the breaking mechanisms leading to the formation of sub-Hinze bubbles. To identify the origin of sub-Hinze bubbles, we decompose the fragmentation cascade into binary events. This decomposition is always possible as no two events can happen exactly at the same time. We call the breaking bubble the *parent* bubble and the product of this fragmentation the two *child* bubbles.

Basilisk does not follow bubbles in time. Therefore, the connection between the parent

bubble and the two child bubbles must be reconstructed *a posteriori*.

2.1 Algorithm principle

At each time step, we output the volume V_i and the position of the center of mass $\mathbf{x_i}$ of every bubble. In between two breakups, individual bubbles are tracked in space and time using the Python package trackpy [5] based on the Crocker-Grier algorithm [49].

When a bubble breaks, the number of bubbles increases by one between two time steps. We identify the parent, at position $\mathbf{x_0}$, of volume V_0 and the two child bubbles, at position $\mathbf{x_1}$ and $\mathbf{x_2}$ and volumes V_1 and V_2 by looking at the three bubbles satisfying the two following relations

$$V_0 = V_1 + V_2 \tag{3.8}$$

$$\mathbf{x_0} V_0 = \mathbf{x_1} V_1 + \mathbf{x_2} V_2 \tag{3.9}$$

up to some error. Note that the parent bubble is define at step j while the two child bubbles exist at step $j+1$. The first relation is the conservation of mass. The second relation relates the center of mass of the child bubbles with the position of the parent bubble. Each criterion has been manually adjusted and tested on simple situations to validate the algorithm robustness. Trees are also manually checked afterward to verify the associations and add missing links, from bubbles position and volume.

PART I

FROM DEFORMATIONS TO BREAKUP - BREAKUP RATE

Chapter 4

Modelling bubble deformations in turbulence - Introduction

This is a purely academic problem.

A reviewer

Abstract

The main objective of part I is to find an expression of the breakup rate of bubbles in turbulence. From this breakup rate we could deduce an expression for the critical Weber number as a function of the residence time. To do so, we investigate the bubble deformation dynamics in the model flow as well as in turbulence. We aim at finding reduced dynamics from which we can infer breakup statistics. In this introductory chapter we first review the bubble deformations strategies in both quiescent and turbulent flows. Then we expose the usual strategies to model the breakup rate and how they differ from our approach. We finally give an outline of part I.

Contents

1 Deformable objects in turbulence

From a theoretical point of view, bubble deformations and breakup in turbulence are one over many examples of the interaction between a turbulent flow and a deformable object. From plants oscillations in the wind [50], to disks [202] and fibers deformations in water [25, 173], many studies have aimed at finding a reduced dynamics for the amplitude of the relevant spatial modes of deformations, in the form of a damped harmonic oscillator, randomly forced by turbulence. The objective can be either to understand the object deformations, as in the case of crops, whose growth is influenced by the wind, or to understand a distribution of fragment sizes, as for the microplastic size distribution in the oceans. A usual approach to describe the object deformations is to model all the coefficients of an ordinary differential equation, as well as the statistics of a random forcing term that model the turbulent forcing. Dislocation typically occurs when a given deformation threshold or stress is exceeded.

In this part, we choose another approach. We propose to directly measure the coefficients of the reduced dynamics as well as the effective forcing from the deformations of bubbles. We expect the forcing to be stationary in the model configuration, and stochastic in turbulence.

We first review the bubble oscillation dynamics in quiescent flows and their phenomenological extensions to turbulent flows. We eventually show how to capture bubble breakup from deformation model and review other breakup rate modeling.

2 Modeling bubble deformations

2.1 Bubble dynamics in quiescent flows

Rayleigh et al. [159] investigated the oscillation dynamics of inviscid drops in vacuum and bubbles in a quiescent inviscid flow. In the linear limit of deformation, the local radius of a bubble (or a drop) can be decomposed into axi-symmetric modes using the basis of Legendre functions, which are indexed by the integer $\ell \in [2, \infty]$. Rayleigh showed that the amplitude of each mode ℓ follows an harmonic oscillator equation, with a characteristic natural frequency written as

$$\omega_\ell^2 = 8(\ell - 1)(\ell + 1)(\ell + 2)\frac{\gamma}{\rho d^3} \tag{4.1}$$

for bubbles, with $f_\ell = \omega_\ell^q/(2\pi)$ the characteristic frequency. Latter on, Lamb [101] extended this work to gas bubbles oscillating in a liquid of low kinematic viscosity, ν. He found that bubbles' modes oscillate at the Rayleigh frequency with a damping rate λ_ℓ, defined by

$$\lambda_\ell = 8(\ell + 2)(2\ell + 1)\frac{\nu}{d^2}, \tag{4.2}$$

for bubbles of negligible inertia and viscosity. In three dimensions, bubble shape can be decomposed into the real spherical harmonics base, $Y_\ell^m(\theta, \phi)$ introduced in chapter 3 where θ and ϕ are the co-latitude and longitudinal angles in spherical coordinates. The axi-symmetric modes of Rayleigh and Lamb correspond to $m = 0$. We denote the dimensionless amplitude of the modes in the spherical harmonics base by $x_{\ell,m}$. The dynamics found by Lamb [101] and Rayleigh et al.

[159] applies to each spherical harmonics mode amplitude $x_{\ell,m}$, so that they follow a damped harmonic oscillator equation with natural frequency ω_ℓ and damping rate λ_ℓ independent of m,

$$\ddot{x}_{\ell,m} + \lambda_\ell \dot{x}_{\ell,m} + \omega_\ell^2 x_{\ell,m} = 0. \tag{4.3}$$

When time is made dimensionless using the natural frequency ω_ℓ, this equation reads,

$$x''_{\ell,m} + p(\ell)\mathrm{Oh}\, x'_{\ell,m} + x_{\ell,m} = 0 \tag{4.4}$$

where $p(\ell) = 2\sqrt{2}(\ell+2)(2\ell+1)/[(\ell-1)(\ell+1)(\ell+2)]^{1/2}$ and, $'$ stands for derivative with respect to the dimensionless time $\omega_\ell t$. The Ohnesorge number $\mathrm{Oh} = \mu/\sqrt{\rho\gamma d}$ with $\mu = \nu\rho$ compares viscous to capillary effects, and controls the quality factor $Q_\ell = \omega_\ell/\lambda_\ell \sim \mathrm{Oh}^{-1}\,\ell^{-1/2}$ of the Lamb oscillations.

To estimate the damping rate of small oscillations, Lamb [101] computed the velocity gradients of the irrotational inviscid velocity field. Doing so, he underestimated the dissipation rate, as shown latter by Miller et al. [130], as most of the dissipation takes place within the bubble boundary layer, even when viscosity is low. Another approach is given by the normal-mode analysis [34, 35, 161], for the spherical harmonics modes. This theory predicts an evolution of the bubble natural frequency and damping rate with the Ohnesorge number. No explicit formulation can be however derived: one needs to solve a characteristic equation for each value of Oh. This approach correctly takes into account viscous effects but only holds at long times, presumably when oscillations have already been completely damped, and do not describe transient dynamics. Miller et al. [130] demonstrated that, in the limit of vanishing viscosity, the normal-mode solution converges to the irrotational one in the bubble case. For drops, the same demonstration has been done by Chandrasekhar [34] and Reid [161].

Latter on, Prosperetti [149, 150] unified the two approaches by studying the initial-value problem of a drop or a bubble oscillating is an initially quiescent flow. He demonstrated that, regardless of the value of Oh, the damped harmonic oscillator dynamics of Lamb [101] holds at short times compared to the viscous timescale, $t \ll R_0^2/\nu$, where $R_0 = d/2$ is the bubble equivalent radius. On the other hand, the normal mode description of Chandrasekhar [34] holds at long times, $t \gg R_0^2/\nu$. At intermediate timescales, Prosperetti [149, 150] demonstrated that the dynamics is more complex due to the existence of a memory term in the equation of motion of the modes, which couples the dynamics with the past evolution.

2.2 Bubble deformations in turbulence

For a bubble immersed in a turbulent flow, additional dimensionless parameters may control the deformation. Let us consider a bubble of negligible inertia and viscosity, equivalent diameter d, immersed in a fluid of density ρ, dynamic viscosity μ, with surface tension γ. When the surrounding flow field is an homogeneous and isotropic turbulent flow, characterized by an energy dissipation rate ϵ, and an integral length scale L_{int}, the Buckingham's Π theorem predicts that the dynamics is controlled by three dimensionless numbers. Choosing a set of dimensionless numbers which decouples viscous effects from capillary effects, we obtain that a generic measure

of shape deformation δ can be written as,

$$\frac{\delta}{d} = F\left(\mathrm{We}(d), \mathrm{Re}(d), \frac{d}{L_{int}}\right). \tag{4.5}$$

where F is a dimensionless function. The Weber number $\mathrm{We}(d) = 2\rho\epsilon^{2/3}d^{5/3}/\gamma$ compares inertial and capillary forces at the bubble scale. The Reynolds number $\mathrm{Re}(d) = \sqrt{2}\rho\epsilon^{1/3}d^{4/3}/\mu$ balances inertial and viscous forces at the bubble scale. Finally, the ratio d/L_{int} is the scale separation between the bubble scale and the integral length scale. Note that using ϵ and d we can define a characteristic velocity $U = \sqrt{2}(\epsilon d)^{1/3} = \langle \delta u^2(d) \rangle^{1/2}$, the velocity increment at the bubble scale in homogeneous and isotropic turbulence [142]. When the bubble size lies within the inertial range of the turbulent cascade, the surrounding flow is scale invariant and we expect the dynamics to be independent of d/L_{int}. The bubble dynamics will then be primarily controlled by the Weber number. In the presence of gravity g, one must also include the Bond number $\mathrm{Bo} = \rho g d^2/\gamma$, comparing gravity to capillary effects. For simplicity, we will not consider gravity in this study. This assumption is valid for bubble diameter smaller than the capillary length $\sqrt{\gamma/(\rho g)} \sim 2\,\mathrm{mm}$. In practice, looking at temporal evolution of bubble deformation, our model may describe shape oscillations slightly above the capillary length.

In this work we focus on bubbles which do not break, corresponding to a bubble size d within the inertial range of the turbulent cascade and $d < d_h$. For a typical turbulent flow with $\epsilon = 1\ \mathrm{m^2 s^{-3}}$, and $\mathrm{We}_c \approx 3$, $d_h = (\mathrm{We}_c\gamma/(2\rho\epsilon^{2/3}))^{3/5} \approx 8$ mm and $\mathrm{Re}(d_h) \approx 2300$. Note that $\mathrm{Re}(d_h) \sim \rho^{1/5}\gamma^{4/3}/(\epsilon^{1/5}\mu)$ decreases as ϵ increases for a given pair of liquid-gas. It is worth mentioning that, as a consequence, an increase of the global Reynolds number of the flow induces more viscous effects at the Hinze scale.

To model bubble deformations in turbulence, Risso et al. [165] introduced a forced linear damped oscillator equation to describe the dynamics of sub-Hinze bubbles. They assumed that the deformed radius $R(t)$ evolves following

$$\ddot{R} + \lambda\dot{R} + \omega^2 R = F_{ex}(t) \tag{4.6}$$

where λ is a damping rate, ω a natural frequency and $F_{ex}(t)$ an instantaneous forcing from turbulence. Bubble deformations and breakup are mainly controlled by the second spherical harmonics modes $\ell = 2$, which correspond to oblate-prolate oscillation [141, 158, 165]. As a consequence, as a first guess, they used the Rayleigh natural frequency of mode 2, $\omega = \omega_2$, equation (4.1), and the Lamb damping rate $\lambda = \lambda_2$, equation (4.2), even though these values only hold in a quiescent irrotational flow. Then, following the original idea from Kolmogorov [97] and Hinze [84], they assumed that the turbulent forcing from turbulence scales as the square of the instantaneous velocity increment at the bubble scale $\delta u(d,t)^2$, leading to a forcing $F_{ex}(t) = Kd^{-1}\delta u(d,t)^2$ from dimensional analysis, where K is a numerical constant of order 1. Doing so, they assumed that the presence of the bubble does not strongly affect the flow properties, so that the flow statistics correspond to the single fluid case. Expressing length in units of d, and time in units of $1/\omega_2$, equation (4.6) is written as

$$r'' + 20\sqrt{2/3}\,\mathrm{Oh}\,r' + r = \tilde{K}\mathrm{We}(t) \tag{4.7}$$

where $\tilde{K}$ is also a numerical constant and $\mathrm{We}(t) = 2\rho\delta u(d,t)^2 d/\gamma$ is the instantaneous bubble Weber number. This model is essentially the same as equation (4.4), with an additional random forcing term. This equation has been widely used for bubbles [100, 122, 123, 158] and drops [71, 82, 115, 169] oscillations in turbulence with the adequate expressions of the damping rate and natural frequency.

However, there is no guarantee that the bubble natural frequency and damping rate remain unchanged compared to the quiescent case. They may *a priori* depend on both Re and We. Indeed, surrounding flows are known to modify the natural frequency and the damping rate. For instance, for bubbles in a uniaxial inviscid straining flow, Kang et al. [91] showed that the flow couples modes $\ell = 2$ and 4, inducing a reduction linear in We, of the mode $\ell = 2$ natural frequency at linear order. In addition, in inertial flows, bubble deformations are primarily driven by Eulerian pressure increments at the bubble scale [154], which do not share the same statistics than velocity increments squared.

2.3 From deformations to breakup

A linear model cannot capture breakup. However, Risso et al. [165] noticed that the average bubble deformation increases linearly with We, up to the threshold for bubble breakup. This observation suggests that a linear dynamics could describe bubble deformations up to this point. The breakup time is then time taken to reach the critical value from which we can define a breakup rate κ_b.

Note that this approach differs from the modeling strategies reviewed in Lasheras et al. [102] and Liao et al. [111]. As emphasized by Liao et al. [111], the main approach is to model breakup induced by turbulent fluctuations or collisions with eddies. They classified breakup rate model into four distinct categories, plus a last one combining the previous approaches. The first one considers that drops/bubbles break when their kinetic energy is larger than some critical value. In the second category, drops/bubbles break when the velocity fluctuations at the particle size is larger than some value. In the third and fourth categories, it is the kinetic energy or the inertial force of the bombarding eddy respectively which are greater than some constants. We quickly review here the main physical ingredients.

One of the first work on breakup rate modeling was done by Coulaloglou et al. [47] in 1977. They defined the breakup rate as

$$\kappa_b = \frac{1}{\text{breakup time}} \cdot \text{fraction of drops breaking.} \tag{4.8}$$

The breakup time is a fraction of the eddy turnover time with possible corrections to account for viscous effects. To model the fraction of breaking drops, they assume that eddies and drops share the same distribution of kinetic energy. The fraction of breaking drops then corresponds to the fraction of drops such that their average kinetic energy is greater than their surface tension energy (ie $\mathrm{We} > O(1)$). The distribution of kinetic energy gives the distribution of breaking drops. Coulaloglou et al. [47] used a normal function, while Chatzi et al. [36] (and following papers [37, 38]) used a Maxwell's law. Both models fall into the first category of Liao et al. [111].

In the second category, which originates from the work of Narsimhan et al. [135], the particle breaks under due to a difference in relative velocity at the particle interface. Narsimhan et al. [135] modeled the probability distribution of velocity fluctuations at the particle scale with a normal law. The breakage criterion compares the kinetic energy of the fluctuations with the surface energy of the product of fragmentation assuming a symmetric binary breakup.

Finally, the third and fourth categories assume that drop/bubble breakage is controlled by the collision with eddies. Prince et al. [148] proposed a model similar to the coalescence frequency where the breakup rate results from the collision rate with eddies multiplied by the collision efficiency. This model was later improved by Luo et al. [114] to include the dependency on the child size.

Many refinements can be found in the literature which include viscous effects for instance, the fact that turbulence is not a succession of discrete eddies etc.. For examples [104, 118, 214] to cite only a few.

All these models assume that the effect of turbulence on the bubble can be modeled using the single phase statistics. They also involve quantities which are not easily accessible in practice such as the collision frequency or the collision efficiency. In this manuscript, we therefore use a parallel approach and try to infer a breakup rate from the deformation statistics of bubbles.

3 Conclusion: outline of the part

In this part, we aim at obtaining an expression for the breakup rate of bubbles as a function of the controlling parameters. From this expression, we would be able to derive an expression for the critical Weber number as a function of the parameters and the residence time (question *Q1*). To do so, we aim at describing bubble deformations in turbulence and infer the breakup statistics and the breakup rate. We therefore start by investigating bubble deformations and breakup in the model geometry of the uniaxial straining flow in chapter 5. This study allows us to find a reduced dynamics for bubble deformations. We then follow a similar approach in chapter 6 to infer a reduced dynamics for bubble deformations in isotropic turbulence. Finally, in chapter 7, we use this reduced dynamics to obtain an expression for the probability for a bubble to break, from which we define a critical Weber number depending on the residence time.

Chapter 5

A simplified geometry: The uniaxial straining flow [1]

Extension of p4 of Landau.

A colleague

Abstract

The equilibrium shape of bubbles in a uniaxial straining, as well as their linear stability have been studied theoretically and numerically. However, a description of the non linear dynamics as well as the influence of the initial conditions is still lacking, while necessary to predict breakup under various initial conditions. In this chapter, we investigate the bubble dynamics and breakup in such flows, starting from initial shapes far from the equilibrium shapes. We evidence that the breakup threshold is significantly smaller than the previous linear predictions and that it depends on both the Reynolds number at the bubble size, and the initial bubble shape (ellipsoids). To rationalize the bubble dynamics and the observed thresholds, we propose a reduced model for the oblate/prolate oscillations (second Rayleigh mode) based on an effective potential that depends on the control parameters and the initial bubble shape. Our model successfully reproduces bubble oscillations, the maximal deformation below the threshold and the bubble lifetime above the threshold.

Contents

1. Most of the chapter content have been published in in Rivière et al. [166].

1 Introduction

Revuelta, Rodríguez-Rodríguez and co-authors [162] noticed that bubbles in turbulence tend to elongate in a cigare-shape, especially before breakup. They hypothesized that this shape results from a local flow geometry mainly stretching along one direction, the bubble axis, combined with a compression along the two other directions. As breakup is a fast event, they assumed that the flow remains stationary during breakup and mainly axi-symmetric. They concluded that the steady uniaxial straining flow could model the local flow geometry around stretched and breaking bubbles. In order to model the breakup rate in turbulence, they focused on the breakup time in the straining flow and, in particular, on the effect of the density and viscosity ratios between the bubble and the surrounding liquid [162, 163, 170]. It is only recently, in 2021, that Masuk et al. [123] evidenced experimentally that uniaxial straining flows were indeed one of the main local flow geometry controlling bubble deformations and breakup in turbulence. As a consequence, before studying bubble deformations in turbulence, which is the subject of chapter 6, we focus on the dynamics in this model flow geometry.

The stability of bubbles in a uniaxial straining point has been studied theoretically through the help of linear stability analysis. By investigating the stationary shapes and their linear stability, it has been shown that below a critical Weber number, We_c^S, a stable and an unstable stationary solutions coexist. At We_c^S, the two solutions merge and no stationary solution remains beyond We_c^S: any bubble will surely break [90, 129, 177, 183]. However, this transition, called a saddle node bifurcation, only defines an upper bound for the critical Weber number, We_c, which separates breaking from non breaking bubbles in a given experimental or numerical setup. In sub-critical transitions, the knowledge of We_c^S is insufficient to predict the dynamics in realistic conditions since finite amplitude perturbation can lead to a state change well below the critical value of global stability loss. Such transitions have been evidenced for instance in parallel flows [39], open flows [43] or in spatially extended systems [48] such as dissipative solitons [70, 78], and in viscous drop breakup [187, 188]. As a consequence, a dynamical description is needed in order to predict whether the bubble breaks or not, depending on the initial conditions. Kang et al. [91] predicted theoretically the small amplitude dynamics around the equilibrium positions. However, a dynamical description of bubble deformations far from the stable states is still lacking.

In this chapter, we thus investigate numerically the dynamics of a bubble in a uni-axial straining flow, starting from initial shapes and flow configuration far from the equilibrium configuration.

2 Sub-critical bubble breakup

2.1 Phenomenology

As describe in chapter 2, we first run single phase numerical simulations in order to create a stagnation point flow. Then we use the result of these simulations as flow initial condition for bubble injection. The bubble equivalent radius, R_0, to box size ratio is 10. We create six stagnation point flows, of characteristic shear E, at a given Reynolds number $\mathrm{Re} = Ed^2/\nu \in$

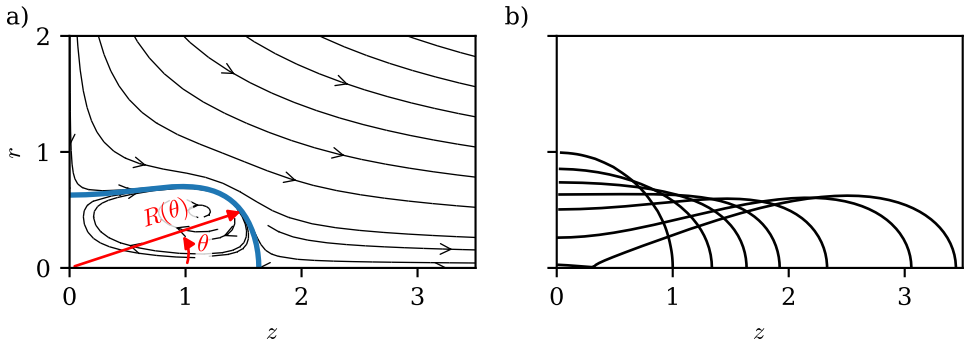

Figure 5.1 – a) Enlargement around a bubble experiencing its maximum deformation at Re = 400 and We = 7.3 ≈ We_c(Re = 400). z is the axis of symmetry, r the radial direction. The blue line denotes the bubble interface, black lines, isocontours of the stream function. b) Enlargement around a typical breakup sequence, exemplified at Re = 200, We = 10. Pinch-off does not occur on the plane of symmetry.

$[25, 50, 100, 200, 400, 800]$, where $d = 2R_0$ is the bubble equivalent diameter and ν the kinematic viscosity of the fluid, plus an inviscid flow, by setting viscosity to zero. In units of R_0 and E^{-1} the flow field is written as

$$u_\theta(R, \theta) = -\frac{3}{2} R \cos(\theta) \sin(\theta) \tag{5.1}$$

$$u_R(R, \theta) = \frac{1}{2} R (3\cos(\theta)^2 - 1) \tag{5.2}$$

where R and θ are defined on figure 5.1a. Once we have reached a stationary flow, we inject a bubble at the center of the stagnation point flow. The bubble is characterized by its Weber number $\mathrm{We} = \rho E^2 d^3/\gamma$, where ρ is the liquid density and γ the gas-liquid surface tension. To be consistent with the next chapters, density and viscosity ratios are 850 and 25 respectively, close to the air-water ratios.

We first consider initially spherical bubbles. Figures 5.1 illustrate the deformation dynamics. At low Weber number, the bubble first elongates, reaching its maximum deformation, and then relaxes to an equilibrium shape, either via damped oscillations (for Re typically larger than 100), or monotonic relaxation (Re < 50). Viscous shear at the bubble interface induces a recirculation inside the bubble, which can be visualised in figure 5.1a for a bubble experiencing its maximum deformation, at Re = 400 and We = 7.3. The equilibrium shape is not spherical [91, 129] and the overall shape depends on the value of the Reynolds number. At low Reynolds number, Re < 100, the equilibrium shape is mainly controlled by viscous shear at the interface. This field being dipolar (see equations (5.1),(5.2)), the result is an elongated shape with pointy ends [3, 91, 177, 219]. On the contrary, for Re ≥ 100, pressure gives the dominant contribution to the stress balance. From Bernouilli theorem, pressure is maximum at the two stagnation point (on the two axis, see figure 5.1a). The interface is thus pushed inwards and the equilibrium shape is closer to a cylinder [91, 177]. For sufficiently large We the bubble elongates along the z direction and breaks, as illustrated on figure 5.1b at Re = 200 and We = 10. As can be visualized in figure 5.1b, breakup does not occur on the axis of symmetry, creating at least one satellite bubble

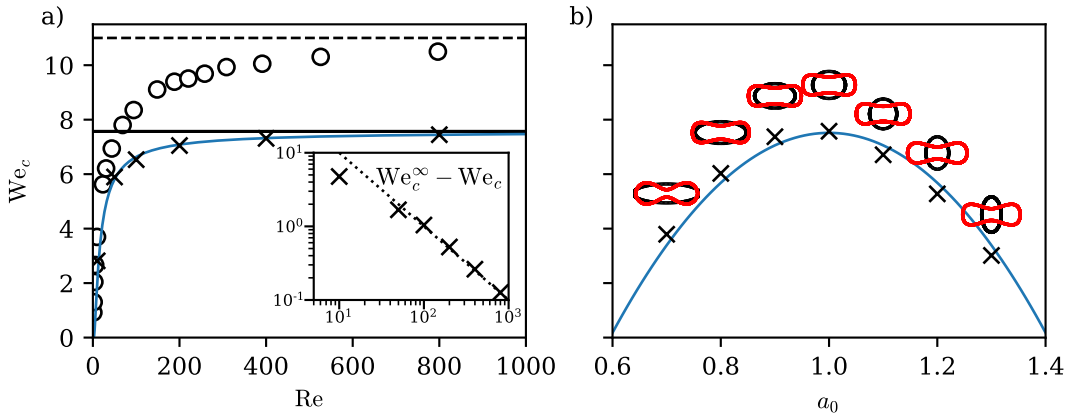

Figure 5.2 – a) Critical Weber number, We_c versus Re (crosses) with an error inferior to 10^{-2}. The solid black line is the inviscid value We_c^∞. The blue curve has expression $\mathrm{We}_c^\infty \exp(-100/(\mathrm{We}_c^\infty \mathrm{Re}))$. Open circles and dashed line are $\mathrm{We}_c^S(\mathrm{Re})$ and its inviscid limit as computed by Sierra-Ausin et al. [183] and Miksis [129] respectively. The inset shows the viscous correction to We_c^∞. The dotted line follows $100/\mathrm{Re}$. b) Critical Weber number versus the ellipsoid shape parameter a_0, for inviscid simulations. The blue curve is a polynomial fit of degree 2 with a maximum at $a_0 = 1$. Initial (black) and critical (red) shapes are represented for every a_0.

whose size depends on both Re and We. The study of the generation of this satellite bubble will be the subject of chapter 10.

2.2 Phase diagram: an initial-value problem

Lets first investigate the domain of stability of a bubble in this flow. We denote by We_c the critical Weber number which separates breaking from non breaking configurations. We measure We_c as a function of Re using a bisection method.

Role of inertia: The static critical Weber number We_c^S has previously been investigated by several authors from quasi-static deformations [129, 177] or linear stability analysis [183]. The recent computation of We_c^S as a function of the Reynolds number from Sierra-Ausin et al. [183] is shown in figure 5.2a (open circles) together with the inviscid limit from Miksis [129] (dashed line). We find that the critical Weber number We_c (black crosses) is significantly smaller than We_c^S at all Reynolds number. Indeed, in practice, the threshold We_c^S would be observed for quasi-static deformations of bubbles, henceforth neglecting inertial effects. Starting from an initially spherical bubble, at large Reynolds number $\mathrm{Re} \gg 1$, inertia cannot be neglected. Above the breakup threshold, $\mathrm{We}_c < \mathrm{We} < \mathrm{We}_c^S$, there still exists a stable shape surrounded by a finite basin of attraction, but the initial conditions, *i.e.* the initial shape and flow, lead to the escape from this basin, and therefore, to breakup. The observed breakup transition is henceforth sub-critical. For such bifurcations, the response to an initial finite perturbation is dramatic, and the dynamics cannot be investigated using only linear stability analysis [43]. For viscous drops in extensional flows at low Reynolds number, similar sub-critical breakups have been evidenced experimentally and numerically [72, 155, 187, 188].

Viscous correction: As Re increases, the critical Weber number converges to the inviscid value (solid line), We_c^∞, with a viscous correction, $\mathrm{We}_c^\infty - \mathrm{We}_c$, following $1/\mathrm{Re}$ (inset plot). We observe that reducing Re for a fixed We allows the bubble to pass from a stable to an unstable configuration. Indeed, viscosity not only damps the dynamics, it also plays a destabilizing role through viscous shear at the interface. This correction can be understood heuristically by looking at the initial stress balance at the spherical bubble interface. In particular, we focus on the additional Laplace pressure necessary to compensate viscous stresses at the bubble interface. Using $1/E$ as a time unit, d as a length unit and ρd^3 as a mass unit, the initial dimensionless normal stress jump at the interface of a bubble of negligible viscosity reads

$$-[p] + \frac{2}{\mathrm{Re}}\partial_n u_n = \frac{1}{\mathrm{We}}\kappa \tag{5.3}$$

where $[\cdot]$ denotes the difference across the interface, between liquid and gas, p is the dimensionless pressure, n is an outward unit vector, normal to the bubble interface, $\partial_n u_n$ is evaluated in the liquid phase, and κ is the dimensionless local curvature. In order to get the evolution of We_c with Re, we develop equation (5.3) in power or $1/\mathrm{Re}$.

Let us first consider an initially spherical inviscid bubble at We_c, in an inviscid flow. In this case, at order 0 in $1/\mathrm{Re}$, the initial dimensionless normal stress jump at the interface reads

$$-[p]^\infty = \frac{1}{\mathrm{We}_c^\infty}\kappa \tag{5.4}$$

where the exponent $\cdot^\infty$ denotes the inviscid values.

For a large but finite Re, at criticality, $\mathrm{We} = \mathrm{We}_c = \mathrm{We}_c^\infty + \delta\mathrm{We}_c$, we can develop the pressure jump at first order in $1/\mathrm{Re}$: $[p] = [p]^\infty + 1/\mathrm{Re}\,\delta[p]$. Equation (5.3) evaluated at $\mathrm{We} = \mathrm{We}_c$, at first order in $1/\mathrm{Re}$ then reads

$$-[p]^\infty - \frac{1}{\mathrm{Re}}\delta[p] + \frac{2}{\mathrm{Re}}\partial_n u_n = \frac{1}{\mathrm{We}_c}\kappa.$$

Using equation (5.4) into the previous balance, we get

$$\kappa\frac{\delta\mathrm{We}_c}{\mathrm{We}_c^\infty} = \frac{1}{\mathrm{Re}}(\delta[p] - 2\partial_n u_n)$$

and therefore,

$$|\mathrm{We}_c^\infty - \mathrm{We}_c| \propto \frac{1}{\mathrm{Re}}. \tag{5.5}$$

Importance of the initial conditions: To test the sensitivity to the initial conditions, and the boundaries of the basin of attraction of the stable equilibrium, we also consider ellipsoids of revolution of the same volume, $4/3\pi R_0^3$, with a local radius $R(\theta)$, in a inviscid flow (see figure 5.1a for the definition of θ). The semi axis $a_0 = R(\pi/2)/R_0$ sets the whole initial shape from volume conservation, with prolate shapes corresponding to $a_0 < 1$ and oblate shapes to $a_0 > 1$. We find that the critical Weber number (fig. 5.2b) dramatically depends on the initial bubble shape, as expected for a sub-critical transition. The critical Weber number is maximum for the sphere, and decreases for both oblate and prolate shapes as the additional surface energy participate to

the breakup process. Near the maximum at $a_0 = 1$, we expect a linear dependency of We_c with the surface increase compared to the sphere. This increase of surface should scale as $(1 - a_0)^2$. It follows that We_c evolve quadratically with the distance to the sphere $|1 - a_0|$, as shown by the parabolic fit (blue line) in figure 5.2b. Note that plotting We_c as a function of the initial surface instead of a_0 does not restore the symmetry between oblate and prolate shape. Indeed, We_c is controlled by the initial shape and the initial velocity at the bubble interface, the latter also depends on the initial shape. Figure 5.2b also shows the initial bubble shape (in black) as a function of a_0. This shape are compared to the critical bubble shapes, corresponding to the maximum bubble elongation. Strikingly, there is a large dependency on the initial bubble shape. This variability might come from the different values of We_c or from the initial bubble shape which also varies the dynamics. Assuming the variability only originates from We, we get that changing the initial bubble shape allows us to explore the unstable branch of the bifurcation diagram. Sierra-Ausin et al. [183] investigated the unstable shapes as a function of We, for fixed Ohnesorge number $\mathrm{Oh} = \sqrt{\mathrm{We}/\,\mathrm{Re}}$. Qualitatively, they observed the same effect: the radius at the plane of symmetry sinks when We decreases. Nevertheless, a watchful reader may notice that the critical shape at $a_0 = 0.7$ is more stretched and sank than its oblate counterpart at $a_0 = 1.3$, even though the latter corresponds to a lower We. Therefore, the point at which the bubble shape leaves the basin of attraction of the stable shape also depend on the initial conditions.

Bubble fate depends on its initial shape. As a consequence, one must take into account the whole deformation dynamics in order to predict breakup. In the next section, we aim at finding a reduced model to describe the dynamics which takes into account the initial bubble shape, the Reynolds number and the Weber number.

3 A reduced non linear model for bubble dynamics

3.1 Temporal evolution of the oblate-prolate mode

To describe bubble deformations with a reduced model, we decompose the local bubble radius into the spherical harmonics base $Y_{\ell,m}(\theta, \phi)$ and follow the amplitude of each mode $x_{\ell,m}$ in time. Modes $m = 0$ are the only axi-symmetric modes. Therefore, in this axi-symmetric geometry bubble radius reads

$$R(\theta) = R_0[1 + \sum_{\ell=2}^{\infty} x_{\ell,0}(t) Y_{\ell,0}(\theta)]. \tag{5.6}$$

This decomposition in modes decouples temporal evolution from spatial shape. More details about the spherical harmonics decomposition can be found in chapter 3. Since oblate-prolate deformations, corresponding to the mode $\ell = 2$, dominate the dynamics, in this chapter, we focus on the dynamics of this mode, that we denote x for the sake of simplicity.

Figure 5.3 illustrates three dynamics of mode $\ell = 2$ for initially spherical bubbles at $\mathrm{Re} = 400$: a stable bubble far from We_c (blue curve in 5.3a), a stable bubble at $\mathrm{We} \approx \mathrm{We}_c$ (blue curve in 5.3b), and an unstable bubble at $\mathrm{We} \approx \mathrm{We}_c$ (grey curve in 5.3b). Time is made dimensionless using the Rayleigh natural frequency [101, 159], $\omega_2 = [12\gamma/(\rho R_0^3)]^{1/2}$. Far from We_c the mode amplitude, x, exhibits damped oscillations and converges to a finite value x_∞, corresponding to a

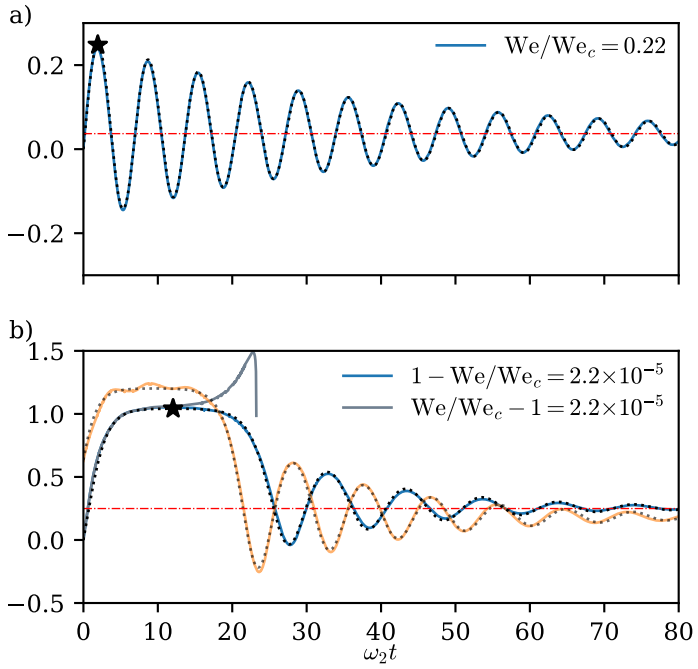

Figure 5.3 – a) & b) Several typical temporal evolution of x at Re = 400. Simulation data are in color, the model (5.7) is superimposed (black dotted line). The black star and the dashed red lines correspond to the maximum, $x_{\max}$, and equilibrium values, x_∞, respectively for the two blue trajectories (spheres). a) An initially spherical bubble at low We. b) Three evolutions close to $\mathrm{We}_c(a_0)$, for a stable sphere (blue line), an unstable sphere (grey line) and a stable ellipsoid (orange line, $a_0 = 0.8$).

non spherical stable shape, as shown in figure 5.3a for an initially spherical bubble at Re = 400. Its maximum value is denoted by the black star. The same behaviour is also observed for different initial conditions (not shown). Figure 5.3b illustrates the dynamics near the critical threshold. Slightly below the critical Weber number We_c, for an initially spherical bubble (blue curve), the amplitude first approaches a plateau and eventually converges to a stable shape. The maximum value $x_{\max}$ (black star) is close to its critical value x_c above which the bubble breaks. Just above the threshold (grey curve), the dynamics is initially indistinguishable from the stable case, until the amplitude grows exponentially and finally decays abruptly, right before breakup. In the final stage, as the bubble pinches, all modes must be taken into account to describe bubble deformations. In addition note that the spherical decomposition breaks down close to breakup as the local radius is not mono-valued in θ anymore. The time spent close to the critical point diverges as We approaches We_c. For a different initial shape, as illustrated in figure 5.3b with $a_0 = 0.8$ (orange curve), we observe the same behaviour, however the critical deformation x_c at threshold increases, as this behavior is obtained for a larger value of We (see figure 5.2b).

The behavior near x_c is symptomatic of a sub-critical transition with a stable and a unstable equilibrium positions, in which the stability depends on both the control parameters (We and Re) and the initial conditions. In the next section, we rationalize these observations using the reduced model.

3.2 Non linear oscillator equation

We assume that the dynamics of mode x can be described by a damped non linear oscillator of the form

$$\ddot{x} + \lambda \dot{x} = -\nabla V(x, \mathrm{We}, \mathrm{Re}, a_0), \tag{5.7}$$

where $V(x, ...)$ is an effective potential that may depend on all control parameters (We, Re and a_0). Time is made dimensionless using the mode natural frequency ω_2. The damping factor $\lambda = 20\sqrt{2/3}\mathrm{Oh}$, is the theoretical linear damping factor as computed by Lamb [101]. The case of a harmonic potential was investigated by Kang et al. [91] by considering small amplitude oscillations around the equilibrium shape. Here, we look for a stationary polynomial potential, V, of degree 3, the minimum degree allowing to have two equilibrium positions. To do so we minimize, for every simulation, the mismatch between left and right hand side of equation (5.7), that is to say the quantity

$$I = \int (\ddot{x} + \lambda \dot{x} - p_0 - p_1 x - p_2 x^2)^2 \mathrm{d}t \tag{5.8}$$

by optimizing p_0, p_1 and p_2.

This model perfectly describes the temporal evolution of x, both far from We_c (see black dotted line in figure 5.3a) and close to We_c (figure 5.3b), for both sphere and ellipsoids. Note that to obtain the curves on figure 5.3, one has to estimate the initial position and velocity of x. The initial value of x can be computed exactly from the initial bubble shape. Similarly, one can estimate the initial velocity $\dot{x}_0$ knowing the initial velocity along the bubble interface. The initial velocity around the bubble corresponds to the theoretical uniaxial straining flow as it has not yet been modified by the presence of the bubble. As an example, for an initially spherical

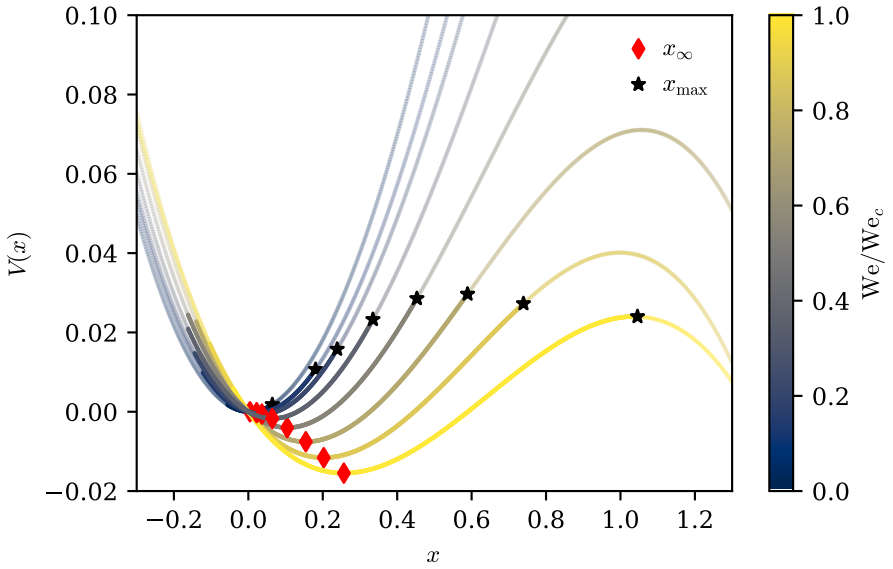

Figure 5.4 – Evolution of the potential V, defined in equation (5.7), with We for initially spherical bubbles at Re = 400. The range of explored x values have a more intense color. Stable equilibrium positions, x_∞, are denoted by red diamonds (red dashed lines in a and b). The maximum values, $x_{\max}$, are denoted by black stars (same in figures 5.3).

bubble, the normal velocity along the bubble interface u_n is written as,

$$u_n(\theta) = \frac{2}{\sqrt{6}}\mathrm{We}^{1/2}[3\cos(\theta)^2 - 1] = 16\sqrt{\frac{\pi}{30}}\mathrm{We}^{1/2}\, Y_2^0(\theta). \tag{5.9}$$

Computing the spherical harmonic decomposition of u_n, and in particular its modes $\ell = 2$, gives the value of $\dot{x}_0$. For the sphere, the spherical harmonics decomposition is particularly simple, as shown by equation (5.9), as u_n is proportional to $Y_2^0(\theta)$. Importantly, as u_n scales as $\sqrt{\mathrm{We}}$, we have $\dot{x}_0 \propto \sqrt{\mathrm{We}}$, regardless the initial bubble shape. The shape only changes the numerical prefactor. Therefore, as We increases the initial velocity, $\dot{x}_0$ increases. In practice, to plot figure 5.3, far from We_c, we directly measure the initial velocity in the simulations as the dynamics weakly depends on the initial conditions. On the contrary, close to criticality, initial conditions dramatically affect the dynamics and small initial errors completely change the outcome. For these cases, we use the theoretical initial value of x and then manually adjust the initial velocity to best fit the temporal evolution of x.

For all cases, we find that the dynamics of mode 2 can indeed be described by a reduced model in the form of a damped oscillator in a non linear potential. This model captures the linear regime as well as the non linear dynamics, The shape of the potential depends on the relevant dimensionless numbers, We and Re, as well as on the initial bubble shape. In the next section, we investigate the influence of every parameter on the potential shape and their consequences on the value of We_c.

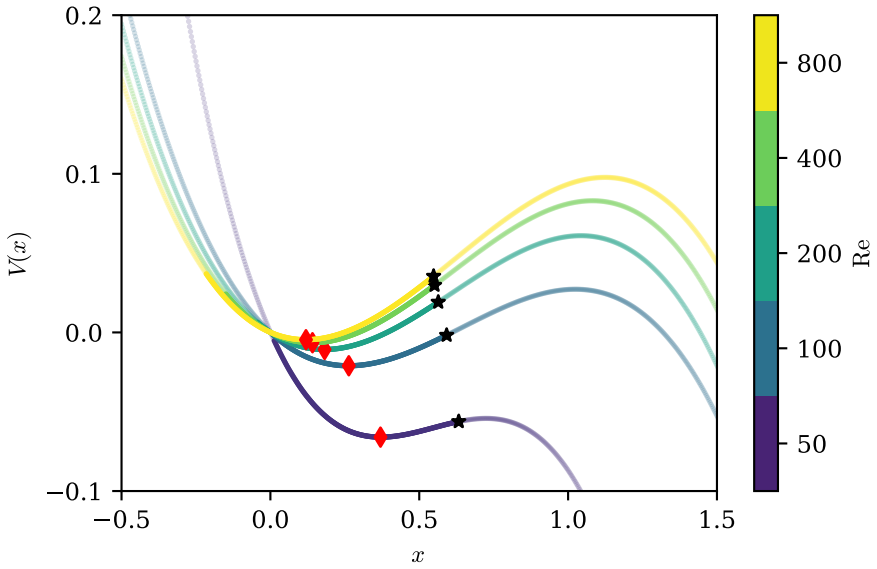

Figure 5.5 – Evolution of the potential V with Re for initially spherical bubbles at We = 5. The range of explored x values have a more intense color. Stable equilibrium positions are denoted by red diamonds (red dashed lines in a and b). The maximum values, $x_{\max}$, are denoted by black stars (same in figures 5.3).

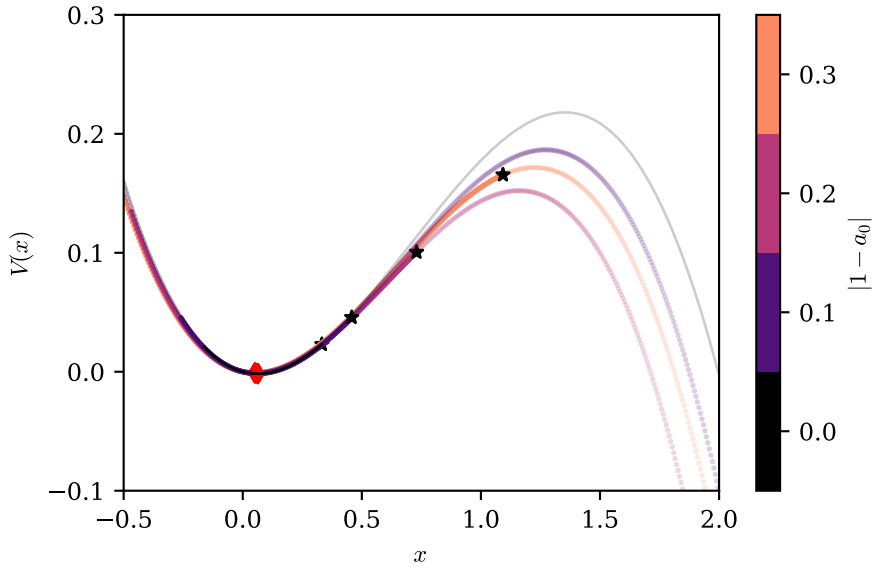

Figure 5.6 – Evolution of the potential V with the initial bubble shape a_0, for prolate ellipsoid at Re = 400 and We = 2.7. The range of explored x values have a more intense color. Stable equilibrium positions are denoted by red diamonds (red dashed lines in a and b). The maximum values, $x_{\max}$, are denoted by black stars (same in figures 5.3).

3.3 Shape of the effective potential and We_c

The effective potential V depends on We (figure 5.4), as well as on Re (figure 5.5) and a_0 (figure 5.6 for prolate shapes). It is interesting to investigate individually the effects of these three parameters on the potential shape and bubble dynamics.

We-dependency: Figure 5.4 illustrates the We-dependency of the effective potential for Re = 400, where blue curves correspond to We $\to$ 0 and yellow curves to We $\to$ We_c. During one simulation, a bubble only explore some values of x (up to $x_{\max}$). The range of x values explored by the bubble has a more intense color. This is the region where we expect the potential shape to be more accurately determined. For a given Reynolds number, as Weber increases, the stable equilibrium x_∞ (red diamonds) increases, in agreement with the literature [91, 129, 183]: increasing We leads to more elongated shapes at equilibrium. Concomitantly, as We increases, the initial velocity, $\dot{x}_0 \propto \sqrt{We}$, increases and the energy barrier decreases, leading to the critical case where $x_{\max} = x_c$ and We = We_c (yellow curve). As was anticipated in section 2.2, at the critical Weber number, there still exists an equilibrium position but the bubble escapes from its basin of attraction. The value of We_c results from a dynamical effect: initial velocity allows the bubble to overcome the energy barrier and break. Increasing We further more would lead to the merging of the two equilibrium positions at We = We_c^S, corresponding to the global stability loss.

Re-dependency: Conversely, if we fix We and vary Re, we observe that, as Re decreases, the equilibrium position shifts to the positive values [91] as illustrated in figure 5.5 for We = 5. Indeed, at equilibrium, at low Re, the bubble is mainly elongated [3, 91, 177, 219] and mode $\ell = 2$ is large. On the contrary, for large Re, bubble shape is more cylindrical [91, 177]. As a consequence, x is small (and mode $\ell = 4$ will be dominant). We also find that the energy barrier decreases with decreasing Reynolds number. This effect is consistent with the destabilizing role of viscosity which leads to a decrease of We_c with Re, as can be seen on figure 5.2a.

a_0-dependency: Eventually, we investigate the effect of the initial bubble shape, illustrated on figure 5.6 for prolate shapes at Re = 400 and We = 2.7. As expected from the linear stability analysis, the stable equilibrium shape does not depend on a_0: all reds diamond lie on top of each others. We observe a non monotonous dependency of the energy barrier with a_0. Nevertheless, on the range of explored values, the potential shape coincide for all a_0. Indeed, increasing the initial bubble deformation increases the range of explored x. The variability that we observe originates from the limited range of explored x. Therefore, for prolate shapes, we find not effect of a_0 on V. Equation 5.7 is valid for all a_0 and the initial bubble shape only influences the initial conditions.

Potential coefficients: Figures 5.7 show the evolution of the three coefficients p_0, p_1 and p_2 of equation (5.8) with We and Re, for initially spherical bubbles. Circles denote finite Reynolds number simulations while black crosses are for inviscid simulations. For all Re, the constant forcing p_0, depends linearly on We (figure 5.7a), as was found theoretically in the inviscid

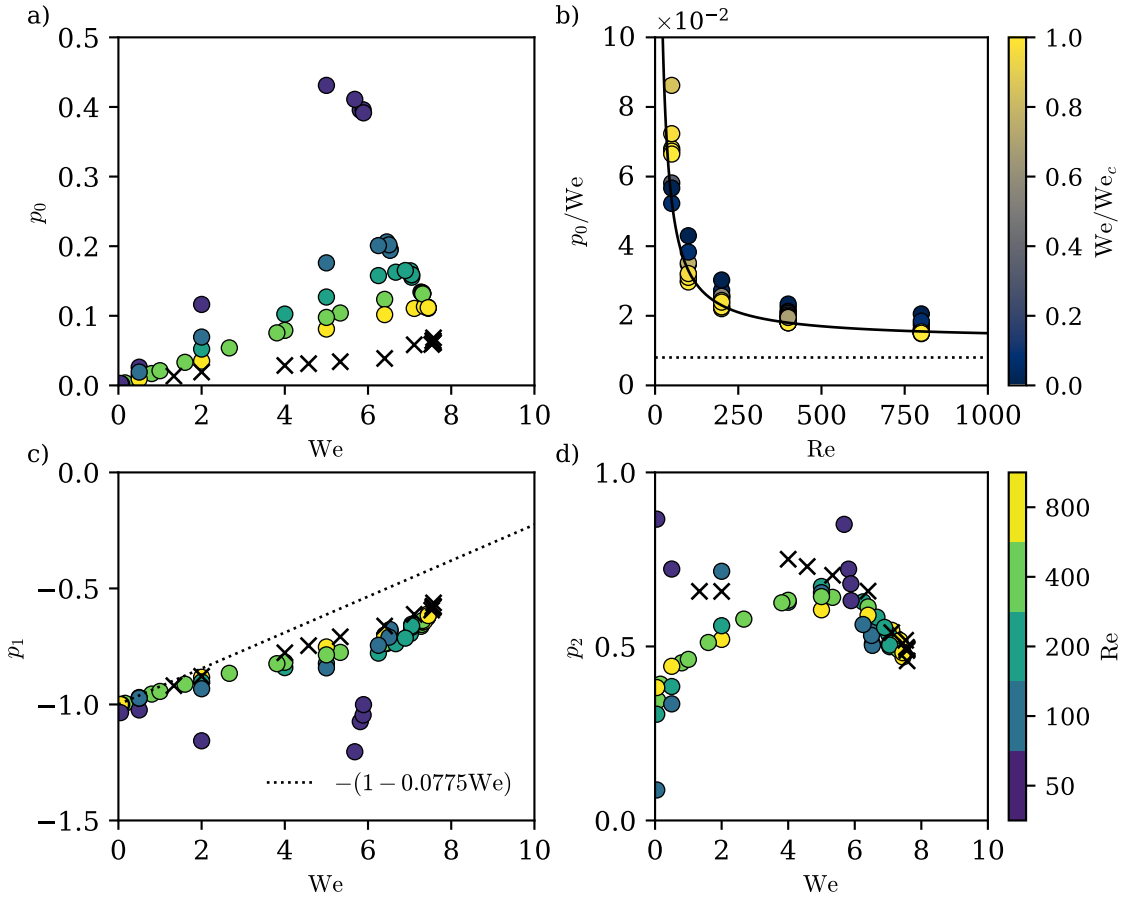

Figure 5.7 – Evolution of the coefficients of the three parameters defined in (5.8) with Re and We for initially spherical bubbles. Colored circles correspond to finite Re simulations and black crosses to inviscid simulations. a) Constant coefficient p_0 as a function of We. p_0 evolves linearly with We. b) Evolution of p_0 with Re. The dotted black line is the average inviscid value. We recover a more efficient forcing at small Re, compatible with a $1/\mathrm{Re}$ scaling (solid black line). c) Evolution of the linear coefficient p_1 with Re. The black dotted line is the prediction of the pulsation from Kang et al. [91] found from a linear development. d) Evolution of the quadratic coefficient p_2 with We.

case by Kang et al. [91]. However, there was no theoretical prediction for the Re-dependency. Figure 5.7b shows that p_0 decreases with Re, in agreement with the destabilizing effect of viscosity and converges to its inviscid value (black dotted line). The shape is compatible with a $1/\mathrm{Re}$ decay (solid black line), reminiscent of the Reynolds dependency of We_c. The linear coefficient p_1 is found to always be negative (figure 5.7c): the linear restoring force is positive, and $-p_1$ is the oscillator angular frequency. For all Reynolds number, we recover that $-p_1$ converges to 1 as We converges to 0. At this limit, the bubble natural frequency is the bubble natural frequency in a quiescent flow, as computed by Rayleigh et al. [159] and Lamb [101]. We found a marginal dependency of p_1 with Re ranging from 100 to 800. For the lowest Reynolds number $\mathrm{Re} = 50$, the value of p_1 is under-determined, as the oscillations are overdamped. As We increases, the angular frequency $|p_1|$ decreases, as can be visualized on figures 5.3. For small We, $\mathrm{We} < 2$, the dynamics is well approximated by a linear oscillator, and we recover the theoretical prediction from Kang et al. [91] (black dotted line). By developing the modes dynamics around the equilibrium position, they show that the coupling between modes $\ell = 2$ and $\ell = 4$ induces an effective modification of the natural frequency of mode 2 at linear order. The nonlinear coefficient p_2 is found to be always positive, in agreement with the existence of an unstable equilibrium position for x. p_2 is always of order 1, and exhibits non monotonic evolution with the Weber number (figure 5.7d). However, p_2 values are underdetermined for small and moderate values of We, $\mathrm{We} < 4$, for which the dynamics is mostly linear, as was illustrated for prolate shapes on figure 5.6. We did not find a clear dependency of p_2 with Re. Indeed, at large Reynolds number, we expect non linear effects to come from the non linear term of the Navier-Stokes equations, which do not depend on viscosity.

3.4 Equilibrium positions

In this section, we compare the equilibrium position of the effective potential with the linear stability analysis equilibrium positions.

Figure 5.8 shows the theoretical inviscid equilibrium positions from Kang et al. [91]. At a given Weber number, there are two equilibrium position. The lower branch represents the stable position, while the upper branch is the unstable position. At a critical Weber number, $\mathrm{We}_c^S = 11$, the two branches merge and there is no stable position anymore.

Figure 5.8a shows the stable equilibrium positions of the effective potential for every Reynolds and Weber number, for spheres. The rightest symbol for every Re corresponds to the critical Weber number. We recover the results from the previous section: stretching increases with increasing We and decreasing Re. As Re increases, the stable equilibrium converges to the linear inviscid prediction from Kang et al. [91].

In our simulations, the best estimate of x_c is obtained with the maximum deformation, $x_{\max}$, at We_c. Figure 5.8b shows the maximum deformation as a function of We for each Re, as well as the inviscid simulation (black stars), for initially spherical bubbles. As Weber increases, for all Reynolds, the maximum deformation increases. The maximum deformation for each Re corresponds to x_c. As Re increases, x_c converges to the inviscid value (red star). However, the inviscid critical value does not lie on the unstable (upper) branch from Kang et al. [91]. We conclude that x_c does not correspond to the unstable position predicted by the linear stability

analysis. This result confirms the observation made on figure 5.2b, that critical shapes vary with the initial bubble shape. Inertial effects allows the bubble to explore other branches of the bifurcation diagram.

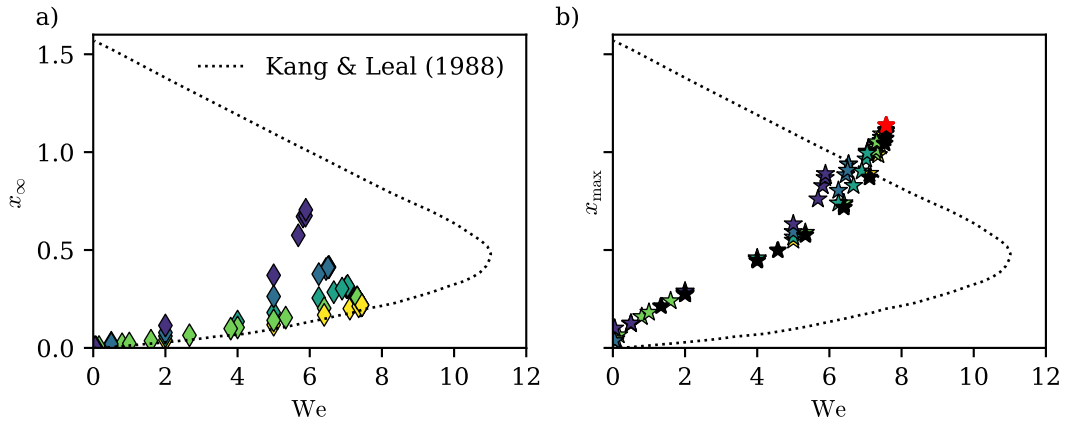

Figure 5.8 – Comparison between the equilibrium values of the effective potential for spheres and the linear stability values. The black dotted line represents the theoretical inviscid prediction from Kang et al. [91]. The stable branch is the lower one. The unstable branch the upper one. Re is color-coded (See colorbar of figure 5.7). a) Stable equilibrium positions as a function of We for each Re. b) Maximum deformations for spheres. Black symbols represent the inviscid simulations. The red star is inviscid value of x_c.

4 Dynamics close to the critical point

We have identified an effective potential which describes the full dynamics of mode $\ell = 2$. We now use the reduced model to investigate the dynamics close to the critical point x_c, for both stable bubbles and unstable bubbles at $\mathrm{We} \approx \mathrm{We}_c$.

4.1 Maximum deformation

First, we use the effective potential V description for the dynamics of x, to quantify the evolution of the maximal deformation as $\mathrm{We} \to \mathrm{We}_c^-$. For the sake of simplicity, we consider the limit of negligible dissipation, in which energy is conserved,

$$\frac{1}{2}\dot{x}_0^2 + V(x_0, \mathrm{We}) = \frac{1}{2}\dot{x}^2 + V(x, \mathrm{We}), \tag{5.10}$$

with the initial condition $\dot{x}_0 = \sqrt{2\mathrm{We}}$. Without any loss of generality we set $V(x_0, \mathrm{We}) = 0$ for all We. We define $\max(x) = x_{\max}$. At the maximum deformation, velocity is zero $\dot{x}_{\max} = 0$. It results from equation (5.10) that $x_{\max}$ is solution of

$$\mathrm{We} = V(x_{\max}, \mathrm{We}). \tag{5.11}$$

As x_c is one of the equilibrium position of V, $\partial_x V|_{x_c} = 0$, developing (5.11) around the unstable position x_c, at the lowest orders in $\mathrm{We}_c - \mathrm{We}$ and $x_c - x_{\max}$ gives

$$\mathrm{We}_c + (\mathrm{We} - \mathrm{We}_c) = V_c + (\mathrm{We} - \mathrm{We}_c)\partial_{\mathrm{We}} V|_c + \frac{1}{2}(x_c - x_{\max})^2 \partial_{xx} V|_c \tag{5.12}$$

where $V_c = V(x_c, \mathrm{We}_c)$ and $|_c = |_{x_c, \mathrm{We}_c}$. Since, by definition, $\mathrm{We}_c = V_c$ we get:

$$(x_c - x_{\max})^2 = A(\mathrm{We}_c - \mathrm{We}) \tag{5.13}$$

with $A = 2(\partial_{\mathrm{We}} V|_c - 1)/\partial_{xx} V|_c$ and $A > 0$ by definition. Figures 5.4, 5.5 and 5.6 show that $\partial_{xx} V|_c$ is always negative, (x_c is a maximum), and that $\partial_{\mathrm{We}} V|_c < 0$ (the energy barrier decreases with increasing We). This confirms that $A > 0$ so that $x_c - x_{\max}$ reads

$$x_c - x_{\max} = \sqrt{A}\sqrt{\mathrm{We}_c - \mathrm{We}}. \tag{5.14}$$

In this article, we use the spherical mode decomposition which allows to decouple different modes of deformations. However, in experiments, reconstructing the whole bubble shape is challenging as it requires the use of several high speed cameras. Measuring the length of the main bubble axis is more accessible. To give a simpler description of the shapes close to the critical point, we introduce the deformation parameter $\mathcal{D} = 1 - R(\pi/2, t)/R(0, t)$ with $\mathcal{D} < 0$ for oblate shapes, $\mathcal{D} > 0$ for prolate shapes and $\mathcal{D} \to 1$ for an infinitely long gas filament along z. This quantity could be evaluated experimentally from pictures. Figure 5.9a shows $\mathcal{D}$ for both the inviscid ellipsoids (triangles) and the spheres at finite Re (circles). For $\mathrm{We} \to 0$, the bubble is insensitive to the surrounding flow and $\mathcal{D}_{\max} \to \mathcal{D}_0 = 1 - a_0^3$ when $a_0 \leq 1$. Conversely, for $\mathrm{We} \to \mathrm{We}_c$ the maximum deformation converges to a critical value $\mathcal{D}_c$, which depends on both Re and a_0. We find that both the initial bubble deformation and the Reynolds number increases the critical deformation $\mathcal{D}_c$, with a slight difference between oblate and prolate shapes for the same distance to the sphere $|1 - a_0|$. As already discussed, the discrepancy between oblate and prolate shapes comes from the different We values at which the critical shapes are reached. The total deformation being mainly given by the amplitude x, we expect $\mathcal{D}$ to follow

$$\mathcal{D}_c - \mathcal{D}_{\max} = \alpha\sqrt{1 - \mathrm{We}/\mathrm{We}_c}, \tag{5.15}$$

as We approaches We_c. For each Re and a_0 values, we fit the two parameters α and $\mathcal{D}_c$ of equation (5.15). All data sets collapse on the same master curve as represented in the inset of figure 5.9a for sphere, showing that equation (5.15) also holds for non conservative systems (finite Re). Figures 5.9b and 5.9c show the evolution of $\mathcal{D}_c$ with Re and a_0 respectively, while 5.9d and 5.9e present the evolution of the slope α. In both 5.9b and 5.9d, the black dotted line (which corresponds to $a_0 = 1$ in 5.9c and 5.9e) represents inviscid values. $\mathcal{D}_c$ increases with Re and decreases with the distance to the sphere. These dependencies are reminiscent of the evolution of We_c with both Re and a_0. Indeed, since larger deformations need to be reached in order to break for larger Re or distance to the sphere, We_c increases. The deformation $\mathcal{D}_c$ varies strongly with a_0, which implies that bubble fate is highly dependent on history. The critical

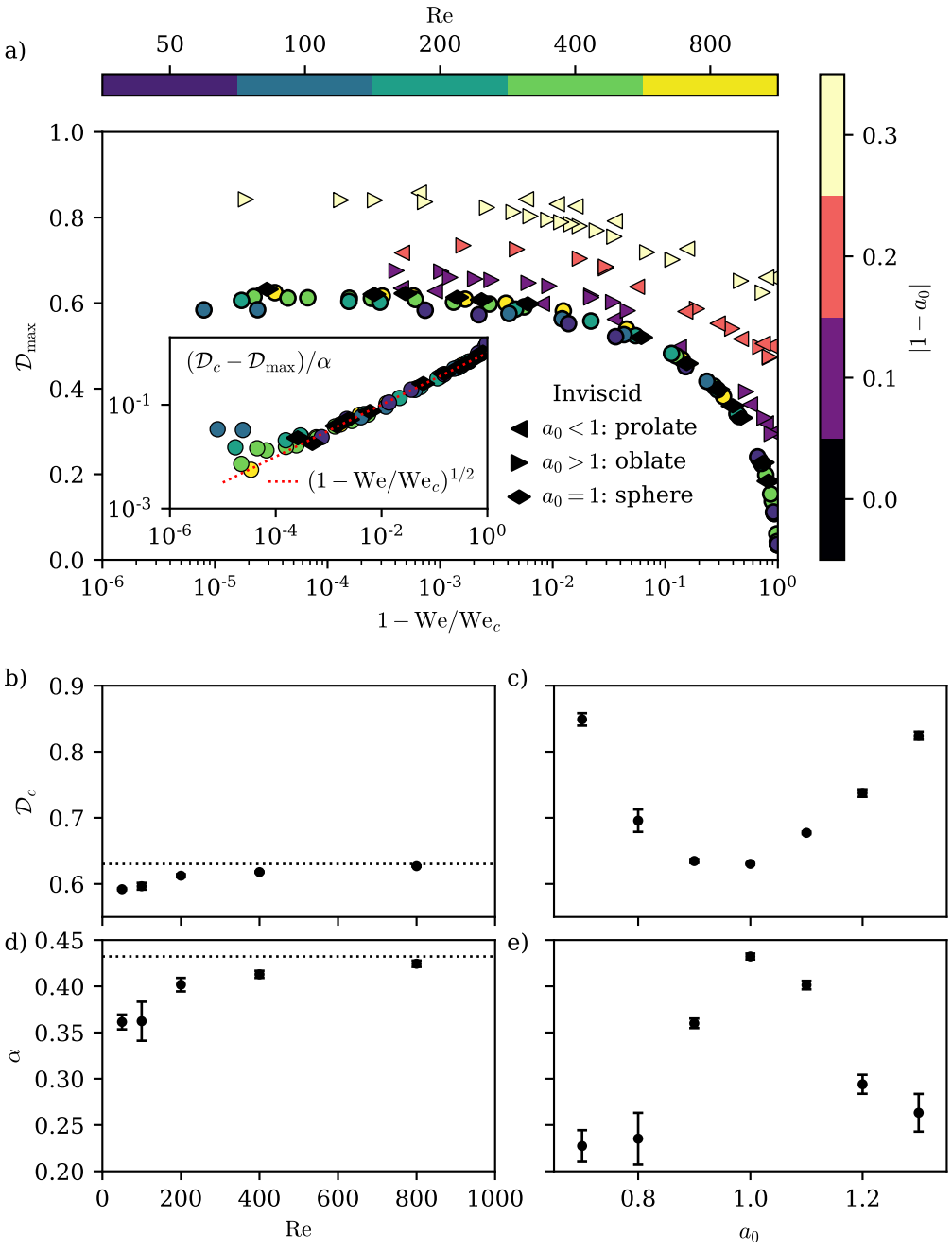

Figure 5.9 – a) Maximal deformation as a function of the distance to We_c. Finite Re simulations are denoted with circles, inviscid ellipsoids by triangles and inviscid spheres by diamonds. As $\mathrm{We} \to \mathrm{We}_c$, the maximal deformation converges to its critical value $\mathcal{D}_c$. Inset plot: Rescaled $\mathcal{D}_{\max}$ for the spheres, with two parameters that depend on Re: $\mathcal{D}_c$ and α. In b) the black dotted line denotes the inviscid value for spheres (and correspond to $a_0 = 1$ in c). b) & c) Evolution of $\mathcal{D}_c$ with Re and a_0 respectively. d) & e) Similar plots for the evolution of the slope with Re and a_0.

shapes show that bubbles are more deformed at criticality when the initial shape is not spherical (see figure 5.2b), revealing the importance of inertial effect in the breakup process.

4.2 Bubble lifetime

Similar developments can be performed to model the lifetime slightly above the critical Weber number. Indeed, for unstable bubbles, when $\mathrm{We} \to \mathrm{We}_c^+$, the bubble lifetime is dominated by the time spent close to the unstable shape, as visualized on figure 5.3b. In comparison bubble pinch-off in itself is extremely fast. We show in Appendix A, by developing the minimum speed reached at x_c, that this time can be expressed as

$$ET = ET(2\mathrm{We}) - \beta \log(\mathrm{We}/\mathrm{We}_c - 1) \tag{5.16}$$

where $ET(2\mathrm{We})$ and β are two numerical constants, and $\mathrm{We} > \mathrm{We}_c$. Figure 5.10a shows the dimensionless lifetime, ET, as a function of the distance to the critical point. In the limit of large Weber number, for all cases, the lifetime converges to the advection time $1/E$ with a viscous correction following $1/\mathrm{Re}$, as reported previously [162]. Near $\mathrm{We} = \mathrm{We}_c$, the lifetime diverges logarithmically. In this range of Re, the breakup time close to the critical We marginally depends on Re. Breakup is primarily controlled by the potential shape and the initial velocity. For both oblate and prolate shapes, breakup occurs faster than for spheres. Indeed, capillary effects accelerate the dynamics. After adjusting the two constants of equation (5.16) for each dataset, all the data collapse onto a single curve, as shown on the inset plot of figure 5.10a for initially spherical bubbles. Similarly to the maximum deformation, we find that equation (5.16) also holds at finite Reynolds number even though is was derived in the inviscid limit. Figures 5.10b-e show the evolution of β and $ET(2\mathrm{We})$ with both Re for spheres and a_0 for inviscid ellipsoids. Again, the black dotted line is figures 5.10b and 5.10d corresponds to the inviscid spheres ($a_0 = 1$ in figures 5.10c and 5.10e). Figures 5.10b and 5.10c show that $ET(2\mathrm{We}) \approx 1$ a value that is independent on both Re and a_0. On the contrary, the slope β increases as the initial shape gets away from the sphere (see figure 5.10e) and slightly increases with Re (figure 5.10d).

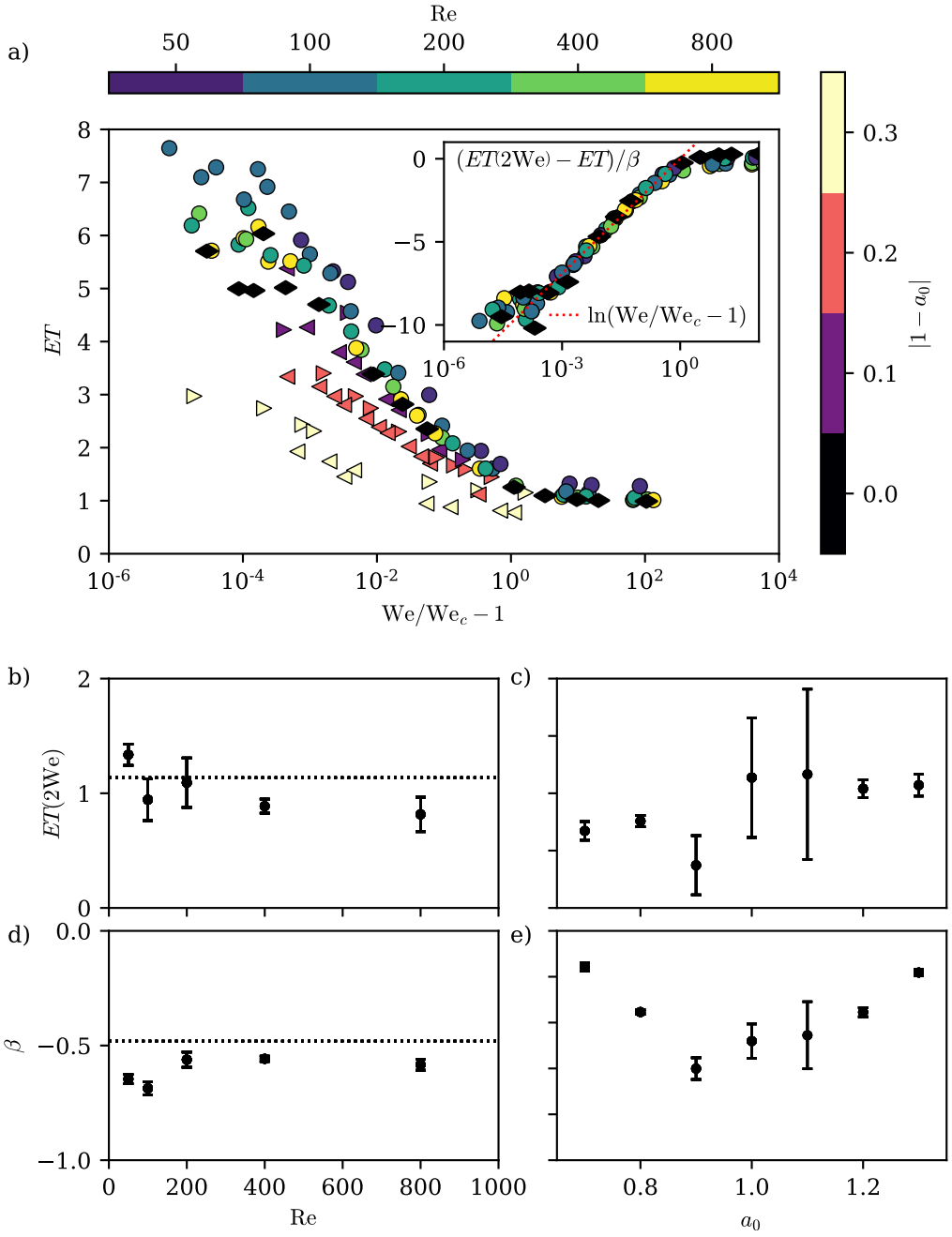

Figure 5.10 – a) Dimensionless lifetime, ET, as a function of the distance to We_c. Finite Re simulations are denoted with circles, inviscid ellipsoids by triangles and inviscid spheres by diamonds. See figure 5.9a for the meaning of left and right triangles. As $\mathrm{We} \to \mathrm{We}_c$, the lifetime diverges logarithmically. Inset plot: Rescaled ET for the spheres, with two parameters that depend on Re: $ET(2\mathrm{We})$ and β. In b & c the black dotted line denotes the inviscid value for spheres (and correspond to $a_0 = 1$ in c & e). b) & c) Evolution of $ET(2\mathrm{We})$ with Re and a_0 respectively. d) & e) Similar plots for the evolution of the slope β with Re and a_0.

5 Conclusion: Call for a dynamical description

In this chapter, we evidenced that inertia cannot be neglected when predicting bubble breakup. Indeed, even when there exists a stable equilibrium position, the initial bubble shape and flow configuration can allow the bubble to break. As a consequence, we find that critical Weber number above which the bubble breaks depends on the Reynolds number, as the linear stability analysis predicted [90, 91, 183], but also on the initial bubble shape. The critical Weber number is selected dynamically by the initial conditions. Since, in real configurations bubbles dynamics are rarely quasi-static, these results have practical important consequences: history matters. The critical Weber number at which bubbles break should always be considered together with a set of initial conditions. For non steady flows, the critical Weber number must be defined in a statistical sense: one can define the distribution of initial bubble shapes and deduce the probability to break.

We also demonstrated that the dynamics of the second spherical harmonics mode, corresponding to oblate-prolate oscillations, can be described by a simple uncoupled one dimensional oscillator, which depends on We, Re and on the initial bubble shape. We evidence that We and Re control the shape of the effective potential, while the initial conditions are controlled by We and the initial bubble shape. This reduced dynamics reproduces the maximum deformation for stable bubbles as well as the lifetime for unstable bubbles, for We close to its critical value. In addition, we evidenced that the energy barrier is always finite. For all We and Re there exists a set of initial conditions for which the bubble breaks. As a consequence, in turbulent flows, even though the probability that a bubble encounters a large pressure or velocity fluctuation depends on its size (*i.e.* Re and We), all bubbles can in principle break.

The uniaxial straining flow is one of the most relevant flow geometry for bubble breakup in turbulence. To model bubble dynamics in these turbulent environment, one could model the flow as a succession of uniaxial straining flows of random amplitude and duration. For each of these local geometries, knowing the amplitude of the local strain and the initial bubble shape, one can simulate the one dimensional equation to predict whether or not the bubble breaks. This approach is similar to the work of Revuelta et al. [163] who modeled turbulence as a succession of uniaxial straining flow with random orientations, except that we solve a one-dimensional equation instead of the full Navier-Stokes equations. In order to capture the correct statistics for the flow surrounding bubbles, one could measure the statistics of E around bubbles as was done by Masuk et al. [124]. The statistics of the local strain are non trivial (temporally correlated and non Gaussian), but it is important to provide the right statistics of E, in order to capture the correct bubble dynamics.

The success of the reduced dynamics in the stagnation point flow encourages us to follow the same approach for the turbulent case. In the next chapter, we will investigate the linear deformations of bubbles in a turbulent flow and look for a reduced model in the form of a stochastic linear oscillator on the oblate-prolate mode of deformations.

Chapter 6

Bubble deformations in turbulence

Everything which comes from numerics must be trashed.

A colleague

Abstract

In this chapter, we investigate bubble deformations in the homogeneous and isotropic turbulent flow. We examine interface deformations by decomposing bubble shapes into the spherical harmonics base. We show that the dynamics of each mode, for low Weber numbers, can be modeled by a forced stochastic linear oscillator. We measure the coefficients of the model directly from the modes' statistics. We find that the natural frequency corresponds to the Rayleigh frequency, derived in a quiescent flow. However, dissipation increases by a factor 7 compared to the quiescent case, at $\mathrm{Re}_\lambda = 55$. This enhanced dissipation originates from a thick boundary layer surrounding the bubble. We demonstrate that the effective forcing, originating from the integration of pressure over the bubble surface, is independent on bubble deformability. Therefore, the interface deformations are only one-way coupled to the flow. Eventually, we investigate the pressure modes' statistics in the absence of bubbles and compare them to the effective forcing statistics. We show that both fields share the same pdf, characterized by exponential tails, and a characteristic timescale corresponding to the eddy turnover time at the mode scale.

Contents

1 Introduction: Infer bubble deformations dynamics from data

We know from the pioneering works of Kolmogorov [97] and Hinze [84] that, for bubble size lying within the inertial range of the turbulent cascade, there exists a critical size, the Kolmogorov-Hinze scale d_h statistically separating breaking $d > d_h$ from non breaking bubbles $d < d_h$. However, the main physical mechanism leading to breakup remained to be understood. Sevik et al. [180] proposed a resonant mechanism, in which bubble breaks due to series of excitation at its natural frequency, while other authors argue that large fluctuations are necessary for a bubble to break [103, 114, 214]. To address this question, several authors describe bubble deformation dynamics, either with the help of a linear damped harmonic oscillator [123, 158, 165] on the bubble Rayleigh modes [159], or via a tensorial equation for the main bubble axis of deformations [122]. The latter assumes that bubble shape is mostly ellipsoidal while the former allows any bubble shape and describes each mode dynamics.

In the last chapter, we showed that we can successfully reproduce most of bubble deformations using a non linear oscillator model on the oblate prolate modes. In this chapter, we therefore follow a similar approach. In this chapter, following Risso et al. [165], we assume a linear damped oscillator equation with a stochastic forcing for the oscillations of each mode of bubble deformation. However, we do not presume any values for the coefficients of equation (4.6) and the form of the forcing. Instead, we directly measure from the deformations dynamics, the effective natural frequency and damping rate and compare them to the quiescent values. We then deduce the statistical properties of the effective forcing. To identify the origin of the effective forcing, we study the statistics of the pressure field evaluated on a sphere of bubble radius R_0. Eventually, we investigate the flow structure around bubbles and the local dissipation rate to discuss the origin of bubble dynamics dissipation in turbulent flows.

2 Bubble deformations in HIT

2.1 Numerical set-up: DNS of a single bubble in HIT

The numerical set-up is described in details in chapter 2. We recall here the main ingredients. We perform direct numerical simulations of an incompressible gas bubble immersed in an homogeneous and isotropic turbulent flow of an incompressible liquid. Density and viscosity ratios are set to 850 and 25, respectively, close to air-water ratios. The simulation goes in two steps. We first create an homogeneous isotropic turbulent flow by solving the one phase incompressible Navier-Stokes equations with an additional forcing term proportional to the velocity [172]. After a transient regime, the flow reaches a statistically stationary homogeneous and isotropic turbulent state. In this chapter, the Taylor Reynolds number of the flow is $\mathrm{Re}_\lambda = u_{rms}\lambda/\nu = 55$. We then extract snapshots of the flow and use them as flow initial conditions for bubble injection. Snapshots are separated by at least $6\,t_c$ to make sure initial conditions are independent. The spherical bubble is injected at the center of the simulation box by changing locally the density and viscosity. The bubble size is chosen so that it lies within the inertial range of the turbulent cascade where the flow is scale invariant. The bubble diameter to box length ratio is 0.13. During this second stage, forcing is maintained to sustain turbulence, but only in the

We	2.9	2	1.43	1	0.71	0.46	0.36	0.27
N	5	5	3	3	5	3	3	5
$T_{tot}/t_c(d)$	62	126	94	94	156	94	84	94

Table 6.1 – Number of simulations and total simulated time per values of the Weber number.

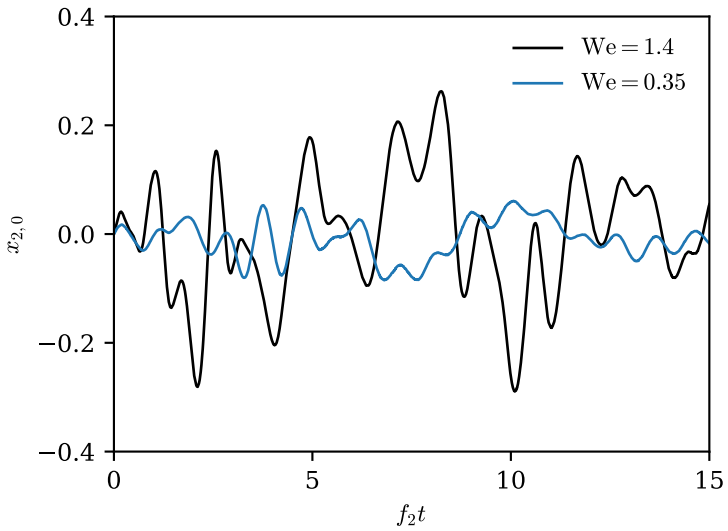

Figure 6.1 – Typical temporal evolution for the mode $(2, 0)$ at two different Weber numbers. Time is made dimensionless using the Rayleigh frequency f_2. Modes exhibit random oscillations, with an amplitude increasing with We.

liquid phase to guaranty that bubble deformations only come from the fluid forcing. In both steps, we use adaptive meshgrid refinement in order to save computational time while resolving all the physical length scales of the problem. The minimum grid size corresponds to 34 points per bubble radius.

In this study we keep the flow Reynolds number constant and we vary the bubble Weber number by changing the value of the surface tension coefficient. The bubble Reynolds number is $\mathrm{Re}(d) = 124$. We explore eight values of We ranging from $\mathrm{We}_c \approx 3$ to $0.1\mathrm{We}_c$. For each Weber number, we run between 3 and 5 simulations. Except when the bubble breaks (at We = 2.9), we run every simulation for at least $20\,t_c$, so that the total time per ensemble is about $100\,t_c$. Table 6.1 summarizes the exact number of simulations and total computational time per Weber number we perform.

2.2 Modes of deformations

To quantify bubble deformations, we decompose the local bubble radius R into the real spherical harmonics base $Y_\ell^m(\theta, \phi)$, where ℓ and m are the principal and secondary numbers respectively, and θ and ϕ the co-latitude and longitude,

$$R(\theta, \phi, t) = R_0\big[1 + \sum_{\ell=2}^{\infty} \sum_{m=-\ell}^{\ell} x_{\ell,m}(t) Y_\ell^m(\theta, \phi)\big], \tag{6.1}$$

and we track the modes' amplitude $x_{\ell,m}$ over time. Bubble shape is described in the bubble frame of reference so that all harmonics $\ell = 1$, corresponding to bubble translation, are null by definition. The procedure to compute the spherical harmonics is described in detail in [141] as well as in chapter 3.

Figure 6.1 shows two typical temporal evolution for the mode $(\ell, m) = (2, 0)$, at two different Weber numbers. Time is made dimensionless using the Rayleigh frequency f_2. For both We, we observe random oscillations around zero and the predominance of the bubble resonant frequency f_2. The amplitude of the oscillations increases with We.

Since we do not prescribe any special orientation relative to the bubble shape, all modes with the same principal number ℓ are statistically equivalent. Indeed, one can verify that a rotation of a mode can be expressed as a linear combination of all the other modes with the same principal number. As a consequence, we omit m in what follows. For instance $x_\ell(t)$ represents a typical temporal evolution of one of the modes ℓ. In addition, assuming that $x_{\ell,m}$ are independent, the ensemble averaging operation $\langle\cdot\rangle$ is computed over different simulations and over the m values for a given ℓ. Roa et al. [169] used a reference frame dynamically oriented with the bubble principal axis of deformations. In practice, their reference frame maximizes the amplitude of mode $(2, 0)$, such that the differential elongation can be studied as the invariance by rotation is broken.

3 Determination of the reduced dynamics

3.1 Model: a stochastic linear oscillator

Following Risso et al. [165], we introduce a linear stochastic model to describe each mode dynamics,

$$\ddot{x}_\ell + \Lambda_\ell(\mathrm{We})\dot{x}_\ell + \Omega_\ell(\mathrm{We})^2 x_\ell = \mathcal{T}_\ell(\mathrm{We}, t), \tag{6.2}$$

where Λ_ℓ and Ω_ℓ are the damping rate and natural frequency respectively and $\mathcal{T}_\ell$ is a random variable which models the turbulent forcing. In this section, we aim at measuring Λ_ℓ, Ω_ℓ and the statistical properties of $\mathcal{T}_\ell$ from the deformation dynamics. Both parameters Λ_ℓ and Ω_ℓ, as well as the forcing statistics, may depend on the Weber number We. Conversely to what other authors have done, time is made dimensionless using the eddy turnover time at the bubble scale $t_c(d) = \epsilon^{-1/3} d^{2/3}$ and, from now on, $\dot{}$ denotes derivatives with respect to this dimensionless time. This choice avoid *a priori* to have a forcing term depending on bubble properties such as surface tension. It decorrelates the turbulent forcing (righ hand side), from the bubble response (the left hand side). In these units, the Rayleigh frequency and the Lamb damping rate write $\omega_\ell^2 = 16(\ell - 1)(\ell + 1)(\ell + 2)/\mathrm{We}$ and $\lambda_\ell = 8\sqrt{2}(\ell + 2)(2\ell + 1)\,\mathrm{Re}(d)^{-1}$ respectively. Note that, in this study, we have not varied the eddy turnover time. When the bubble size lies within the inertial range of the turbulent cascade its dynamics is primarily controlled by inertial effects, and the parameters may not depend explicitly on the bubble Reynolds number, as long as $\mathrm{Re}(d) \gg 1$.

In order to measure the coefficients and the force statistics of equation (6.2), we make the following assumptions:

(H1): Modes dynamics are linear and uncoupled, which is valid for $x_\ell \ll 1$, corresponding to

We $\ll 1$.

(H2): The bubble deformation is one way-coupled to the flow. This hypothesis is discussed in section 3.5.

(H3): The forcing $\mathcal{T}_\ell$ is statistically stationary.

(H4): The damping rate and the natural frequency do not depend on time.

From hypothesis (H2) the effective $\mathcal{T}_\ell$ in unit of the eddy turnover time, is independent of We. From hypothesis (H3), the effective forcing is completely determined by its auto-correlation function (or equivalently its spectrum), and its probability distribution function (pdf).

Under these hypothesis, in the next sections, we will show that

1. The natural frequency is not modified by the presence of the flow: $\Omega_\ell = \omega_\ell$.
2. There is an effective viscosity, driven by turbulence, so that $\Lambda_\ell = 0.6(\ell+2)(2\ell+1)$ for $\mathrm{Re}(d) = 124$.

Combining (1), (2) and equation (6.2) we will deduce the statistical properties of the forcing $\mathcal{T}_\ell$.

3.2 Frequency response of the oscillator - Amplitude of the Fourier transform

To rationalize the qualitative observations of figure 6.1 and identify the angular frequency Ω_ℓ, we investigate the frequency response of the bubble. To do so, we compute the temporal Fourier transform, $\hat{x}_\ell$ of x_ℓ for all ℓ and We,

$$\hat{x}_\ell(\omega) = \int_{-\infty}^{\infty} x(t) e^{-i\omega t} \mathrm{d}t, \tag{6.3}$$

where $\hat{x}_\ell$ is also a random variable. Similarly, we introduce $\hat{\mathcal{T}}_\ell$, the Fourier transform of the effective forcing,

$$\hat{\mathcal{T}}_\ell(\omega) = \int_{-\infty}^{\infty} \mathcal{T}(t) e^{-i\omega t} \mathrm{d}t \tag{6.4}$$

Figures 6.2 shows the ensemble average $\langle|\hat{x}_\ell|\rangle$ as a function of the frequency, $f = \omega/(2\pi)$, normalized by the corresponding Rayleigh frequency, f_ℓ.

For $f < f_\ell$, for every We, $\langle|\hat{x}_\ell|\rangle$ is approximately constant. The low frequency dynamics is similar to that of a white noise.

At $f = f_\ell$ (back dotted line), for We ≤ 0.46 we observe a peak that resembles the resonant response of an oscillator at its natural frequency. This peak does not exist for larger values of We. Nevertheless, for every ℓ, we observe a transition at this very frequency.

For $f > f_\ell$, at all We, we report a sharp power-law decay, following at least $(f/f_\ell)^{-4}$.

Finally, for $f > 3f_\ell$, the spectrum amplitude is above the noise level. Note that this part also corresponds to the end of the inertial range.

Dimensional measurements of bubble deformation dynamics were performed by Ravelet et al. [158] in the context of bubbles rising in turbulence. They measured the temporal spectrum of the horizontal bubble main axis, a proxy for the amplitude of the second Rayleigh mode. The overall shape of their power spectrum was similar : weak variation for $f < f_2$, no resonance at

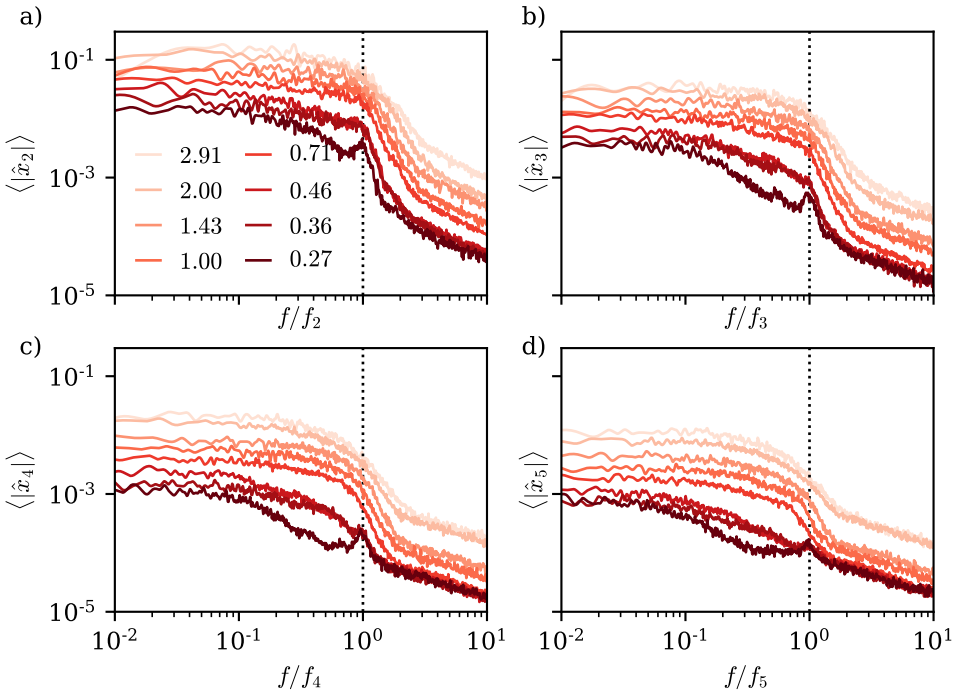

Figure 6.2 – Amplitude of the modes' Fourier transform for all We as a function of the frequency normalized by the corresponding Rayleigh frequency. The Weber number value is color-coded.

f_2 and an a strong decay for $f > f_2$. In the absence of gravity, Risso et al. [165] also reported a transition at f_2, with a rapid decay for $f > f_2$ of the projected area spectrum.

The cut-off frequency being f_ℓ for all considered cases, we deduce that the bubble natural frequency in turbulence, Ω_ℓ of equation (6.2), is not modified by the presence of the surrounding turbulent flow and that,

$$\Omega_\ell = \omega_\ell = 4\left[\frac{(\ell-1)(\ell+1)(\ell+2)}{\mathrm{We}}\right]^{1/2} \tag{6.5}$$

It is surprising that the bubble natural frequency remains unchanged. Indeed, Prosperetti [150] showed, for a bubble in an initially quiescent flow, that viscous effects induces an additional memory term in bubble dynamics. This memory term can be modeled by an effective natural frequency and damping term. The surrounding flow field can also modify the natural frequency. In a uniaxial straining flow for instance, Kang et al. [91] demonstrated that a coupling between modes $\ell = 2$ and $\ell = 4$ decreases the mode 2 natural frequency at linear order, with a corrective term linear in We. We hypothesize that the stochastic nature of turbulence cancels, in average, these contributions. In the following, we use the theoretical expression of ω_ℓ, for the bubble natural frequency, Ω_ℓ.

3.3 Zero frequency limit and We-dependency of the forcing

In this section, we investigate the zero frequency limit, and discuss the consequence for the We-dependency of the forcing. By computing the Fourier transform of equation (6.2), combined

with (6.5), we obtain an expression linking $\hat{x}_\ell$ and $\hat{\mathcal{T}}_\ell$,

$$|\hat{x}_\ell|(\mathrm{We},\omega) = \frac{|\hat{\mathcal{T}}_\ell|(\mathrm{We},\omega)}{\sqrt{(\omega^2-\omega_\ell(\mathrm{We})^2)^2+\Lambda_\ell(\mathrm{We})^2\omega^2}} \tag{6.6}$$

The spectral behavior of each x_ℓ is a combination of the forcing spectrum $\hat{\mathcal{T}}_\ell$ and the bubble response. In the limit case $\omega = 0$, using the expression of the bubble natural frequency (6.5), we have

$$|\hat{x}_\ell|(\mathrm{We},0) = \frac{|\hat{\mathcal{T}}_\ell|(\mathrm{We},0)}{\omega_\ell(\mathrm{We})^2} = \frac{\mathrm{We}}{16(\ell-1)(\ell+1)(\ell+2)}|\hat{\mathcal{T}}_\ell|(\mathrm{We},0). \tag{6.7}$$

We can use this expression to investigate the We-dependency and ℓ-dependency of $\hat{\mathcal{T}}_\ell$ at $\omega = 0$. We extract $\langle|\hat{x}_\ell|\rangle(\mathrm{We},0)$ by averaging $\langle|\hat{x}_\ell|\rangle(\mathrm{We},\omega)$ over the range $5.10^{-3} < f/f_\ell < 10^{-1}$ where the spectrum is constant.

Figure 6.3a shows $\langle|\hat{x}_\ell|\rangle(\mathrm{We},0)$ as a function of We. Solid lines of slope 1 are superimposed, showing that $\langle|\hat{x}_\ell|\rangle(\mathrm{We},0)$ increases linearly with We for $\ell < 4$, up to $\mathrm{We} = 2.9 \approx \mathrm{We}_c$, when non-linear effects start to be important. This effect might originate from non-linear coupling with lower order modes. It follows from equation (6.7) that $\langle|\hat{\mathcal{T}}_\ell|\rangle(\mathrm{We},0)$ is independent of We for $\ell < 4$, the most energetic modes. This result justifies that the effective forcing from turbulence does not depend on bubble deformability at low frequency. The modification of the flow induced by bubble oscillations does not impinge back on bubble dynamics. A similar phenomenon has been observed for drops by Vela-Martín et al. [200]. They investigated the interfacial stress generated by eddies depending on their distance to the interface. They concluded that eddies further that $0.2d$ from the drop interface (outer eddies) generate most of the stress. They reported that these contributions are, in addition, independent of We, as these eddies are too far from the interface to be affected by drop deformations. We can assume that a similar mechanism may hold also for bubble dynamics so that $\hat{\mathcal{T}}_\ell$ does not depend on We either. These results justify hypothesis (H2) at low frequency, and we assume that (H2) holds for all frequencies. From now on, we therefore assume that $\mathcal{T}_\ell$ does not depend on We. This hypothesis will be further validated and tested in section 3.5. The zero frequency limit also depends on the mode order ℓ. Figure 6.3b shows the compensated spectrum limit $\langle|\hat{x}_\ell|\rangle(\omega = 0)/\mathrm{We}$ as a function of ℓ. We find that the zero frequency limit decreases slightly faster than $\omega_\ell^{-2} \sim [(\ell-1)(\ell+1)(\ell+2)]^{-1}$ of equation (6.7) (red line). It suggests that $|\hat{\mathcal{T}}_\ell|$ weakly decreases with ℓ, with $|\hat{\mathcal{T}}_\ell| \sim 1/\sqrt{\ell}$. Higher order modes are associated with smaller scales that are less energetic. However, the direct investigation of pressure modes in section 5.2 showed a much faster decrease of the mode energy with ℓ. The high order modes $\ell \geq 3$ may also be indirectly forced from non linear coupling with the mode 2 changing the ℓ-dependency of the forcing.

3.4 Determination of the effective damping factor: Additional damping due to turbulence

In this section, we present a method to compute the damping factor Λ_ℓ of equation (6.2) from the numerical data.

Let us consider $\hat{x}_a$ and $\hat{x}_b$ the Fourier transform $\hat{x}_\ell$ of the same mode ℓ for two Weber numbers

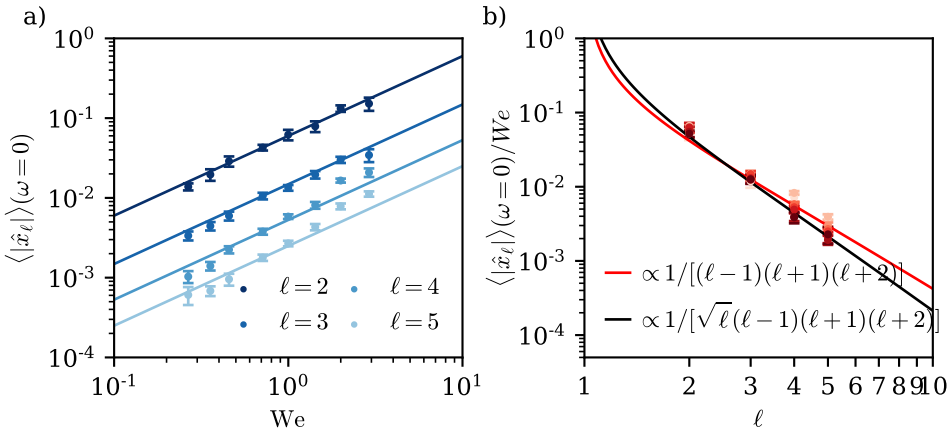

Figure 6.3 – a) Zero frequency limit of the modes' Fourier transform as a function of We for all ℓ. Theoretical prediction $\langle|\hat{x}_\ell|\rangle(\omega = 0) \propto$ We is superimposed in solid lines. Error bars are estimated using the standard deviation of the spectrum value for $5.10^{-3} < f/f_\ell < 10^{-1}$. b) Compensated limit $\langle|\hat{x}_\ell|\rangle(\omega = 0)/$We, as a function of ℓ. Colors encode the We (see figure 6.2). Assuming $\mathcal{T}_\ell$ independent of ℓ gives the scaling plotted in red. Assuming $|\mathcal{T}_\ell| \sim 1/\sqrt{\ell}$ gives the scaling plotted in black.

We_a and We_b. For simplicity here, we denote ω_a and λ_a, the natural frequency and damping rate associated with We_a at this ℓ. Under hypothesis (H2), the ratio R_{ab}

$$R_{ab}(\omega) = \left(\frac{\langle|\hat{x}_a|\rangle}{\langle|\hat{x}_b|\rangle}\right)^2 = \frac{(\omega^2-\omega_b^2)^2+\Lambda_b^2\omega^2}{(\omega^2-\omega_a^2)^2+\Lambda_a^2\omega^2} \tag{6.8}$$

is independent on $\hat{\mathcal{T}}_\ell$.

Since the two natural frequencies ω_a and ω_b are known (equation (6.5)), one can estimate the two damping factors, Λ_a and Λ_b, using $R_{ab}(\omega_a)$ and $R_{ab}(\omega_b)$, the ratios at the two natural frequencies

$$R_{ab}(\omega_a) = \frac{(\omega_a^2-\omega_b^2)^2+\Lambda_b^2\omega_a^2}{\Lambda_a^2\omega_a^2} \tag{6.9}$$

$$R_{ab}(\omega_b) = \frac{\Lambda_b^2\omega_b^2}{(\omega_a^2-\omega_b^2)^2+\Lambda_a^2\omega_b^2} \tag{6.10}$$

by solving this two-equations system. Note that an optimization of Λ_a and Λ_b on the whole range of frequencies was less reliable. The signal over noise ratio is optimal near the resonance, and decreases both at high and low frequencies. Indeed, high frequencies, which are the more noisy, then dominate the optimization procedure.

Figure 6.4a illustrates the computation of Λ_ℓ. The ratio $R_{0.71,0.27}$ for $\ell = 2$, $\text{We}_a = 0.71$ and $\text{We}_b = 0.27$ is represented as a function of the frequency f (grey curve). The black and red vertical lines denote the position of the two natural frequencies ω_a and ω_b respectively, at which we measure $R_{0.71,0.27}$. Inverting system (6.9)-(6.10) gives an estimate of $\Lambda_{0.71}$ and $\Lambda_{0.27}$. Using these computed values of $\Lambda_{0.71}$ and $\Lambda_{0.27}$ we plot the theoretical expression of equation (6.8) at all frequencies (black line). This expression captures the main features of the ratio $R_{0.71,0.27}(\omega)$:

We	2.9	2	1.43	1	0.71	0.46	0.36	0.27
Λ_2	14.2	11.7	11.9	11.1	11.0	13.8	11.9	17.1
σ^2_Λ	1.1	1.6	1.8	2.2	2.9	3.6	3.1	5.9
Λ_3	20.1	16.7	17.2	16.2	17.0	30.5	25.4	29.7
σ^3_Λ	3.4	4.0	4.6	4.4	5.3	13.2	12.6	18.4

Table 6.2 – Average damping parameter Λ_ℓ and corresponding standard deviation, for every We.

the low frequency limit, the position and amplitude of the peak.

We then follow this procedure for every pair $(\mathrm{We}_a, \mathrm{We}_b)$ and obtain 14 estimations of Λ_ℓ per Weber number per mode ℓ. We did not find a significant bias on the estimated value of $\Lambda_\ell(\mathrm{We})$ as a function of the Weber ratio $\mathrm{We}_a/\mathrm{We}_b$. We then average over all values of We_b values to estimate $\Lambda_\ell(\mathrm{We}_a)$. The values of Λ_ℓ for $\ell = 2$ and $\ell = 3$ as a function of We, and their standard deviation are reported in table 6.2. For $\ell \geq 4$, equation (6.6) fails to describe the ratio R_{ab}. Figure 6.4b shows Λ_ℓ as a function of We for $\ell = 2$ and $\ell = 3$ with errorbars encoding the standard deviation σ^ℓ_Λ. We find no clear variation of Λ_ℓ with We, especially for $\ell = 2$. When ℓ increases, the dissipation also increases, as smaller scales are more efficient to dissipate energy. The increase of Λ_ℓ with ℓ is compatible with the ℓ-dependency in a quiescent environment from Lamb [101]. From our observations we found the following expression for the damping factor,

$$\Lambda_\ell = 0.6(\ell + 2)(2\ell + 1). \tag{6.11}$$

In quiescent environments, the damping coefficient is also independent on We, $\lambda_\ell = 8\sqrt{2}(\ell + 2)(2\ell + 1)\,\mathrm{Re}(d)^{-1}$, as it originates from molecular diffusion in the liquid. However, we find $\Lambda_2 \approx 6.6\lambda_2$. The surrounding flow field induces an additional effective damping. Experimentally, Ravelet et al. [158] also observed an additional damping for bubbles rising in turbulence but attributed it to the presence of the wake. Yet, similar observations come from drop oscillations in space. In the presence of a turbulent internal flow, drop oscillations are significantly damped [17, 20]. This additional damping is interpreted in terms of a turbulent eddy viscosity [217]. In addition, Vela-Martín et al. [200] showed that there is a transfer of energy from the drop interface to eddies closer than $0.2\,d$ from the drop interface and inside the drop. They call them inner eddies. These small eddies efficiently dissipate energy. This transfer of energy suggests that the enhanced damping comes from an increase in the local effective diffusivity.

It is advantageous to estimate the size of an equivalent mixing length L_t. This characteristic length of momentum transport has first been introduced by Prandtl [22, 147, 217] to describe, in a turbulent flow, the logarithmic profile of velocity near a wall. By dimensional considerations, one can estimate the effective turbulent viscosity ν_t, using L_t and a typical velocity scale of velocity fluctuations at that scale, $\langle \delta u(L_t)^2 \rangle^{1/2}$,

$$\nu_t = \langle \delta u(L_t)^2 \rangle^{1/2} L_t = \sqrt{2}\epsilon^{1/3} L_t^{4/3}. \tag{6.12}$$

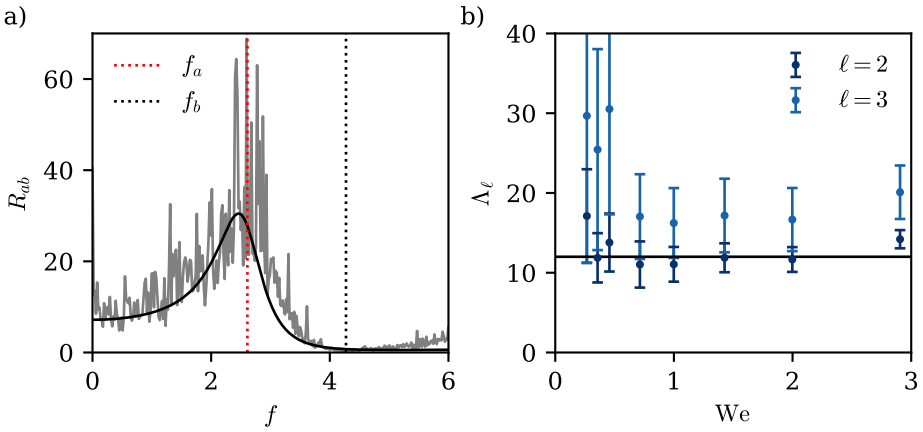

Figure 6.4 – a) Ratio between the Fourier spectrum at $\mathrm{We}_a = 0.71$ and $\mathrm{We}_b = 0.27$ for the mode $\ell = 2$. The red and black vertical lines denotes the position of the Rayleigh frequency at these two We where we evaluate R_{ab}. The black line is the prediction from equation (6.8). b) Damping factor as a function of We for $\ell = 2$ and $\ell = 3$. The error bars represent the standard deviations. The solid black line corresponds to $\Lambda_2 = 12$.

Expressing the effective damping rate in terms of this effective turbulent viscosity gives,

$$\Lambda_\ell = 8(\ell+2)(2\ell+1)\frac{\nu_t d^{2/3}}{d^2\epsilon^{1/3}} = 8\sqrt{2}(\ell+2)(2\ell+1)\left[\frac{L_t}{d}\right]^{4/3}. \tag{6.13}$$

Injecting equation (6.11), gives an estimate for L_t,

$$L_t = \frac{d}{10} = \frac{R_0}{5}. \tag{6.14}$$

Being of the same order of magnitude as the bubble radius, we hypothesize that the mixing length originates from a geometric effect, similar to the separation between inner and outer eddies from Vela-Martín et al. [200]. We further investigate the origin of this additional damping in the last section, by looking at the local velocity gradients close to the bubble interface.

3.5 Effective forcing statistics: Temporal correlations and distribution

Since the left hand side of equation (6.2) is now completely determined, we can compute the right hand side, and interpret it as a forcing term from the turbulent flow.

To interpret and comment the statistics of the forcing term we will obtain, let briefly discuss the physical origin of the forces acting on a bubble in a turbulent flow. To the best of our knowledge, there is no theoretical description of the forcing statistics acting on a bubble. For particles lying within the inertial range, the force exerted by the flow is often modeled by the Eulerian pressure gradient, integrated over the particle surface [28], a framework that can also be applied to bubbles [212]. Decomposed in the spherical harmonics base, the pressure on a

sphere of radius R reads

$$p(\theta,\phi) = P_c\big[\sum_{\ell=0}^{\infty}\sum_{m=-\ell}^{\ell} P_{\ell,m}(t)\, Y_\ell^m(\theta,\phi)\big], \tag{6.15}$$

where $P_c = \rho\delta u(d)^2$ is a characteristic pressure fluctuations. There is no direct experimental measurement of these pressure coefficients. In practice, only two point pressure measurements (pressure increments) have been studied. From force balance on a finite-size particle in a turbulent flow, the modes $\ell = 1$ are the components of the hydrodynamic force, equal to the Lagrangian particle acceleration. Practically speaking, the pressure increments are a good proxy for the Lagrangian particle acceleration.

For the higher order modes ($\ell \geq 2$) there is no measurements in turbulence. Moreover, to describe deformations rather than motions, the framework used for particle acceleration cannot be simply extended. The interface deformations are primarily driven by the velocity gradients at the interface, which themselves depend on the presence of the bubble. Still, these gradients are closely related to the pressure statistics at the bubble scale.

Therefore, from time to time, we will compare our statistics of $\mathcal{T}_\ell$ ($\ell \geq 2$) with statistical quantities closely related to P_1, namely the Lagrangian acceleration statistics and the pressure increments. A direct measure of the statistics of P_ℓ ($\ell \geq 2$) in the absence of bubble is provided in section 5.

Practically, we compute $\mathcal{T}_\ell$ from the modes' Fourier transform $\hat{x}_\ell$ using the following relation

$$\mathcal{T}_\ell(t) = \frac{1}{2\pi}\int_{-\infty}^{\infty} \hat{x}_\ell(\omega)(\Omega_\ell^2 - \omega^2 + i\Lambda_\ell\omega)e^{i\omega t}\mathrm{d}\omega, \tag{6.16}$$

where we use the expressions of Λ_ℓ and Ω_ℓ from Eqs. (6.5) and (6.11).

As expected from rotational invariance, we find that the average forcing $\langle\mathcal{T}_\ell\rangle$ vanishes for all We. The standard deviation of $\mathcal{T}_\ell$, $\sigma_\mathcal{T}^\ell$ is shown in figure 6.5 as a function of We for $\ell = 2$ and 3 (color-coded). $\sigma_\mathcal{T}^\ell$ is found to be almost independent of the Weber number. We found that the effective forcing from the turbulent flow does not depend on bubble deformability. Therefore, bubble deformations are only one-way coupled to the flow.

In physical units, the force $\mathcal{T}_\ell$ then scales as $\alpha(\ell)\epsilon^{2/3}d^{-1/3}$, where α_ℓ is a function of the mode order. The standard deviation slightly decreases with ℓ, compatible with $\alpha_\ell \sim \ell^{-1/2}$.

In the context of Lagrangian particle acceleration in turbulence, the standard deviation of acceleration also decreases with particle size as $d^{-1/3}$. This scaling can be predicted using a scale invariant pressure fluctuations argument [154, 211, 213]. In addition, Lagrangian acceleration statistics do not depend explicitly on the Reynolds number at the particle size $\mathrm{Re}(d)$, as long as the particle lies within the inertial range. Only a marginal effect of the flow Taylor Reynolds number Re_λ on the variance of the acceleration [213] was found. As a consequence, we expect the effective forcing to be independent of Re_λ, $\mathrm{Re}(d)$ and the Weber number.

Beyond the first two moments of the effective forcing distribution, it is interesting to look at the full distribution. Figures 6.6a and 6.6b show the probability distribution of $\mathcal{T}_2$ and $\mathcal{T}_3$ respectively for all We, normalized by their standard deviation $\sigma_\mathcal{T}^\ell$. We find that the shape of the distribution is also independent of the Weber number. These distributions are characterized

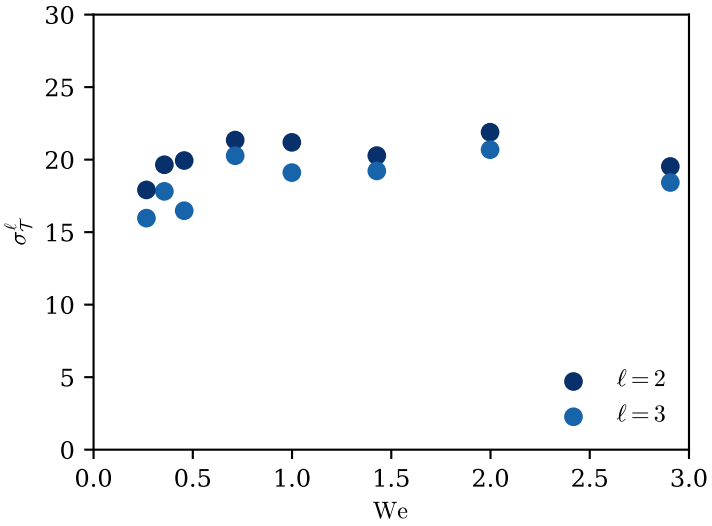

Figure 6.5 – Standard deviation of $\mathcal{T}$ as a function of We for $\ell = 2$ and $\ell = 3$. No We-dependency is observed, while $\sigma_{\mathcal{T}}$ decreases slightly for larger ℓ.

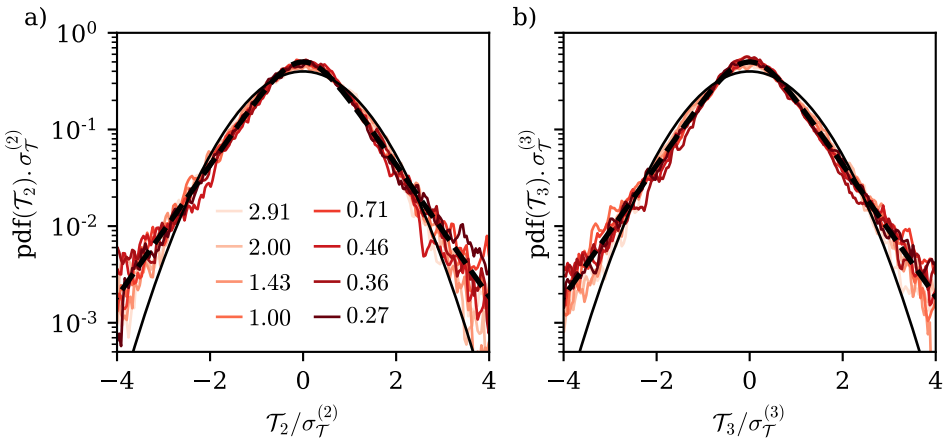

Figure 6.6 – Probability density functions of $\mathcal{T}_2$ (a) and $\mathcal{T}_3$ (b) for all We (color-coded), normalized by their standard deviations. The shape of the distribution is independent of We. The dashed line represents the hyperbolic secant distribution, while the solid line is the Gaussian distribution.

by exponential tails, and are well described by the hyperbolic secant distribution (black dashed line),

$$\mathrm{pdf}(\mathcal{T}) = \frac{1}{2\sigma_{\mathcal{T}}^{\ell}} \operatorname{sech}\left(\frac{\pi}{2}\frac{\mathcal{T}}{\sigma_{\mathcal{T}}^{\ell}}\right) \tag{6.17}$$

which depends on a single parameter, the standard deviation $\sigma_{\mathcal{T}}^{\ell}$. The probability that a large forcing occurs is way larger than that of a Gaussian distribution (solid black line).

It is again tantalizing to compare this distribution to Lagrangian acceleration statistics for both particles and bubbles [85, 146, 154, 178, 212, 213]. For small, neutral tracers and particles of Kolmogorov scale size, the acceleration distributions exhibit larger tails, decreasing slower than exponential. However, for larger particles ($d/\eta > 10$), the shape exhibits exponential tail, independent of bubble size and therefore of $\mathrm{Re}(d)$ [154, 211, 213]. The pdf shape of the Lagrangian acceleration is well described by the following expression, initially proposed for tracer particles [131, 154]

$$\mathrm{pdf}(x) = \frac{e^{3s^2/2}}{4\sqrt{3}}\left[1 - \mathrm{erf}\,(\frac{\log\left(|x/\sqrt{3}|\right) + 2s^2}{\sqrt{2}x})\right] \tag{6.18}$$

where x is the standardized variable and s an additional fitting parameter. In the range of resolved scale, the two expressions, equations (6.17) and (6.18), are compatible with our experimental data.

To characterize the temporal evolution of the effective forcing $\mathcal{T}_\ell$, we study its ensemble averaged Fourier transform $\langle|\hat{\mathcal{T}}_\ell|\rangle$. Injecting equations (6.5) and (6.11) within equation (6.6) we obtain an expression in Fourier space for $\langle|\hat{\mathcal{T}}_\ell|\rangle$:

$$\langle|\hat{\mathcal{T}}_\ell|\rangle = \langle|\hat{x}_\ell|\rangle.\left[(\omega^2 - \Omega_\ell(\mathrm{We})^2)^2 + \Lambda_\ell^2\omega^2\right]^{1/2}. \tag{6.19}$$

Figure 6.7a and 6.7b show $\langle|\hat{\mathcal{T}}_2|\rangle$ and $\langle|\hat{\mathcal{T}}_3|\rangle$ respectively as a function of $f\ell^{-2/3}$, where $\ell^{2/3}$ is the eddy turnover time at scale d/ℓ (in units of $t_c(d)$). For all frequencies, we found that the effective forcing spectrum does not depend on the Weber number. At low frequencies ($f < 0.2\,\ell^{2/3}$), the forcing amplitude is constant, corresponding to a white noise. For $f > \ell^{2/3}$, the decay of $\langle|\hat{\mathcal{T}}_\ell|\rangle$ is compatible with $1/f^2$. The limit between these two regimes is set by the eddy turnover time at scale d/ℓ. We found that the spectrum of the effective forcing only depends on the turbulence parameters, and is therefore independent of the bubble deformations. As was anticipated in section 3.1, model (6.2) decouples the turbulent forcing (the right hand side) from the bubble response (the left hand side). The observation of a cut off frequency at the characteristic time scale of turbulent fluctuations at the mode scale d/ℓ can be interpreted as a filtering process originating from the integration over the bubble surface. This filtering operation is further discussed in section 5.

From the previous observations, we propose the following expression for the forcing spectrum,

$$\langle|\hat{\mathcal{T}}_\ell|\rangle(f) = \frac{\tau_\ell}{1 + [f\ell^{-2/3}]^2}, \tag{6.20}$$

where τ_ℓ is a numerical constant, accounting for the ℓ-dependency of $\mathcal{T}_\ell$, that is adjusted on the data. From equation 6.7 and figure 6.3, we estimate $\tau_\ell \sim \ell^{-1/2}$. The expression (6.20) captures

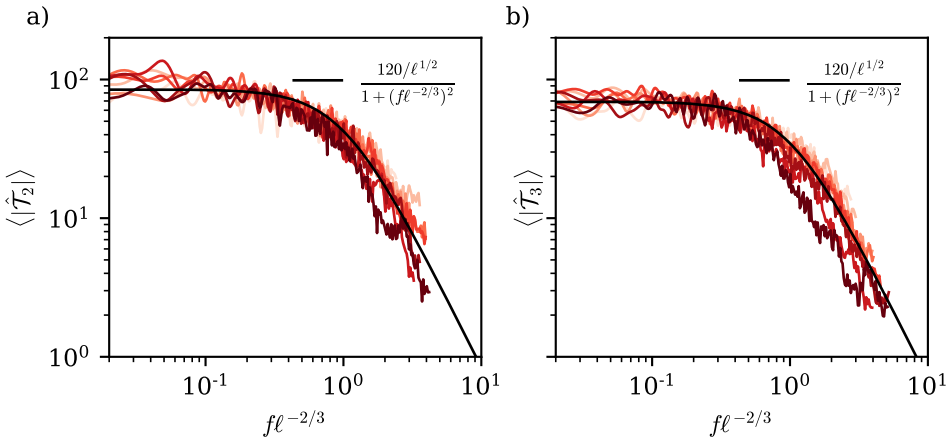

Figure 6.7 – Effective forcing spectrum for $\ell = 2$ (a) and $\ell = 3$ (b) deduced from equation (6.19) as a function of the frequency normalized by the eddy turnover time at scale d/ℓ. The Weber number is color-coded with the same colorbar as in figure 6.2).

quantitatively the effective forcing spectrum (solid black line in figures 6.7a and 6.7b).

In the context of Lagrangian particle accelerations, Voth et al. [213] followed by Volk et al. [212], computed the temporal autocorrelation of inertial particle accelerations in turbulence. The temporal acceleration statistics of a finite size particle is usually attributed to a filtering effect of the small scale turbulent fluctuations at the particle scale [154]. As a consequence, the correlation time of acceleration for neutrally buoyant particle is given by the eddy turnover time $t_c(d)$. This result has been recently extended to buoyant particle that exhibits a modified correlation time $t \sim t_c(d)\beta^{-1/2}$ [67], where $\beta = 3\rho/(2\rho + \rho_p)$ is a function of the fluid density ρ and the particle density ρ_p. For a bubble, we have $\beta = 3$, corresponding to a correlation time of order t_c. In our case, the temporal auto-correlation function $C_{\mathcal{T}_\ell}(t) = \langle \mathcal{T}_\ell(0)\mathcal{T}_\ell(t)\rangle/(\sigma_{\mathcal{T}}^\ell)^2$ for the modes $\ell > 1$ can be deduced from the spectrum $\hat{\mathcal{T}}_\ell$ and is written as:

$$C_{\mathcal{T}_\ell}(t) = \exp\Big(-2\pi\ell^{2/3}t\Big)(1 + 2\pi\ell^{2/3}t). \tag{6.21}$$

We found that the correlation time in physical units is given by $t_c(d)\ell^{-2/3}/(2\pi)$, which also scales as $t_c(d)$, with an additional dependency in the mode order ℓ. The prefactor being smaller than one, the mode oscillations decorrelate faster that the velocity fluctuations at the bubble scale.

In summary, we found that all the statistics of $\mathcal{T}_\ell$ are independent of We which confirms the initial intuition of Risso et al. [165] that bubble dynamics and turbulent forcing are decoupled. We found that the bubble deformation by the flow field can be described by a one-way coupling model: the flow field generated by bubble oscillations does not significantly impinges back on bubble dynamics. In addition, experimental results from the literature suggest that these statistics are likely to be independent on $\mathrm{Re}(d)$, as long as we consider bubbles larger than the Kolmogorov scale.

From the stationary hypothesis (H3), the forcing is completely characterized by its distribution and temporal autocorrelation function. The combination of an explicit form for the pdf

(eq. (6.17)) and for the autocorrelation function (eq. (6.21)) then provides a complete model of a synthetic stochastic effective forcing for bubbles deformations in turbulence. Previous modelling approaches have used two points velocity measurements to model an effective forcing term [100, 123, 165], following the original idea from Kolmogorov [97] and Hinze [84]. Here we found that the statistics of the effective forcing differ significantly from two points statistics, in particular due to the volumetric filtering effect at the particle size.

4 Model validation

To describe the bubble deformation, we have inferred step by step an equation including, damping, natural frequency and a statistical model for the effective forcing term $\mathcal{T}_\ell$. To validate and draw the limits of our model, we compare the output of the linear model to our DNS data

4.1 Modes' standard deviation and distributions

We first look at the modes' standard deviation σ_x^ℓ and statistics. Figure 6.8a shows the modes's standard deviation as a function of the Weber number for $\ell \in [2, 5]$. We find that σ_x^ℓ can be approximated by $\sigma_x^\ell \approx \mathrm{We}/[(\ell-1)(\ell+1)(\ell+2)]$, with a constant of order one. We compute σ_x^ℓ from the model in Fourier space using expressions of equations (6.5), (6.11) and (6.20) and the Parseval identity. The results are superimposed in solid line for $\ell = 2$ and 3, showing a quantitative agreement with the numerical data.

A scaling for σ_x^ℓ as a function of We and ℓ can be deduced analytically in model cases. One natural case is to consider $\mathcal{T}_\ell$ as a Gaussian white noise of autocorrelation function $C(t) = D\delta(t)$, where δ is the Dirac function, and D is independent of the Weber number. In this case, from the analysis of stochastic harmonic oscillators [76] the standard deviation reads

$$\sigma_x^\ell \sim \left[\frac{D}{\Lambda_\ell \Omega_\ell^2}\right]^{1/2}. \tag{6.22}$$

From the coefficients Λ_ℓ and Ω_ℓ we extracted, this model predicts $\sigma_x^\ell \propto \mathrm{We}^{1/2}$, which does not correspond to the observed scaling. A finite correlation time has be taken into account. We then consider $\mathcal{T}_\ell$ as an exponentially correlated Gaussian noise of autocorrelation function $\langle \mathcal{T}_\ell(t)\mathcal{T}_\ell(t')\rangle = (\sigma_\mathcal{T}^\ell)^2 \exp(-|t-t'|/t_\ell)$, where $t_\ell = \ell^{-2/3}/(2\pi)$ is the correlation time of the effective forcing deduced from equation 6.21, and D is independent of We. In this case the mode's standard deviation is written as [76],

$$\sigma_x^\ell = \sigma_\mathcal{T}^\ell \left[\frac{t_\ell(1+\Lambda_\ell t_\ell)}{\Omega_\ell^2 \Lambda_\ell (1+\Lambda_\ell t_\ell + \Omega_\ell^2 t_\ell^2)}\right]^{1/2}. \tag{6.23}$$

The scaling of σ_x^ℓ now becomes a function of the ratios $\Lambda_\ell t_\ell$ and $\Omega_\ell t_\ell$. In practice, we have $\Omega_\ell t_\ell \gg 1$ and $\Omega_\ell t_\ell \gg \Lambda_\ell t_\ell$ for sufficiently small Weber. Considering the limit $\Lambda_\ell t_\ell \gg 1$,

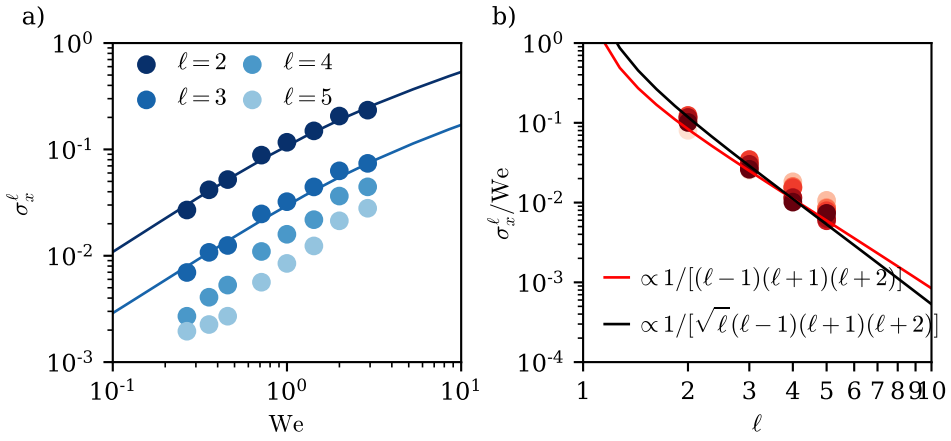

Figure 6.8 – a) Modes standard deviation as a function of the Weber number for all ℓ. The two straights lines are the predictions from our linear model, for modes $\ell = 2$ and $\ell = 3$. b) Modes' standard deviation compensated by We as a function of the mode principal number.

equation (6.23) simplifies as

$$\sigma_x^\ell = \frac{\sigma_{\mathcal{T}}^\ell}{\Omega_\ell^2} = \frac{\sigma_{\mathcal{T}}^\ell}{(\ell-1)(\ell+1)(\ell+2)}\mathrm{We}. \tag{6.24}$$

We then recover the observed scaling for small Weber number. For larger Weber number, the ratio $\Omega_\ell t_\ell$ decreases, and we expect a transition to a shallower increase of σ_x^ℓ with We. This transition should occur for larger Weber number as ℓ increases, an interpretation compatible with the numerical data shown in figure 6.8a. The observed scaling of σ_x^ℓ with Weber thus corresponds to a saturation of the bubble deformations dominated rather by the long correlation time of the forcing (frozen turbulence hypothesis applied to bubble deformations [176]) than an accumulation of random forcing events on a time scale $1/\Lambda_\ell$. It is worth noticing that the estimate of the correlation time of the forcing is therefore essential to predict the amplitude of bubble deformations.

To further check the dependency in ℓ, figure 6.8b shows the compensated standard deviation $\sigma_x^\ell/\mathrm{We}$. We recover that the decrease of the modes' amplitude with ℓ can be mainly attributed to the increase of the natural frequency with ℓ, with a small correction originating from the weak dependency of $\mathcal{T}_\ell$ with ℓ. Eventually, we found a quantitative agreement between the standard deviation x_ℓ and the result from the linear model. The model captures the evolution of σ_x^ℓ with both We and ℓ.

The linear increase of σ_x^ℓ with We, up to the critical Weber number (We ≈ 3 in our case) has important consequences when modelling bubble breakup. Risso et al. [165] suggested that the threshold for breakup is close to the value above which the deformations start to be non linear. A linear model would then be sufficient to describe bubble deformations up to the breakup threshold.

We then look at the entire statistics of the x_ℓ. Figures 6.9 show the probability density functions of the modes $\ell = 2$ for all Weber numbers (6.9a) normalized by their standard deviation. We find that the shape of the pdf does not depend on the Weber number and corresponds to

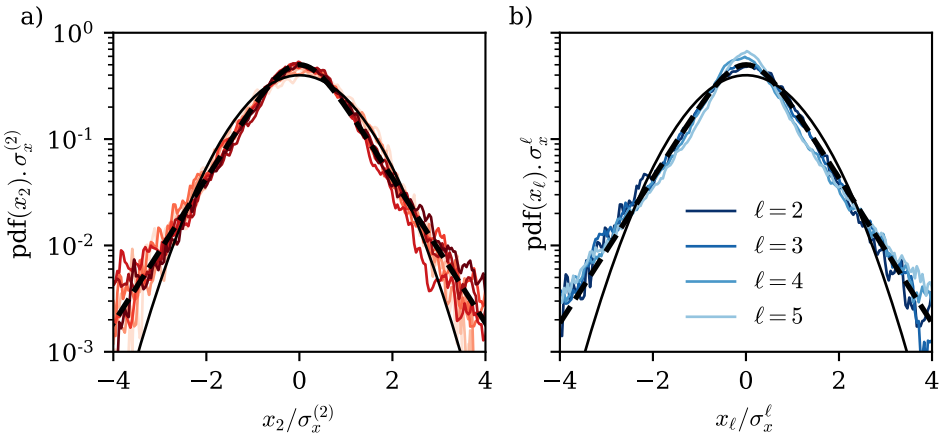

Figure 6.9 – a) Normalized pdf of x_2 for all We. b) Normalized pdf at We = 1 for different ℓ. a)&b) The black dashed line is the hyperbolic secant distribution. The solid black line the Gaussian distribution.

the hyperbolic secant distribution (black dashed line), equivalent to the pdf of the effective force $\mathcal{T}_\ell$. Both the forcing and the mode amplitude share the same pdf that deviates from gaussianity (solid black line) with exponential tails. As the distributions exhibit fat tails, the probability that bubbles experience large deformations leading to breakup is large compared to a Gaussian distribution (black dotted line). Moreover, for larger ℓ, the deviation from gaussian distribution increases, as shown in figure 6.9b for We = 1.

4.2 Deformation spectrum

Figure 6.10 compares the modes' Fourier transforms with the model prediction (6.6) combined with equations (6.11), (6.5) and (6.20) (dotted lines). For all Weber numbers, the model accurately reproduces the zero-limit frequency as well as the amplitude of the spectrum at the bubble natural frequency f_2 and the position and slope of the decay at larger frequencies. At the lowest Weber number (We = 0.27), the model overestimates the spectrum just below the resonance. We remind here that for frequencies larger than $2.5f_2$ the spectrum is dominated by numerical noise. For all the other We, in the absence of resonance, the model captures the spectrum close to the bubble natural frequency.

4.3 Consequences for bubble breakup

Thanks to the quantitative model we develop, we can revisit the breakup scenario and the criterion for breakup. Two main breakup scenarios have been proposed for bubbles in turbulence. Bubbles can break either when they encounter a pressure fluctuation larger than some threshold values [103, 114, 122, 214] or after series of small excitation at their natural frequency which induce a resonance [165, 180]. The ability for a bubble to store energy on a mode ℓ, is quantified by the quality factor $Q_\ell = \Omega_\ell/\Lambda_\ell$. The quality factor Q_ℓ sets the number of periods over which energy can be stored. For large Q_ℓ, energy can be accumulated while it is dissipated in a few bubble periods for low Q_ℓ. Our linear model provides a quantitative measure of Q_ℓ. Combining

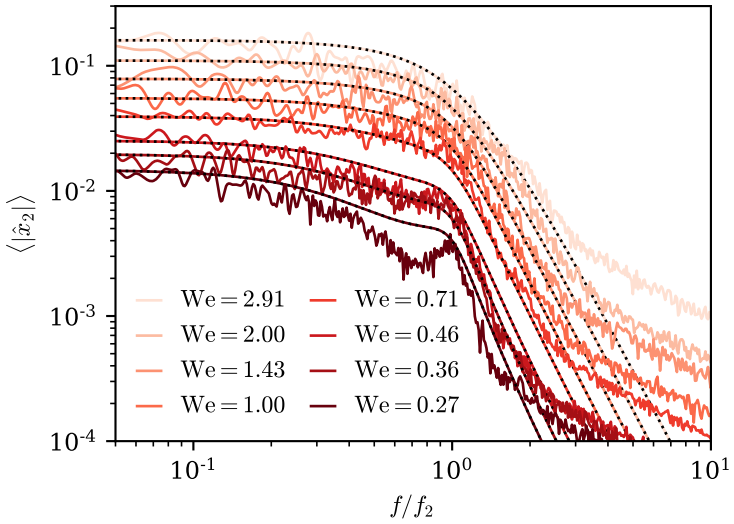

Figure 6.10 – Comparison of the Fourier spectrum amplitude between the DNS and the model (dotted line). The model spectrum is obtained by combining equations (6.11), (6.5) and (6.20) in (6.6), for the mode $\ell = 2$. The model captures the low frequency limit, the position of the transition as well as the high frequency decay for all We.

equations (6.5) and (6.11) we have an explicit expression for Q_ℓ as a function of We and ℓ,

$$Q_\ell = 4\sqrt{\frac{(\ell-1)(\ell+1)}{0.6(\ell+2)(2\ell+1)^2}}\mathrm{We}^{-1/2}. \tag{6.25}$$

In turbulence, bubbles mainly break after oblate-prolate deformations, meaning deformations along their second modes $\ell = 2$ [123, 141, 158, 165]. For the typical critical Weber numbers reported in the literature, $0.1 < \mathrm{We}_c < 10$ [118, 165, 167, 180], our estimate of the quality factor for the mode $\ell = 2$ ranges from 0.3 ($\mathrm{We}_c = 10$) to 3 ($\mathrm{We}_c = 0.1$). These quality factors are too low to observe significant energy storage over several period of oscillations. Resonance can still occur for the largest $Q_\ell \approx 3$. However, we expect the resonant mechanism to be subdominant at this quality factor. We conclude that large pressure fluctuations set the value of the critical Weber number rather than resonant mechanism.

Note that a sequence of oscillations at the bubble natural frequency may be observed for sufficiently large quality factor, typically $Q_2 > 10$, corresponding to $\mathrm{We} < 8.10^{-3}$. Even though such a Weber number corresponds to bubbles size much smaller than the Kolmogorov Hinze scale, which will never break, it may be observed experimentally.

5 Link between model coefficients and surrounding turbulent fields

In this section, we aim at connecting the effective variables we identified, namely the forcing $\mathcal{T}_\ell$ and the damping coefficient Λ_ℓ, to flow statistics in turbulence. The presence of a bubble modifies the flow statistics in its surrounding, through dynamical boundary conditions at the interface and incompressibility. Nevertheless, for drops, it has been shown that the outer eddies

(further than $0.2d$ from the interface) generate most of the normal stress [200]. These outer eddies may be less affected by the presence of the interface. Therefore, it is natural to compare the flow statistics on a sphere in the absence of a bubble to the effective force statistics. In section 3.5, we argued that the pressure modes are a good proxy for the effective forcing. In this section, we then compare the statistics of $\mathcal{T}_\ell$ to the pressure modes statistics in the single phase case. On the other hand, the damping is expected to arise eddies contained in the boundary layer near the interface [200]. To rationalise the origin of the additional damping from the flow statistics, we will therefore study the local dissipation in the bubble boundary layer.

5.1 Point statistics of the pressure field

As a reference case, we first consider the Eulerian point statistics of pressure in homogeneous and isotropic turbulence, at the same Taylor Reynolds number $\mathrm{Re}_\lambda = 55$, corresponding to the two phases flow case. To compare with the bubble dynamics, we will still express length scales in units of d, timescales in units of $t_c(d)$ and therefore velocity in term of velocity increments at the bubble scale $\langle \delta u(d)^2 \rangle^{1/2}$.

We run single phase direct numerical simulations and record the Eulerian pressure fluctuations $p(x,t)$ at seven different fixed location well separated in space. We run three simulations for a total of $245 t_c(d)$. Resolution is increased compared to the two-phase problem and would be equivalent to 68 points per bubble radius and 3.6 points per Kolmogorov length. Note that increasing the resolution was not necessary but allows us to obtain more precise results, especially in the viscous range. In this section, ensemble averages are performed over the three simulations and the seven locations.

Figure 6.11a illustrates two temporal evolution of pressure, normalized by the characteristic pressure difference at the bubble scale, $P_c = \rho \delta u(d)^2$. We found a pressure standard deviation $\sigma_p = 0.67 P_c$. Pressure exhibits random oscillations of small amplitude around zero, together with large negative drops. This asymmetry between positive and negative pressure fluctuations is better observed on the pressure pdf plotted on figure 6.11b. We recover that negative values are exponentially distributed, while positive pressure values follow a Gaussian distribution (dashed black line). The existence of the large negative peaks leading to an asymmetric pdf is well known and has been reported both in experiments [1, 27, 152] and direct numerical simulations of homogeneous isotropic turbulence [31, 198]. It has been shown that these large negative peaks correspond to vorticity filaments [27, 59, 69] passing through the measurement point. As the bubble moves in the fluid, it may experience different pressure statistics and the Lagrangian pressure statistics could also be relevant.

Lagrangian pressure statistics have also been investigated numerically. Numerical studies involve measuring pressure statistics along the paths of point particles [9], as well as (sub-Kolmogorov) finite-size bubbles [10, 11] whose dynamics are modeled using a pure advection or a Maxey-Riley equation [125, 192] respectively. They found that larger particles have a higher probability to be within low pressure regions. Nevertheless, the overall shape of the pressure pdf, with an exponential tail for negative values and a Gaussian distribution of positive values, is conserved.

To investigate the frequency statistics of the local pressure, we compute the temporal Fourier

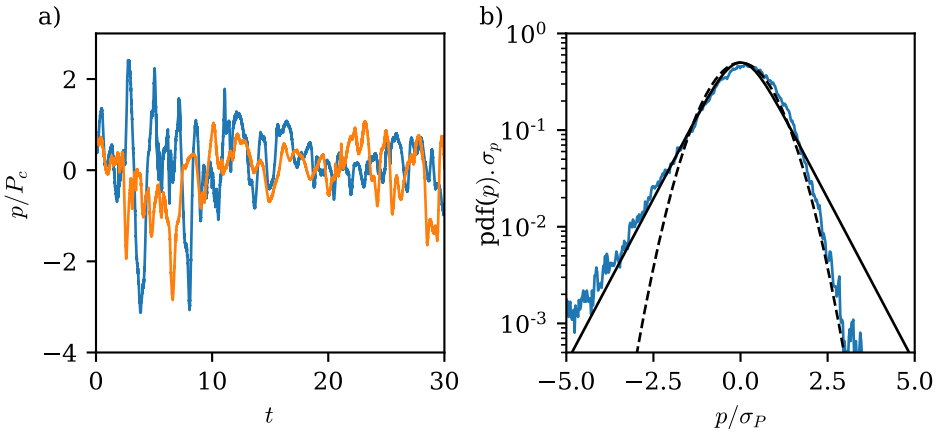

Figure 6.11 – a) Typical temporal evolution of the pressure at two points in space. We observe small amplitude oscillations together with rare intense negative peaks. b) Local pressure distribution normalized by its standard deviation $\sigma_p = 0.67P_c$. The solid black line follows the hyperbolic secant distribution centered while the black dashed line follows a Gaussian distribution with standard deviation 4/5.

transform of each pressure signal $\hat{p}$,

$$\hat{p}(\omega) = \int_{-\infty}^{\infty} p(t)e^{-i\omega t}\mathrm{d}t. \tag{6.26}$$

The average amplitude of its Fourier transform $\langle|\hat{p}|\rangle$ is plotted on figure 6.12. The corresponding inertial range in frequency space is delimited by the inverse of the eddy turnover time at the integral scale $f_c(L) = 1/t_c(L)$ (black dotted line) and the inverse of the eddy turnover time at the Kolmogorov scale, $f_c(\eta)$ (dashed line). For low frequencies, $f < f_c(L)$, $\langle|\hat{p}|\rangle$ slowly decreases with f. Abry et al. [1] have shown that this evolution at low frequencies originates from the contribution of vorticity filaments, since their typical lifetime is the integral timescale [59, 152]. Removing their contributions flattens the low frequency spectrum [1].

In the inertial range of the turbulent cascade, $f_c(L) < f < f_c(\eta)$, $\langle|\hat{p}|\rangle$ decays down to the noise level near $f_c(\eta)$. In the spatial Fourier space, and *a fortiori* in the temporal Fourier space, there is no consensus for the scaling of the pressure power spectrum within the inertial range [151]. A Kolmogorov-like scaling predicts $|\hat{p}(k)|^2 \sim \epsilon^{4/3}k^{-7/3}$ (reported by Ishihara et al. [88] for instance) but other authors have also reported a $k^{-5/3}$ scaling [79, 198]. To transform the spatial power spectrum into a temporal power spectrum, a classical way is to consider that the small scale structures are advected by the large scales. This is the sweeping hypothesis [99, 189], which has been successfully used to reproduce pressure temporal autocorrelation [218]. Combining this argument with the Kolmogorov prediction, we find that $\langle\hat{p}\rangle$ should scale as $\hat{p}^K \sim \epsilon^{2/3}u_{rms}^{5/6}\omega^{-4/3}$, with a proportionality constant of order 1. We find a reasonable agreement, as shown by the compensated spectrum $\langle\hat{p}\rangle/\hat{p}^K$ in the inset of figure 6.12. As evidenced by Pullin et al. [151], Pumir [152], and Vedula et al. [198] the Kolmogorov scaling might only hold in a narrow range of frequencies, corresponding to scales just below the integral scale, due to the limited inertial range. The proportionality constant is around 3 in our case (solid black line) lower than the value of 7 proposed by Pumir [152]. The third regime $f > f_c(\eta)$, corresponds to the end of the

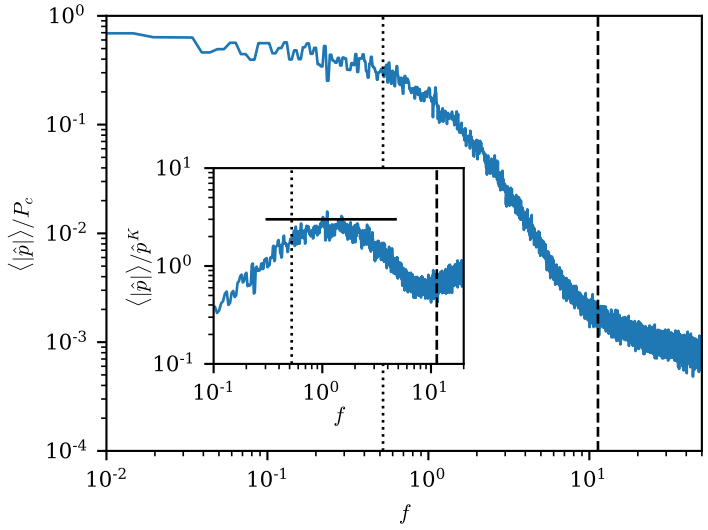

Figure 6.12 – a) Amplitude of the local pressure Fourier transform. The vertical dotted line corresponds to the frequency $f_c(L)$ of eddies of integral length scale in size, while the dashed line corresponds to the frequency $f_c(\eta)$ of eddies of Kolmogorov length scale in size, . Inset plot: Compensated Fourier transform $\langle|\hat{p}|\rangle p^{-K}$ with $K = -4/3$. The solid line corresponds to $\langle|\hat{p}|\rangle = 3p^K$.

inertial range and is close to the limit of resolution of our DNS, as $f_c(\Delta x) = 3f_c(\eta)$, where Δx is the minimum grid size.

5.2 Pressure field on a sphere

To compare the pressure statistics with the effective forcing $\mathcal{T}_\ell$, we interpolate the pressure field $p_S(\theta, \phi)$ in the single phase DNS on a sphere of radius R_0, and compute its spherical harmonics decomposition

$$p_S(\theta,\phi) = P_c\big[\sum_{\ell=0}^{\infty}\sum_{m=-\ell}^{\ell} P_{\ell,m}(t)\, Y_\ell^m(\theta,\phi)\big]. \tag{6.27}$$

Similarly to the modes of deformation $x_{\ell,m}$, the statistics of $P_{\ell,m}$ are independent of m. Ensemble averages are then computed over the three simulations and the m values. For pressure, the modes $\ell = 0$ and $\ell = 1$ are non zero, however we focus in the following on modes $\ell \geq 2$ which are relevant for bubble deformations. Figure 6.13a shows that the standard deviation of each mode ℓ, σ_P^ℓ, varies exponentially with ℓ. A higher ℓ is associated with fluctuations at a smaller scale, which are known to be less energetic. However we have no explanation for the exponential scaling. We also observed a decay of $\sigma_\mathcal{T}^\ell$ with ℓ (figure 6.5). The symmetry between positive and negative values is restored, as shown on figure 6.13b. Distributions now show exponential tails for both negative and positive pressure values. The shape of the distribution is found independent of ℓ, corresponding to the same hyperbolic secant distribution (eq. (6.17)) than the effective forcing distribution we previously identified.

Eventually, we compute the temporal Fourier transform $\hat{P}_\ell$ of the spherical pressure modes

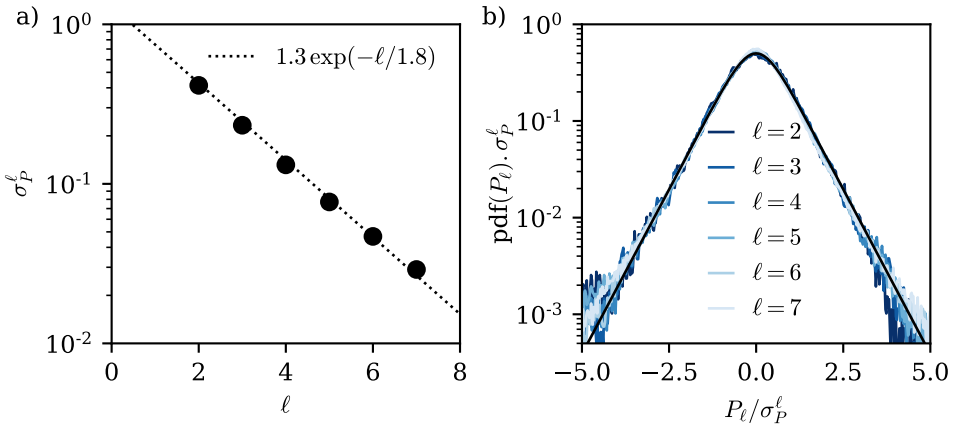

Figure 6.13 – a) Pressure standard deviation, σ_P^ℓ as a function of ℓ, showing an exponential decay with ℓ (black dotted line) b) Distributions of P_ℓ, normalized by σ_P^ℓ, as a function of ℓ. All the pressure modes share the forcing distribution given in equation (6.17).

P_ℓ. Figure 6.14a shows the ensemble average of the norm, $\langle|\hat{P}_\ell|\rangle$ as a function of the frequency. For each ℓ, we recover the three regimes we observed for the point pressure spectrum and $\mathcal{T}_\ell$. The transition between the two first regimes depends on the mode ℓ. Considering that the pressure spectrum share the same characteristic frequency than the effective forcing spectrum, we expect the transition to occur at $f = \ell^{2/3}$, the frequency associated with eddies of size d/ℓ, in units of $t_c(d)$. We show in figure 6.14b the spectra $\langle|\hat{P}_\ell|\rangle$ normalized by their low frequency limit, $\hat{P}_\ell^0$, as a function of the frequency normalized by $\ell^{2/3}$, the eddy turnover time at scale d/ℓ. All curves collapse on a single master curve, showing that pressure and effective forcing share the same time scales. Below the critical frequency ($f < f_\ell$), the spectrum amplitude converges to a constant value, significantly above the integral frequency f_L. Similarly to Abry et al. [1], the pressure spectrum at low frequency is now constant. We can assume that the averaging over the sphere has filtered the contribution from localized structures, and in particular the vorticity filaments. A flat spectrum in the range $f_c(L) < f < \ell^{2/3}$ also indicates that the contribution of eddies larger than d/ℓ, which are roughly homogeneous at the mode scale, has also been filtered out: a bubble is mainly deformed by eddies at its scale. For $\ell^{2/3} < f < f_\eta$, $\langle|\hat{P}_\ell|\rangle$ follows f^{-3}. This decay is steeper than the ℓ-dependency of $\langle|\hat{\mathcal{T}}_\ell|\rangle$ which follows f^{-2}. This might be attributed to the discrepancy between Eulerian and Lagrangian statistics. From sweeping effect [99], the temporal decorrelation of Eulerian quantities are expected to occur faster than their Lagrangian counterpart.

To summarize, we have shown that the effective forcing $\mathcal{T}_\ell$ deforming a bubble shares the same statistics as the corresponding pressure modes integrated over a sphere of same radius. As a consequence of the filtering effect induced by the integration over a sphere, the characteristic frequency associated with each mode ℓ is the eddy turnover time at scale d/ℓ, the frequencies smaller than $\ell^{2/3}$ are well described by a white noise, and the forcing amplitude decreases with ℓ.

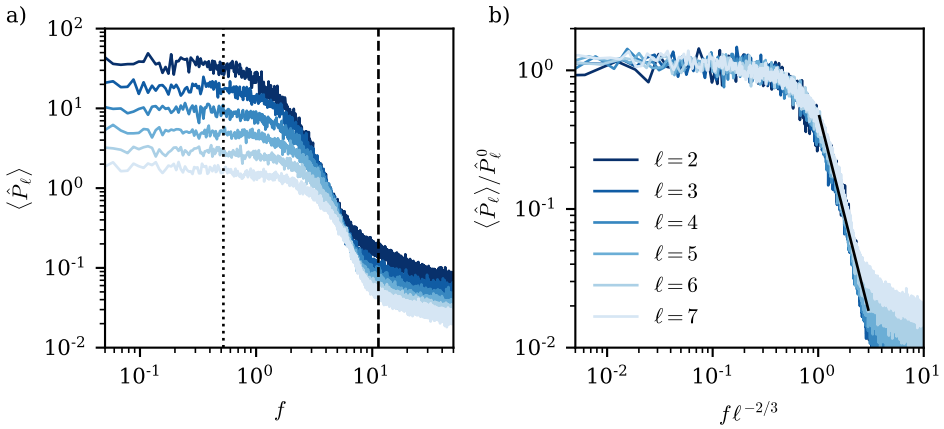

Figure 6.14 – a) Amplitude of the pressure Fourier transform $\langle |\hat{P}_\ell| \rangle$ for each mode ℓ as a function of the frequency in unit of the eddy turn over time at the bubble scale. The black dashed line is represents the eddy turnover time at scale η. The black dotted line is the eddy turnover time at the integral length scale. b) Normalised pressure Fourier transform as a function of frequency in unit of the eddy turnover time at scale d/ℓ. The black line follows f^{-3}.

5.3 Dissipation profiles

Our analysis of bubble deformation shows that (i) The effective forcing originates from pressure fluctuations near the bubble, and it is not affected by bubble deformability. (ii) The damping of bubble oscillations is significantly enhanced compare to the quiescent case. This damping can either originate from additional dissipation in the turbulent boundary layer or an energy transfer from the bubble oscillations to the turbulent flow. Both mechanisms depend on the boundary layer thickness. Using a turbulent viscosity hypothesis we estimated that energy was transported on a boundary layer of size $L_t = R_0/5$, independent of We. In this section we investigate the velocity gradient profile near the bubble, on a distance comparable to bubble typical deformation. To do so, we need to compute a local distance r to the interface, which is not provided by the Basilisk VOF algorithm. This computation, as well as the investigation of the dissipation profile, was the internship of Kamel Abhari, a master student from ENSTA.

The method principle is the following. For every bulk point, we find the closest grid point on the interface. We then interpolate the bubble surface around this point, using a quadratic interpolation on the 20 closest neighbouring interfacial points. To find the neighbours efficiently, the interfacial grid points are stored in a k-d tree structure. The distance r to the interface is then found by minimizing the distance from the bulk point to the quadratic manifold. We follow this procedure for both outside ($r > 0$) and inside ($r < 0$) bulk points.

We diagnose the additional dissipative term of the linear model by investigating the local dissipation rate profile around the bubble. The energy dissipation rate per unit of mass in a elementary volume is related to the local velocity gradients by

$$\langle \epsilon \rangle(x) = 2\nu \langle (\partial_i u_j + \partial_j u_i)^2 \rangle, \tag{6.28}$$

where we use Einstein notations. For each run, we output snapshots of the full flow field at

We	2	1.43	1	0.71	0.46	0.36	0.27
N	48	68	68	27	46	24	52

Table 6.3 – Number of snapshots per Weber number used to compute the flow profiles.

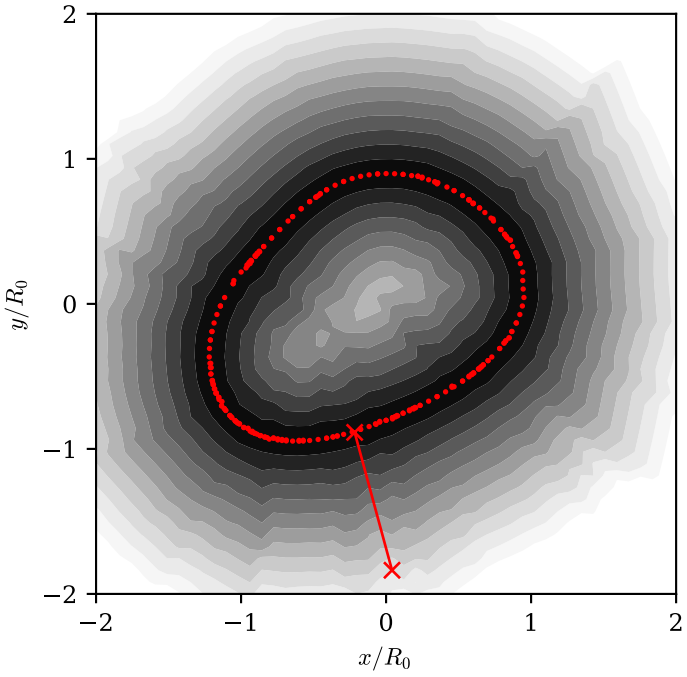

Figure 6.15 – Example of the distance computation on a slice of a bubble at We = 2. The red points are on the interface. Isocontours are separated by $0.0625R_0$. We also show the association between one bulk point and the corresponding interfacial point.

times separated by at least one eddy turnover time at the bubble scale, to ensure statistical independence. We then compute profiles of the local dissipation near the interface by averaging on shells of constant distance from the bubble interface, as illustrated on figure 6.15. Eventually, for each Weber number, we ensemble average the flow snapshots (see table 6.3) to extract a mean profile.

Figure 6.16a shows the average local dissipation, divided by the kinematic viscosity, $\langle\epsilon\rangle(r)/\nu$, as a function of the distance r to the bubble interface. Far from the bubble interface, for $r > R_0/2$ and $r < -R_0/2$, the local dissipation converges to a constant. In the gas, velocity gradients are maximum at $r = -R_0/15$. The existence of a maximum inside the bubble near the interface originates from the nearly no slip boundary condition imposed by the denser fluid on the gas inside the bubble. Similar boundary layer has indeed been observed near solid particle surface (no slip boundary condition) [41, 181]. For bubbles, we therefore expect that decreasing the gas density increases the amplitude of the peak. The velocity gradients inside and outside the bubble share the same order of magnitude: the dissipation hence mainly takes place outside the bubble, in the liquid, where the dynamical viscosity is much larger. To understand the origin of the additional damping we then focus on the outside boundary layer.

For $r > 0$, we observe a thick boundary layer of typical size $R_0/5$ (see figure 6.16a), com-

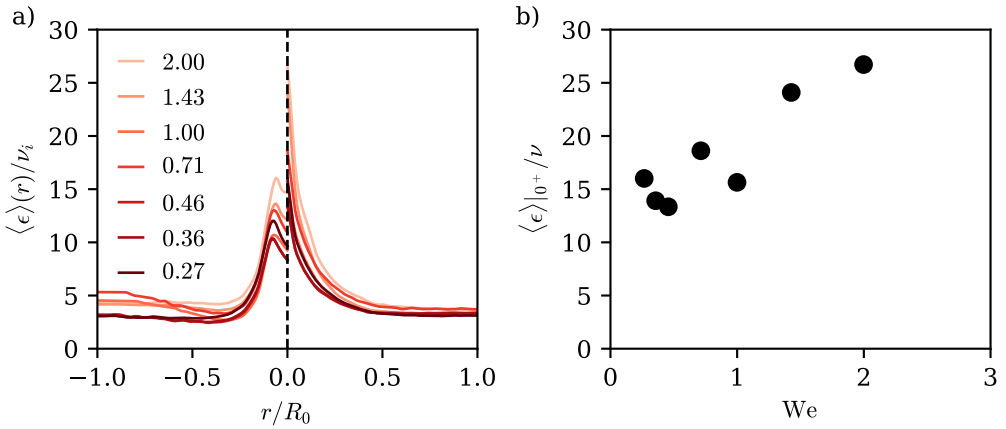

Figure 6.16 – a) Local velocity gradient inside and outside the bubble as a function of the distance to the interface, for all We. b) Limit of the dissipation rate at the bubble interface in the liquid phase as a function of the Weber number.

patible with our estimation of L_t (see equation (6.14)). Figure 6.16b shows the dissipation rate value at the interface, in the liquid $\langle\epsilon\rangle|_{0^+}$ as a function of the Weber number. At vanishing Weber number, we find a non zero dissipation originating from a geometrical boundary layer. The interfacial value varies between 3 times (We = 0.27) and four times (We = 2) larger than in the bulk. In addition, we find an increase compatible with a linear dependency of the interfacial dissipation with We. If we interpret this additional dissipation as an energy transfer rate from the surface deformation to the flow, it would scale as $\Lambda_\ell(\dot{x}_\ell)^2$. We have $(\dot{x}_\ell)^2 \sim (\omega_\ell \sigma_x^\ell)^2 \propto$ We. This interpretation is therefore compatible with a damping coefficient Λ independent of We.

In the absence of flow, the thickness of the boundary layer of the oscillating bubble can be estimated by $\sqrt{2\nu/\omega_2}$. For a Weber number ranging from 2.9 to 0.27, this estimation gives a boundary layer of size ranging from $0.07R_0$ to $0.04R_0$, which is much thinner than the boundary layer thickness we measured. We conclude that the boundary layer originates from a geometrical turbulent boundary layer, and not from bubble oscillations. The existence of a thick boundary layer was completely disregarded in the computation of Lamb [101] for a potential flow far from the interface. The thick boundary layer we observed for the dissipation profile is then consistent with an effective damping one order of magnitude larger than in the quiescent case.

6 Conclusion

In summary, we have shown that the deformations of bubbles in turbulence can be described in terms of a stochastic linear oscillator on the Rayleigh modes of oscillations up to a Weber of order unity. Conversely to previous works, we have directly measured using DNS of bubbles in turbulence the coefficients of this reduced model, namely, the damping rate and the natural frequency, together with the statistical properties of the effective forcing. We have shown that the natural frequency associated with each mode of deformation is not modified compared to the quiescent case. For the effective dissipation, we found that the damping is one order of magnitude larger than the laminar viscous dissipation computed by Lamb. Looking at the

dissipation profiles near the interface, we confirmed that the additional dissipation originates from a thick geometrical boundary layer of size $L_t \approx R_0/5$. In physical units, we expect the damping coefficients Λ_ℓ to scale as u_{rms}/d. Eventually, we found that the effective forcing does not depend on the Weber number. This observation confirms that bubble deformations are one-way coupled to the flow: the back-reaction of bubble deformations on the surrounding turbulent flow can be neglected. This effective forcing is characterized by a probability distribution with exponential tails and a typical correlation time which scales with the eddy turnover time at the mode's scale $t_c(d/\ell)$. We also looked at the statistics of pressure fluctuations on a sphere in the absence of bubbles, and we showed that the effective forcing shares the same pdf as the pressure modes' pdf as well as the same characteristic timescale. Due to the enhanced dissipation compared to the quiescent case, we showed that the resonant oscillation mechanism is not statistically relevant to explain break-ups. Indeed, at Weber of order unity, the bubble cannot accumulate deformation energy on several periods of oscillations as the quality factor $Q = \omega_2/\lambda$ of the main bubble oscillations is too small. As a consequence, bubbles break rather from short and large turbulent fluctuations than from series of small amplitude excitations at the bubble natural frequency (resonant mechanism).

In the next chapter, we use this reduced dynamics to predict the breakup statistics.

Chapter 7

Bubble breakup rate in turbulence

The sex of angels.

A colleague

Abstract

Bubble fate in turbulence is controlled by the Weber number, but also by the time spent within the turbulent region. In real flows, which are inhomogeneous and time-dependent by essence, the residence time significantly affects the survival probability. In this chapter, we use the stochastic linear model derived in chapter 6 to infer the breakup probability of bubbles in turbulence as function of both the Weber number and the residence time. Our model shows that bubble breakup is a memoryless process, whose breakup rate varies exponentially with We^{-1}. This linear model successfully reproduces breakup rates from the literature on experiments in bubbles breakups. The explicit expression for the breakup rate can be used in population model equations. Finally, we propose a new definition for the critical Weber number, which depends on the residence time.

Contents

1 Introduction

In turbulence, since any bubble can encounter a large enough pressure fluctuation and break, We_c, is only defined in a statistical sense [138, 201]. In addition, in practical situations, flows are inhomogeneous (bubble columns) or unsteady (breaking waves) or both, and the time spent by a bubble within a homogeneous turbulent region, called the residence time, strongly affects the critical Weber number We_c. In this chapter, using the stochastic linear model inferred in chapter 6, we propose to link the individual bubble deformation dynamics to the probability of breakup. Our approach is based on the reminiscent idea that non linear effects may be negligible before the critical deformation for breakup is reached [165], and that bubble lifetime is given by a linear timescale, as pinch-off is a fast process. The linear oscillator model has been used previously by several authors for bubbles [71, 100, 123, 165] and drops [169]. However, all authors used the quiescent theoretical parameters [101, 159], in particular for the damping rate, which turns out to be at least one order of magnitude larger in the presence of a turbulent background flow. In addition, turbulent forcing was estimated using temporal sequences of a velocity increment at scale d, measured in single phase flows. These two key differences will impact the breakup statistics.

The chapter is organized as follows: We first recall the main features of the stochastic linear model before discussing the breakup criterion. Then, running our reduced dynamics, we measure the probability for a bubble to break as a function of We and the residence time. We eventually compare the predicted breakup rate to experimental datasets and discuss practical applications in inhomogeneous and unsteady flows. Finally, we introduce a new definition of the critical Weber number, which depends explicitly on the residence time.

2 From a linear model to breakup quantification

2.1 Bubble deformations dynamics

In chapter 6, we investigated the linear deformations of bubbles in turbulence at low and moderate Weber number. We demonstrated that each mode of deformation follows a linear stochastic oscillator equation, and inferred the coefficient values as well as the forcing statistics from the data. In this chapter we extrapolate this linear dynamics at all Weber number with the aim of describing bubble breakup.

As said earlier, the five modes $\ell = 2$, illustrated on figure 7.1a, dominate the deformation dynamics [141, 165]. Consequently, we focus on their dynamics in this chapter. Since they all share the same dynamics, in this chapter, we denote by x the amplitude of any of these modes. As in the previous chapter, time is made dimensionless using the eddy turnover time $t_c(d)$. In these units, we have shown that x evolves following

$$\ddot{x} + \lambda\dot{x} + \omega^2 x = \mathcal{T}(t), \tag{7.1}$$

with $\omega^2 = 192/\mathrm{We}$ the natural frequency in a quiescent flow [101, 159], $\lambda = 12$, the damping rate, about 15 times larger than the Lamb prediction [101] and the forcing term, $\mathcal{T}$, a

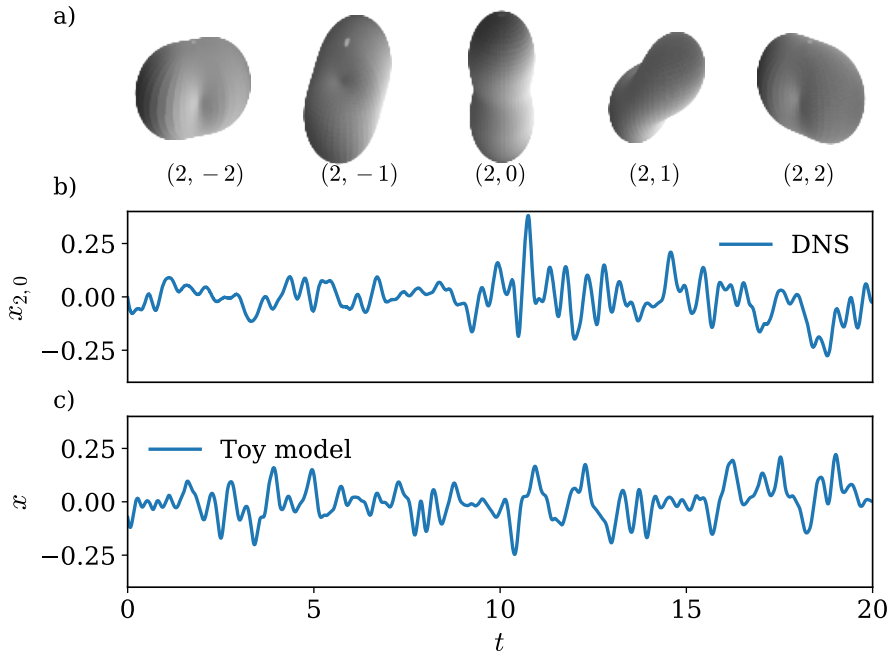

Figure 7.1 – a) Shape of deformation of the five modes $\ell = 2$. b) Typical temporal evolution of a mode $\ell = 2$, at We $= 0.71$. c) Typical temporal evolution given by the linear stochastic model defined by equation (6.2), at We $= 0.71$.

random variable which represents the stochastic forcing from turbulence. Being statistically stationary, the forcing $\mathcal{T}$ is completely characterized by its probability distribution function (PDF), and its auto-correlation function. The forcing PDF is the hyperbolic secant distribution $1/(2\sigma_\mathcal{T})/\cosh(\pi/2x/\sigma_\mathcal{T})$, which depends on a single parameter, the standard deviation $\sigma_\mathcal{T} = 20$. The autocorrelation function of $\mathcal{T}$ is $\exp\left(-2\pi.2^{2/3}t\right)(1 + 2\pi.2^{2/3}t)$, where the $2^{2/3}$ factor comes from the eddy turnover time at the scale d/ℓ with $\ell = 2$. The strength of this model is that we can generate arbitrarily many artificial temporal signals of the forcing without relying on experimental measurements. The procedure to generate random forcing sequences with the correct PDF and auto-correlation function, using Gaussian Copulas, can be found in Appendix B. Figure 7.1 compares qualitatively one temporal evolution of the mode $x_{2,0}$ at We $= 0.71$ measured both in the DNS (7.1b) and generated from the data (7.1c). Since the two signals share the same pdf and temporal correlation, we recover qualitatively the same behavior. Small amplitude oscillations are followed by large amplitude events corresponding to the interaction between the bubble and large pressure events. These large events are generally followed by a few large amplitude oscillations, before the energy is completely dissipated.

2.2 Breakup criterion

When breakup occurs due to a linear instability, the drop or bubble lifetime is essentially given by the growth rate of the most unstable mode. Indeed, in comparison, the non-linear pinch-off dynamics is order of magnitudes faster. The Rayleigh-Plateau instability, for instance, governs the timescales of filament breaking [207], including in the turbulent case, as we will see in chapter 9. As a consequence, bubble lifetime can be estimated by the time taken by

deformations to reach a critical value which needs to be estimated.

In a previous work [141], we investigated the short term deformation dynamics of modes and the breakup time of bubbles at large Weber number. We found that, at short times, the average deformation $\zeta = (\sum_\ell \sum_m x_{\ell,m}^2)^{1/2}$ grows linearly in time for all simulations. In addition, the ensemble average slope is independent of the Weber number. We showed that this linear increase originates from an advection of the interface by the surrounding velocity: for times small compared to the capillary time scale or equivalently the mode period, surface tension does not play any role. The initial dynamics is only driven by the initial conditions, and therefore the statistics of the initial velocity increments at the bubble surface. In the limit of zero surface tension, or infinite We, we expect the deformations to grow linearly in time until it reaches a maximum deformation and breaks. One can then transform the velocity statistics, which control the linear increase of deformations, into lifetime statistics.

In order to predict the threshold value, in Perrard et al. [141], for the large Weber number data ($15 \leq \mathrm{We} \leq 45$), we approximated the bubble shape at breakup by an ellipsoid of same volume and whose longest axis corresponds to the maximum distance between two points on the bubble interface. The average standard deviation of the local bubble radius gives an estimate of the maximum deformation experienced by the bubble and, as a consequence, of the critical mode amplitude. In the limit of very large Weber numbers, this critical value, combined with the velocity statistics measured on a sphere of radius R_0 allowed us to successfully reproduce the average lifetime. In this chapter, we extend this criterion to every Weber number.

As a consequence, in this chapter, we use the critical value measured in Perrard et al. [141], $x_c = 0.74$ (but the breakup phenomenology does not depend on the value of x_c).

3 Memoryless bubble breakup

We now simulate thousands of reduced dynamics and investigate the breakup statistics emerging from the model.

3.1 Single mode breakup probability and breakup rate

We define the breakup time of each oscillator as the first time at which the amplitude reaches x_c. Accordingly, we introduce $p_b(t)$, the probability that the amplitude of one mode reaches x_c before a certain observation time t. p_b is the cumulative breakup probability. Figure 7.2 shows the survival probability, $1-p_b(t)$, as a function of the observation time, for several Weber numbers in the toy model. For each Weber number, the survival probability decays exponentially in time, as expected for a memoryless process, with a constant breakup rate $\kappa(\mathrm{We})$ associated with one mode of deformation. For a breakup time much larger than the correlation time of both the pressure fluctuations at the bubble scale and the bubble deformation, the evolution of the forcing can indeed be modeled as a succession of independent fluctuations. Eventually, the cumulative breakup probability associated with one mode x reads

$$p_b(t) = 1 - \exp[-\kappa(\mathrm{We})t], \tag{7.2}$$

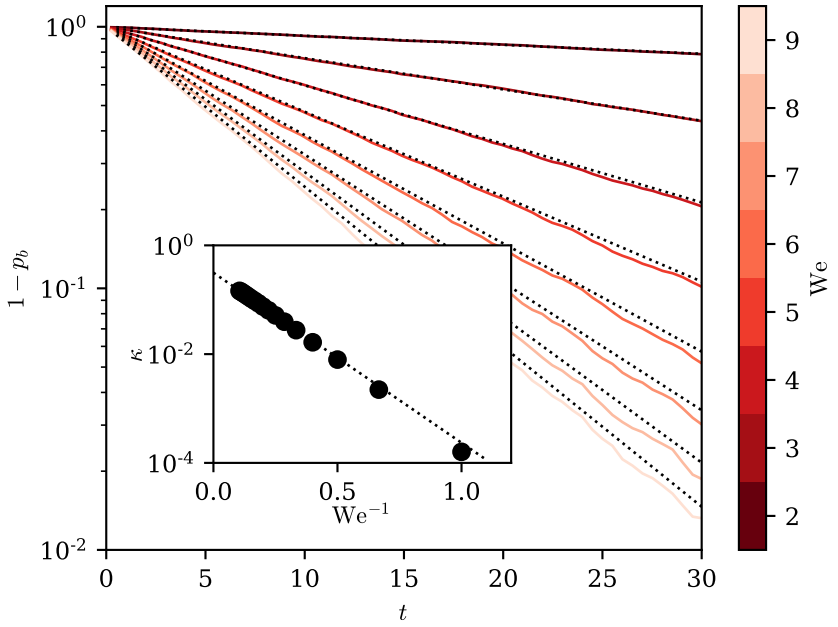

Figure 7.2 – Survival probability as a function of time for several We (solid color lines) in the model (7.1). Black dotted lines are exponential fits for each Weber number. Inset plot: breakup rate as a function of We. The black dotted line is an exponential fit, see equation (7.3).

which extends the previous experimental observation of memoryless bubble breakups at large Weber number by Ravelet et al. [158]. Such a memoryless breakup process was also observed numerically for drop breakups [201].

These results quantify one of the physical process driving fragmentation. Indeed, in turbulence, fragmentation involves two steps [168, 175]: first, inertial deformations from turbulence, governed by equation (7.2), second, a cascade of capillary fragmentation. In population balance equations, the first stage is described by the breakup rate, while the second one is encoded in the breakup kernel and the number of child bubbles. The number of child bubbles produced during the second stage depends on We. It varies from two at low We (We ~ 1), to dozens at large We (typically We > 15) [167]. These rapid correlated events do not fall under the scope of model (7.1), which describes independent events but will be deeply investigated in chapter 9.

The breakup rate, κ varies exponentially with We^{-1} (see inset figure 7.2),

$$\kappa = \alpha \exp\left[-\beta \mathrm{We}^{-1}\right] \tag{7.3}$$

with $\alpha = 0.314$ and $\beta = 7.20$, two numerical factors obtained by a least-square fit. This law, which suggests a mechanism of random activation process, was first proposed by Coulaloglou et al. [47] in 1977, in the context of emulsions, based on the idea of drop-eddy collisions. Note that the dependency on the bubble Reynolds number is not included. When bubble size lies within the inertial range of the turbulent cascade, large bubble breakups are purely inertial and we expect equation (7.3) to hold for any Reynolds, as for drops [201].

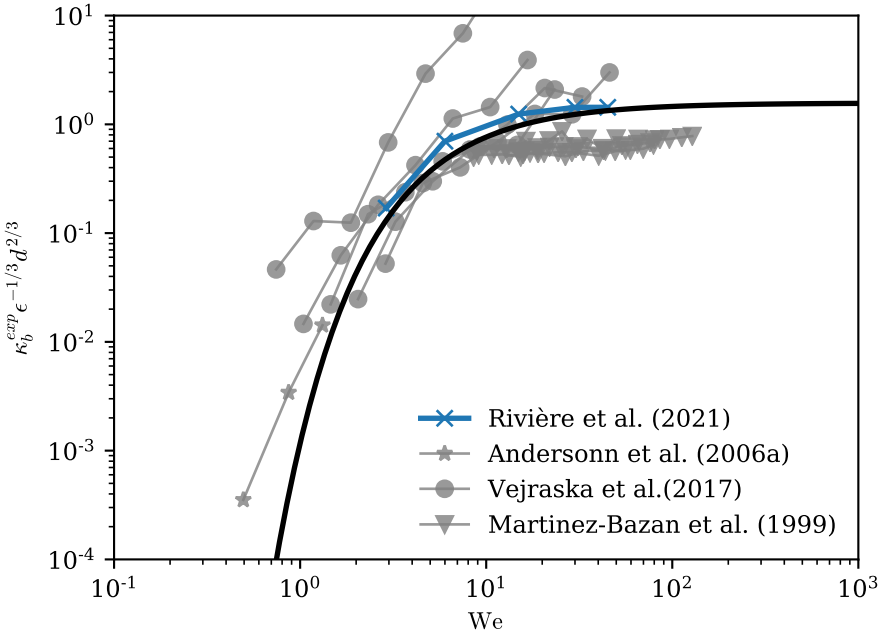

Figure 7.3 – Comparison between our predicted breakup rate and several experimental datasets [6, 118, 167, 199]. Without any fitting parameters, the predicted breakup rate lies on top of the experimental data.

3.2 Comparison with experimental datasets

To compare the breakup rates with the experimental data, one has to remember that a bubble can deform through five modes $\ell = 2$, represented on figures 7.1a. These modes, in the linear limit, are uncoupled and follow the same dynamics given by equation (7.1). As a consequence, in the model, a bubble breaks as soon as one of the five modes reaches x_c. The bubble lifetime is the minimum of the lifetime associated with each mode $\ell = 2$. As they all share the same law, the probability that a bubble breaks before t is given by $P_b(t) = 1 - (1 - p_b(t))^5$. Combining equations (7.2) and (7.3) we find that the bubble breakup rate κ_b is five times larger than that of one single oscillator: $\kappa_b = 5\kappa$. Similar developments for fiber breakup in turbulence can be found in Brouzet et al. [25]. In their case, since a fiber is described as a collection of N elementary rigid elements, the number of breakup modes can be approximated by the number N of fragments. Figure 7.3 compares κ_b with the breakup rates, κ_b^{exp} in s^{-1}, measured in various experimental conditions [6, 118, 199], together with the DNS data from our previous work [167]. Note that, experimental breakups rates are estimated using different expressions, which induces an additional scattering of the data [81]. Even though the datasets come from different experimental facilities, with different turbulence intensities and heterogeneities, our linear model follows experimental points. In particular, it predicts a convergence of the lifetime with We toward a time of order the eddy turnover time, and a divergence of the lifetime at small We, in agreement with all breakup rates models that can be found in the literature [114, 118, 196, 214, 220]. We emphasize here that the linear model does not contain any fitting parameters, every parameter of the dynamics have been determined independently at low Weber numbers, and the threshold was estimated in the limit of large Weber numbers. This result confirms the

intuition of Risso and Fabre [165] that bubble lifetime distribution can be predicted using a linear model.

4 Breakup probability and We_c

In real flows, homogeneous turbulent regions have a finite extent in both space and time. As a consequence, bubbles remain only a finite time, the residence time, t_R in second, within the turbulent region with a probability to break of

$$P_b(t_R, \mathrm{We}) = 1 - \exp\left[\frac{-5\alpha t_R}{\epsilon^{-1/3} d^{2/3}} \exp\left(-\frac{\beta}{\mathrm{We}}\right)\right]. \tag{7.4}$$

Using the previous equation, we can now rigorously define $We_c(t_R)$ as the Weber number for which $P_b(t_R, We_c) = 0.5$. This equation is an implicit equation for We_c. As shown in figure 7.4, by the red line, We_c strongly depends on t_R for $t_R < 10t_c(d)$. As time goes to infinity, as in principle any bubble can break, We_c logarithmically converges to zero. In practice, the evolution of We_c with time is so slow (in $\log(t)$) that low Weber number bubbles ($We < 0.1$) will never break. Note that, in some situations, for instance when buoyancy is important, t_R might depend on We and must be modeled accordingly. Figure 7.4 also shows the probability to break as a function of both We and the residence time in unit of the eddy turnover time. For short residence times, P_b gently varies with We. As a consequence, there is a diverging range of We for which a bubble may break ($0.1 < P_b < 0.9$). The stochastic forcing has smoothed the transition around $P_b = 0.5$. Conversely, at long residence time compared to the eddy turnover time ($t_R > 40t_c$), the limit between breaking and non breaking bubbles is sharp.

Even though other mechanisms might dominate over turbulent fluctuations in some practical situations, such as shear and vorticity [46, 89, 133, 166], it is tantalizing to compare the results from our linear stochastic model to time-dependent and inhomogeneous flows. In what follows, we discuss three different situations - plunging jets, oceanic bubbles and industrial bubble columns - which correspond to three different regions of the diagram of figure 7.4. For example, for a typical plunging jet, with speed 5 $\mathrm{m.s^{-1}}$ [94] at the interface, the bubble jet depth is about 50 mm, leading to a residence time of 0.01 s. The energy dissipation rate can be estimated using the velocity fluctuations u', which is typically 0.1% of the entrance velocity [94], and the integral lengthscale which is the nozzle radius $D \sim 10$ mm, giving $\epsilon = (u')^3/D \sim 10\ \mathrm{m^2 s^{-3}}$. As a consequence, the residence time is of the order of two eddy turnover times. At this residence time merely all bubbles can break (see figure 7.4). We expect the coexistence of large bubbles with much smaller ones, leading to a broad bubble size distribution, which is indeed the case below plunging jets and waterfalls. In the oceans, underneath breaking waves, turbulence is sustained for approximately 1/3 of the wave period, which is of the order of one to few seconds, with a turbulent intensity of 1 $\mathrm{m^2 s^{-3}}$. For centimetric to millimetric bubbles the residence time ranges from 6 to 30 eddy turnover time, corresponding to a critical Weber number between 3 and 5, consistent with the experimental datasets [52]. In industrial bubble columns, bubbles rise with a velocity of about 0.1 $\mathrm{m.s^{-1}}$ on meter columns, inducing a weak turbulence of around 0.1 $\mathrm{m^2 s^{-3}}$ [92]. The residence time for millimetric bubbles is then of the order of 1000 eddy

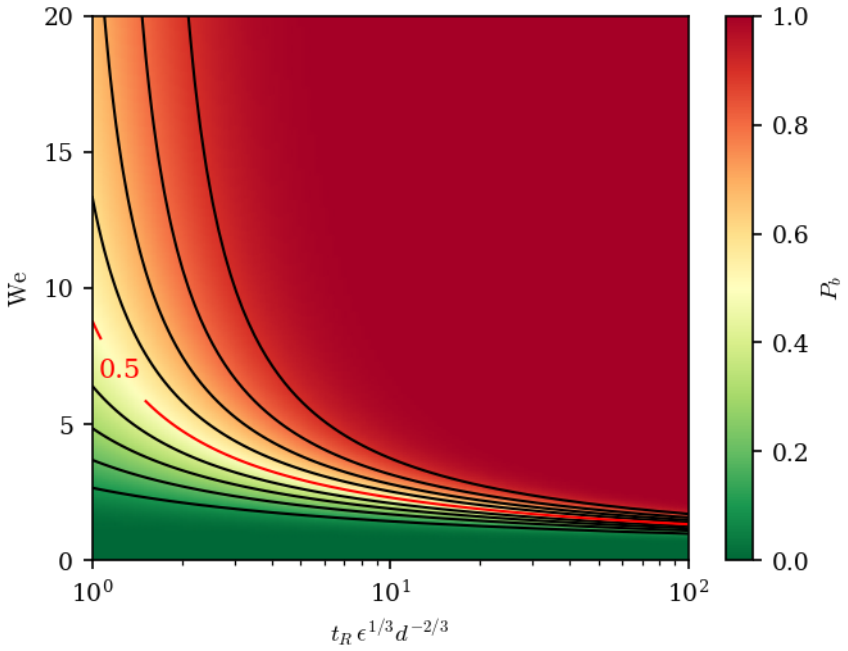

Figure 7.4 – Probability for a bubble to break depending on its We and the residence time normalize by the eddy turnover time. Black lines are isoprobability separated by 0.1. The red line corresponds to a breakup probability of 1/2.

turnover time, where the breaking transition is extremely sharp. In this regime, all bubbles will have $\mathrm{We} < \mathrm{We}_c \approx 1$.

5 Conclusion: A new definition of We_c

In this chapter we have explored the statistics of bubble breakup in HIT. We show that a set of five uncoupled stochastic linear oscillators combined with a critical deformation is sufficient to reproduce bubble breakup statistics when bubble damping and forcing statistics are adequately modeled. We evidence that, for times larger than the eddy turnover time at the bubble scale, bubble breakup is a memoryless process. The associated breakup rate varies exponentially with We^{-1} similar to a transition rate in bistable systems with noise. The Weber number plays the role of the ratio of a noise amplitude to the energy barrier size. Note that in chapter 5, We was already controlling the size of the energy barrier. Thanks to this simple model, we obtain an explicit expression for the breakup probability as a function of both We and the residence time. Provided that turbulent fluctuations dominate over other breaking mechanisms, this model can then be applied to many practical situations which are time-dependent and inhomogeneous by nature. In particular, one can use the explicit expression for the breakup rate in a population model equation. Finally, using this expression, we could rigorously define $\mathrm{We}_c(t_R)$, the Weber number at which, for a given residence time, the probability to break is 1/2.

PART II

FRAGMENTATION PROCESSES - BREAKUP KERNEL

Chapter 8

Fragmentation - Introduction

> The authors really don't do themselves (nor the community) a good service by sending this incremental paper.
>
> A reviewer

Abstract

In this part, we aim at identifying the physical processes leading to the production of sub-Hinze bubbles. There exists two independent approaches to obtain a bubble size distribution of child sizes. The first one consists in modeling the breakup kernel in turbulence, through either statistical or phenomenological models. The second one, widely used in the absence of flow, investigates the size distribution generated by surface instabilities. We argue that both approaches should be combined to understand the sub-Hinze BSD.

Contents

1 Modeling bubble fragmentation

The phenomenon of bubble breakup in turbulence has received considerable attention both experimentally and theoretically. To understand the BSD and its evolution, together with breakup rate models, one must describe the products of fragmentation by modeling the number and the size distribution of child bubbles. We introduce here two different approaches to describe a child size distribution.

1.1 Bubble fragmentation in turbulence

To close the population balance equation, one needs to provide models for the average number of child bubbles $m(\Delta)$ and the breakup kernel $f(d, \Delta)$. We recall here the main approaches, reviewed by both Lasheras et al. [102] and Liao et al. [111]. The latter classified the modeling strategies into three categories: empirical, statistical and phenomenological, the two last ones being the most popular.

Statistical models consider the child size as a random variable whose distribution follows a simple law. Delta, normal [37, 38, 47], beta [103] and uniform distributions [135, 148, 157] are often used. In statistical models, the parameters describing the shape of the distribution are empirically fitted on the data, in order to reproduce the empirical distributions. Statistical models perform well for stochastic systems, in which a large number of independent random events happen. However, when only a finite number of bubbles are present or only a few can break, for instance, if their size is close to d_h, the statistical description fails. In addition, most of these models completely disregard the physical mechanisms leading to the proposed distribution.

Phenomenological models aim at reproducing empirical correlations between the statistical properties of turbulence and the distribution of child bubbles. Liao et al. [111] identified three shapes of breakup kernel: Bell-shape [120], U-shape [114, 196] and M-shape [105, 214], illustrated on figure 8.1. U-shape gives a larger probability for symmetric breakups, whereas it is not observed in practice, while U-shape favors very asymmetric breakups. Lastly, for M-shape, there exists an optimum breakup. As summarized by Lasheras et al. [102], the phenomenological models are based on the change in surface energy of the breaking bubble. They are either based on the probability of sufficiently energetic eddy collision or rely on a stress balance at the bubble interface. In practice, these models rely on quantities which are hardly accessible, such as the eddy collision frequency or efficiency making the validation difficult or even impossible. Importantly, none of them predict the $\mathcal{N}(d) \propto d^{-3/2}$ for the sub-Hinze BSD.

The interaction with turbulence is not the only physical process driving breakup in turbulence. Indeed, as soon as a bubble is deformed, surface instabilities can be triggered, leading to their own child size distribution.

1.2 Surface instabilities

It is noted that bubbles can break due to surface instabilities even in the absence of a surrounding flow field, as Chu et al. [46] emphasized. For instance, very large bubbles rising in a quiescent flow are unstable and can break into several child bubbles. A canonical instability

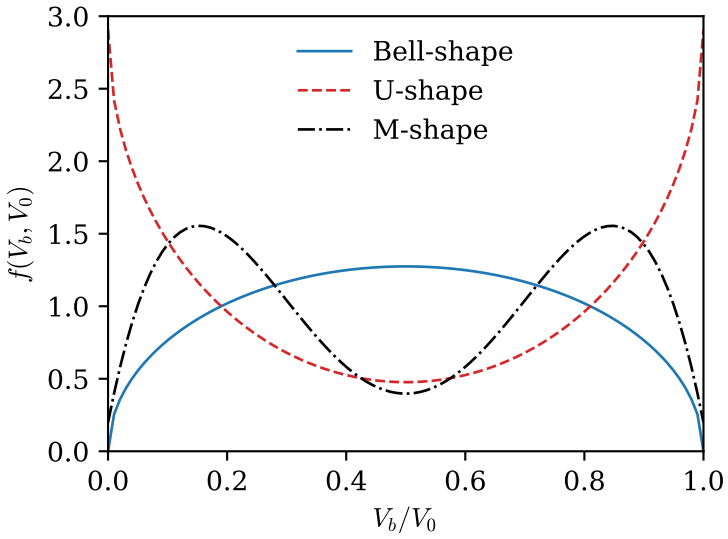

Figure 8.1 – Schematic representation of the three phenomenological breakup kernel identified by Liao et al. [111].

is the destabilisation of a gas or liquid thread by surface tension. This instability, originally described for liquid threads in void, is know as the Rayleigh-Plateau instability. It is known to produce a bimodal distribution of drop sizes in the liquid case (see for instance Pal et al. [140], for the drop size distribution of rough liquid threads). The largest bubble size corresponds to the most unstable capillary wavelength. The smallest size corresponds to the satellite bubble created to accommodate for the asymmetry around pinch-off [63, 64, 107].

In turbulence, pressure and velocity fluctuations produce highly deformed bubble shapes on which surface instabilities can develop. When these instabilities lead to fragmentation, the resulting children size distribution combines the distribution from turbulence and instabilities. However, to our knowledge, no model takes into account surface instabilities when modeling the breakup kernel, while they might be at the origin of the production of sub-Hinze bubbles.

2 Conclusion : Focus on elementary breakup process

In this work, we aim at rationalizing the child size distribution of sub-Hinze bubbles by identifying the elementary physical process leading to their formation. This identification would constrain the shape of the breakup kernel associated with sub-Hinze bubbles.

To identify the elementary breakup processes leading to the formation of sub-Hinze bubble, in chapter 9 we study the fragmentation of bubbles in turbulence. We decompose the sequence of breakups into binary events. We focus on the lifetime of bubbles producing one sub-Hinze bubble. We find that these tiny bubbles originate from the rupture of gas filaments. In chapter 10, we focus on the generation of these gas filaments in the model flow geometry to understand in which configurations they are produced. Lastly, in chapter 11, we study the fragmentation of a single gas filament and deduce the shape of the breakup kernel, for sub-Hinze bubbles.

Chapter 9

Sub-Hinze bubble formation [1]

Extremely badly written.

A colleague

Abstract

In dilute environments, the bubble size distribution (BSD), $\mathcal{N}(d)$, is solely controlled by breakups. A typical situation where breakup controls the BSD is bubble fragmentation below breaking waves. In this configuration, the BSD exhibits two power-law regimes: the well-known $\mathcal{N}(d) \propto d^{-10/3}$ for super-Hinze bubbles ($d > d_h$), and a shallower slope for sub-Hinze bubbles ($d < d_h$), which remained to be understood. The latter drive mass fluxes across the ocean-atmosphere interface even though individually these bubbles are negligible in volume. Thus, it is essential to understand its origin to quantify mass fluxes. Combining experimental and numerical approaches, we report a power law scaling $d^{-3/2}$ for the small bubble size distribution, for sufficiently large separation of scales between the injection size and the Hinze scale. From an analysis of individual bubble breakups, we show that small bubbles are generated by capillary effects, and that their breakup time scales as $d^{3/2}$, which physically explains the sub-Hinze scaling observed. We conclude that two breakup mechanisms happen concomitantly: one local in size, controlled by turbulence, and another, nonlocal, which results from the capillary fragmentation of filaments generated during the deformation of large super-Hinze bubbles.

Contents

1. Most of the results of this chapter have been published in Rivière et al. [168] and Ruth et al. [175].

1 Introduction: BSD in dilute medium - The case of breaking waves

In view of its importance for mass transfers between the atmosphere and the ocean, bubble fragmentation below breaking waves has received a considerable attention over the last decades. Indeed, bubble fragmentation drives gas dissolution, in particular of low-solubility gases, such as O_2, by drastically increasing the exchange surface between phases. For instance, up to 40% of the total CO_2 uptake by the ocean is due to bubble-mediated gas transfer [55, 93, 160]. Bubbles also play a major role in clouds formation. Indeed, bubble bursting at the surface of the ocean is the primary mechanism for aerosols production, which can serve as cloud condensation nuclei [51, 53, 109, 185]. More specifically, it is the bubble size distribution that controls gas transfer [8, 53, 106] and spray production as bubbles burst at the surface [15, 53, 54, 75, 185]. As a consequence, the fragmentation of bubbles has been extensively studied in model experiments [100, 119, 153, 165] as well as under breaking waves both experimentally [19, 52, 113, 171] and numerically [33, 56, 132].

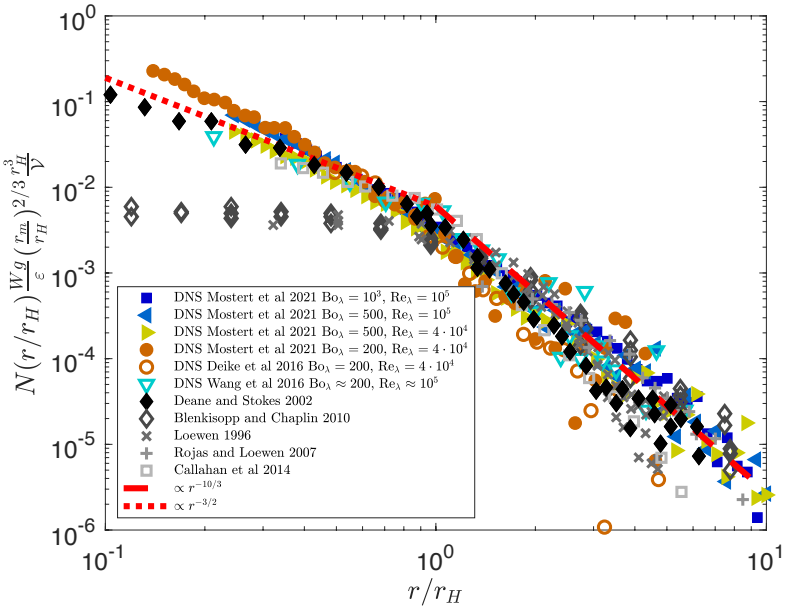

Figure 9.1 – Figure adapted from Deike [53]. Review of the reported bubble size distribution below experimental and numerical breaking waves, as a function of bubble radii normalized by the Kolmogorov-Hinze scale r_h (d_h in the text).

As discussed earlier, there exists a critical Weber number, We_c, of typical value between 0.5 and 8 [52, 84, 118, 165, 180, 199], or equivalently a size, $d_h = (\gamma We_c/(2\rho\epsilon^{2/3}))^{3/5}$ called the Kolmogorov-Hinze scale [84, 97], which separates statistically breaking from non breaking bubbles. In oceans, d_h lies typically between 500 μm to 2 mm [52, 53]. Starting from the seminal work of Deane et al. [52], most experimental and numerical studies have reported two power-law scalings for the BSD, $\mathcal{N}(d)$, (see figure 9.1) depending on the value of d/d_h. For large bubbles, $d > d_h$, a consensus has been reached on the bubble size distribution, described

as $\mathcal{N}(d) \propto d^{-10/3}$ [19, 113, 132, 171]. Garrett *et al.* [73] argued that this law arises from a self-similar breakup cascade, driven by turbulence with a bubble lifetime controlled by the eddy turnover time at the bubble scale $t_c(d) = \epsilon^{-1/3} d^{2/3}$. Far small bubbles $d < d_h$, the bubble size distribution always exhibits a gentler slope than $\mathcal{N}(d) \propto d^{-10/3}$ and most of the data collapse on a $d^{-3/2}$ scaling, although there is variability among the experimental studies [19, 52, 113, 171]. As detailed in the introduction, chapter 1, Deane et al. [52] showed that the two power-laws of the bubble size distribution strongly depend on the time at which the distribution is measured. For sub-Hinze bubbles, they found a robust $d^{-3/2}$ scaling when measuring the BSD in the fragmentation phase, while other power-laws were reported in the quiescent phase. They argue that the quiescent power-laws, which vary in time, originate from the aging of the BSD due to bubble-size-dependent rising speeds. Therefore, bubble fragmentation produces a $d^{-3/2}$ scaling for the sub-Hinze bubbles which needs to be understood to describe the latter evolution of the BSD. This scaling was still lacking a physical explanation [52] despite being the most important when quantifying gas exchanges and aerosol production.

In this chapter, in order to understand the physical mechanisms leading to two different power-law scalings for the BSD, we run direct numerical simulations of a single bubble breaking in turbulence. We then conduct an analysis of the individual breakup events happening within the cascade of breakups and focus, in particular, on the timescale setting bubble lifetime.

2 From breaking waves to a single bubble breakup

Studying bubble fragmentation below breaking waves is challenging due to the unsteadiness and inhomogeneity of the flow underneath the surface. Nevertheless, during the fragmentation cascade, the flow has developed into a fully 3D turbulent flow [132]. One can then test whether the model configuration involving a single bubble deforming and breaking in a homogeneous flow is able to reproduce the key physical ingredients below breaking waves.

2.1 A minimum experimental configuration

In order to test the validity of the single bubble breakup for modeling BSD below breaking waves Luc Deike, Stéphane Perrard and Daniel Ruth designed an experiment to inject a unique large air cavity inside a homogeneous and isotropic turbulent flow, as described in [168]. In a water tank, they create a turbulent flow using four pumps pointing toward the center. The resulting velocity field is characterized by $\epsilon = 0.7\mathrm{m}^2.\mathrm{s}^{-3}$, $u_{rms} = 0.25\mathrm{m.s}^{-1}$, $\mathrm{Re}_\lambda = 340 \pm 40$. The large initial bubble is created by filling with air a thin latex membrane (a balloon) at the bottom of the tank. The ratio between the initial bubble size d_0 and the Kolmogorov-Hinze scale in the experiment is $d_0/d_h = 8.3$ (using $\mathrm{We}_c = 3$). They release the air by piercing the membrane which triggers a rapid opening of the cavity. A typical breakup sequence can be visualized on snapshots figure 9.2. At very short times, the retraction of the latex sheet shears the air-water interface triggering transiently a Kelvin-Helmoltz instability. The surface modulation is rapidly damped by viscous effects. The large bubble then rises and deforms due to the combined action of buoyancy and turbulence. Compared to the quiescent case, the initial cavity experiences large deformations and a broad range of bubble sizes is obtained.

Figure 9.2 – (Pictures from L.D., S.P. and D.R.) Successive snapshots of the release of a large bubble in turbulence. The initial cavity diameter is 4 cm. Initially, an air pocket is trapped within an extended thin rubber sheet. At $t = 0$, the latex sheet is pierced by the needle (the vertical black line). The sheet opening triggers a Kelvin-Helmoltz instability, visible after 2 ms, which is eventually damped by dissipation. Then, the bubble deforms and breaks under the action of buoyancy and the turbulent background flow creating a broad distribution of bubble sizes.

Figure 9.3 compares the balloon BSD with the seminal data set from Deane et al. [52], measured experimentally below breaking waves, and the numerical BSD from Mostert et al. [132]. The agreement between the three data sets is excellent. For bubbles larger than d_h, the balloon BSD shows a short range of scales following $\mathcal{N}(d) \propto d^{-10/3}$ in agreement with previous measurements below breaking waves [19, 52, 113, 171]. For bubbles smaller than d_h, the balloon BSD presents a clear $\mathcal{N}(d) \propto d^{-3/2}$ scaling (red dashed line) over slightly less than two decades.

The fact that the bubble size distribution measured under breaking waves is in close agreement with the data obtained from single bubble breakup in turbulence, suggests that the same underlying mechanisms are at play for the sub-Hinze bubble production. As a consequence, single bubble breakup experiment will allow us to identify the origin of sub-Hinze bubbles in the open ocean.

2.2 Importance of the scale separation

In a previous study [167], we investigated numerically the breaking mechanisms depending on the scale separation between the initial bubble size and the Kolmogorov-Hinze scale d_0/d_h. To do so, we ran direct numerical simulation of a single bubble in homogeneous and isotropic turbulence. We have shown that the succession of breaking events differs tremendously depending on the value of d_0/d_h, leading to very different child bubble sizes. In particular, the largest the initial scale separation, not only the largest the number of child bubbles but also the largest the proportion of sub-Hinze bubbles produced [167]. This result was later confirmed experimentally by Ruth et al. [175]. Daniel Ruth designed an experiment to control precisely the initial bubble size. The experiment is analogous to the balloon experiment. The main difference is the bubble creation. In this experiment, a reversed spoon is put directly within the turbulent zone. The initial bubble size is controlled by monitoring the amount of air injected in the reversed spoon. At the beginning of the experiment, the spoon flips and the air is released within the turbulent region. He found that, for initial bubbles such that $d_0/d_h > 3$, more sub-Hinze bubbles are produced than super-Hinze bubbles, even though the range of reachable super-Hinze sizes increases with d_0. He then performed a systematic experimental study of the evolution of the BSD with the scale separation between the injection size and the Kolmogorov-Hinze scale d_0/d_h.

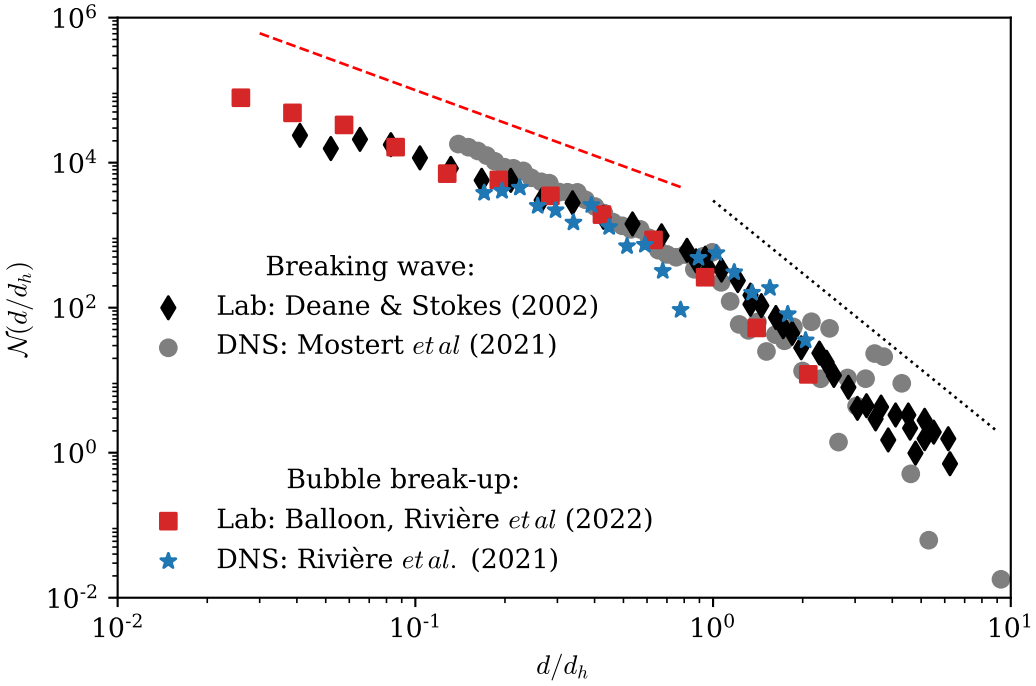

Figure 9.3 – BSD obtained both experimentally and numerically in two different geometries: under breaking waves and for a single bubble breaking. The black dotted line follows $(d/d_h)^{-10/3}$ while the red dashed line follows $(d/d_h)^{-3/2}$.

We report here his results (published in Ruth et al. [175]).

Figure 9.4 (extracted from Ruth et al. [175]) shows the evolution of the BSD with d_0/d_h. Figure 9.4a shows that, as the initial bubble size increases, the number of sub-Hinze bubbles is increased and the sub-Hinze power-law distribution steepens. When plotted against d/d_0 (figure 9.4b) the BSD of the largest cavities ($d_0/d_h > 3$) exhibit $\mathcal{N}(d) \propto d^{-3/2}$ for all bubble sizes. Figure 9.4c shows the exponent obtained from a power-law fit of the portion of curves above the noise limit (data below the red dotted line are not considered statistically converged) as a function of d_0/d_h. It shows a $-3/2$ scaling for all initial cavity sizes greater than $3d_h$.

Hence, a large scale separation between the injection size and d_h is essential to obtain the $d^{-3/2}$ scaling for sub-Hinze bubbles. In addition, as only a few sub-Hinze bubbles are produced for smaller initial cavities, we deduce that sub-Hinze bubbles are directly produced by the breakup of large super-Hinze bubbles through a non-local (in size) cascade. The breakup mechanism producing sub-Hinze bubbles remains to be identified. In what follows, we perform direct numerical simulations of a large initial bubble compared to the Kolmogorov-Hinze scale and aim at identifying the process leading to the small bubble generation.

2.3 Numerical set-up: DNS of a single bubble in turbulence

To investigate the statistics of individual bubble breakup, we run direct numerical simulations (DNS) of a single bubble in homogeneous isotropic turbulence. The details of the numerical set-up are given in chapter 2 (as well as in [167]). We only recall here the main information. We first create a homogeneous and isotropic turbulent flow, at $\mathrm{Re}_\lambda = 38$, following the method described

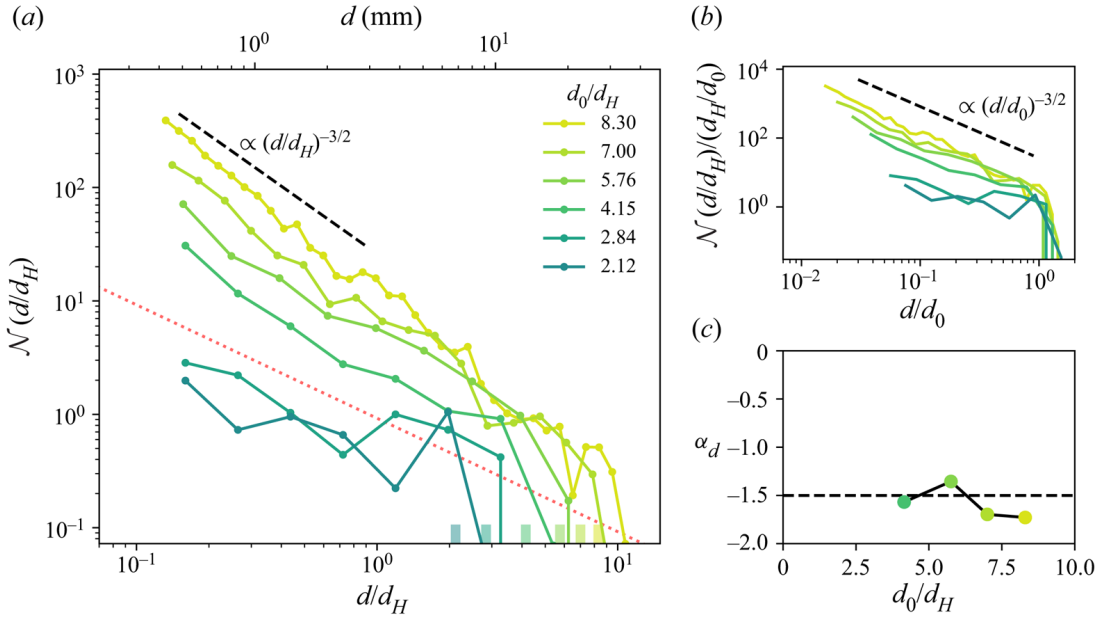

Figure 9.4 – Extracted from Ruth et al. [175]. Evolution of the BSD with the scale separation between the initial bubble and the Hinze scale ($d_H = d_h$), as a function of d/d_h (in a) or d/d_0 (in b). The initial bubble size, d_0, is denoted by the position of the coloured notches along the bottom axis. c) Exponent of the sub-Hinze distribution for the portion above the noise threshold above which the BSD is statistically converged (red dotted line) as a function of d_0/d_h.

by Rosales et al. [172]. Then, we inject a spherical bubble at the center of the numerical domain by changing locally density and viscosity, while maintaining turbulence in the liquid phase. Density and viscosity ratios are 850 and 25 respectively, close to water-air ratios. Bubble radius to box size ratio is 1/15. The air volume fraction is then 1.2%, small enough so that coalescence is effectively negligible in our DNS. We perform at least ten simulations per value of the initial bubble size d_0/d_h (1, 1.5, 2.9, 4.1, 5.2) with a spatial resolution of 135 points per diameter. These ratios correspond to Weber numbers 3, 6, 15, 30 and 45 respectively, with $\mathrm{We}_c = 3$. We analyze the breakup of all bubbles of diameter larger than four grid points.

We first compute the bubble size distribution for the largest value of $d_0/d_h = 5.2$. We have previously shown in Rivière et al. [167], by measuring the temporal evolution of the number of bubbles in the DNS, that most of bubble fragmentation happen before $4t_c(d_0)$ in our DNS, where $t_c(d_0)$ is the eddy turnover time at the initial bubble scale. After this time, only a few bubbles are generated, no matter the initial Weber number. Figure 9.3 reports the DNS BSD measured at $t = 4t_c(d_0)$. Even though statistical convergence is difficult to achieve in the numerical configuration, the numerical BSD is compatible with the experimental power-laws.

3 Individual breakup study

Before investigating the individual breakups, we recall the main theoretical ingredients needed to describe the BSD and its evolution.

3.1 Modeling BSD

To predict the scaling of the BSD, one should build a population model equation, or population balance equation (PBE), which describes how the BSD evolves in time. The PBE involves fluxes between scales encoding for the different physical mechanisms at stake, as detailed in the general introduction, chapter 1. In particular, in dilute media, the bubble size distribution is only controlled by bubble breakups. The associated bubble flux $\Phi(\Delta, d, t)$ from scale Δ to scale d at time t is the production rate of bubbles of diameter d from the breakup of a bubble of size Δ. The mean bubble flux can be decomposed into the product of an average number of child bubbles $m(\Delta)$, a breakup rate $\kappa(\Delta)$ and a child size probability density $f(\Delta, d)$ per unit of diameter and can be written as [66, chapter 4, equation 2.1],[156],

$$\Phi(\Delta, d, t) = m(\Delta) f(\Delta, d) \kappa(\Delta) \mathcal{N}(\Delta, t), \tag{9.1}$$

where $\mathcal{N}(\Delta, t)$ is the number density of bubbles of size Δ at time t. The factor $m(\Delta)$ is usually taken as 2 (binary breakups) as discussed in greater details in [111, 119, 121, 153]. The breakup rate $\kappa(\Delta)$ is the average number of breakup events of bubble of size Δ per unit of time, also called breakup frequency. The probability density f is often referred to as the child bubble size distribution and is the probability density function to generate a child of size d from the breakup of a bubble of size Δ.

From equation 9.1, we obtain the temporal evolution of the bubble size distribution from the fragmentation of an initial bubble of size d_0 as the difference between a birth term and a death term [119]

$$\frac{\partial \mathcal{N}(d, t)}{\partial t} = \int_d^{d_0} \Phi(\Delta, d, t) \mathrm{d}\Delta - \kappa(d) \mathcal{N}(d), \tag{9.2}$$

considering the total bubble size distribution in a spatially homogeneous configuration, henceforth neglecting the spatial advection terms, due, for instance, to buoyancy. The birth term integrates the contribution of breakups of all bubbles larger than d, which has a child of size d. The death term encode the decrease of the number of bubble of size d due to their breakup.

In this chapter, we aim at modelling the production of sub-Hinze bubbles, hence the flux $\Phi(\Delta, d, t)$ where $d < d_h$. Two characteristic timescales may control the breakup rate $\kappa(d)$: first, the correlation time of velocity fluctuations at scale d, the eddy turnover at the bubble size

$$t_c(d) = \epsilon^{-1/3} d^{2/3}. \tag{9.3}$$

The eddy turnover time is known to control the breakup of large super-Hinze bubbles [73, 118, 199]. The second characteristic time is the capillary time $T_2(d)$,

$$T_2(d) = \frac{1}{2\sqrt{3}} \left(\frac{\rho}{\gamma} \right)^{1/2} d^{3/2}. \tag{9.4}$$

The capillary time $T_2(d)$ is the inverse of the angular frequency of oscillation of the principal mode of oscillation of an inviscid bubble in a quiescent fluid [101]. The capillary time also corresponds to the growth rate of Rayleigh Plateau instability of a bubble filament of radius

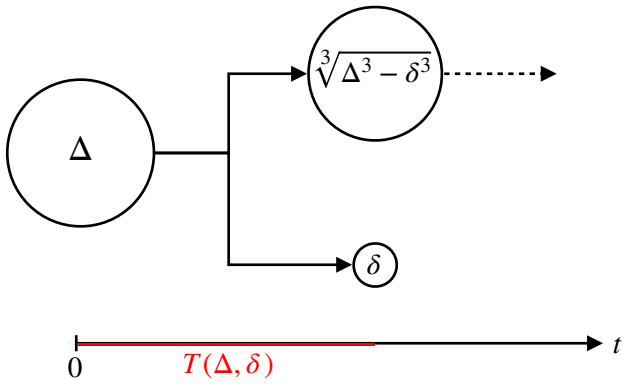

Figure 9.5 – Illustration of the binary breakup decomposition. A bubble of size Δ breaks into two bubbles, the smallest having size δ, in a time $T(\Delta, \delta)$. In the breakup schematized here, $\delta < d_h$ and the smallest child bubble does not break anymore.

d [207]. It is the relevant timescale for drops fragmentation [207] and might play a role in gas fragmentation as well.

In order to understand what physical mechanism controls the production of sub-Hinze bubbles, we now focus on individual bubble breakup. In particular, we develop an algorithm to identify for each breakup, the bubble lifetime and the child bubbles.

3.2 Family trees

We decompose the succession of breakup events into binary breakups and associate a lifetime $T(\Delta, \delta)$ to each parent bubble of size Δ producing two child bubbles, the smallest having size δ. Figure 9.5 schematize a binary breakup where $\delta < d_h$. In this case, the smallest bubble does not break anymore. The originality of this procedure is to consider that bubble lifetime is also a function of the child bubble size. This is a non causal approach which allows us to discriminate between breakups producing large bubbles, which would feed the $d > d_h$ part of the distribution and breakups producing sub-Hinze bubbles, which will contribute to $\mathcal{N}(d < d_h)$. Note that a bubble lifetime that depends on both the parent and the child bubble size was introduced by Wang et al. [214]. We compute the values of the equivalent diameters Δ and δ from parent and child bubble volumes. The second child bubble size is $\sqrt[3]{\Delta^3 - \delta^3}$ from volume conservation. For equal-size child bubbles we have $\delta = c\Delta$ with $c = 2^{-1/3} \approx 0.79$ a numerical constant. Such binary decomposition is always possible as no two breakups happen exactly at the same time. Doing so, we expect some breakups to be correlated as they originate from the same breakup sequence. The algorithm to reconstruct each breaking events is detailed in chapter 3. The processing is systematically applied to simulations where $d_0/d_h \geq 2.9$, and leads to the identification of 4329 breaking events, using 78 different 3D DNS realizations of bubble breakup. In the following, we focus on events happening before $4t_c(d_0)$, during the fragmentation cascade.

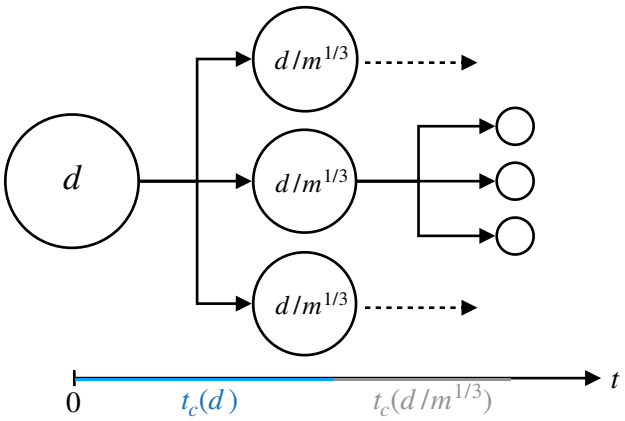

Figure 9.6 – Illustration of the self-similar breakup process from Garrett et al. [73]. A bubble of size d breaks into m fragments of equal size in one eddy turnover time $t_c(d)$. The same scenario repeats itself for each child bubble.

4 Super-Hinze distribution

Before investigating the small bubble production, we test the validity of Garrett's *et al.* model for super-Hinze bubbles.

4.1 Garrett's *et al.* model: a self-similar cascade

For super-Hinze bubbles $d > d_h$, we recall the argument proposed by Garrett et al. [73] and illustrated on figure 9.6. In this self similar model, a bubble of size d breaks, in a time given by the eddy turnover time at its scale $t_c(d) = \epsilon^{-1/3} d^{2/3}$, into m fragments of equal diameter, $m^{-1/3}d$, from volume conservation. Each of these child bubbles then breaks in a time $t_c(d/m^{1/3}) = \epsilon^{-1/3}(m^{-1/3}d)^{2/3}$. In the classic decomposition given in equation 9.1, it means that $\kappa(d) = 1/t_c(d)$ and $f(d, \delta, t)$ is the Dirac function at $\delta = m^{-1/3}d$. Assuming that the BSD is stationary, the bubble flux from size d to size $m^{-1/3}d$, must equal the flux from $m^{-1/3}d$ to smaller sizes. This condition imposes that

$$\frac{1}{t_c(d)} m\mathcal{N}(d)\mathrm{d}d = \frac{1}{t_c(m^{-1/3}d)} \mathcal{N}(m^{-1/3}d)\, \mathrm{d}\left(m^{-1/3}d\right). \tag{9.5}$$

The left hand side represents the production of bubbles at size $m^{-1/3}d$ originating from the breakup of bubbles of size d. The right hand side encodes the loss of bubbles of size $m^{-1/3}d$ due to their own breakup. Injecting the expression of $t_c(d)$ in the above expression and simplifying we obtain a relation between the number of bubbles at size d and the number of bubbles at size $m^{-1/3}d$

$$\mathcal{N}(d) = m^{-10/9}\mathcal{N}(m^{-1/3}d). \tag{9.6}$$

Assuming a power-law distribution, $\mathcal{N}(d) \propto d^{\alpha}$, the previous expression imposes,

$$\alpha = -\frac{10}{3}, \tag{9.7}$$

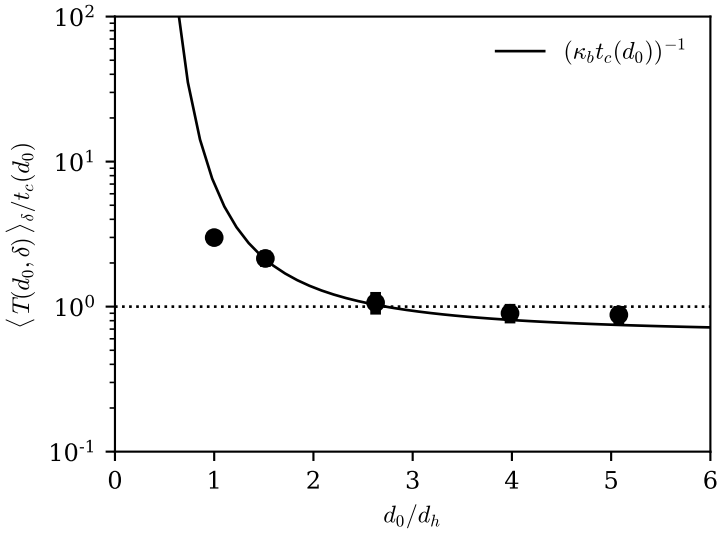

Figure 9.7 – Average lifetime of the initial bubble in units of the eddy turnover time at scale d_h, as a function of scale separation d_0/d_h. Error bars encode the standard error. The solid black is the prediction from chapter 7, reminded in equation (9.8). As d_0/d_h increases the average lifetime converges to the eddy turnover time at scale $t_c(d_0)$ with a prefactor of order 1. On the contrary, when $d_0 \to 0$, the average bubble lifetime diverges.

the exponent of super-Hinze BSD.

4.2 Average bubble lifetime

Garrett's *et al.* model works as long as the breakup rate $\kappa(d)$, or equivalently the average bubble lifetime $\langle T(d,\delta\rangle_\delta) \sim 1/\kappa(d)$, is controlled by turbulence. In what follows, we compute the average bubble lifetime in two situations: (i) for the initial bubble and (ii) for bubbles within the fragmentation cascade for which history effects might become important.

First bubble lifetime: We measure the first bubble lifetime $T(d_0,\delta)$, as a function of d_0/d_h for the six values of d_0/d_h, and average over the realizations. Figure 9.7 shows the average lifetime of bubble of size d_0, $\langle\, T(d_0,\delta)\,\rangle_\delta$, in units of $t_c(d_0)$, as a function of d_0/d_h. As d_0/d_h increases, $\langle\, T(d_0,\delta)\,\rangle_\delta$ converges to the eddy turnover time $t_c(d_0)$ with a prefactor of order 1, as reported experimentally [118, 199]. When capillary effects are negligible, bubble lifetime is given by the advection of its interface by turbulence. This time scales as the eddy turnover time at the bubble scale. Conversely, as d_0 decreases, the average lifetime increases, reaches $4t_c(d_0)$ for $d_0/d_h = 1$ and would diverge for $d_0 \to 0$. Indeed, as discussed in chapter 5, in turbulence, all bubbles can break. When d_0 is of the order of d_h or smaller, we expect capillary effects to come into play and to modify bubble lifetime. The solid black line is the prediction from chapter 7,

$$\kappa_b^{-1} = \frac{t_c(d_0)}{5\alpha}\exp(\beta/\mathrm{We}) \tag{9.8}$$

where $\alpha = 0.314$ and $\beta = 7.20$ are two numerical constants determined previously (see chapter 7). This expression holds for independent breakup events and therefore captures the lifetime of the

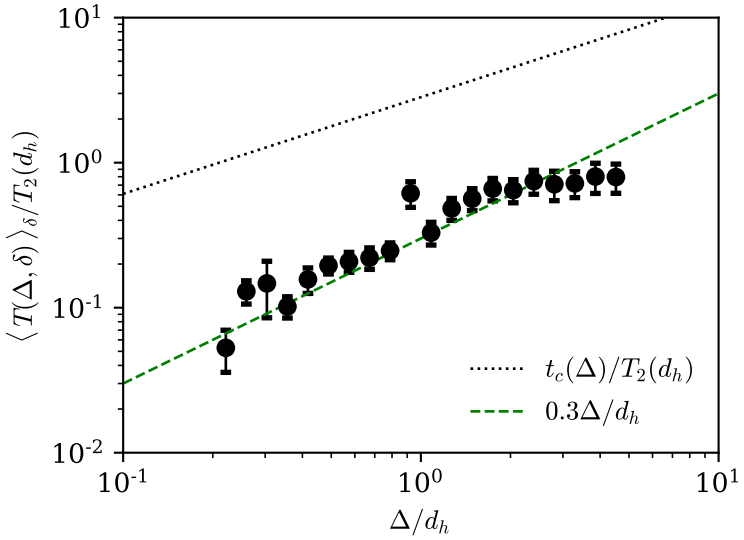

Figure 9.8 – Average bubble lifetime within the fragmentation cascade in units of the capillary timescale at scale d_h as a function of the scale separation Δ/d_h. Error bars encode the standard error. The green dashed line scales as Δ, a scaling which does not correspond to any characteristic timescale of the problem. The black dotted line is the eddy-turnover time at scale Δ.

initial bubble for all scale separation d_0/d_h. As long as $d_0/d_h > 1.5$, it predicts that capillary effects are negligible. Breakup rate (henceforth bubble lifetime) is driven by the eddy turnover time at the bubble scale, confirming the assumption of Garrett's *et al.*.

Bubble lifetime within the fragmentation cascade: We compute the average bubble lifetime $\langle T(\Delta,\delta)\rangle_\delta$ for arbitrary parent size Δ, within the fragmentation cascade. Figure 9.8 shows $\langle T(\Delta,\delta)\rangle_\delta$, in units of the capillary timescale at the Kolmogorov-Hinze scale d_h, $T_2(d_h)$, as a function of the scale separation Δ/d_h. The average lifetime is found to be one order of magnitude smaller than the eddy turnover time at scale Δ. Within the fragmentation cascade, bubbles break much faster than the turbulent timescale in a succession of rapid correlated events.

In addition, for all parent sizes Δ, the average lifetime is proportional to the parent scale Δ. This scaling does not correspond to any characteristic timescale of the problem: nor the turbulent timescale $t_c(\Delta) \sim \Delta^{2/3}$, nor the capillary timescale $T_2(\Delta) \sim \Delta^{3/2}$. The parent size is not the physically relevant length scale for fragmentation within the fragmentation cascade. We expect two types of breakup to occur within the fragmentation cascade: the turbulent breakups described by Garrett *et al.* which are independent from one another, and other breakups, much faster, whose nature needs to be determined.

5 Sub-Hinze distribution

We have seen that the lifetime of the first bubble is indeed controlled by the eddy turnover time at the bubble scale, and falls into Garret's *et al.* model. However, within the fragmentation cascade, where sub-Hinze bubbles are created, breakups happen on a much faster time scale. In this section we aim at identifying the breakup mechanisms leading to the sub-Hinze bubble

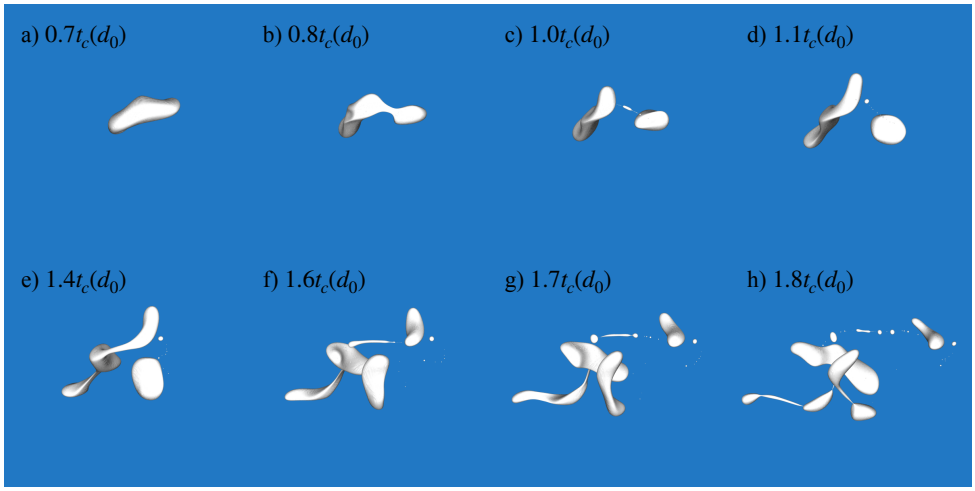

Figure 9.9 – DNS snapshots of a typical break-up sequence, with the initial bubble size $d_0/d_h = 2.9$. The bubbles' interface is represented in white. The first images (a,b) show large scale deformation due to turbulence, happening over the eddy turn over time at the size of the initial bubble scale d_0, $t_c(d_0) = \epsilon^{-1/3} d_0^{2/3}$, leading to the formation of thin filaments (c,d). Successive splitting events of the filament are visible (e,f,g,h) leading to multiple child bubbles. The filaments quickly break creating a wide range of bubble sizes, the smallest being orders of magnitude smaller than the initial one.

production.

5.1 Capillary breakups

Figure 9.9 presents snapshots of a large bubble (giving an initial separation of scales $d_0/d_h = 2.9$) subject to large deformations. The initial breakup, which occurs within one eddy turnover time at the bubble scale $t_c(d_0)$ [167], is followed by the rapid fragmentation of elongated structures created during bubble deformations, and results in the production of dozens of sub-Hinze bubbles. These events, which we call *splitting events*, occur on a much faster time scale than the eddy turnover time at the parent size Δ. Indeed, as soon as the filaments are created, the relevant characteristic length scale for fragmentation is the filament radius whose size is comparable to the sub-Hinze bubble size produced. In addition, as the filament radius are small compared to the parent size capillary forces may dominate the dynamics.

Figure 9.10 shows the average lifetime of bubbles producing a child of size δ, $\langle T(\Delta, \delta)\rangle_\Delta$, as a function of the child size δ. Error bars encode the standard error. The average lifetime is always smaller than the eddy turnover time at the small child bubble's scale, $t_c(\delta)$ (black dotted line). This suggests that these splitting events are not primarily instigated by turbulent deformations at the small child scale. However, $\langle T(\Delta, \delta)\rangle_\Delta$ matches the capillary time scale $T_2(\delta)$ *i.e.* the typical capillary time at the length δ (shown in red dashed line), up to $\delta = d_h$, without any adjustable parameters. We recall that this time scale corresponds to the growth rate of the Rayleigh-Plateau instability on a gas cylinder of typical size δ [207]. For $\delta > d_h$, the breakup time seems to converge to a value independent of δ.

Therefore, the production of small bubbles ($d < d_h$) is controlled by bubble *splitting events*, in which elongated filaments become unstable under a Rayleigh-Plateau-like mechanism [207].

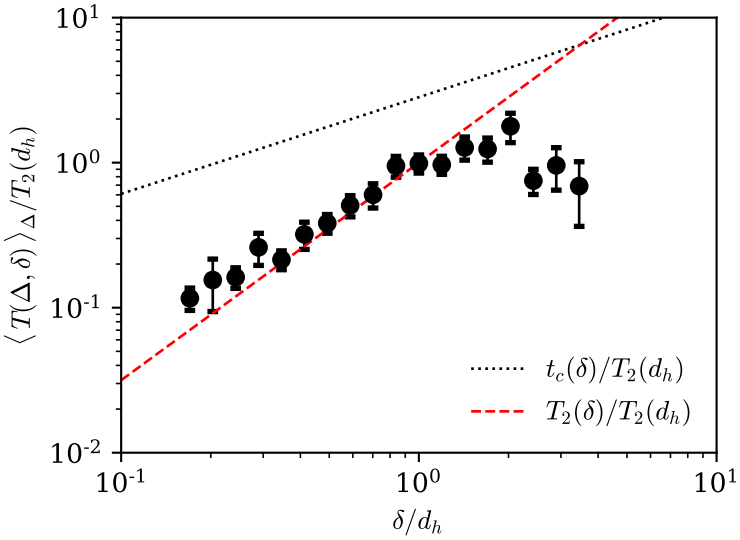

Figure 9.10 – Average lifetime of bubbles producing a child bubble of size δ, $\langle T(\Delta,\delta)\rangle_\Delta$ as a function of the child size. Error bars encode the standard error. The black dotted line is the eddy turnover time at scale δ. The red dashed line is the capillary timescale at scale δ.

This stems from the "freezing" in place of the turbulent flow relative to the accelerating collapse dynamics in the final moments before rupture, which was shown experimentally in Ruth et al. [176]. The cascade of splitting events leads to the formation of sub-Hinze bubbles, whose size δ are comparable to the diameter of the filament, and one larger bubble. The exact geometry of the filament and the splitting time varies from one realization to the other, but considering an ensemble average, the splitting time $T(\Delta,\delta)$ will be given by the capillary time $T_2(\delta)$. To our knowledge, the Rayleigh Plateau instability dynamics for a gas filament in presence of an external noise has never been investigated. A recent study on liquid filament [140] has shown that indeed, initial noise on the filament shape induces a widening of the satellite drop size distribution. The velocity fluctuations associated with the turbulent flow around the bubble could also play a crucial role, by inducing various filament shapes. However, a study by Ruth et al. [176] showed that for the final stage of evolution, *i.e.* the pinch-off of a single bubble in a turbulent flow, the shrinking dynamics of the bubble neck is only slightly modified compared to the quiescent case.

5.2 From the capillary timescale to BSD

By decomposing the fragmentation cascade into binary events, we have identified that the relevant timescale for sub-Hinze bubble production is the capillary timescale at the child size δ. From this knowledge, we propose a model to explain the origin of the sub-Hinze BSD.

In equation (9.1) the rate $\kappa(\Delta)$ at which a bubble breaks up does not distinguish between processes which produce equally sized child bubbles or highly asymmetrically sized child bubbles, for which at least one child bubble is smaller than the Hinze scale. These two types of events, however, occur on very different timescales, $t_c(\Delta)$ and $T_2(\delta)$ respectively. Here, we consider that the fragmentation statistics depends on both the parent size Δ and smallest child size δ,

a framework that has been used previously for models based on bubble-eddy interactions [214]. While the two breakup mechanisms we consider are happening concomitantly, O(10-100) splitting events follow a single breakup event for $\Delta \gg d_h$ (see figure 9.9), so that the capillary timescale dominates the production of sub-Hinze bubbles $\langle T(\Delta,\delta)\rangle = T_2(\delta)$.

To integrate the splitting events within the population balance framework, we propose a new decomposition of the flux Φ from equation (9.1) in terms of the newly introduced timescale, $\langle T(\Delta,\delta)\rangle$,

$$\Phi(\Delta,d,t) = 2\frac{F(\Delta,\delta(d))}{\langle T(\Delta,\delta(d))\rangle}\mathcal{N}(\Delta,t) \tag{9.9}$$

$$= 2\frac{F(\Delta,\delta(d))}{T_2(\delta(d))}\mathcal{N}(\Delta,t), \tag{9.10}$$

where $m(\Delta) = 2$ follows from the binary events decomposition, $\delta(d) = d$ if the child bubble considered is the smaller one of the two produced (that is, if $d < c\Delta$) and $\delta(d) = \sqrt[3]{\Delta^3 - d^3}$ if it is the larger of the two (that is, if $d > c\Delta$), since the production is controlled by the faster of the two timescales. To alleviate notations, in the following we write δ instead of $\delta(d)$. The function $F(\Delta,\delta)$ needs to be determined and arises from flux conservation. Equating equation (9.1), with equation (9.10) (flux conservation) gives an interpretation of $F(\Delta,\delta)$

$$f(\Delta,d)\kappa(\Delta) = \frac{F(\Delta,\delta)}{T_2(\delta)}. \tag{9.11}$$

Indeed, by integrating the previous equation over the possible child size, and remembering that, by definition $\int_0^\Delta f(\Delta,d)\mathrm{d}d = 1$, we obtain

$$\kappa(\Delta) = \int_0^\Delta \frac{F(\Delta,\delta)}{T_2(\delta)}\mathrm{d}d \tag{9.12}$$

and $F(\Delta,\delta)$ is the weight associated with each breakup frequency $T_2(\delta)^{-1}$. It can also be interpreted as the likelihood of breakup of a bubble of size Δ into a bubble of size δ. As $\delta \ll \Delta$, we expect the physics at the scale of the filament to be independent of the physics at the parent scale. In addition, since there is no characteristic length scale in a turbulent flow, any filament size can be selected. Therefore we assume that the weight associated with each filament radius is independent of δ, $F(\Delta,\delta) \equiv F(\Delta)$. Proving the independence of the weight factor $F(\Delta)$ on δ would require a complete analysis of the filament geometry, which is not accessible with our numerical dataset. Nevertheless, this question will be further addressed in the next chapter (chapter 10) by looking at the filament radius selection in the model geometry of the stagnation point flow. We will work with the assumption that $F(\Delta)$, independent of δ, in the remaining of the theoretical discussion.

For $d < cd_h$, using equation (9.11) into equation (9.2), we split the birth term into two parts, one term taking into account breaking for $d < c\Delta$ (d is the smallest child size) and one for $d > c\Delta$ (d is the largest child size), and we obtain:

$$\frac{\partial\mathcal{N}(d,t)}{\partial t} = \int_{d/c}^{d_0} 2\frac{F(\Delta)}{T_2(d)}\mathcal{N}(\Delta,t)\ \mathrm{d}\Delta + \int_d^{d/c} 2\frac{F(\Delta)}{T_2(\sqrt[3]{\Delta^3-d^3})}\mathcal{N}(\Delta,t)\ \mathrm{d}\Delta - \kappa(d)\mathcal{N}(d,t) \tag{9.13}$$

where d_0 is the largest bubble size in the system. Assuming that bubbles smaller than d_h do not break implies that the second integral and the death term vanish, and that the lower bound of the first integral is d_h. We therefore obtain the evolution equation of the BSD of sub-Hinze bubbles,

$$\frac{\partial \mathcal{N}(d,t)}{\partial t} = \int_{d_h}^{d_0} 2\frac{F(\Delta)}{T_2(d)}\mathcal{N}(\Delta,t)\ \mathrm{d}\Delta. \tag{9.14}$$

Integrating over time, we obtain for $d < cd_h$

$$\mathcal{N}(d,t) = d^{-3/2}\int_0^t I_{\mathcal{N}}(d_0/d_h, s)\mathrm{d}s, \tag{9.15}$$

with,

$$I_{\mathcal{N}}(d_0/d_h,t) = \int_{d_h}^{d_0} 4\sqrt{3}F(\Delta)\left(\frac{\rho}{\gamma}\right)^{-1/2}\mathcal{N}(\Delta,t)\mathrm{d}\Delta. \tag{9.16}$$

The integral $I_{\mathcal{N}}$ does not depend on the child bubble size d, so that the bubble size distribution for $d < cd_h$ follows

$$\mathcal{N}(d,t) \propto d^{-3/2}. \tag{9.17}$$

We predict that the details of the breakup cascade above the Hinze scale and its temporal evolution only affects the total number of sub-Hinze bubbles produced while the scaling exponent $d^{-3/2}$ is not affected and is independent of time.

6 Conclusion: A two steps breakup process

Below breaking waves, BSD exhibits two power-law scalings. For $d > d_h$ [52], the bubble size distribution reads

$$\mathcal{N}(d) = Q\epsilon^{-1/3}d^{-10/3}, \quad \text{for } d > d_h \tag{9.18}$$

where Q is the volume of air injected to the breaking cascade per volume of water per second, and can be evaluated from the breaker geometry and energetics [53, 56, 132]. For $d < d_h$, the bubble size distribution follows a shallower scaling $\mathcal{N}(d) \propto d^{-3/2}$. The prefactor for the sub-Hinze distribution can be evaluated using the continuity of $\mathcal{N}$ at d_h, and reads

$$\mathcal{N}(d) = Q\left(\frac{\mathrm{We}_c}{2}\frac{\gamma}{\rho}\right)^{-11/10}\epsilon^{2/5}d^{-3/2}, \quad \text{for } d < d_h. \tag{9.19}$$

More generally, these two scaling laws arise in dilute environments, where coalescence can be neglected, provided there is a large scale separation between the injection size d_0 and the Kolmogorov-Hinze scale d_h. When $d_0 \gg d_h$, large-scale inertial breakups and small-scale capillary splitting events occur concurrently and each of them result in one power-law scaling for $\mathcal{N}(d)$. As schematized on figure 9.11, the background turbulence sets the geometry of each breakup event over a time $t_c(\Delta)$ and then freezes relative to the capillary time scale [176], over which a cascade of small-scale *splitting events* occur. From this fragmentation sequence results

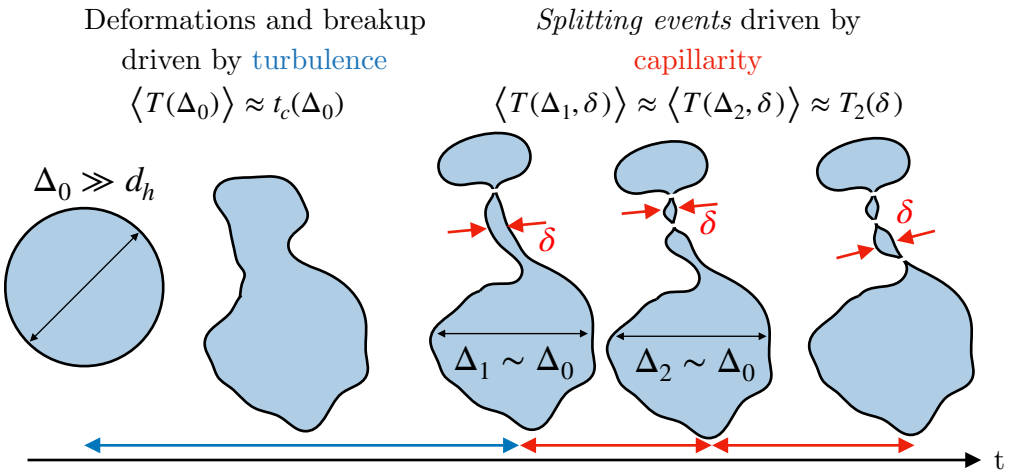

Figure 9.11 – Summary of the fragmentation processes in turbulence: The turbulent background flow deforms large super-Hinze bubbles on a timescale given by $t_c(\Delta)$, creating two large bubbles of sizes comparable with Δ and an elongated structures. The first turbulent breakup is then followed by dozens of *splitting events*, controlled by surface tension at the filament scale δ.

generally one or two large bubbles of similar size and dozens of sub-Hinze bubbles. The large bubbles feed the self-similar cascade of Garrett et al. [73], as schematized by the black arrow in figure 9.12. This self-similar cascade is local in size as large bubbles have sizes similar to the parent size. The cascade stops when the parent size is of the order of d_h. On the other side, the sub-Hinze bubbles feed a non-local, in size, breakup cascade as there is a large scale separation between Δ and δ (red arrow in figure 9.12). This non-local cascade is controlled by capillarity at the filament scale. Gas filaments break through a Rayleigh-Plateau like instability. As dozens of sub-Hinze bubbles are produced during the fragmentation of a gas filament, and are associated with short timescales, the averaged parent lifetime is not given by the turbulent timescale. This fragmentation scenario extends to sub-Hinze bubble production the framework of Villermaux [207], who stated that for liquids, ligaments may universally control fragmentation processes. Contrary to many fragmentation processes in which a physical length scale sets the average fragmentation size, there is no such specific length scale in turbulence, and a power-law distribution is observed instead of a gamma distribution.

We have demonstrated that elongated structures are created during the deformation of large super-Hinze bubbles. Nevertheless, the physical mechanism which selects the length and volume of the filament remain unknown. To fully characterize the sub-Hinze production, in the next chapter, we investigate the filament production in the model flow geometry of the uniaxial straining flow.

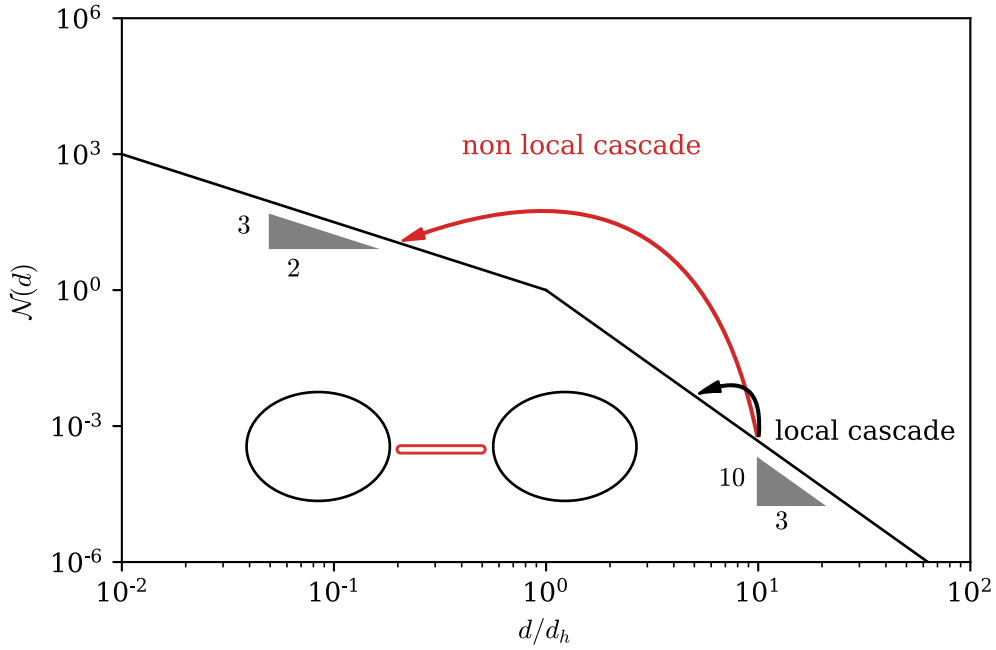

Figure 9.12 – Schematic representation of the bubble size distribution below breaking waves and the associated fluxes between sizes created by breakup. When a bubble breaks, it creates two large child bubbles of size close to its size (black bubbles), and a large number of bubbles smaller than d_h, through the splitting of a filament (in red). The large bubbles feed a local cascade in size generating a $\mathcal{N}(d) \propto d^{-10/3}$ distribution for super-Hinze bubbles. The filament splitting feeds a non-local cascade in size and creates a $\mathcal{N}(d) \propto d^{-3/2}$ distribution of sub-Hinze sizes.

Chapter 10

Filament characterization in a simplified geometry

For once I might be interested.

A PhD advisor

Abstract

In the previous chapter, we identified that sub-Hinze bubbles originate from the fragmentation of gas filaments produced during the deformation of large super-Hinze bubbles. In this chapter, we characterize the size of these filaments in the model geometry of the stagnation point flow. We show that bubbles of size larger but close to the Kolmogorov-Hinze scale are more efficient to feed the sub-Hinze BSD. The larger the initial bubble size, the smaller the child bubbles. We show that viscous effects at the filament scale control the filament volume and that the gas dynamics may control the filament size selection.

Contents

1 Introduction: Filament generation in model geometries

By investigating the breakup dynamics in turbulence, we have identified that sub-Hinze bubbles originate from the fragmentation of long filaments produced during the deformation of super-Hinze bubbles. Despite recent works to identify the bubble topology [42], identifying a filament in the turbulent simulations remains a challenging task. In this context, the model geometry of the uniaxial straining flow provides us with a convenient numerical set-up to investigate the production of gas filaments.

Filament generation in two fluids configuration has been studied extensively. For drops in a fluid of low inertia and viscosity, the filament production has received considerable attention due to its importance for industrial processes like ink-jet printing or fiber spinning [64]. Experimental configurations include jets (reviewed in Eggers et al. [65]), dripping drops [24, 182] and liquid bridges [74, 117]. The interest for bubble pinch-off is more recent and focuses on the neck dynamics. For bubbles, two main configurations are used: a bubble detaching from a needle in an otherwise quiescent flow [21, 26, 77, 191] and a closing open cavity generated by an object pulled through a liquid surface [13, 14, 61]. In the former, bubbles rise under the action of a constant acceleration (gravity). In the latter, the air pocket is produced either with an object moving at constant velocity [13, 14] or falling under gravity [61]. Most studies focus on the neck dynamics close to breakup with the aim of finding critical exponents describing the singularity. Burton et al. [26] investigated the neck dynamics of bubbles rising in a fluid of varying dynamic viscosity. They showed that the critical exponent α, controlling the neck radius r_{neck} evolution in time, $r_{\text{neck}} \sim \tau^{\alpha}$, where $\tau = T - t$ is the time before breakup, undergoes a transition with the liquid viscosity. For a liquid viscosity lower than 10 cP, the pinch-off dynamics results from a balance between capillary forces and inertia, resulting in $\alpha \approx 0.5$. On the other limit, for fluid viscosity larger than 100 cP, viscosity balances surface tension and $\alpha \approx 1$. They also report the production of a long gas thread of constant radius, leading to the formation of a least one gas bubble, for liquid viscosity in the intermediate range where $0.5 < \alpha < 1$. For low viscosity fluid (water), they observed two satellite bubbles of size of the order of 10 μm, believed to originate from a surface instability. Thoroddsen et al. [191] performed a similar study and extended the characterization of the gas filament. Conversely to Burton et al. [26], they found that gas filaments are always produced and that their length increases continuously with the liquid viscosity.

Whereas there is some information on the filament length generation as a function of the liquid viscosity, a quantification of the filament radius is still needed. In turbulence for instance, the filament radius is believed to control the size of the sub-Hinze bubbles generated via filament splitting (chapter 9). In addition, all the studies mentioned earlier, focus on bubble neck dynamics in a quiescent surrounding flow. However, one can expect the flow to modify the filament production and its breaking dynamics via additional compression or stretching for instance, in the presence of an extensional flow. In this chapter, we investigate the effect of uniaxial straining on the production of gas filaments. In particular, we aim at understanding what controls the filament volume in order to quantify the flux from super-Hinze to sub-Hinze sizes in turbulence, as well as the length and radius selection.

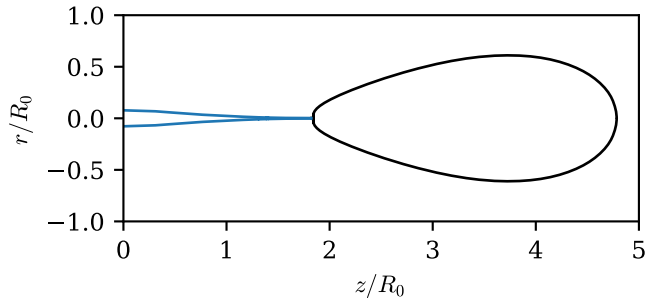

Figure 10.1 – Typical bubble shape at breakup, here for Re = 50 and We = 1250. We call *filament* the blue part, *ie* the air located at the left of pinch-off. The black part is called the *head*.

2 Filament shape

2.1 Numerical set-up and filament definition

We use in this chapter the extensional flow configuration introduced in chapter 2. As detailed in chapter 2, we first generate a uniaxial straining flow at a given flow Reynolds number Re, by varying the typical strain rate E. We then inject a spherical gas bubble, of radius R_0, diameter $d = 2R_0$, centered at the stagnation point flow. The density ratio is $\rho_R = 850$. Conversely to all the previous chapters, we use $\mu_R = 55$, closer to the air-water ratio. We investigate six precursor simulations associated with a Reynolds number at the bubble scale,

$$\mathrm{Re} = \frac{Ed^2}{\nu} \tag{10.1}$$

ranging from 20 to 400. We vary the bubble Weber number

$$\mathrm{We} = \frac{\rho E^2 d^3}{\gamma} \tag{10.2}$$

by varying the surface tension, γ. In this chapter, we focus on breaking bubbles, *i.e.*, bubbles such that $\mathrm{We} > \mathrm{We}_c(\mathrm{Re})$, where, from chapter 5,

$$\mathrm{We}_c(\mathrm{Re}) = \mathrm{We}_c^\infty \exp(-100/(\mathrm{We}_c^\infty\,\mathrm{Re})) \tag{10.3}$$

with $\mathrm{We}_c^\infty = 7.8$ the inviscid critical Weber number.

At all Reynolds and Weber numbers, when the bubble breaks it creates one small satellite bubble and two larger bubbles, of size close to the initial bubble. Indeed, for small but finite gas density, an angle asymmetry in between the two sides of the neck, as demonstrated theoretically by Leppinen et al. [107]. In our numerical study, we impose symmetry with respect to the plane $z = 0$, and simulate only the half-domain $z \geq 0$. As a consequence, we will omit the symmetric domain, and thus the second large child bubble, in the rest of the discussion. By convention, we say that the satellite bubble is at the left of the pinch-off point, while the larger bubble is at the right of the pinch-off point (see figure10.1). The satellite bubble can possibly break into

smaller pieces depending on the value of the Reynolds and Weber number. In this chapter, we use the following convention: we call *filament* the air encapsulated in the first satellite bubble (blue part of figure 10.1), therefore the air which is at the left of the first pinch-off point which will eventually fragment into smaller bubbles.

We first investigate how the filament volume varies with varying Reynolds and Weber number before describing the filament shape at pinch-off.

2.2 Filament volume and consequences for bubbles in turbulence

We have seen in the previous chapter that large bubbles compared to the Kolmogorov-Hinze scale, $d/d_h \gg 1$, produce sub-Hinze bubbles through a non-local breakup mechanism in scales. In practice, satellite bubbles are therefore orders of magnitude smaller than their parent size. However, at this point, we do not know what fraction of air feeds the non-local cascade at each breakup event. To better quantify the volume flux from super-Hinze to sub-Hinze bubbles, we measure the filament volume as a function of the Reynolds and Weber number in the model configuration.

The evolution of the filament volume V_f, in units of the parent volume V_0, with the Weber number is presented on figure 10.2a. The Reynolds number is color-coded. Symbols encode the maximum level of refinement as discussed in chapter 2. At a fixed Reynolds number, we observe that the filament volume increases with We and converges to a constant when $\mathrm{We} \to \infty$. The plateau value dramatically depends on the value of the Reynolds number. Strikingly, the smallest the Reynolds number the largest the filament volume, which varies from $10^{-1}\,V_0$ at $\mathrm{Re} = 20$, to $10^{-5}\,V_0$ at $\mathrm{Re} = 400$. In addition, as We approaches the critical Weber number, we observe that the filament volume decreases. At this stage, we cannot conclude whether a filament of finite size is produced at the critical Weber number or if the bubble breaks on the plane of symmetry. Eggers [63] showed theoretically that predeformed axi-symmetric void cavity in a fluid of low viscosity pinches on the plane of symmetry. Leppinen et al. [107] investigated the case of an inviscid drop pinching in an inviscid fluid for moderate liquid to drop density ratio (including the case of a liquid denser than the drop). The difference in angles between the two sides of pinch-off generates a satellite bubble. These results suggest that at We_c, a finite size tiny satellite bubble is likely to be generated.

By investigating the evolution of the plateau value as a function of Re, we found that $V_f/V_0 \propto \mathrm{Re}^{-3}$ in the limit of infinite Weber number. Figure 10.2b shows the compensated filament volume as a function of $\mathrm{We}/\mathrm{We}_c(\mathrm{Re})$, where $\mathrm{We}_c(\mathrm{Re})$ is defined by equation (10.3). We find that the compensated data follow a single master curve so that the Re^{-3} scaling holds at all Weber number. The Weber number mainly affects the filament volume for $\mathrm{We}/\mathrm{We}_c(\mathrm{Re}) < 10$. We therefore propose the following parametrization for the volume encapsulated in the filament

$$V_f/V_0 = \frac{A}{\mathrm{Re}^3} f(\mathrm{We}/\mathrm{We}_c) \tag{10.4}$$

where A is a numerical constant and $f(x)$ an unknown function such that $\lim_{x\to\infty} f(x) = 1$, which quantifies the impact of the Weber number. Assuming, for simplicity, that at the critical Weber number, bubbles break on the plane of symmetry, we also impose $f(1) = 0$. To fix the

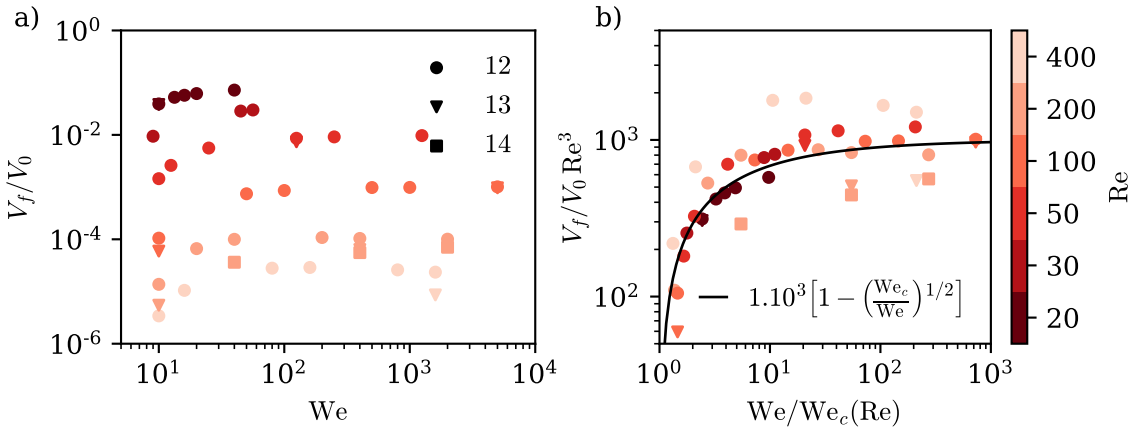

Figure 10.2 – a) Filament volume V_f in unit of the initial bubble volume V_0, as a function of the Weber number. The Reynolds number is color-coded. Different symbols encode different maximum level of refinements. b) Compensated filament volume V_f/V_0 Re^3 as a function of $\mathrm{We}/\mathrm{We}_c(\mathrm{Re})$. The expression of $\mathrm{We}_c(\mathrm{Re})$, derived in chapter 5, is recalled in equation (10.3). The solid black line is an empirical law which reasonably describes our data set.

ideas, in the following of the discussion, we use $f(x) = 1 - x^{-1/2}$ and $A = 10^3$. Using these expressions for f and A equation (10.4) reasonably describes our data set, as illustrated by the solid black line in figure 10.2. Complementary studies need to be performed in order to better quantify f, in particular close to We_c. A qualitative explanation for the $\mathrm{We}^{-1/2}$ might be found in Vincent et al. [210]. Vincent et al. [210] investigated the breakup of an axisymmetric liquid column of low viscosity, driven at constant velocity in a capillary bridge experiment. They argue that the typical wavelength of the wave travelling at the imposed velocity sets the length, an henceforth the mass m, of the remnant drop, the liquid mass which stays attached to the support. Equating the phase velocity of this capillary wave with the driving velocity predicts $m \propto \mathrm{We}^{-1/2}$, also observed experimentally. A theoretical derivation supporting this argument can also be found in Duchemin et al. [60]. Applying the same reasoning to the bubble predicts that the filament volume should scale as $\mathrm{We}^{-1/2}$.

In a turbulent flow, for a given pair of gas and liquid, we cannot vary independently the bubble Reynolds and Weber numbers. Consequently, it is instructive to investigate the evolution of the filament volume as a function of d/d_h and the turbulent properties, predicted by equation (10.4). Assuming we can replace the expression of Re, We and We_c with their turbulent counterpart $\mathrm{Re}_t = \sqrt{2}\epsilon^{1/3}d^{4/3}/\nu$, $\mathrm{We}_t = 2\rho\epsilon^{2/3}d^{5/3}/\gamma$ and We_c^t, we have $\mathrm{We}_t/\mathrm{We}_c^t = (d/d_h)^{5/3}$, where $d_h = (\mathrm{We}_c^t/2)^{3/5}(\gamma/\rho)^{3/5}\epsilon^{-2/5}$. We define $V_h = \pi/6 d_h^3$ the Kolmogorov-Hinze volume, the volume of a bubble of diameter the Kolmogorov-Hinze size. By multiplying equation (10.4) by d^3/d_h^3 we obtain the following expression for the filament volume in unit of V_h as a function of the scale separation d/d_h and the Reynolds number

$$V_f/V_h = \frac{A}{\mathrm{Re}_t^3}\frac{d^3}{d_h^3} f((d/d_h)^{5/3}) = \frac{A}{2^{3/2}}\frac{\nu^3}{\epsilon d_h^3}\frac{1}{d} f((d/d_h)^{5/3}). \tag{10.5}$$

In agreement with the previous discussion, we find that the filament volume increases as the

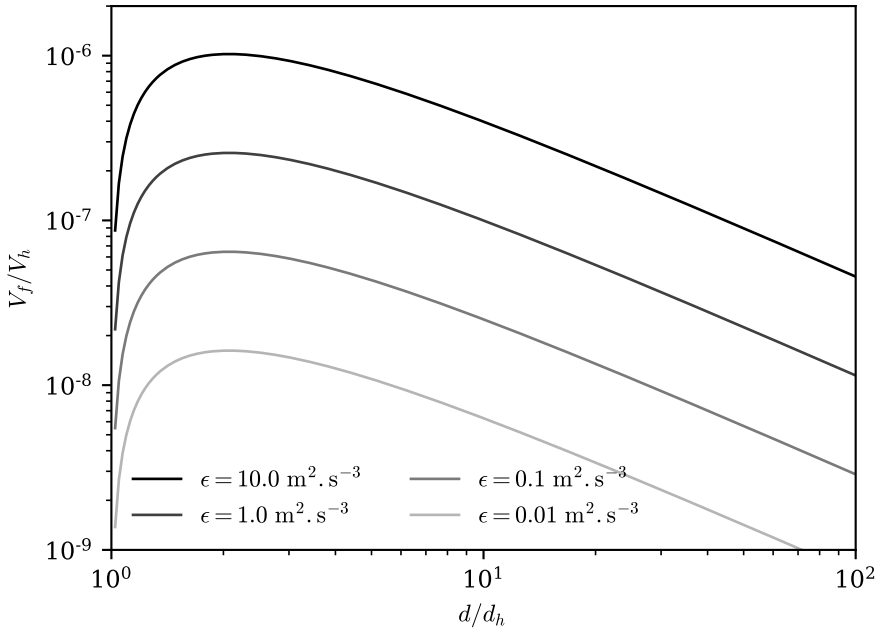

Figure 10.3 – Evolution of the filament volume in unit of the Kolmogorov-Hinze volume, predicted by equation (10.5) as a function of the scale separation d/d_h, for an air bubble in water. Different colors indicate different turbulence intensity ϵ. To estimate V_f, we take $\mathrm{We}_c = 3$.

liquid viscosity increases.

Figure 10.3 illustrates the evolution of the filament volume for an air bubble in water ($\rho = 1000$ kg.m^{-3}, $\gamma = 72$ mN.m^{-1}, $\mu = 1.10^{-3}$ N.s.m^{-2} and $\mathrm{We}_c = 3$), as a function of the scale separation d/d_h, for different turbulent intensity ϵ. Importantly, at a given scale separation d/d_h, we find that the filament volume increases with ϵ. Mathematically, as $d_h \propto \epsilon^{-2/5}$, expression (10.5) predicts that $V_f/V_h \propto \epsilon^{1/5}$. Physically, increasing the turbulence intensity decreases the Kolmogorov-Hinze scale. It follows that viscous effects close to d_h become more important as quantified by the Reynolds number at the Kolmogorov-Hinze scale $\mathrm{Re}(d_h) \sim \rho^{1/5}\gamma^{4/3}/(\epsilon^{1/5}\mu)$. We indeed find that $\mathrm{Re}(d_h)$ decreases when ϵ increases.

At large scale separation, $d/d_h \gg 1$, since $f \sim 1$, V_f/V_h decreases with the bubble size following d^{-1}. In terms of volume flux from super-Hinze bubbles to sub-Hinze bubbles, it follows that the largest the initial bubble size, the smallest its contribution to the volume feeding the sub-Hinze distribution and the smallest the child bubbles produced.

When $d \to d_h$, the filament volume also decreases as f converges to 0. From these two results, it follows that there exist an optimum bubble size, at which the filament volume is the largest. The position of this optimum depends on the exact expression of f. We conclude that most of the air volume transferred to the sub-Hinze BSD originates from the breaking of bubbles of size lying between d_h and approximately $10d_h$.

2.3 Filament shape

In order to understand the origin of the Re^{-3} scaling for the filament volume we focus on the filament shape at very large Weber number. Figure 10.4 shows the bubble shape at the

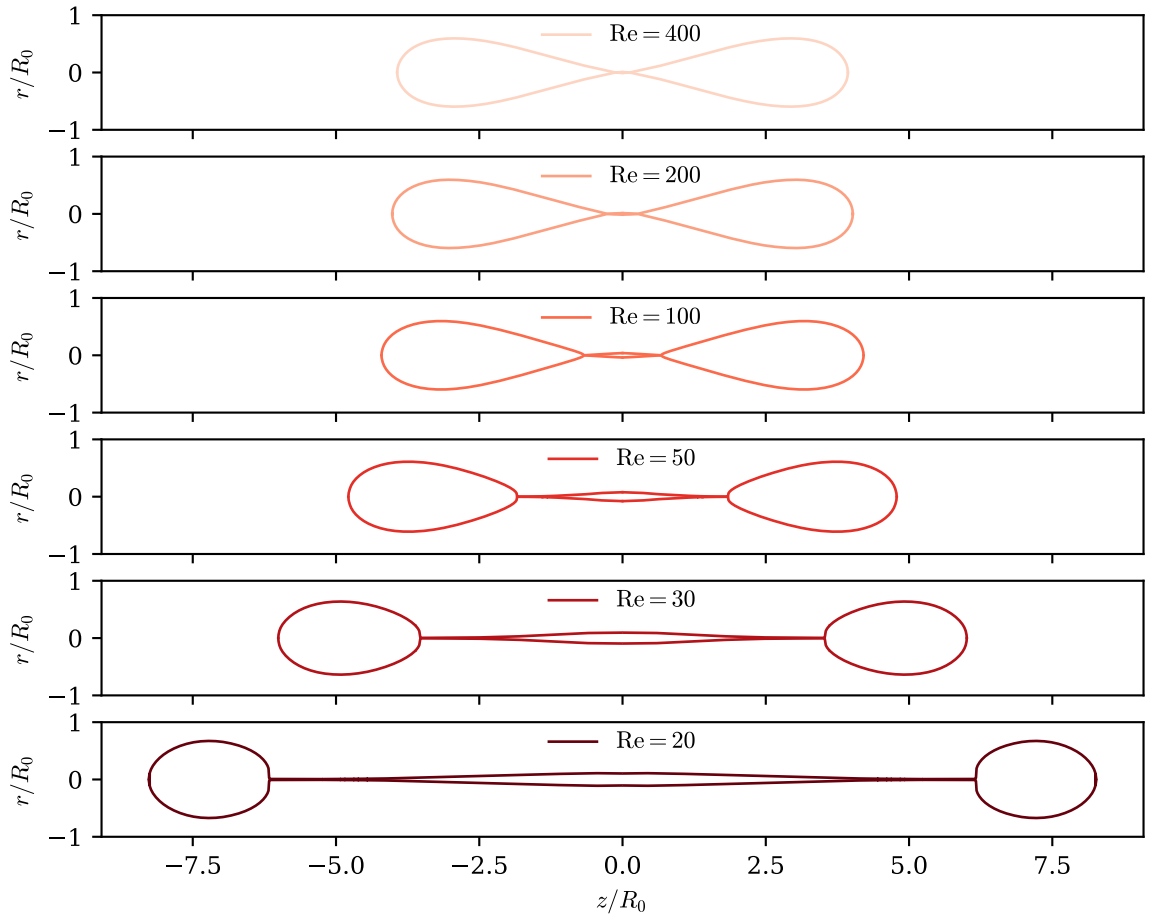

Figure 10.4 – Evolution of the bubble shape at pinch-off with the Reynolds number, in the limit of very large Weber number.

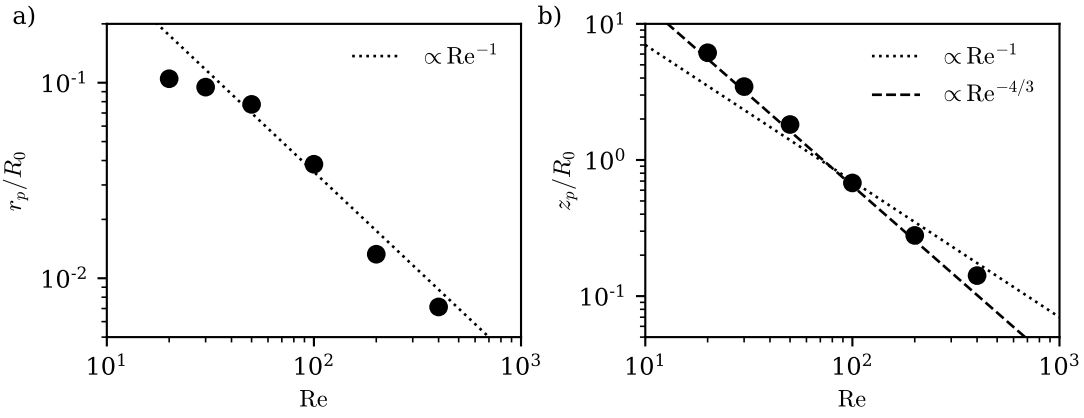

Figure 10.5 – a) Evolution of the filament radius r_p in units of R_0 as a function of the Reynolds number, in the limit of very large We. b) Evolution of the length of the filament, given by the pinch-off position z_p as a function of the Reynolds number, in the limit of very large We.

pinch-off time as a function of the Reynolds number, in the limit of very large Weber number. We observe that, as Re decreases, the filament elongates dramatically, in qualitative agreement with bubble pinch-off experiments [26, 191]. The length varies from about $10^{-1}\,R_0$ at $\mathrm{Re} = 400$ to approximately $10\,R_0$ at $\mathrm{Re} = 20$. The radius on the plane of symmetry, r_p, is also a decreasing function of the Reynolds number. Lastly, the large bubble shape varies close to the pinch-off point. We find a pointy shape at large Reynolds number and a round shape when Re decreases. At low Reynolds number, the slow breakup dynamics allows the main bubble shape to relax before pinch-off.

As a first approximation, one can model the filament shape as a combination of two cones of basis radius r_p, and height z_p, the position of the pinch-off. The filament volume will then scale as $r_p^2 z_p$.

Figure 10.5 shows the evolution of the radius on the plane of symmetry r_p and the pinch-off position z_p as a function of Re in the limit of large We.

The filament radius r_p is found to decrease as $1/\mathrm{Re}$ (figure 10.5a). A similar tendency has been observed experimentally by Mikami et al. [128] for a drop of liquid suspended in a viscous plane hyperbolic flow. For an iso-dense drop of dynamic viscosity 15 times smaller than the surrounding fluid, they also found that the filament radius at breakup decreases with increasing straining rate E. Pulling faster creates thinner filaments. At large Reynolds number, $\mathrm{Re} \geq 100$, the evolution of z_p is compatible with Re^{-1} which corroborate the Re^{-3} scaling for the filament volume. For $\mathrm{Re} \leq 10$, z_p exhibits a steeper scaling and follows $\mathrm{Re}^{-4/3}$. Indeed, as can be visualized on figure 10.4, for the three lowest Reynolds number, there is a very thin thread of gas produced close to the pinch-off point, so that the cone approximation breaks down. Kowalewski [98] investigated the liquid fragmentation of a viscous fluid in a liquid jet experiment. Together with the presence of the filament, which he called *macro-thread*, he also reported the existence of *micro-thread*, of micrometric radius, close to pinch-off. The length of this micro thread is found to increase with decreasing Reynolds number. Similar structures were found experimentally by Shi et al. [182] for viscous drops falling under the action of gravity. They found that the process can repeat itself until breakup, leading to the formation of a cascade of thin threads of decreasing radius. For these very small structures, the gas dynamics is likely to play a role and is therefore visible only for the lowest Reynolds number in our simulations. The volume encapsulated in these thin threads is however negligible compared to the cone part, which results in a Re^{-3} scaling for the filament volume.

3 Deformation dynamics

In the previous section, we have shown that the filament volume evolves as Re^{-3} in the limit of very large Weber number. This scaling can be understood by looking at the filament radius r_p and length z_p. In this section, we aim at understanding when and how the filament radius and length are selected.

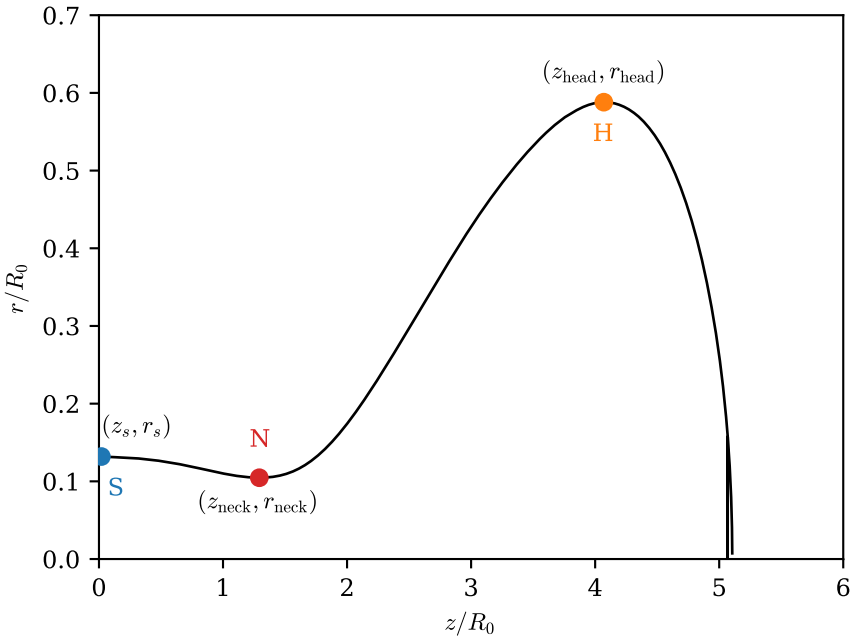

Figure 10.6 – Definition of the three points of interest: S, the radius on the plane of symmetry (blue point), N, the neck position (red point) and H, the position of the head (orange point).

3.1 Characterization of the filament formation

To describe the shape evolution we follow the temporal evolution of three characteristic points represented on figure 10.6:

- S: The interface position on the plane of symmetry, of coordinates (z_s, r_s), with $z_s = 0$ by definition (blue point). The radius r_s coincides with r_p at pinch-off.
- H: The head position, of coordinate $(z_{\text{head}}, r_{\text{head}})$ (orange point). We define it as the point where the radius is maximum.
- N: The neck position, of coordinate $(z_{\text{neck}}, r_{\text{neck}})$ (red point). The neck corresponds to the smallest radius position lying between $z_s = 0$ and z_{head}. At pinch-off, we have $r_{\text{neck}} = 0$ and $z_{\text{neck}} = z_p$.

In each simulation, we follow the position of S, H and N in time to understand when the filament is created. Figure 10.7 shows one example of the temporal evolution of r_s, r_{neck} and r_{head}, for one simulation at $\text{Re} = 50$ and $\text{We} = 25$. We define $\tau = T - t$, the time interval before pinch-off, so that time goes from right to left on figure 10.7.

In the early dynamics, the three points coincide, and are located on the plane of symmetry. Their radius decreases linearly in time. Indeed, at short times, the interface is purely advected by the stagnation point flow at a rate given by the flow shear rate in the radial direction $|E|/2$.

At C_1, corresponding to $E\tau \approx 0.5$ (red triangle) the head position jumps from the axis to a finite position $z_{\text{head}} > 0$. This the head formation. It conserves the same radius until pinch-off. At this stage, N and S share the same position: N is on the plane of symmetry.

From C_1 to $E\tau \approx 0.1$, r_s and r_{neck} keep decreasing linearly in time. At $Et \approx 0.1$ their decrease accelerates.

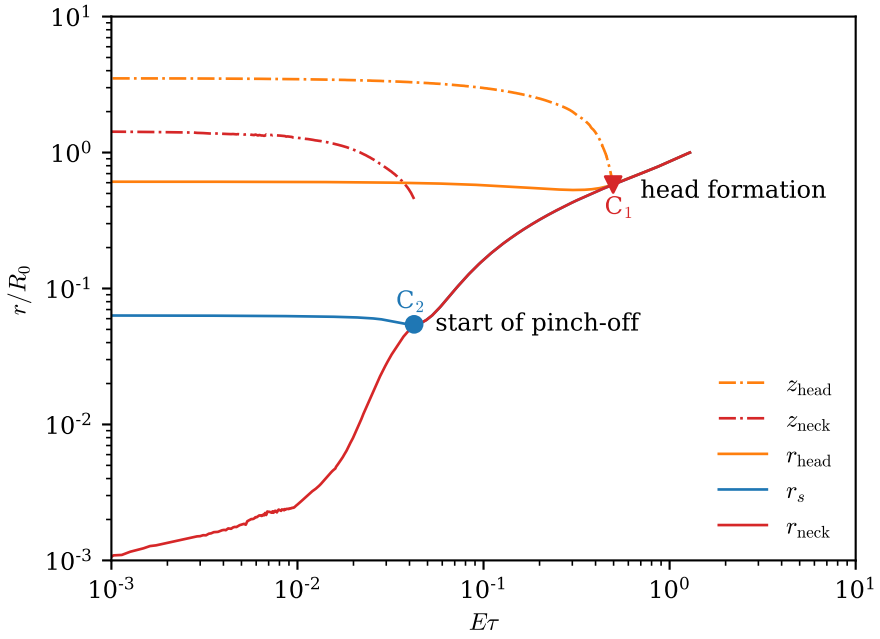

Figure 10.7 – Typical temporal evolution of the three points of interest as a function of the time interval before pinch-off τ, in units of the advective timescale $1/E$, for Re = 50 and We = 25. The red triangle corresponds to the time at which the head forms: the position of the head z_{head} jumps to a finite value and r_{head} is constant. The blue circle denotes the beginning of the pinch-off dynamics: the neck position jumps to a finite value $z_{\text{neck}} > 0$ and r_s is now constant.

At C_2, which we call the *critical point*, corresponding to $E\tau = 4.10^{-2}$ (blue circle), the neck position jumps from the axis to $z_{\text{neck}} > 0$. Similarly to the head dynamics, from this point, r_s freezes. This radius corresponds to the filament radius r_p at pinch-off. The separation between r_s and r_{neck} marks the beginning of the pinch-off dynamics. At this stage, the filament volume is selected. The filament becomes unstable under Rayleigh-Plateau instability. The position of pinch-off might results from a competition between the growth rate of the capillary instability and the filament stretching by the flow. This competition would explain why the pinch-off position exhibits a steeper dependency that Re^{-1} (figure 10.5), while modifying marginally the filament volume. This mechanism is analogous to the formation of the Pele's hair described by Villermaux [206]. Hot filaments are stretched by violent air flows. When stretching is fast compared to the capillary instability, long hair are produced.

From the previous dynamics we identify three phases in bubble deformations, illustrated on figure 10.8 by the deformations of a bubble at Re = 50 and We = 25.

From the beginning of the simulation, to C_1, the bubble shape is concave and evolves due to an advection of its interface by the surrounding flow. The bubble shape associated with C_1 is represented in red on figure 10.8. When the head forms, the bubble shape is close to a cylinder.

In the second phase, the head, of constant radius, is advected by the flow while the bubble shrinks on the axis of symmetry (grey curve in figure 10.8). At C_2, the critical point, the air filament is selected (blue shape in figure 10.8). One can clearly separate what will be contained in the filament (cylinder of radius $r_s \approx 0.05\,R_0$ and length $z_{\text{neck}} \approx 0.6\,R_0$) from the head.

The last stage corresponds to the pinch-off dynamics. In the example presented in figure 10.8,

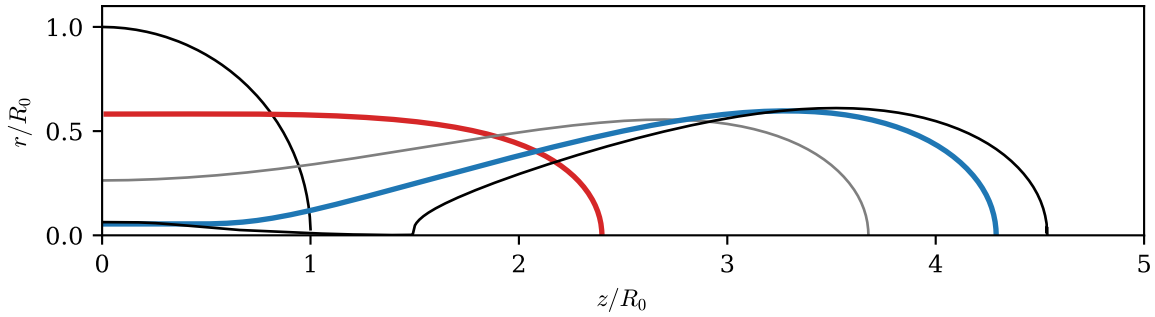

Figure 10.8 – Typical shape evolution, illustrated at Re = 50 and We = 25. The initially spherical bubble deforms in a succession of concave shape until the head forms. The red shape corresponds to the position of C_1 in figure 10.7. The bubble then shrinks on the plane of symmetry, until pinch-off starts (blue curve, corresponding to the position of C_2 in figure 10.7). The last black shape is the shape at breakup.

as the Reynolds number is low, the pinch-off dynamics creates a thin thread of air and the final length of the filament, $z_p \approx 1.5\,R_0$, is significantly longer than $0.6\,R_0$, the initial filament length selected at the critical point. However, when the Reynolds number is larger (Re $\geq$ 50), the pinch-off dynamics is fast and the two lengths are comparable. Note that the filament shape, for $z < 0.6\,R_0$ does not change between the critical point and pinch-off. The left part of the filament is frozen during this stage.

3.2 Filament volume selection by viscous effects

In the previous section, we have shown that the volume selection happens at C_2 when S and N separate. The radius r_s, and position z_{neck} at the critical point control the filament volume. We denote these two values by $r_s^\star$ and $z_{\text{neck}}^\star$ respectively. We now investigate the dynamics of r_s as a function of Re and We to understand the origin of C_2.

Figure 10.9a shows the temporal evolution of r_s in all the simulations performed at different Weber numbers (color) and Reynolds number (color of the circle point) as a function of time, in units of the advective timescale $1/E$. The end of each curve indicates the breakup time. For each curve, we denote by a colored circle the position of the critical point C_2. At short times, for $Et \leq 0.25$, all curves superimpose on the prediction given by a pure advection of the interface (dotted black line): assuming $\dot{r}_s = u_r(r_s) = -\frac{E}{2}\,r_s$ we have

$$r_s(t) = R_0 \exp\left(-\frac{E}{2}t\right), \tag{10.6}$$

which simplifies into

$$r_s(t) \approx R_0\left(1 - \frac{E}{2}\,t\right) \quad \text{for} \quad t \ll \frac{2}{E}. \tag{10.7}$$

The linearized solution is shown by the solid black line in figure 10.9. At latter times, we observe a clear ordering of the curves with We, no matter the value of the Reynolds number. Bubbles at large Weber number (in red) break faster than bubbles of lower Weber number (green curves), irrespective of their Reynolds number. In the limit of infinite Weber number, the bubble lifetime

is given by the advective time scale $1/E$. This is the time necessary to advect the bubble on a distance R_0 along the z axis.

On the contrary, the filament radius $r_s^\star$ is mainly controlled by the Reynolds number and scales as Re^{-1}, as can be visualized on figure 10.9b, which represents the compensated radius $r_s^\star/R_0\,.\,\mathrm{Re}$ as a function of the Weber number. In this range of Weber numbers, we find no dependency of $r_s^\star$ with We and we can approximate $r_s^\star$ by

$$r_s^\star/R_0 = \frac{3}{\mathrm{Re}}. \tag{10.8}$$

Qualitatively, on the plane of symmetry, the outside pressure, scaling as ρU^2, with U a characteristic velocity, is balanced by the normal stress in the fluid. As the radius is small, the inside stress is viscous and scales as $(\mu/\mu_R)\,U/r_s^\star$. At $r_s^\star$ we thus have

$$r_s^\star \sim \frac{\mu}{\mu_R}.\frac{1}{\rho U}. \tag{10.9}$$

Assuming that the characteristic velocity is defined by the bubble scale, $U = Ed$, and dividing by R_0, we get

$$r_s^\star/R_0 \sim \frac{1}{\mu_R}.\frac{1}{\mathrm{Re}}. \tag{10.10}$$

The filament radius corresponds to the scale at which viscous effects dominate over inertia, at the filament scale. This scaling argument also predicts that increasing the gas dynamic viscosity increases the filament radius.

To discriminate between the influence of inertia and viscosity within the gas, in parallel of this study, we run two simulations varying the density and viscosity ratios respectively, while keeping the bubble Reynolds and Weber number constant, $\mathrm{Re} = 50$ and $\mathrm{We} = 125$. We therefore only change the gas properties. The results are summarized in table 10.1.

When the density ratio is divided by approximately 5 ($850/200 = 4.25$), *i.e.* when the gas is about 5 times denser, we observe a moderate increase of the filament volume compared to the reference case. The volume is multiplied by two, while r_p increases by 30%. Note that $\sqrt{4.25} = 2.06$, suggesting that the filament volume scales as ${\rho_R}^{-1/2}$. We also have that $4.25^{1/6} = 1.27$. This scaling suggests that r_p follows $\rho_R^{-1/6}$. Experimentally, Thoroddsen et al. [191] investigated the effect of the density ratio of the neck dynamics of a rising bubble in water. They compared three gases, Helium, air and SF6, therefore changing the gas density, and consequently the density ratio, by a factor 37, while keeping the liquid to gas density ratio greater than 161. They found only little differences in the neck dynamics for these three gases. They concluded that the gas density has minimal effect on the bubble shape at pinch-off in agreement with our results.

We observe a dramatic increase of the filament volume when dividing the dynamic viscosity ratio by approximately 5 ($55/10 = 5.5$), *i.e.* when increasing the gas dynamic viscosity. The filament volume is multiplied by 21.6 while r_p increases by a factor 2.3. Note that $\sqrt{5.5} = 2.3$, the change in filament radius. This result suggests that the filament radius is selected by viscous effects occurring in the gas filament and that r_p scales as ${\mu_R}^{-1/2}$. The negative power of μ_R is in agreement with the previous reasoning on stress balances. However, the power law

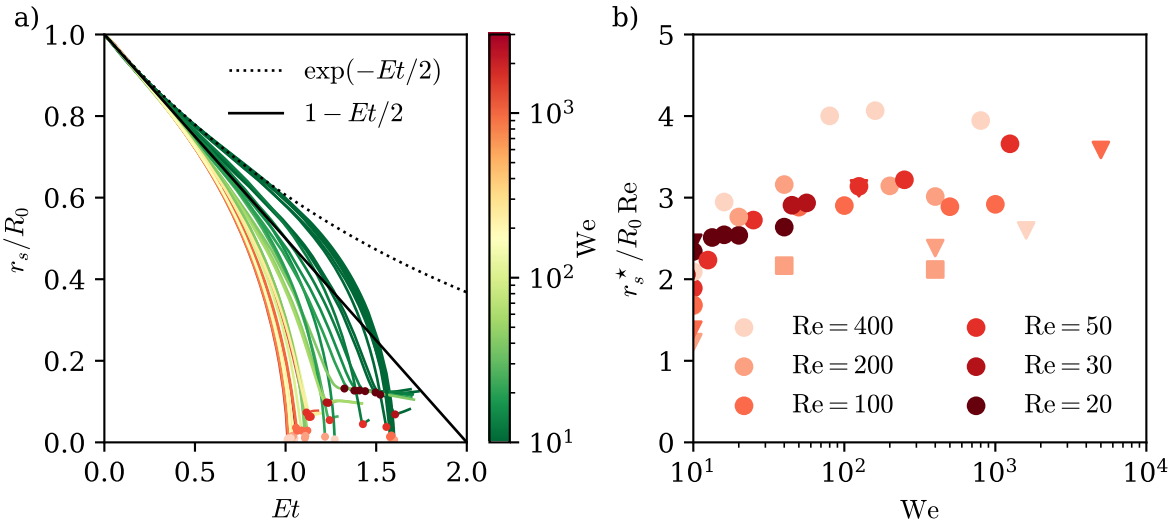

Figure 10.9 – a) Temporal evolution of r_s in all simulations, for various Re and We. The black line is the prediction given by the interface advection. The Weber number is color-coded and trajectories clearly order according to its value. Points indicate the position and time at which the pinch-off dynamics starts. b) Compensated radius $r_s^\star/R_0$ Re as a function of the Weber number. The Reynolds number is color-coded. Symbols indicate the maximum level of refinement (see figure 10.2). We find no dependency with We.

differs from equation (10.10), suggesting that the filament selection is more complex. Additional investigations need to be performed.

Case	We	Re	μ_R	ρ_R	V_f/V_0	V_f/V_f^{ref}	r_p/R_0	r_p/r_p^{ref}
reference	125	50	55	850	$8.61\,10^{-3}$	-	$7.12\,10^{-2}$	-
dense bubble	125	50	55	200	$1.79\,10^{-2}$	2.08	$9.26\,10^{-2}$	1.3
viscous bubble	125	50	10	850	$1.86\,10^{-1}$	21.6	$1.66\,10^{-1}$	2.3

Table 10.1 – Evolution of the filament volume and radius with μ_R and ρ_R. All simulations are performed at the same We and Re. We denote by V_f^{ref} and r_p^{ref} the filament volume and radius respectively obtained in the reference simulation.

We conclude that the filament volume is controlled by viscous dissipation occurring at the filament scale and that the gas dynamics cannot be neglected when describing the filament formation. However, at this stage, we have no argument to support the Re^{-3} scaling of the filament volume, nor the $\mu_R^{-1/2}$ dependency of the radius.

3.3 Head shape

If the filament shape dramatically depends on viscous effects, this is not the case of the head shape.

Figure 10.10 compares the critical shapes obtained for different Reynolds numbers, in the limit of very large Weber number. To compare the head shapes, for each Reynolds number, we have shifted the z-origin so that the positions of the rightest point on the head z_r coincide. Note that, on figure 10.10, the axis do not share the same scale and that bubbles do have the same

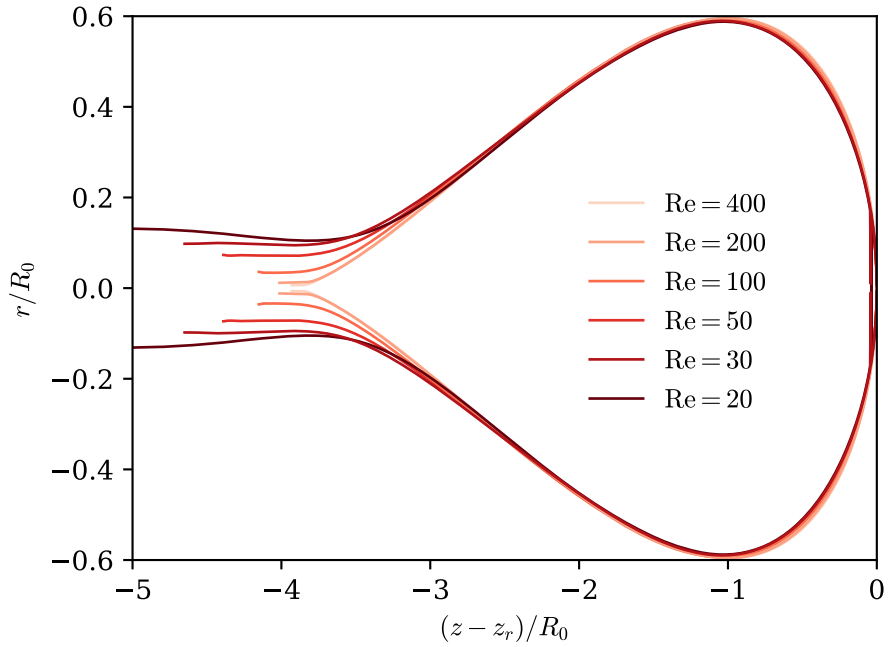

Figure 10.10 – Critical profiles as a function of the Reynolds number, obtained in the limit of very large Weber number. The shapes are shifted to the left so that their rightest point coincide. While the filament shape and volume dramatically depend on Re, the head is nearly identical. Note that axis do not share the same scale and that all bubbles do share the same volume.

volume. As emphasized previously, we observe a clear dependency of the filament radius and length with the Reynolds number. However, the shape of the head only weakly depends on Re. In particular, we find no dependency on the apparent angle of the left part of the head with Re. This observation corroborates the remark made on figure 10.4: the different head shapes, and apparent angles observed at pinch-off originate from the comparison between the breakup time and the bubble relaxation time. When bubble relaxation is fast compared to the breakup time, the bubble adopts a round shape at breakup (low Reynolds number limit), while a cone-like shape is observed when breakup is fast (larger Reynolds number).

From these shapes, we conclude that the head shape, which controls the volume of the large child bubble, is driven by inertial effects at the head scale. However, the filament generation and shape is controlled by viscous effects at its scale. Note that, if capillarity does not control the volume and shape of the filament, it will control the filament fragmentation.

4 Conclusion: A non-local cascade

To summarize, we investigated the filament production for a bubble immersed in a uniaxial straining flow. We find that the bubble Reynolds number controls the volume encapsulated in the ligament, which scales as Re^{-3}, while the Weber number has only a marginal effect for $\mathrm{We} \geq 50$. We characterized bubble deformations and found that the filament volume is selected at the time at which the radius on the axis of symmetry stops to decrease. At this specific time, the bubble shape exhibits a thin cylinder of gas close to the plane of symmetry. The

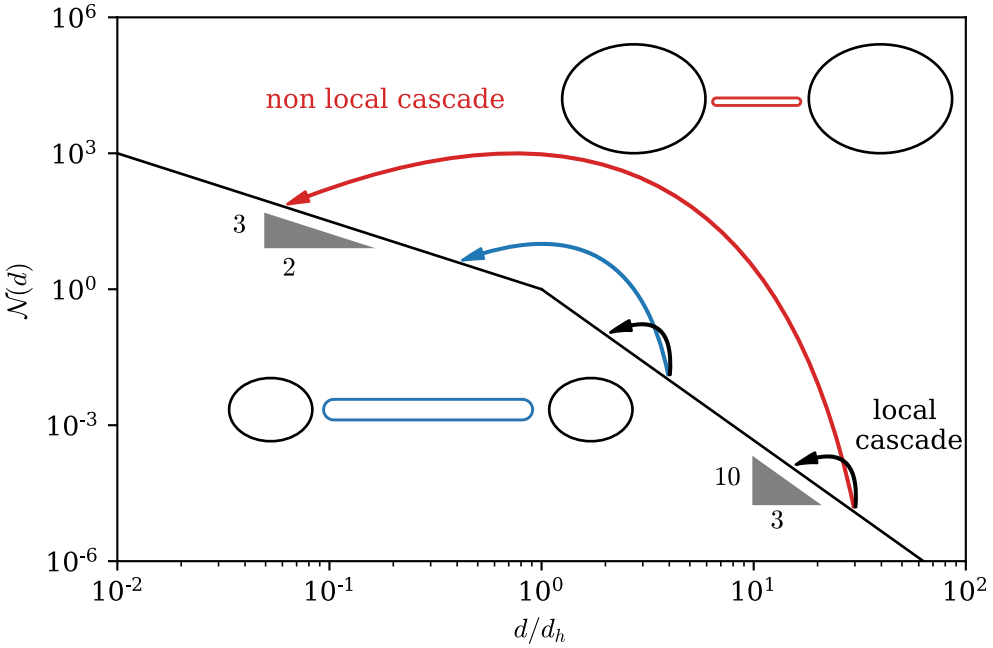

Figure 10.11 – Schematic representation of the fluxes induced by breakup depending on the parent size d/d_h, on the BSD measured below breaking waves. When a bubble breaks, it creates two large bubbles (in black), feeding a local cascade. It also produces a filament, whose size largely depends on d/d_h. The largest bubbles produce the smallest filament and therefore the smallest child bubbles.

radius and length of this filament both scale as $1/\mathrm{Re}$ which decompose the origin of the Re^{-3} dependency for the filament volume into two simpler quantities. At the critical point, the head shape however is only weakly affected by the value of the Reynolds number.

At this point, we have no clear explanation for the selection of the filament shape. However, our analysis suggests that the gas dynamics, driven by viscosity, is probably not negligible. The Reynolds number at the filament scale being of order unity, we also expect viscous effects at the filament scale to drive the dynamics.

The model geometry informs us on the generation of sub-Hinze bubbles in turbulence. First, we find that the largest the initial scale separation between the bubble size and the Kolmogorov Hinze scale, d/d_h, the smallest the filament volume, as schematized on figure 10.11. In terms of volume, the largest amount of sub-Hinze bubbles originate from the fragmentation of bubbles of size close to d_h. It follows that most of the volume flux from super-Hinze to sub-Hinze bubbles, comes from bubbles of turbulence Weber number $\mathrm{We}^t \leq 50$. Second, in agreement with the previous chapter, we recover that the filament selection is a local phenomenon: its radius and length are controlled by viscosity at the filament scale.

In this chapter, we identified that the largest volume flux from the super-Hinze to the sub-Hinze distribution originate from bubbles at moderate Reynolds number. In the next chapter, we focus on the fragmentation dynamics of a single filament at moderate Reynolds number, to investigate the origin of the sub-Hinze distribution.

Chapter 11

Filament fragmentation

There is not a single surprising finding in the paper.

A reviewer

Abstract

In this chapter, we focus on the splitting of a gas filament in the model configuration of the stagnation point flow. We show that a single sequence of filament splitting is sufficient to produce a $\mathcal{N}(d) \propto d^{-3/2}$, independently on the value of the Reynolds and Weber number. We conclude that the sub-Hinze bubble size distribution comes from the fragmentation of filaments, all creating a distribution following $d^{-3/2}$. Eventually, we discuss the shape of the breakup kernel and the relative contribution of different parent bubble sizes.

Contents

1 Introduction

We have shown in chapter 9 that we can decompose each sequence of correlated breakups into two stages: first, deformations by turbulence creating two large bubbles of similar size and a filaments. The duration of this phase is given by the correlation time of turbulence at the mother scale. Second, a rapid succession of splitting events within the filament, creating a large number of sub-Hinze bubbles. We showed that the timescale of filament splitting is controlled by capillarity at the filament scale. However, at this point, the bubble size distribution generated by the fragmentation of a single filament is still unknown. For a single pinch-off event, Ruth et al. [176] investigated experimentally the neck dynamics of bubbles in turbulence. They showed that turbulence freezes relative to the capillary pinch-off and that the final neck dynamics is universal, independent of the initial bubble shape and turbulent state. These results suggest that the splitting dynamics of a single filament in turbulence may be independent of the flow configuration which has generated it. Building on this idea, in this chapter, we aim at characterizing the filament fragmentation and the bubble size distribution it produces in the model flow configuration, hopping for a universal behavior.

The fragmentation of liquid ligaments has received a considerable amount of attention over the last decades, owing to its important consequences for industrial applications [205, 207]. Understanding the drop size distribution originating from the ligament destabilization is key for instance in the generation of sprays [208], or jets [65]. In comparison, only a few studies report the fragmentation of gas filaments. To our knowledge, the only study describing the fragmentation of a gas filament is from Thoroddsen et al. [191]. They observed that a bubble detaching from a needle in a viscous quiescent fluid can generate a large number of child bubbles of varying size, depending on the value of the liquid viscosity. No quantification of the bubble size distribution is however reported.

We have shown in the previous chapter, that the largest filaments are produced by the fragmentation of parent bubbles of size close to the Kolmogorov-Hinze scale, due to the importance of viscous effects. We expect sub-Hinze bubbles to predominantly originate from the fragmentation of these large filaments. In this chapter, we therefore restrain ourselves to the fragmentation of bubbles at moderate Reynolds number, $\mathrm{Re} \leq 50$. We use the same numerical set-up as in the previous chapter, with $\mu_R = 55$ and $\rho_R = 850$. We first describe the phenomenology of filament splitting. Then we discuss the corresponding breakup kernel and connect the result with the BSD of sub-Hinze bubbles.

2 A fragmentation cascade

Regardless of the values of the Reynolds and Weber number, we always observe the production of one satellite bubble, whose volume is described in chapter 10. We focus here on the consequent splitting of this small bubble, called filament.

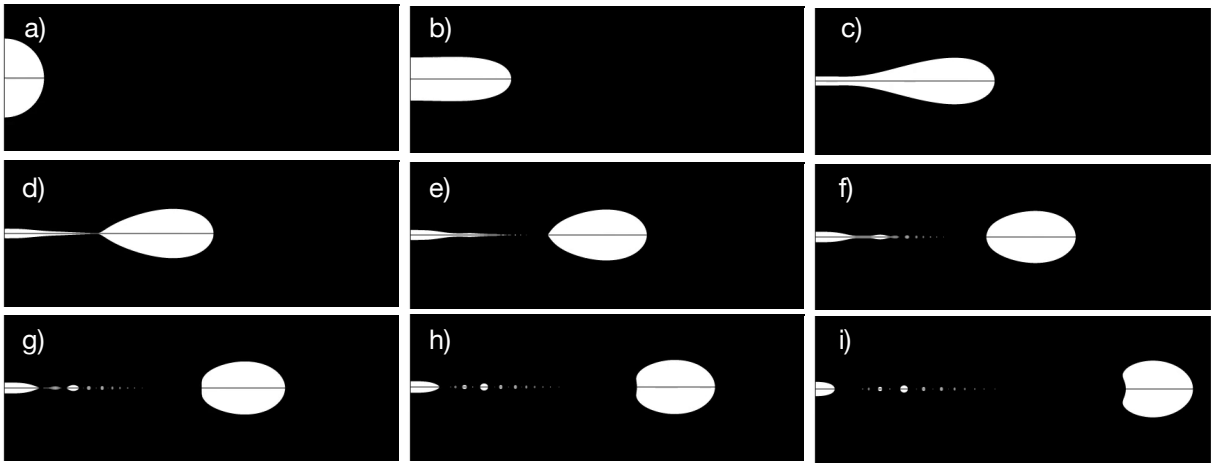

Figure 11.1 – Typical fragmentation cascade of a filament for a simulation at Re = 20, We = 10. The bubble is in white, the liquid in black. The axis of symmetry is the horizontal axis. The flow goes from top and bottom to the right. a) Initial conditions: the bubble is spherical. b) The bubble deforms creating a head. c) Critical point when pinch-off starts. d) Breakup. e-f) A few bubbles are ejected from the tip of the filament while the main satellite bubble deforms. g-h) The satellite bubble breaks, creating new child bubbles. i) All bubbles are advected by the flow.

2.1 Phenomenology

In this section, we illustrate the phenomenology of the filament splitting on one example at Re = 20 and We = 10 but the dynamics is shared among simulations at Re $\leq$ 50 and Weber values. For larger Reynolds number, the filament volume is so small, that the numerical resolution we use is insufficient to resolve the filament fragmentation.

Figure 11.1 shows a typical fragmentation cascade occurring within the filament. The bubble is represented in white and the liquid in black. The axis of symmetry is the horizontal axis. We reconstruct the bottom plane by mirroring the simulation results from top to bottom. Each snapshot is an enlargement, centered around the axis of symmetry of the whole simulation. The initially spherical bubble (snapshot a) deforms under the action of the surrounding straining flow, creating a filament whose shapes is described in chapter 10 (b to c). The critical shape (c), defines the filament volume at the time of breakup (d), $Et \sim 1.75 = ET$. Once the satellite bubble is formed, due to the stretching imposed by the surrounding flow, and the flow generated by the first pinch-off, it continuously deforms. A few very small bubbles are ejected from the tip of the filament (in e), while the main satellite bubble shrinks in its middle. The size of the bubble ejected from the tip increases from right to left, as the filament gets thicker. This spatial distribution of sizes is more visible on figure f. In f, a new filament is also formed, which leads to the formation of new child bubbles (g), which themselves fragment into smaller bubbles (h). In the last snapshots, the snapshot resolution allows us to distinguish 15 child bubbles of very different sizes, but more are probably generated. All the child bubbles are then continuously advected by the surrounding flow field. The whole fragmentation process, from the initial breakup to the last filament splitting, lasts approximately $0.35/E$.

Thoroddsen et al. [191] reported similar breakup cascades for the fragmentation a gas filament

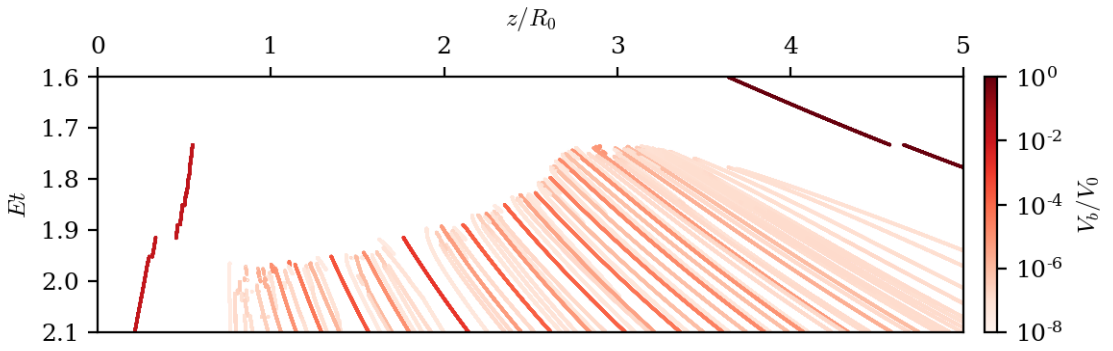

Figure 11.2 – Typical spatio-temporal diagram of the position of the child bubbles as a function of time, for a simulation at $\mathrm{Re} = 20$, $\mathrm{We} = 10$. Each continuous line corresponds to one bubble whose volume is color-coded. Breakups corresponds to line discontinuity. The initial bubble, visible on the top right, breaks at $Et \approx 1.75$. Then, a large number of splitting events follow, leading to a large number of small bubbles. The fragmentation cascade stops at $Et \approx 2$.

generated by the pinch-off of a gas bubble in a viscous liquid. When the liquid viscosity is low, for instance in water, they observed the generation of one satellite bubble of size 5 μm, close to the resolution limit of their optical system. Increasing the liquid viscosity increases the length and radius of the filament, as discussed in chapter 10, and also increases the number of child bubbles generated.

2.2 Splitting dynamics

The fragmentation dynamics is illustrated on figure 11.2 showing the corresponding spatio-temporal diagram of the position of the center of mass of every bubble in time, for the simulation at $\mathrm{Re} = 20$ and $\mathrm{We} = 10$. Every continuous line corresponds to one bubble and its color encodes the bubble volume. The darkest line shows the position of the initial bubble. While the bubble deforms, its center of mass shifts to largest z-values. At $Et \approx 1.75$, (corresponding to 11.1d) the initial bubble breaks, creating a satellite of volume $V_b \approx 10^{-2}\, V_0$. This is the filament, whose center of mass is located at $z \approx 0.5 R_0$. From $Et \approx 1.75$ to $Et \approx 1.9$, dozens of splitting events occur, leading to the formation of a large number of child bubbles (about 45). The rightest ones, of volumes lying between 10^{-6} and $10^{-8}\, V_0$ correspond to the fragmentation of the filament tip. For all the other ones, note the clear alternation of bubbles sizes: in between two larger bubbles, between two and four bubbles smaller bubbles are produced. At $Et \approx 1.9$, the bubble lying on the axis of symmetry breaks, creating the third largest bubble (visible on snapshot 11.1g). Both this bubble and the bubble on the axis of symmetry continue to break until $Et \approx 2$, the end of the fragmentation cascade. In total 68 child bubbles are produced by the filament splitting. On this plot, we observe that every bubble, once formed, drifts to largest values of z due to the presence of the surrounding flow. The drift velocity at a position z is given by the uniaxial straining flow velocity Ez.

The spatio-temporal diagram suggests the existence of a cascade of breakups. After the first breakup, a satellite bubble is produced. This satellite bubble breaks itself creating large fragments and a satellite bubble. Each of these new child bubble can also break, creating large

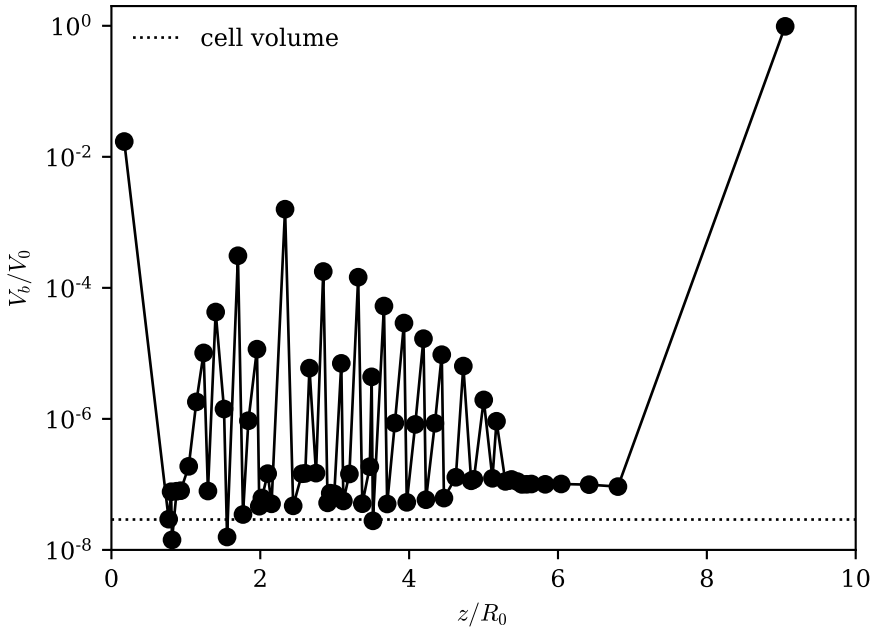

Figure 11.3 – Volume of the child bubbles V_b in units of the initial bubble volume as a function of their position z/R_0, at the end of the fragmentation cascade, for Re = 20 and We = 10. The rightest point corresponds to the largest bubble (the head), while all the other points correspond the bubble produced during the fragmentation of the filaments. Bubbles located between $z = 5R_0$ and $z = 7R_0$ have been ejected at the tip of the filament (figs. 11.1e and 11.1f).

fragments of their size and small satellite bubbles. This breakup cascade results in a peculiar spatial organization of bubble sizes illustrated on figure 11.3. Figure 11.3 shows the final volume of each bubble in units of the initial bubble volume V_b/V_0, as a function of the position of its center of mass z/R_0 at the end of the fragmentation cascade. The points are linked for clarity. The point at $z = 9R_0$, represents the position and volume of the largest bubble of size close to the initial bubble size $V_b \sim V_0$. All the others points, for $z < 7R_0$ correspond to bubbles produced by the filament fragmentation. Bubbles located between $z \approx 5R_0$ and $z \approx 7R_0$, have been produced by the fragmentation of the filament tip illustrated on snapshots 11.1e and 11.1f. For $z < 5R_0$, we recover the size alternation with at minimum one small bubble produced in between two larger bubbles. Consecutive bubbles usually have one decade difference in bubble volume, suggesting that the smaller one, the same splitting mechanism occurred at different bubble scales in a self-similar manner.

2.3 Size distribution generated by filament splitting

For these Reynolds number, Re ≤ 50, each breakup sequence leads to the formation of a large number of child bubbles, between 15 and 70. In order to quantify the size distribution within the filament, we compute the BSD at the end of the fragmentation cascade for each individual simulation. We observe no dependency of the bubble size distribution with the Weber number in the range we consider (We > 10).

Figure 11.4a illustrates the volume distribution obtained for three individual simulations, at

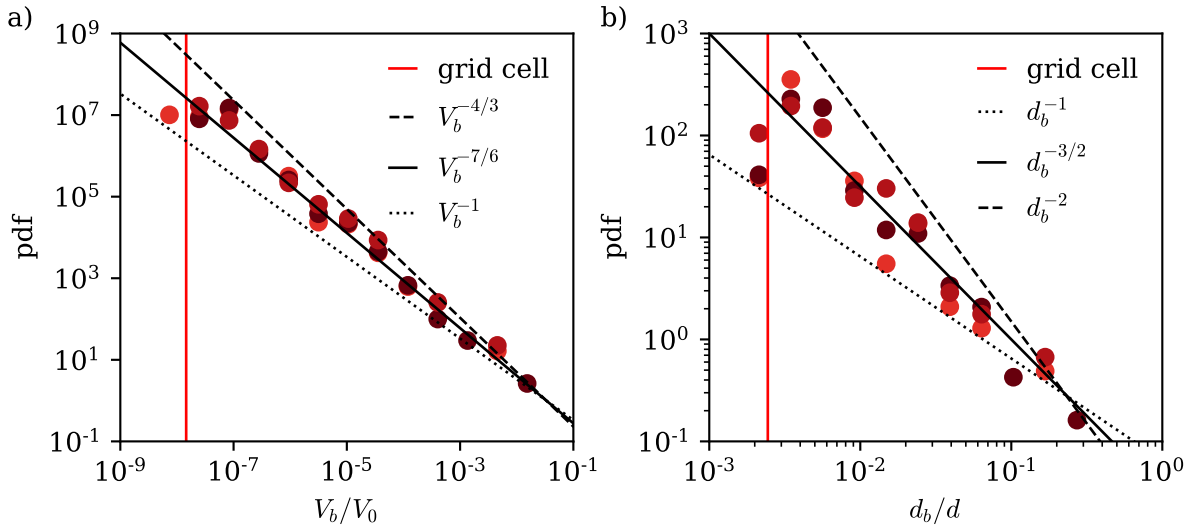

Figure 11.4 – Size distribution of bubbles originating from the filament fragmentation at three different Reynolds number, from the darkest color to the lightest: Re = 20, 30 and 50. Each data set at a given Re corresponds to a single simulation. a) Volume size distribution.The distribution follows $V_b^{-7/6}$ over six decades. b) The corresponding diameter distribution.

Re = 20, 30 and 50, and We = 10 (69 bubbles), We = 9 (27 bubbles) and We = 25 (37 bubbles) respectively. Note that we independently investigated the effect of the Weber number of the size distribution and found no effect on the distribution shape. Colors indicate the Reynolds number. For each individual simulation, we observe that the volume distribution pdf(V), scales as $V_b^{-7/6}$ (solid black line) over a large range of scales (six decades), independently of the value of the Reynolds number. The filament splitting generates a universal power-law size distribution scaling as $V_b^{-7/6}$, independent of both the Reynolds and the Weber number in the range of values we consider.

Importantly, the $V_b^{-7/6}$ scaling corresponds to a diameter distribution pdf(d) scaling as $d^{-3/2}$, shown in figure 11.4b. Indeed, by probability conservation pdf(d) relates to pdf(V) through

$$\text{pdf}(d)\text{d}d = \text{pdf}(V)\text{d}V \tag{11.1}$$

$$\text{pdf}(d)\text{d}d \propto V^{-7/6}d^2\text{d}d \tag{11.2}$$

$$\text{pdf}(d) \propto d^{-3/2}. \tag{11.3}$$

Hence, a single filament splitting is sufficient to build a $-3/2$ distribution of bubble sizes. In turbulence, the sub-Hinze bubble size distribution henceforth originates from the fragmentation of a large number of filaments, all generating their own $-3/2$ BSD. As for the bubble pinch-off, turbulence freezes relative to the filament splitting, which follows a universal dynamics.

Power-law scalings are the signature of a scale-invariant physical process. The length slide of avalanches, the intensity of earthquakes or the energy distribution among scales in fully developed turbulence are ones over many examples of scale invariant processes. Hence, the power law scaling for the size distribution generated by a filament supports the idea of a self-similar breakup cascade, in which the same breakup scenario replicates at smaller and smaller scales.

This scenario is very different from breakups observed in liquid ligaments. When the surrounding liquid has negligible inertia and viscosity, the ligament breakup is controlled by instabilities. These instabilities select a wavelength and therefore a discrete set of sizes corresponding to the most unstable wavelength in the system. This is for instance the case in liquid jets, where the Rayleigh-Plateau instability controls the ligament destabilization [65]. Noise on the initial conditions widens the distribution around these selected sizes but the overall shape remains the same (see for instance Pal et al. [140] for the study of the size distribution generated by the fragmentation of a rough liquid cylinder).

3 From filament breakups to sub-Hinze BSD

3.1 Breakup kernel

In a dilute environment, we showed that the bubble size distribution is driven by breakups only. In chapter 7, we demonstrated that, provided the residence time is long enough compared to the turbulent timescale, there is a sharp separation between breaking and non breaking bubbles. In this situation, only bubbles larger than the Kolmogorov Hinze scale d_h are likely to break. We showed in chapter 9 that, for bubbles of size d smaller than cd_h, where $c = 2^{-1/3}$, the population balance equation simplifies and reads

$$\partial_t \mathcal{N}(d,t) = \int_{d_h}^{d_0} m(\Delta) f(d,\Delta) \kappa(\Delta) \mathcal{N}(\Delta,t) \mathrm{d}\Delta \tag{11.4}$$

where d_0 is the largest bubble size in the system. During one sequence of breakups, which lasts about one eddy turnover time, a bubble of size Δ, produces $m(\Delta)$ children. Two of them have size comparable to Δ. The others result from filaments splitting and are smaller than d_h. The breakup kernel $f(d,\Delta)$ quantifies the fraction of bubbles of size d produced by the breaking of a bubble of size Δ. The previous study suggests that, for bubbles produced via filaments splitting, this fraction universally scales as $d^{-3/2}$, independently of the physical parameters. We deduce that

$$f(d,\Delta) \propto d^{-3/2} \tag{11.5}$$

for bubbles generated by the filament splitting. Note that this forms assumes that there exists a minimum bubble size below which the cascade stops.

We introduce $g(\Delta) = f(d,\Delta) d^{3/2}$. From this decomposition, the PBE reads

$$\partial_t \mathcal{N}(d,t) = d^{-3/2} \int_{d_h}^{d_0} m(\Delta) g(\Delta) \kappa(\Delta) \mathcal{N}(\Delta) \mathrm{d}\Delta. \tag{11.6}$$

Since the integral does not depend on d, we have identified the origin of the $-3/2$ scaling for the sub-Hinze bubbles. The sub-Hinze BSD results from the sum of the contribution of gas filaments, all producing a $d^{-3/2}$ distribution.

3.2 Origin of sub-Hinze bubbles at size d

For a given size $d < cd_h$, it is interesting to compare fluxes from super Hinze bubbles to d, depending on the parent size Δ/d_h. For a given size Δ, we recall that the flux from size Δ to size d reads

$$\Phi(d, \Delta) = m(\Delta) f(d, \Delta) \kappa(\Delta) \mathcal{N}(\Delta). \tag{11.7}$$

Lets recall the evolution of each term with Δ.

1. $m(\Delta)$: As shown in the previous chapter, the filament volume $V_f(\Delta/d_h)$ decreases with Δ/d_h. As the breakup process is scale invariant, we expect $m(\Delta)$ to decrease with decreasing $V_f(\Delta/d_h)$ and therefore with increasing Δ/d_h. We also found that there is an optimal parent size, close to d_h, where the filament volume V_f is maximum, and hence the number of child bubbles $m(\Delta)$ is maximum.
2. $\kappa(\Delta)$: For $\Delta \geq 1.5 d_h$ the breakup rate is given by the inverse of the eddy turnover time $t_c(\Delta)^{-1} = \epsilon^{1/3} d^{-2/3}$ (see chapters 7 and 9). The larger Δ/d_h, the smaller the breakup rate. In addition, for $\Delta \to 0$, $\kappa \to 0$. Hence, there exists an optimal bubble size close to d_h which maximizes the breakup rate.
3. $f(d, \Delta)$: The breakup kernel exhibits the same scaling for sub-Hinze bubbles, no matter the initial bubble size.
4. $\mathcal{N}(d)$: The BSD of super-Hinze bubbles follows $\mathcal{N}(d) \propto d^{-10/3}$: There are significantly more bubbles of size close the Kolmogorov-Hinze scale.

We conclude that, for a given size $d < cd_h$, the largest flux comes from bubbles of size close to d_h. These bubbles produce more child bubbles, break more often and are significantly more numerous.

4 Conclusion: Sub-Hinze bubbles generation

In this chapter, we have demonstrated that the rupture of a single gas filament is sufficient to generate a power-law distribution of bubble sizes following $d^{-3/2}$. This power-law suggests that the filament breakup is self-similar, so that the same breaking scenario repeats itself at each splitting event. We find that the generated bubble size distribution is independent of the physical parameters controlling the problem, namely the Weber and Reynolds, in the range of explored values.

This power-law scaling coincides with the $\mathcal{N}(d) \propto d^{-3/2}$ scaling observed for the sub-Hinze BSD measured below breaking waves. As we have identified in chapter 9, that sub-Hinze bubbles comes from the fragmentation of gas filaments, we conclude that the filament splitting dynamics is universal, independent of the surrounding turbulent flow. Hence, the number of sub-Hinze bubbles at size d sums all the contribution of filaments of varying length and size, which all produce the same size distribution, as schematize on figure 11.5. Importantly, for a given sub-Hinze size d, we predict that most of the generated bubbles comes from the fragmentation of bubbles close to the sub-Hinze scale, no matter the value of d, as indicated by the width of the colored line in figure 11.5.

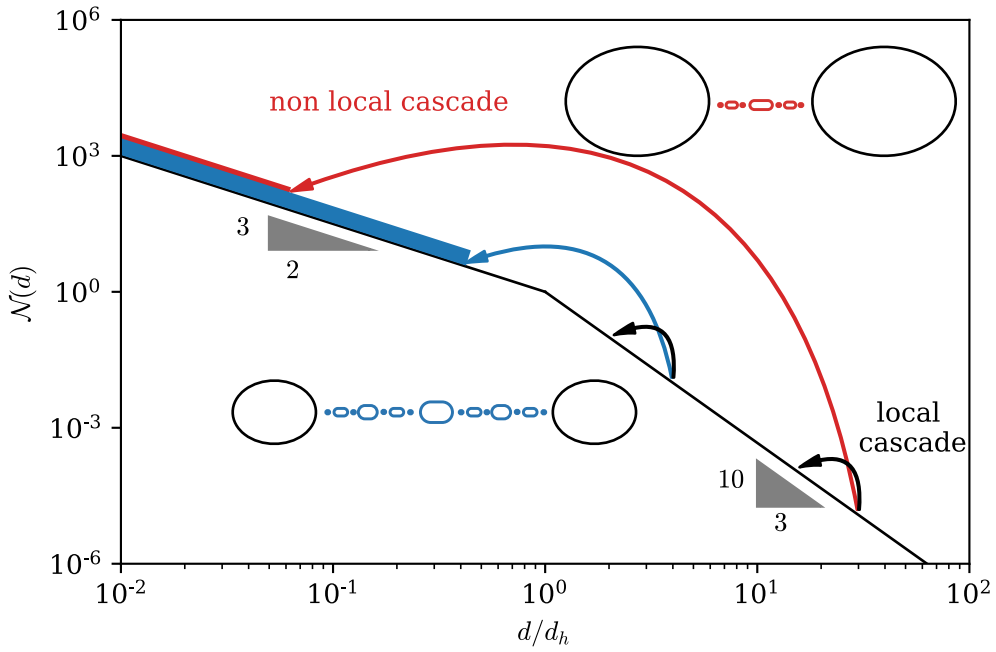

Figure 11.5 – Summary of the fluxes leading to the BSD distribution below breaking waves. A local (black arrow), and non-local (colored arrow) cascade co-exists. The non-local cascade arises from the fragmentation of gas ligaments. Each ligament splitting creates a $d^{-3/2}$ BSD. The smaller the parent bubble size, the larger the flux from super-Hinze to sub-Hinze bubbles (schematize by the width of the colored lines).

In this chapter, we have identified the origin of the sub-Hinze BSD power-law. However, the scale invariant physical mechanism, leading to the emergence of the $d^{-3/2}$ scaling remains to be identified. It would be of particular interest to investigate the sequence of breakups to identify the elementary breaking scenario.

CONCLUSION AND PERSPECTIVES

Conclusion and perspectives

The word *Bubble* appears 1515 times in this manuscript.

Turbulence/Turbulent is only used 510 times.

In this thesis, we investigated the deformation and fragmentation dynamics of bubbles in fully developed 3D turbulence by means of numerical simulations. We performed 3D direct numerical simulations of bubbles in isotropic turbulence as well as simulations of model flows configurations to combine complex realistic simulations with very controlled ones. Starting from the example of the bubble size distribution measured below breaking waves, we identified two main questions which guided the redaction of this manuscript. First, can we define a critical Weber number in turbulence? Second, what is the origin of sub-Hinze bubbles?

We summarize here the main results and the remaining questions.

From deformations to breakup probability and We_c

In part I we aimed at defining a critical Weber number depending of the physical properties and the residence time of bubbles within turbulent regions. With this goal in mind, we looked for a probabilistic description of bubble breakup and aimed at quantifying the probability for a bubble to break, *i.e.* to reach a critical deformation, in a given time window. A dynamical description of bubble deformation was therefore needed.

Before investigating bubble deformations in turbulence, in chapter 5, we first focused on the deformations of a bubble in the model flow configuration of the uniaxial straining flow. We showed that most of bubble deformations can be reproduced with the help of a one dimensional ordinary differential equation on the amplitude of the oblate-prolate mode of deformation. This equation takes the form of a non linear oscillator equation. Both the Weber and Reynolds number control the shape of the effective potential. As the height of the energy barrier is finite for all Weber numbers, we find that there always exists a set of initial conditions allowing the bubble to break. This result confirms the need for a probabilistic description of bubble breakup.

Building on this success, in chapter 6 we investigated the linear deformations dynamics of bubbles in turbulence, by running DNS of fully developed 3D turbulence. We showed that, as in the uniaxial straining flow, the dynamics of each mode of deformation can be captured by a 1D linear oscillator equation randomly forced by turbulence. We measured that the natural frequency associated with each mode is unchanged compared to the quiescent case. However,

turbulence enhances the energy transport from the interface to the flow, which leads to dramatically more dissipation and hence a larger damping rate. We showed that the effective stochastic forcing statistics corresponds to the pressure statistics on a sphere.

Using this one dimensional model, in chapter 7, combined with a critical value for breakup, we found that, for residence times larger than the correlation time of turbulence at the bubble scale, bubble breakup is a memoryless process, hence a Poisson process. We also gave an expression for the breakup rate at a function of the Weber number. From this expression, we derived an expression for the cumulative breakup probability as a function of both We and the residence time t_R. Eventually, we defined the critical Weber number as the one at which the survival probability is 1/2, and were able to quantify its evolution with the residence time. We found that We_c diverges at short residence times and the transition between statistically breaking and non breaking bubbles is smooth. As the residence time increases, We_c decreases and the transition becomes sharp.

In chapter 6 and 7 we focused on the effect of the Weber number on bubble dynamics. This parameter is believed to be the main controlling parameter for bubble sizes lying within the inertial range of the turbulence cascade. Nevertheless, chapter 6 shows that turbulence significantly enhances the effective damping of bubble oscillations. We argued that the effective damping can be modeled by a turbulent dissipation. At this point, further studies, varying the energy dissipation rate ϵ, need to be performed in order to confirm this argument and to find the evolution of the damping rate with the Reynolds number.

Sub-Hinze bubble production

In part II, we focused on the generation of sub-Hinze bubbles, for which the BSD below breaking waves exhibits $\mathcal{N}(d) \propto d^{-3/2}$.

In chapter 9, we showed that the breakage of a single bubble in turbulence is sufficient to reproduce the BSD measured below breaking waves, provided there is a large enough scale separation between the initial bubble size and the Kolmogorov-Hinze scale. This result confirms BSD below breaking waves are controlled by breakups. We then took advantage of bubble lifetimes to identify the origin of sub-Hinze bubbles. We found that breakup sequences, in which all the events are correlated, happen in two concomitant stages, each of them being responsible for one exponent of the total BSD. First, the initial bubble deforms on a time given by the eddy turnover time at its scale. This time sets the bubble lifetime, in agreement with part II. The bubble shape then exhibits filament structures, surrounded by larger structures. The two larger structures create two bubbles of size close to the initial bubble, which will feed the super-Hinze distribution. Filaments split into a large number of bubbles in times given by the capillary timescale at the filament scale. The bubbles generated by these splitting are dramatically smaller than the Kolmogorov-Hinze size and feed the sub-Hinze distribution.

Chapter 10 focuses on the generation of filaments in the model geometry. We found that the filament shape is mostly controlled by the Reynolds number, and we have the intuition that the gas dynamics may not be negligible to understand the filament formation. From the evolution of the filament volume with the controlling parameters, we found that bubbles of size close to

the Kolmogorov Hinze scale produce larger filaments than very large super-Hinze bubbles.

Lastly, in chapter 11, we demonstrated that the fragmentation of a single filament is sufficient to produce a $d^{-3/2}$ bubble size distribution. We argued that this power-law distribution arises from a cascade of scale invariant breakups. Extrapolating this result to bubbles in turbulence suggests that the breakup kernel must scale as $d^{-3/2}$ for child bubbles generated by the splitting of an air filament. We concluded that for a given sub-Hinze size d, the largest flux from super-Hinze size to d originates from bubbles of size close to d_h, as they are more numerous, break faster and produce more child bubbles.

In this part, we have elucidated the origin of sub-Hinze bubbles as coming from the scale invariant fragmentation of air filaments. However, at this stage we do not know where the scaling law comes from. Further investigations, both numerical and experimental are necessary to identify the splitting mechanism. In addition, it would be interesting to know how this distribution evolves in the presence of more complex flows. In particular, in the whole study, we neglected the importance of vorticity. While vorticity seems to be unimportant at the bubble scale, it might stabilize a filament and change the pinch-off dynamics.

APPENDICES

Appendix A

Dynamics close to a critical point

Abstract

We consider the one dimensional dynamics of a particle in a potential V which has at least one unstable equilibrium position at $x = x_c$. The particle starts from a given position with an initial velocity which depends on a control parameter p. The potential shape also depends on p. For a critical value p_c of p, the particle reaches the unstable position of the potential. We show that the time spent close to the unstable point scales as $-\log(|p - p_c|)$ when $p \to p_c$ both in the stable case when the particle does not reach x_c and in the unstable case where the particle crosses x_c.

Contents

1 Notations and physical configuration

Let us consider the following conservative dynamics:

$$\ddot{x} = f(x,p) = -\partial_x V(x,p) \tag{A.1}$$

where p is some control parameter. Dots represent time derivatives. $V(x,p)$ is a potential which for some p has at least one unstable position in x_c. In the simplest case, this means that $f(x_c,p) = 0$ and $\partial_x f(x_c,p) > 0$. The particle starts from $x_0 < x_c$, with a positive initial velocity which depends on p. When $p < p_c$ the particle does not reach x_c and turns back at $x = x_{\max}(p)$. For $p > p_c$, the particle crosses x_c. We want to find how the time spent in the vicinity of x_c depends on $p - p_c$.

We set $u = x_c - x$, $\epsilon = p_c - p$. At lowest order in u and ϵ, equation (A.1) reads:

$$\ddot{u} = u\partial_x f|_c + \epsilon \partial_p f|_c \tag{A.2}$$

Since $\partial_x f(x_c,p_c) = \partial_x f|_c > 0$, in the following we write: $\gamma = \sqrt{\partial_x f|_c}$.

2 Stable case, $p < p_c$

Let us first consider the case when the particle does not reach x_c. In this case, we know that $x_c - x_{\max} = u_{\min} \propto \sqrt{p_c - p}$ (see the main text).

2.1 Forcing independent of p

When f is independent of p, equation (A.2) simplifies to:

$$\ddot{u} = u\partial_x f|_c \tag{A.3}$$

whose solutions are of the form:

$$u(t) = u_0 e^{\gamma t} + u_1 e^{-\gamma t}$$

where u_0 and u_1 are some constants that depend on the initial conditions. Since we are considering a stable trajectory, there exists a point at which the particle turns around and moves away from x_c. To simplify notations, this time is taken as the origin of times. Then, we have

$$u(0) = u_{\min}$$
$$\dot{u}(0) = 0$$

Which gives the solution of (A.3):

$$u(t) = \frac{u_{\min}}{2}(e^{\gamma t} + e^{-\gamma t}) = u_{\min}\cosh(\gamma t)$$

Let U be an arbitrary distance from x_c reached at $t = T$. U reads:

$$U = u_{\min} \cosh(\gamma T)$$

When $p \to p_c$, since $u_{\min} \propto \sqrt{p_c - p}$ (showed in the main text), $u_{\min} \to 0$ and so $\cosh(\gamma T) \to \infty$. In this limit: $\cosh(\gamma T) \sim e^{\gamma T}$. And so:

$$\gamma T \propto -\log(u_{\min}) \propto -\log(p_c - p) \tag{A.4}$$

As p gets closer and closer to p_c, the time spent close to x_c diverges as $-\log(p_c - p)$. Let us now consider the case where the potential also depends on the control parameter p.

2.2 General expression

If now the potential also depends on p, we have to introduce a new variable v such that $v = u + \epsilon \frac{\partial_p f|_c}{\partial_x f|_c} = u + \epsilon C$. v is a solution of equation (A.3):

$$\ddot{v} = v \partial_x f|_c \tag{A.5}$$

with the following initial conditions:

$$\begin{aligned} v(0) &= v_{\min} = u_{\min} + \epsilon C \\ \dot{v}(0) &= 0 \end{aligned}$$

As previously, the solution reads:

$$v(t, p) = v_{\min} \cosh(\gamma t)$$

Using the definition of v and the fact that $v_{\min} = u_{\min} + \epsilon C$ we get:

$$u(t, p) = u_{\min} \cosh(\gamma t) + \epsilon C \cosh(\gamma t) - \epsilon C$$

As before, we fix U, an arbitrary distance from x_c, reached at T.

$$U = u_{\min} \cosh(\gamma T) + \epsilon C \cosh(\gamma T) - \epsilon C$$

Since we still have $u_{\min} \propto \sqrt{\epsilon}$ and so, at lowest order in ϵ, when $p \to p_c$, since $\gamma T \to \infty$:

$$\gamma T \propto -\log u_{\min}$$

We get again the same divergence of T: $\gamma T \propto -\log(p_c - p)$.

3 Unstable Case, $p > p_c$

When $p > p_c$, the particle crosses x_c. We then choose as the origin of times the moment where $x = x_c$, which corresponds to $u = 0$ and to the minimum of $\dot{u}$, written $\dot{u}_{\min}$. We first look

for the scaling of $\dot{u}_{\min}$ with ϵ.

By conservation of energy we get:

$$\frac{1}{2}\dot{x}^2 + V(x,p) = \frac{1}{2}\dot{x}_0^2$$

where V is redefined so that $V(x_0) = 0$. Let us define $g(p)$ such that $\dot{x}_0 = \sqrt{2g(p)}$. The previous equation now reads:

$$\frac{1}{2}\dot{x}^2 = g(p) - V(x,p)$$

Since x_c is a maximum of V, $\dot{x}$ is minimum at $x = x_c$ and reads:

$$\frac{1}{2}\dot{x}_{\min}^2 = g(p) - V(x_c,p)$$

We develop the right hand side at lowest order in ϵ taking advantage of the fact that $g(p_c) = V(x_c,p_c)$. We get:

$$\frac{1}{2}\dot{x}_{\min}^2 = -\epsilon(g'(p_c) - \partial_p V(x_c,p_c))$$

And so:

$$\dot{x}_{\min} = \dot{u}_{\min} = \sqrt{-2\epsilon(g'(p_c) - \partial_p V(x_c,p_c))} \propto \sqrt{p - p_c} \tag{A.6}$$

Now, equation (A.5) still holds in the unstable case with the new initial conditions

$$v(0) = u(0) + \epsilon C = \epsilon C$$
$$\dot{v}(0) = \dot{u}(0) = \dot{u}_{\min}$$

Using the same trick as in the previous section we obtain the general solution in this case:

$$u(t,p) = \epsilon C \cosh(\gamma t) + \frac{\dot{u}_{\min}}{\gamma}\sinh(\gamma t) - \epsilon C \tag{A.7}$$

As before, let us take U, an arbitrary distance from the critical point which is reached at time T.

$$U = \epsilon C \cosh(\gamma T) + \frac{\dot{u}_{\min}}{\gamma}\sinh(\gamma T) - \epsilon C \tag{A.8}$$

When $\epsilon \to 0$, since $\dot{u}_{\min} \propto \sqrt{-\epsilon}$, as previously, we get:

$$U \propto \frac{\dot{u}_{\min}}{\gamma} e^{\gamma T} \tag{A.9}$$

and we recover:

$$\gamma T \propto -\log(p - p_c) \tag{A.10}$$

Appendix B

How to generate a sequence of random forcing with Gaussian Copulas

Abstract

In this appendix, we explain how to generate a realisation of $\mathcal{T}(t)$, the effective forcing from turbulence on bubble shape, using Gaussian copula.

Contents

1 Principle and notations

1.1 Constructing $\mathcal{T}$ from a vector of Gaussian variables

Let $\mathcal{T}$ be the forcing evolution that we want to evaluate and $\{\mathcal{T}_i\}_{i\in[1,N]}$ its discrete counterpart, defined at times $\{t_i\}_{i\in[1,N]}$. We assume the statistics of $\mathcal{T}$ to be stationary, so that all $\mathcal{T}_i$ share the same distribution and the covariance matrix of $\{\mathcal{T}_i\}_{i\in[1,N]}$ is such that $\mathrm{Cov}(\mathcal{T}_i, \mathcal{T}_j)$ only depends on $|t_i - t_j|$. We introduce the following notations:

— $\Phi_{\sigma_\mathcal{T}}$: probability density function of $\mathcal{T}$

— $\sigma_\mathcal{T}$: standard deviation of $\mathcal{T}$

— $A(t)$: autocorrelation function of $\mathcal{T}$

— $Y_i = \mathcal{T}_i/\sigma_\mathcal{T}$

— Σ: covariance matrix of $\{Y_i\}_{i\in[1,N]}$.

By definition of $\{Y_i\}_{i\in[1,N]}$, we have the following properties:

— Y_i has distribution Φ_1, denoted Φ in what follows

— $\Sigma_{i,j} = A(|t_i - t_j|)$

— $\Sigma_{ii} = 1$, ie the standard deviation of Y_i is 1 for all i.

Finally, we introduce F_Φ the cumulative distribution of Φ and F_Φ^{-1} its inverse.

There is no method to directly compute $\{Y_i\}_{i\in[1,N]}$. Instead, we will construct $\{Y_i\}_{i\in[1,N]}$ using a vector of centered gaussian variables $\{X_i\}_{i\in[1,N]}$: this is a gaussian copula method. Since we aim at constructing a stationary process, all the X_i also share the same normal distribution $\mathcal{N}$ with average 0 and standard deviation σ'. We introduce these additional notations:

— Σ': covariance matrix of $\{X_i\}_{i\in[1,N]}$

— $F_\mathcal{N}$: cumulative distribution function of $\mathcal{N}$

— $F_\mathcal{N}^{-1}$: inverse cumulative distribution function of $\mathcal{N}$

We can easily generate a Gaussian random vector $\{X_i\}_{i\in[1,N]}$ of any covariance matrix Σ'. The idea is then to transform $\{X_i\}_{i\in[1,N]}$ into $\{Y_i\}_{i\in[1,N]}$. We know that we can construct Z_i of distribution Φ through

$$Z_i = F_\Phi^{-1}(F_\mathcal{N}(X_i)).$$

However, the covariant matrix of $\{Z_i\}_{i\in[1,N]}$ is not known a priori. As a consequence, the difficulty is to find the right Σ' so that after applying $F_\Phi^{-1}(F_\mathcal{N}(.))$ to each X_i, we get a vector with covariance matrix Σ. In what follows we will determine Σ' and then deduce Y_i using,

$$Y_i = F_\Phi^{-1}(F_\mathcal{N}(X_i)). \tag{B.1}$$

The following expression will also be useful:

$$X_i = F_\mathcal{N}^{-1}(F_\Phi(Y_i)). \tag{B.2}$$

1.2 Explicit expression of each function

The distribution Φ is the hyperbolic secant distribution with standard deviation 1:

$$\Phi(x) = \frac{1}{2}\frac{1}{\cosh(\frac{\pi x}{2})}$$

Its associated cumulative distribution function is,

$$F_\Phi = \frac{2}{\pi}\arctan\left(\exp\left(\frac{\pi x}{2}\right)\right),$$

whose inverse is

$$F_\Phi^{-1} = \frac{2}{\pi}\log\left(\tan\left(\frac{\pi x}{2}\right)\right).$$

The centered normal distribution, $\mathcal{N}$ is

$$\mathcal{N}(x) = \frac{1}{\sigma'\sqrt{2\pi}}\exp\left[-\frac{1}{2}\left(\frac{x}{\sigma'}\right)^2\right].$$

Its cumulative distribution function is,

$$F_\mathcal{N}(x) = \frac{1}{2}\left[1 + \mathrm{erf}(-\frac{x}{\sqrt{2}\sigma'})\right]$$

whose inverse reads

$$F_\mathcal{N}^{-1}(x) = \sigma'\sqrt{2}\,\mathrm{erf}^{-1}[2x-1].$$

We also introduce the joint law of two centered Gaussian variable X_i, X_j such that $\mathrm{Var}(X_i) = \mathrm{Var}(X_j) = \Sigma'_{ii} = (\sigma')^2$ and $\mathrm{Cov}(X_i, X_j) = \mathrm{Cov}(X_j, X_i) = \Sigma'_{ij}$:

$$f_{ij}(x,y) = \frac{1}{2\pi\sqrt{\Delta_{ij}}}\exp\left(-\frac{\Sigma'_{ii}(x^2+y^2) - 2\Sigma'_{ij}xy}{2\sqrt{\Delta_{ij}}}\right) \tag{B.3}$$

where $\Delta_{ij} = (\Sigma'_{ii})^2 - (\Sigma'_{ij})^2$.

Finally, the autocorrelation function of the forcing is,

$$A(t) = \exp\left(-2\pi.2^{2/3}t\right)(1 + 2\pi.2^{2/3}t)$$

2 Determination of the Covariance matrix Σ'

2.1 Diagonal terms

We can explicitly compute Σ'_{ii} from Σ_{ii} using equation (B.2):

$$\begin{aligned}\Sigma'_{ii} &= \mathrm{Var}(X_i) = (\sigma')^2 \\ &= \mathrm{Var}(F_{\mathcal{N}}^{-1}(F_\Phi(Y_i))) \\ &= \int_{\mathrm{R}} F_{\mathcal{N}}^{-1}(F_\Phi(y))^2 \Phi(y)\mathbf{d}y - \left[\int_{\mathrm{R}} F_{\mathcal{N}}^{-1}(F_\Phi(y))\Phi(y)\mathbf{d}y\right]^2 \\ &= I_1(\Sigma_{ii}) - (I_2(\Sigma_{ii}))^2\end{aligned}$$

We estimate numerically these two integral and find $I_1 = 1$ and $I_2 = 0$ (indeed the integrand of I_2 is odd). It follows,

$$\Sigma'_{ii} = (\sigma')^2 = \Sigma_{ii} = 1, \quad \forall i \tag{B.4}$$

2.2 Off-Diagonal terms

This time, we want to evaluate Σ'_{ij} with $i \neq j$. We do not know the joint law of (Y_i, Y_j), which is too costly to be evaluated, but we have an expression for the joint law of two Gaussian variables (equation (B.3)). We then use equation (B.1) to express Σ_{ij} as a function of Σ'_{ij}:

$$\begin{aligned}\Sigma_{i,j} &= \mathrm{Cov}(Y_i, Y_j) \\ &= \mathrm{Cov}[F_\Phi^{-1}(F_{\mathcal{N}}(X_i)), F_\Phi^{-1}(F_{\mathcal{N}}(X_j))] \\ &= \iint_{\mathrm{R}^2} F_\Phi^{-1}(F_{\mathcal{N}}(x_1))F_\Phi^{-1}(F_{\mathcal{N}}(x_2))f_{ij}(x_1,x_2)\mathbf{d}x_1\mathbf{d}x_2 - \left[\int_{\mathrm{R}} F_\Phi^{-1}(F_{\mathcal{N}}(x))\mathcal{N}(x)\mathbf{d}x\right]^2 \\ &= I_a(\Sigma'_{ij}) + I_b^2\end{aligned}$$

Numerically, we find $I_b = 0$ (the integrand is odd).

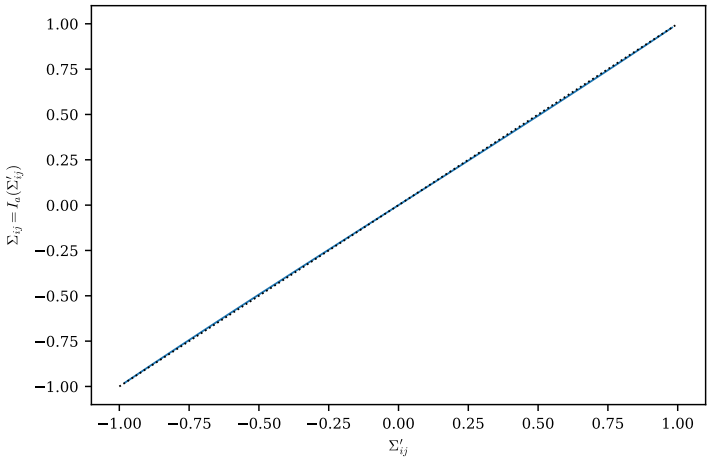

Figure B.1 – Variation of Σ_{ij} with Σ'_{ij}. The blue line is I_a. The black dotted line follows $\Sigma_{ij} = \Sigma'_{ij}$.

We estimate I_a numerically (see figure B.1) and find that $I_a(\Sigma'_{ij}) = \Sigma'_{ij}$ is an excellent approximation. It follows that:

$$\Sigma_{ij} = \Sigma'_{ij}, \quad \forall i \neq j \tag{B.5}$$

2.3 Conclusion

Combining equations (B.4) and (B.5) we have

$$\Sigma = \Sigma' \tag{B.6}$$

making the evaluation of Σ' in our case extremely fast and cheap.

3 Verification

To summarize, we first generate a Gaussian random vector $\{X_i\}_{i\in[1,N]}$ with covariant matrix,

$$\Sigma'_{ij} = A(|t_i - t_j|). \tag{B.7}$$

Then we use equation (B.1) to get $\{Y_i\}_{i\in[1,N]}$. Finally, $\mathcal{T}_i$ is obtained using

$$\mathcal{T}_i = \sigma_{\mathcal{T}} Y_i. \tag{B.8}$$

Figures B.2 and B.3 compare the autocorrelation function and the distribution of $\mathcal{T}_i$, respectively, obtained with the above procedure, to their theoretical expressions. The agreement is excellent.

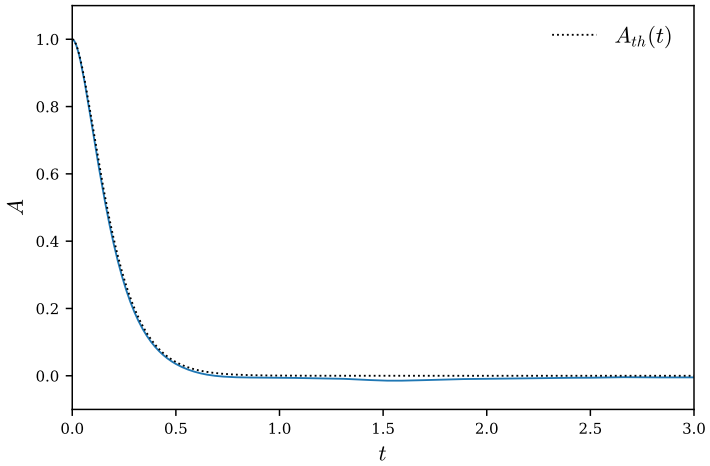

Figure B.2 – Autocorrelation of $\mathcal{T}_i$, ie Σ'_{ij} as a function of time. The black dotted line is the targeted function. The blue line corresponds to the generated forcing signal.

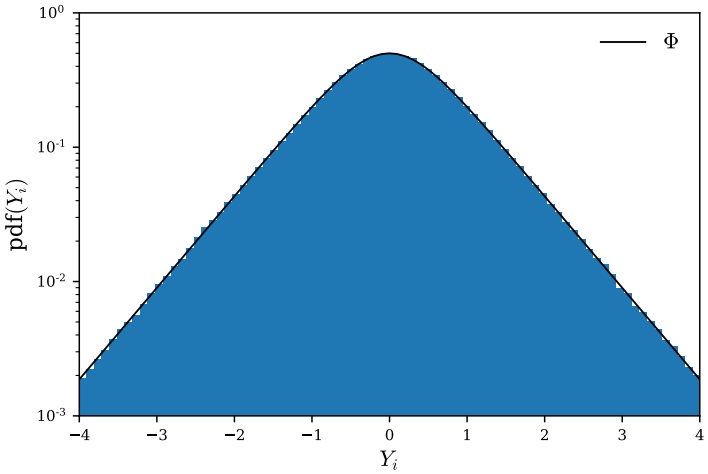

Figure B.3 – Comparison between the distribution of the generated noise (in blue) and the theoretical target distribution (in black). The agreement is excellent.

Bibliography

[1] Patrice Abry, Stephan Fauve, Patrick Flandrin, and C. Laroche. « Analysis of pressure fluctuations in swirling turbulent flows ». *Journal de Physique II* 4.5 (1994), pp. 725–733 (cit. on pp. 91, 92, 94).

[2] Moataz O. Abu-Al-Saud, Stéphane Popinet, and Hamdi A. Tchelepi. « A conservative and well-balanced surface tension model ». *Journal of Computational Physics* (2018) (cit. on p. 24).

[3] Andreas Acrivos. « The breakup of small drops and bubbles in shear flows ». *Annals of the New York Academy of Sciences* 404.1 (1983), pp. 1–11 (cit. on pp. 56, 64).

[4] Thomas Adcock, Kaitao Tang, and Wouter Mostert. « Fragmentation of colliding liquid rims ». *Journal of Fluid Mechanics* (2024) (cit. on p. 24).

[5] D. B. Allan, T. Caswell, N. C. Keim, and C. M. van der Wel. *soft-matter/trackpy: Trackpy v0.4.2*. Version v0.4.2. 2019 (cit. on p. 45).

[6] Ronnie Andersson and Bengt Andersson. « Modeling the breakup of fluid particles in turbulent flows ». *AIChE Journal* 52.6 (2006), pp. 2031–2038 (cit. on p. 104).

[7] Wm. T. Ashurst, A.R. Kerstein, R.M. Kerr, and C.H. Gibson. « Alignment of vorticity and scalar gradient with strain rate in simulated Navier–Stokes turbulence ». *The Physics of fluids* 30.8 (1987), pp. 2343–2353 (cit. on pp. 16, 17).

[8] D. Atamanchuk, J. Koelling, U. Send, and D.W.R. Wallace. « Rapid transfer of oxygen to the deep ocean mediated by bubbles ». *Nature Geoscience* 13.3 (2020), pp. 232–237 (cit. on p. 113).

[9] Mehedi Hasan Bappy, Pablo M. Carrica, and Gustavo Carlos Buscaglia. « Lagrangian statistics of pressure fluctuation events in homogeneous isotropic turbulence ». *Physics of Fluids* 31.8 (2019) (cit. on p. 91).

[10] Mehedi Hasan Bappy, Pablo M. Carrica, Alberto Vela-Martín, Lívia Souza Freire, and Gustavo Carlos Buscaglia. « Pressure statistics of gas nuclei in homogeneous isotropic turbulence with an application to cavitation inception ». *Physics of Fluids* 32.9 (2020) (cit. on p. 91).

[11] Mehedi Hasan Bappy, Alberto Vela-Martín, Gustavo Carlos Buscaglia, Pablo M. Carrica, and Lívia Souza Freire. « Effect of bubble size on Lagrangian pressure statistics in homogeneous isotropic turbulence ». *Journal of Physics: Conference Series*. Vol. 1522. 1. IOP Publishing. 2020, p. 012002 (cit. on p. 91).

[12] Jake J. Beaulieu, William D. Shuster, and Jacob A. Rebholz. « Controls on gas transfer velocities in a large river ». *Journal of Geophysical Research: Biogeosciences* 117.G2 (2012) (cit. on p. 4).

[13] Raymond Bergmann, Devaraj van der Meer, Mark Stijnman, Marijn Sandtke, Andrea Prosperetti, and Detlef Lohse. « Giant bubble pinch-off ». *Physical review letters* 96.15 (2006), p. 154505 (cit. on p. 130).

[14] Raymond Bergmann, Devaraj Van Der Meer, Stephan Gekle, Arjan Van Der Bos, and Detlef Lohse. « Controlled impact of a disk on a water surface: cavity dynamics ». *Journal of Fluid Mechanics* 633 (2009), pp. 381–409 (cit. on p. 130).

[15] Alexis Berny, Luc Deike, Thomas Séon, and Stéphane Popinet. « Role of all jet drops in mass transfer from bursting bubbles ». *Physical Review Fluids* 5.3 (2020), p. 033605 (cit. on pp. 4, 113).

[16] Alexis Berny, Stéphane Popinet, Thomas Séon, and Luc Deike. « Statistics of jet drop production ». *Geophysical Research Letters* 48.10 (2021), e2021GL092919 (cit. on pp. 4, 24).

[17] S.R. Berry, R.W. Hyers, L.M. Racz, and B. Abedian. « Surface oscillations of an electromagnetically levitated droplet ». *International journal of thermophysics* 26 (2005), pp. 1565–1581 (cit. on p. 81).

[18] Duncan C. Blanchard and Lawrence D. Syzdek. « Film drop production as a function of bubble size ». *Journal of Geophysical Research: Oceans* 93.C4 (1988), pp. 3649–3654 (cit. on p. 4).

[19] C. E. Blenkinsopp and J. R. Chaplin. « Bubble size measurements in breaking waves using optical fiber phase detection probes ». *IEEE Journal of Oceanic Engineering* 35.2 (2010), pp. 388–401 (cit. on pp. 113–115).

[20] Valdis Bojarevics and Koulis Pericleous. « Modelling electromagnetically levitated liquid droplet oscillations ». *ISIJ international* 43.6 (2003), pp. 890–898 (cit. on p. 81).

[21] Rocío Bolaños-Jiménez, Alejandro Sevilla, Carlos Martínez-Bazán, Devaraj Van Der Meer, and José Manuel Gordillo. « The effect of liquid viscosity on bubble pinch-off ». *Physics of fluids* 21.7 (2009) (cit. on p. 130).

[22] Joseph Boussinesq. *Essai sur la théorie des eaux courantes*. Impr. nationale, 1877 (cit. on p. 81).

[23] Joseph Boussinesq. « Calcul du pouvoir refroidissant des courants fluides ». *Journal de mathématiques pures et appliquées* 1 (1905), pp. 285–332 (cit. on p. 9).

[24] Michael P. Brenner, Jens Eggers, Kathy Joseph, Sidney R. Nagel, and X.D. Shi. « Breakdown of scaling in droplet fission at high Reynolds number ». *Physics of Fluids* 9.6 (1997), pp. 1573–1590 (cit. on p. 130).

[25] Christophe Brouzet, Raphaël Guiné, Marie-Julie Dalbe, Benjamin Favier, Nicolas Vandenberghe, Emmanuel Villermaux, et al. « Laboratory model for plastic fragmentation in the turbulent ocean ». *Physical Review Fluids* 6.2 (2021), p. 024601 (cit. on pp. 49, 104).

[26] J.C. Burton, R. Waldrep, and P. Taborek. « Scaling and Instabilities in Bubble Pinch-Off ». *Phys. Rev. Lett.* 94.184502 (2005) (cit. on pp. 27, 130, 136).

[27] Olivier Cadot, Stéphane Douady, and Yves Couder. « Characterization of the low-pressure filaments in a three-dimensional turbulent shear flow ». *Physics of Fluids* 7.3 (1995), pp. 630–646 (cit. on p. 91).

[28] Enrico Calzavarini, Romain Volk, Mickaël Bourgoin, Emmanuel Lévêque, Jean-François Pinton, and Federico Toschi. « Acceleration statistics of finite-sized particles in turbulent flow: the role of Faxén forces ». *Journal of Fluid Mechanics* 630 (2009), pp. 179–189 (cit. on p. 82).

[29] Brian J. Cantwell. « Exact solution of a restricted Euler equation for the velocity gradient tensor ». *Physics of Fluids A: Fluid Dynamics* 4.4 (1992), pp. 782–793 (cit. on pp. 17, 18).

[30] Brian J. Cantwell. « On the behavior of velocity gradient tensor invariants in direct numerical simulations of turbulence ». *Physics of Fluids A: Fluid Dynamics* 5.8 (1993), pp. 2008–2013 (cit. on p. 18).

[31] Nianzheng Cao, Shiyi Chen, and Gary D. Doolen. « Statistics and structures of pressure in isotropic turbulence ». *Physics of Fluids* 11.8 (1999), pp. 2235–2250 (cit. on p. 91).

[32] Manuel Caroli, Pedro MM de Castro, Sébastien Loriot, Olivier Rouiller, Monique Teillaud, and Camille Wormser. « Robust and efficient Delaunay triangulations of points on or close to a sphere ». *Experimental Algorithms: 9th International Symposium, SEA 2010, Ischia Island, Naples, Italy, May 20-22, 2010. Proceedings 9*. Springer. 2010, pp. 462–473 (cit. on p. 43).

[33] W. H. R. Chan, P. L. Johnson, P. Moin, and J. Urzay. « The turbulent bubble break-up cascade. Part 2. Numerical simulations of breaking waves ». *J. Fluid Mech.* 912 (2021), A43 (cit. on p. 113).

[34] Subrahmanyan Chandrasekhar. « The oscillations of a viscous liquid globe ». *Proceedings of the London Mathematical Society* 3.1 (1959), pp. 141–149 (cit. on p. 50).

[35] Subrahmanyan Chandrasekhar. *Hydrodynamic and hydromagnetic stability*. Courier Corporation, 2013 (cit. on p. 50).

[36] Eleni Chatzi and James M. Lee. « Analysis of interactions for liquid-liquid dispersions in agitated vessels ». *Industrial & engineering chemistry research* 26.11 (1987), pp. 2263–2267 (cit. on p. 52).

[37] Eleni G. Chatzi, Asterios D. Gavrielides, and Costas Kiparissides. « Generalized model for prediction of the steady-state drop size distributions in batch stirred vessels ». *Industrial & engineering chemistry research* 28.11 (1989), pp. 1704–1711 (cit. on pp. 52, 110).

[38] Eleni G. Chatzi and Costas Kiparissides. « Dynamic simulation of bimodal drop size distributions in low-coalescence batch dispersion systems ». *Chemical Engineering Science* 47.2 (1992), pp. 445–456 (cit. on pp. 52, 110).

[39] T. S. Chen and Daniel D. Joseph. « Subcritical bifurcation of plane Poiseuille flow ». *J. Fluid Mech.* 58 (1973), pp. 337–351 (cit. on p. 55).

[40] Michael Chertkov, Alain Pumir, and Boris I. Shraiman. « Lagrangian tetrad dynamics and the phenomenology of turbulence ». *Physics of fluids* 11.8 (1999), pp. 2394–2410 (cit. on p. 18).

[41] Alessandro Chiarini and Marco Edoardo Rosti. « Finite-size inertial spherical particles in turbulence ». *arXiv preprint arXiv:2404.16475* (2024) (cit. on p. 96).

[42] Leonardo Chirco, Jacob Maarek, Stéphane Popinet, and Stéphane Zaleski. « Manifold death: a volume of fluid implementation of controlled topological changes in thin sheets by the signature method ». *Journal of Computational Physics* 467 (2022), p. 111468 (cit. on p. 130).

[43] Jean-Marc Chomaz. « Global instabilities in spatially developing flows: non-normality and nonlinearity ». *Ann. Rev. of Fluid Mech.* 37 (2005), pp. 357–392 (cit. on pp. 55, 57).

[44] Min S. Chong, Anthony E. Perry, and Brian J. Cantwell. « A general classification of three-dimensional flow fields ». *Physics of Fluids A: Fluid Dynamics* 2.5 (1990), pp. 765–777 (cit. on p. 17).

[45] Min S. Chong, Julio Soria, Anthony E. Perry, J. Chacin, Brian J. Cantwell, and Y. Na. « Turbulence structures of wall-bounded shear flows found using DNS data ». *Journal of Fluid Mechanics* 357 (1998), pp. 225–247 (cit. on p. 18).

[46] Pengbo Chu, James Finch, Ghislain Bournival, Seher Ata, Christopher Hamlett, and Robert J Pugh. « A review of bubble break-up ». *Advances in colloid and interface science* 270 (2019), pp. 108–122 (cit. on pp. 105, 110).

[47] C.A. Coulaloglou and Lawrence L. Tavlarides. « Description of interaction processes in agitated liquid-liquid dispersions ». *Chemical Engineering Science* 32.11 (1977), pp. 1289–1297 (cit. on pp. 52, 103, 110).

[48] P. Coullet, L. Gil, and D. Repaux. « Defects and Subcritical bifurcations ». *Phys. Rev. Lett.* 62 (1989), pp. 2957–2960 (cit. on p. 55).

[49] J. C. Crocker and D. G. Grier. « Methods of Digital Video Microscopy for Colloidal Studies ». *Journal of Colloid and Interface Science* 179.1 (1996), pp. 298–310 (cit. on p. 45).

[50] Emmanuel De Langre. « Effects of wind on plants ». *Annu. Rev. Fluid Mech.* 40 (2008), pp. 141–168 (cit. on p. 49).

[51] Gerrit De Leeuw, Edgar L. Andreas, Magdalena D Anguelova, C.W. Fairall, Ernie R. Lewis, Colin O'Dowd, et al. « Production flux of sea spray aerosol ». *Reviews of Geophysics* 49.2 (2011) (cit. on p. 113).

[52] Grant B. Deane and M. Dale Stokes. « Scale dependence of bubble creation mechanisms in breaking waves ». *Nature* 418.6900 (2002), pp. 839–844 (cit. on pp. 5, 9, 12–14, 25, 105, 113–115, 126).

[53] Luc Deike. « Mass transfer at the ocean-atmosphere interface: the role of wave breaking, droplets, and bubbles ». *Annual Review of Fluid Mechanics* 54 (2022), pp. 191–224 (cit. on pp. 4, 5, 113, 126).

[54] Luc Deike, Elisabeth Ghabache, G. Liger-Belair, A. K. Das, Stéphane Zaleski, Stéphane Popinet, et al. « Dynamics of jets produced by bursting bubbles ». *Physical Review Fluids* 3.1 (2018), p. 013603 (cit. on p. 113).

[55] Luc Deike and W. Kendall Melville. « Gas transfer by breaking waves ». *Geophysical Research Letters* 45.19 (2018), pp. 10–482 (cit. on p. 113).

[56] Luc Deike, W. Kendall Melville, and Stéphane Popinet. « Air entrainment and bubble statistics in breaking waves ». *J. Fluid Mech.* 801 (2016), pp. 91–129 (cit. on pp. 24, 113, 126).

[57] B.O.L. Demars and J.R. Manson. « Temperature dependence of stream aeration coefficients and the effect of water turbulence: A critical review ». *Water Research* 47.1 (2013), pp. 1–15 (cit. on p. 4).

[58] Richard M. Detsch. « Dissolution of 100 to 1000 μm diameter air bubbles in reagent grade water and seawater ». *Journal of Geophysical Research: Oceans* 95.C6 (1990), pp. 9765–9773 (cit. on p. 9).

[59] Stéphane Douady, Yves Couder, and Marc-Etienne Brachet. « Direct observation of the intermittency of intense vorticity filaments in turbulence ». *Physical review letters* 67.8 (1991), p. 983 (cit. on pp. 91, 92).

[60] Laurent Duchemin, Stéphane Le Dizès, Lionel Vincent, and Emmanuel Villermaux. « Self-similar impulsive capillary waves on a ligament ». *Physics of Fluids* 27.5 (2015) (cit. on p. 133).

[61] Vincent Duclaux, F Caillé, C Duez, C Ybert, Lydéric Bocquet, and Christophe Clanet. « Dynamics of transient cavities ». *Journal of Fluid Mechanics* 591 (2007), pp. 1–19 (cit. on p. 130).

[62] Benjamin Duret, Gautier Luret, Julien Reveillon, Thibaut Ménard, Alain Berlemont, and François-Xavier Demoulin. « DNS analysis of turbulent mixing in two-phase flows ». *International Journal of Multiphase Flow* 40 (2012), pp. 93–105 (cit. on p. 32).

[63] Jens Eggers. « Universal pinching of 3D axisymmetric free-surface flow ». *Physical Review Letters* 71.21 (1993), p. 3458 (cit. on pp. 111, 132).

[64] Jens Eggers. « Nonlinear dynamics and breakup of free-surface flows ». *Rev. Mod. Phys.* 69.3 (1997), pp. 865–929 (cit. on pp. 27, 111, 130).

[65] Jens Eggers and Emmanuel Villermaux. « Physics of liquid jets ». *Reports on progress in physics* 71.3 (2008), p. 036601 (cit. on pp. 4, 130, 145, 150).

[66] N. S. Ethier and T. G. Kurtz. *Markov processes: characterization and convergence*. Vol. 282. John Wiley & Sons, Hoboken, New Jersey, 2009 (cit. on p. 118).

[67] Yaning Fan, Cheng Wang, Linfeng Jiang, Chao Sun, and Enrico Calzavarini. « Accelerations of large inertial particles in turbulence ». *Europhysics Letters* (2024) (cit. on p. 86).

[68] Palas Kumar Farsoiya, Quentin Magdelaine, Arnaud Antkowiak, Stéphane Popinet, and Luc Deike. « Direct numerical simulations of bubble-mediated gas transfer and dissolution in quiescent and turbulent flows ». *Journal of Fluid Mechanics* 954 (2023), A29 (cit. on p. 9).

[69] Stephan Fauve, C Laroche, and Bernard Castaing. « Pressure fluctuations in swirling turbulent flows ». *Journal de physique II* 3.3 (1993), pp. 271–278 (cit. on p. 91).

[70] Stephan Fauve and O. Thual. « Solitary Waves Generated by Subcritical Instabilities in Dissipative Systems ». *Phys. Rev. Lett.* 64.3 (1990) (cit. on p. 55).

[71] Sophie Galinat, Frédéric Risso, Olivier Masbernat, and Pascal Guiraud. « Dynamics of drop breakup in inhomogeneous turbulence at various volume fractions ». *Journal of Fluid Mechanics* 578 (2007), pp. 85–94 (cit. on pp. 52, 100).

[72] Giacomo Gallino, Tobias M. Schneider, and Fran çois Gallaire. « Edge states control droplet breakup in subcritical extensional flows ». *Phys. Rev. Fluids* 3 (7 2018), p. 073603 (cit. on p. 57).

[73] C. Garrett, M. Li, and F. Farmer. « The connection between bubble size spectra and energy dissipation rates in the upper ocean ». *Journal of physical oceanography* 30.9 (2000), pp. 2163–2171 (cit. on pp. 114, 118, 120, 127).

[74] S. Gaudet, G.H. McKinley, and Howard A. Stone. « Extensional deformation of Newtonian liquid bridges ». *Physics of Fluids* 8.10 (1996), pp. 2568–2579 (cit. on p. 130).

[75] Elisabeth Ghabache, Arnaud Antkowiak, Christophe Josserand, and Thomas Séon. « On the physics of fizziness: How bubble bursting controls droplets ejection ». *Physics of Fluids* 26.12 (2014), p. 121701 (cit. on p. 113).

[76] Moshe Gitterman. *Noisy Oscillator, The: The First Hundred Years, From Einstein Until Now*. World Scientific, 2005 (cit. on p. 87).

[77] José Manuel Gordillo, Alejandro Sevilla, Javier Rodríguez-Rodríguez, and Carlos Martínez-Bazán. « Axisymmetric bubble pinch-off at high Reynolds numbers ». *Physical review letters* 95.19 (2005), p. 194501 (cit. on p. 130).

[78] L. Gordillo and M. A. Garcia-Nustes. « Dissipation-Driven behavior of Nonpropagating Hydrodynamic Solitons under confinement ». *Phys. Rev. Lett.* 112.164101 (2014) (cit. on p. 55).

[79] Toshiyuki Gotoh and Robert S. Rogallo. « Intermittency and scaling of pressure at small scales in forced isotropic turbulence ». *Journal of Fluid Mechanics* 396 (1999), pp. 257–285 (cit. on p. 92).

[80] G. Gulitski, M. Kholmyansky, W. Kinzelbach, B. Luthi, Arkady Tsinober, and S. Yorish. « Velocity and temperature derivatives in high-Reynolds-number turbulent flows in the atmospheric surface layer. Part 1. Facilities, methods and some general results ». *Journal of Fluid Mechanics* 589 (2007), pp. 57–81 (cit. on pp. 17, 18).

[81] Andreas Håkansson. « On the validity of different methods to estimate breakup frequency from single drop experiments ». *Chemical Engineering Science* 227 (2020), p. 115908 (cit. on p. 104).

[82] Andreas Håkansson. « The Role of Stochastic Time-Variations in Turbulent Stresses When Predicting Drop Breakup—A Review of Modelling Approaches ». *Processes* 9.11 (2021), p. 1904 (cit. on p. 52).

[83] Lu Han and Muthanna H. Al-Dahhan. « Gas–liquid mass transfer in a high pressure bubble column reactor with different sparger designs ». *Chemical engineering science* 62.1-2 (2007), pp. 131–139 (cit. on p. 4).

[84] Julius O. Hinze. « Fundamentals of the hydrodynamic mechanism of splitting in dispersion processes ». *AIChE journal* 1.3 (1955), pp. 289–295 (cit. on pp. 13, 14, 19, 31, 51, 74, 87, 113).

[85] Holger Homann and Jérémie Bec. « Finite-size effects in the dynamics of neutrally buoyant particles in turbulent flow ». *Journal of Fluid Mechanics* 651 (2010), pp. 81–91 (cit. on p. 85).

[86] `http://basilisk.fr` (cit. on p. 24).

[87] Hugh M. Hulburt and Stanley Katz. « Some problems in particle technology: A statistical mechanical formulation ». *Chemical engineering science* 19.8 (1964), pp. 555–574 (cit. on p. 8).

[88] Takashi Ishihara, Yukio Kaneda, Mitsuo Yokokawa, Keníchi Itakura, and Atsuya Uno. « Spectra of energy dissipation, enstrophy and pressure by high-resolution direct numerical simulations of turbulence in a periodic box ». *journal of the physical society of japan* 72.5 (2003), pp. 983–986 (cit. on p. 92).

[89] Daniel D. Joseph. « Cavitation and the state of stress in a flowing liquid ». *Journal of Fluid Mechanics* 366 (1998), pp. 367–378 (cit. on p. 105).

[90] I.S. Kang and L. Gary Leal. « Numerical solution of axisymmetric, unsteady free-boundary problems at finite Reynolds number. I. Finite-difference scheme and its application to the deformation of a bubble in a uniaxial straining flow ». *The Physics of fluids* 30.7 (1987), pp. 1929–1940 (cit. on pp. 55, 72).

[91] I.S. Kang and L. Gary Leal. « Small-amplitude perturbations of shape for a nearly spherical bubble in an inviscid straining flow (steady shapes and oscillatory motion) ». *Journal of Fluid Mechanics* 187 (1988), pp. 231–266 (cit. on pp. 52, 55, 56, 61, 64–67, 72, 78).

[92] Nigar Kantarci, Fahir Borak, and Kutlu O. Ulgen. « Bubble column reactors ». *Process biochemistry* 40.7 (2005), pp. 2263–2283 (cit. on pp. 4, 9, 105).

[93] F. R. Keeling. « On the role of large bubbles in air-sea gas exchange and supersaturation in the ocean ». *Journal of Marine Research* 51.2 (1993), pp. 237–271 (cit. on p. 113).

[94] Kenneth T. Kiger and James H. Duncan. « Air-entrainment mechanisms in plunging jets and breaking waves ». *Annual Review of Fluid Mechanics* 44 (2012), pp. 563–596 (cit. on p. 105).

[95] N.I. Kolev. « Fragmentation and coalescence dynamics in multiphase flows ». *Experimental thermal and fluid science* 6.3 (1993), pp. 211–251 (cit. on p. 10).

[96] Andrey Nikolaevich Kolmogorov. « The local structure of turbulence in incompressible viscous fluid for very large Reynolds numbers ». *Cr Acad. Sci. URSS* 30 (1941), pp. 301–305 (cit. on pp. 5, 13).

[97] Andrey Nikolaevich Kolmogorov. « On the breakage of drops in a turbulent flow ». *Dokl. Akad. Navk. SSSR*. Vol. 66. 1949, pp. 825–828 (cit. on pp. 13, 31, 51, 74, 87, 113).

[98] Tomasz A Kowalewski. « On the separation of droplets from a liquid jet ». *Fluid Dynamics Research* 17.3 (1996), p. 121 (cit. on p. 136).

[99] Robert H. Kraichnan. « Kolmogorov's hypotheses and Eulerian turbulence theory ». *Phys. Fluids* 7.11 (1964), pp. 1723–1734 (cit. on pp. 92, 94).

[100] Benjamin Lalanne, Olivier Masbernat, and Frédéric Risso. « A model for drop and bubble breakup frequency based on turbulence spectra ». *AIChE Journal* 65.1 (2019), pp. 347–359 (cit. on pp. 52, 87, 100, 113).

[101] Horace Lamb. « Hydrodynamics ». *Aufl., Cambridge: Univ. Press 1879–1932* 427 (1932) (cit. on pp. 49, 50, 59, 61, 66, 81, 97, 100, 118).

[102] Juan C. Lasheras, C. Eastwood, Carlos Martínez-Bazán, and Jose L. Montañes. « A review of statistical models for the break-up of an immiscible fluid immersed into a fully developed turbulent flow ». *International Journal of Multiphase Flow* 28.2 (2002), pp. 247–278 (cit. on pp. 10, 11, 52, 110).

[103] Chung-Hur Lee, LE Erickson, and LA Glasgow. « Bubble breakup and coalescence in turbulent gas-liquid dispersions ». *Chemical Engineering Communications* 59.1-6 (1987), pp. 65–84 (cit. on pp. 74, 89, 110).

[104] F. Lehr and D. Mewes. « A transport equation for the interfacial area density applied to bubble columns ». *Chemical engineering science* 56.3 (2001), pp. 1159–1166 (cit. on p. 53).

[105] F. Lehr, M. Millies, and D. Mewes. « Bubble-size distributions and flow fields in bubble columns ». *AIChE journal* 48.11 (2002), pp. 2426–2443 (cit. on pp. 4, 110).

[106] Timothy G. Leighton, David G.H. Coles, Meric Srokosz, Paul R. White, and David K. Woolf. « Asymmetric transfer of CO2 across a broken sea surface ». *Scientific reports* 8.1 (2018), pp. 1–9 (cit. on p. 113).

[107] David Leppinen and John R. Lister. « Capillary pinch-off in inviscid fluids ». *Physics of fluids* 15.2 (2003), pp. 568–578 (cit. on pp. 111, 131, 132).

[108] Veniamin Grigorevich Levich and Charles W. Tobias. « Physicochemical hydrodynamics ». *Journal of The Electrochemical Society* 110.11 (1963), p. 251C (cit. on p. 9).

[109] Ernie R. Lewis and Stephen E. Schwartz. *Sea salt aerosol production: mechanisms, methods, measurements, and models*. Vol. 152. American geophysical union, 2004 (cit. on p. 113).

[110] Jun-Hong Liang, James C McWilliams, Peter P. Sullivan, and Burkard Baschek. « Modeling bubbles and dissolved gases in the ocean ». *Journal of Geophysical Research: Oceans* 116.C3 (2011) (cit. on p. 4).

[111] Yixiang Liao and Dirk Lucas. « A literature review of theoretical models for drop and bubble breakup in turbulent dispersions ». *Chemical Engineering Science* 64.15 (2009), pp. 3389–3406 (cit. on pp. 10, 11, 52, 110, 111, 118).

[112] Yixiang Liao and Dirk Lucas. « A literature review on mechanisms and models for the coalescence process of fluid particles ». *Chemical Engineering Science* 65.10 (2010), pp. 2851–2864 (cit. on p. 10).

[113] M. R. Loewen, M. A. O'Dor, and M. G. Skafel. « Bubbles entrained by mechanically generated breaking waves ». *J. Geophys. Res.* 101 (1996), pp. 20759–20769 (cit. on pp. 113–115).

[114] Hean Luo and Hallvard F. Svendsen. « Theoretical model for drop and bubble breakup in turbulent dispersions ». *AIChE journal* 42.5 (1996), pp. 1225–1233 (cit. on pp. 53, 74, 89, 104, 110).

[115] Riccardo Maniero, Olivier Masbernat, Eric Climent, and Frédéric Risso. « Modeling and simulation of inertial drop break-up in a turbulent pipe flow downstream of a restriction ». *International journal of multiphase flow* 42 (2012), pp. 1–8 (cit. on p. 52).

[116] Florence Marcotte, Guy-Jean Michon, Thomas Séon, and Christophe Josserand. « Ejecta, corolla, and splashes from drop impacts on viscous fluids ». *Physical review letters* 122.1 (2019), p. 014501 (cit. on p. 24).

[117] Philippe Marmottant and Emmanuel Villermaux. « Fragmentation of stretched liquid ligaments ». *Physics of fluids* 16.8 (2004), pp. 2732–2741 (cit. on p. 130).

[118] Carlos Martínez-Bazán, Jose L. Montañes, and Juan C Lasheras. « On the breakup of an air bubble injected into a fully developed turbulent flow. Part 1. Breakup frequency ». *Journal of Fluid Mechanics* 401 (1999), pp. 157–182 (cit. on pp. 8, 14, 53, 90, 104, 113, 118, 121).

[119] Carlos Martínez-Bazán, Jose L. Montañes, and Juan C. Lasheras. « On the breakup of an air bubble injected into a fully developed turbulent flow. Part 1. Breakup frequency ». *J. Fluid Mech.* 401 (1999), pp. 157–182 (cit. on pp. 113, 118).

[120] Carlos Martínez-Bazán, Jose L. Montañes, and Juan C. Lasheras. « On the breakup of an air bubble injected into a fully developed turbulent flow. Part 2. Size PDF of the resulting daughter bubbles ». *Journal of Fluid Mechanics* 401 (1999), pp. 183–207 (cit. on p. 110).

[121] Carlos Martínez-Bazán, Javier Rodríguez-Rodríguez, Grant Deane, Jose L. Montañes, and Juan C. Lasheras. « Considerations on bubble fragmentation models ». *Journal of Fluid Mechanics* 661 (2010), pp. 159–177 (cit. on pp. 11, 118).

[122] Ashik Ullah Mohammad Masuk, Yinghe Qi, Ashwanth K.R. Salibindla, and Rui Ni. « Towards a phenomenological model on the deformation and orientation dynamics of finite-sized bubbles in both quiescent and turbulent media ». *Journal of Fluid Mechanics* 920 (2021), A4 (cit. on pp. 52, 74, 89).

[123] Ashik Ullah Mohammad Masuk, Ashwanth K.R. Salibindla, and Rui Ni. « Simultaneous measurements of deforming Hinze-scale bubbles with surrounding turbulence ». *Journal of Fluid Mechanics* 910 (2021) (cit. on pp. 14, 16, 20, 52, 55, 74, 87, 90, 100).

[124] Ashik Ullah Mohammad Masuk, Ashwanth K.R. Salibindla, and Rui Ni. « The orientational dynamics of deformable finite-sized bubbles in turbulence ». *Journal of Fluid Mechanics* 915 (2021), A79 (cit. on pp. 21, 72).

[125] Martin R Maxey and James J Riley. « Equation of motion for a small rigid sphere in a nonuniform flow ». *The Physics of Fluids* 26.4 (1983), pp. 883–889 (cit. on p. 91).

[126] W. Kendall Melville. « The role of surface-wave breaking in air-sea interaction ». *Annual review of fluid mechanics* 28.1 (1996), pp. 279–321 (cit. on p. 4).

[127] Charles Meneveau. « Lagrangian dynamics and models of the velocity gradient tensor in turbulent flows ». *Annual Review of Fluid Mechanics* 43 (2011), pp. 219–245 (cit. on pp. 15–18).

[128] T. Mikami, R.G. Cox, and S.G. Mason. « Breakup of extending liquid threads ». *International Journal of Multiphase Flow* 2.2 (1975), pp. 113–138 (cit. on p. 136).

[129] Michael J. Miksis. « A bubble in an axially symmetric shear flow ». *The Physics of Fluids* 24.7 (1981), pp. 1229–1231 (cit. on pp. 55–57, 64).

[130] C.A. Miller and L.E. Scriven. « The oscillations of a fluid droplet immersed in another fluid ». *Journal of fluid mechanics* 32.3 (1968), pp. 417–435 (cit. on p. 50).

[131] Nicolas Mordant, Alice M Crawford, and Eberhard Bodenschatz. « Three-dimensional structure of the Lagrangian acceleration in turbulent flows ». *Physical review letters* 93.21 (2004), p. 214501 (cit. on p. 85).

[132] Wouter Mostert, Stéphane Popinet, and Luc Deike. « High-resolution direct simulation of deep water breaking waves: transition to turbulence, bubbles and droplets production ». *Journal of Fluid Mechanics* 942 (2022) (cit. on pp. 12, 24, 113–115, 126).

[133] Nadina Müller-Fischer, Philip Tobler, Marco Dressler, Peter Fischer, and Erich J Windhab. « Single bubble deformation and breakup in simple shear flow ». *Experiments in fluids* 45 (2008), pp. 917–926 (cit. on p. 105).

[134] John A. Mullin and Werner J.A. Dahm. « Dual-plane stereo particle image velocimetry measurements of velocity gradient tensor fields in turbulent shear flow. II. Experimental results ». *Physics of Fluids* 18.3 (2006) (cit. on p. 16).

[135] G. Narsimhan, J.P. Gupta, and D. Ramkrishna. « A model for transitional breakage probability of droplets in agitated lean liquid-liquid dispersions ». *Chemical Engineering Science* 34.2 (1979), pp. 257–265 (cit. on pp. 53, 110).

[136] Aurore Naso and Andrea Prosperetti. « The interaction between a solid particle and a turbulent flow ». *New Journal of Physics* 12.3 (2010), p. 033040 (cit. on p. 32).

[137] Aurore Naso and Alain Pumir. « Scale dependence of the coarse-grained velocity derivative tensor structure in turbulence ». *Physical Review E* 72.5 (2005), p. 056318 (cit. on pp. 18, 19).

[138] Rui Ni. « Deformation and breakup of bubbles and drops in turbulence ». *Annual Review of Fluid Mechanics* 56 (2023) (cit. on pp. 11, 100).

[139] Andrew Ooi, Jesus Martin, Julio Soria, and Min S. Chong. « A study of the evolution and characteristics of the invariants of the velocity-gradient tensor in isotropic turbulence ». *Journal of Fluid Mechanics* 381 (1999), pp. 141–174 (cit. on p. 18).

[140] Sagar Pal, Daniel Fuster, Marco Crialesi-Esposito, and Stéphane Zaleski. « Statistics of drops generated from ensembles of randomly corrugated ligaments ». *ArXiv* arXiv:2106.16192v2 (2021) (cit. on pp. 111, 124, 150).

[141] Stéphane Perrard, Aliénor Rivière, Wouter Mostert, and Luc Deike. « Bubble deformation by a turbulent flow ». *Journal of Fluid Mechanics* 920 (2021), A15 (cit. on pp. 23, 28, 36, 43, 44, 51, 76, 90, 100, 102).

[142] S. B. Pope. *Turbulent flows*. Cambridge university press, Cambridge, UK, 2000 (cit. on pp. 5–7, 31, 33–35, 51).

[143] Stéphane Popinet. « Gerris: a tree-based adaptive solver for the incompressible Euler equations in complex geometries ». *J. Comput. Phys.* 190.2 (2003), pp. 572–600 (cit. on p. 24).

[144] Stéphane Popinet. « An accurate adaptive solver for surface-tension-driven interfacial flows ». *Journal of Computational Physics* 228 (2009), pp. 5838–5866 (cit. on p. 24).

[145] Stéphane Popinet. « A quadtree-adaptive multigrid solver for the Serre–Green–Naghdi equations ». *Journal of Computational Physics* 302 (2015), pp. 336–358 (cit. on p. 24).

[146] Vivek N Prakash, Yoshiyuki Tagawa, Enrico Calzavarini, Julián Martínez Mercado, Federico Toschi, Detlef Lohse, et al. « How gravity and size affect the acceleration statistics of bubbles in turbulence ». *New journal of physics* 14.10 (2012), p. 105017 (cit. on p. 85).

[147] Ludwig Prandtl. « Report on investigation of developed turbulence ». *Zeitschrift fuer Angewandte Matematik und Mechanik* 5.NACA-TM-1231 (1949) (cit. on p. 81).

[148] Michael J Prince and Harvey W Blanch. « Bubble coalescence and break-up in air-sparged bubble columns ». *AIChE journal* 36.10 (1990), pp. 1485–1499 (cit. on pp. 53, 110).

[149] Andrea Prosperetti. « Viscous effects on perturbed spherical flows ». *Quarterly of Applied mathematics* 34.4 (1977), pp. 339–352 (cit. on p. 50).

[150] Andrea Prosperetti. « Free oscillations of drops and bubbles: the initial-value problem ». *Journal of Fluid Mechanics* 100.2 (1980), pp. 333–347 (cit. on pp. 50, 78).

[151] D.I. Pullin and Robertt S. Rogallo. « Pressure and higher-order spectra for homogeneous isotropic turbulence ». *Stanford Univ., Studying Turbulence Using Numerical Simulation Databases. 5: Proceedings of the 1994 Summer Program* (1994) (cit. on p. 92).

[152] Alain Pumir. « A numerical study of pressure fluctuations in three-dimensional, incompressible, homogeneous, isotropic turbulence ». *Physics of Fluids* 6.6 (1994), pp. 2071–2083 (cit. on pp. 91, 92).

[153] Y. Qi, M. M. Ashik Ullah, and R. Ni. « Towards a model of bubble breakup in turbulence through experimental constraints ». *International Journal of Multiphase Flow* 132 (2020), p. 103397 (cit. on pp. 113, 118).

[154] Nauman M. Qureshi, Mickaël Bourgoin, Christophe Baudet, Alain Cartellier, and Yves Gagne. « Turbulent transport of material particles: an experimental study of finite size effects ». *Physical review letters* 99.18 (2007), p. 184502 (cit. on pp. 52, 83, 85, 86).

[155] J.M. Rallison. « A numerical study of the deformation and burst of a viscous drop in general shear flows ». *Journal of Fluid Mechanics* 109 (1981), pp. 465–482 (cit. on p. 57).

[156] D. Ramkrishna. *Population balances. Theory and application to particular systems in engineering*. Academic Press, San Diego, 2000 (cit. on p. 118).

[157] A.D. Randolph. « Effect of crystal breakage on crystal size distribution in mixed suspension crystallizer ». *Industrial & Engineering Chemistry Fundamentals* 8.1 (1969), pp. 58–63 (cit. on pp. 8, 110).

[158] Florent Ravelet, Catherine Colin, and Frédéric Risso. « On the dynamics and breakup of a bubble rising in a turbulent flow ». *Physics of Fluids* 23.10 (2011) (cit. on pp. 51, 52, 74, 77, 81, 90, 103).

[159] Lord Rayleigh et al. « On the capillary phenomena of jets ». *Proc. R. Soc. London* 29.196-199 (1879), pp. 71–97 (cit. on pp. 49, 59, 66, 74, 100).

[160] Brandon G. Reichl and Luc Deike. « Contribution of sea-state dependent bubbles to air-sea carbon dioxide fluxes ». *Geophysical Research Letters* 47.9 (2020), e2020GL087267 (cit. on p. 113).

[161] William Hill Reid. « The oscillations of a viscous liquid drop ». *Quarterly of Applied Mathematics* 18.1 (1960), pp. 86–89 (cit. on p. 50).

[162] Antonio Revuelta, Javier Rodríguez-Rodríguez, and Carlos Martínez-Bazán. « Bubble break-up in a straining flow at finite Reynolds numbers ». *Journal of Fluid Mechanics* 551 (2006), pp. 175–184 (cit. on pp. 21, 55, 70).

[163] Antonio Revuelta, Javier Rodríguez-Rodríguez, and Carlos Martínez-Bazán. « On the breakup of bubbles at high Reynolds numbers and subcritical Weber numbers ». *European Journal of Mechanics-B/Fluids* 27.5 (2008), pp. 591–608 (cit. on pp. 55, 72).

[164] Frédéric Risso. « Agitation, mixing, and transfers induced by bubbles ». *Annual Review of Fluid Mechanics* 50 (2018), pp. 25–48 (cit. on pp. 4, 5).

[165] Frédéric Risso and Jean Fabre. « Oscillations and breakup of a bubble immersed in a turbulent field ». *Journal of Fluid Mechanics* 372 (1998), pp. 323–355 (cit. on pp. 7, 13, 14, 31, 51, 52, 74, 76, 78, 86–90, 100, 105, 113).

[166] Aliénor Rivière, Laurent Duchemin, Christophe Josserand, and Stéphane Perrard. « Bubble breakup reduced to a one-dimensional nonlinear oscillator ». *Physical Review Fluids* 8.9 (2023), p. 094004 (cit. on pp. 54, 105).

[167] Aliénor Rivière, Wouter Mostert, Stéphane Perrard, and Luc Deike. « Sub-Hinze scale bubble production in turbulent bubble break-up ». *Journal of Fluid Mechanics* 917 (2021), A40 (cit. on pp. 23, 28, 35–38, 90, 103, 104, 115–117, 123).

[168] Aliénor Rivière, Daniel J Ruth, Wouter Mostert, Luc Deike, and Stéphane Perrard. « Capillary driven fragmentation of large gas bubbles in turbulence ». *Physical Review Fluids* 7.8 (2022), p. 083602 (cit. on pp. 103, 112, 114).

[169] Ignacio Roa, Marie-Charlotte Renoult, Christophe Dumouchel, and Jorge César Brändle de Motta. « Droplet oscillations in a turbulent flow ». *Frontiers in Physics* 11 (2023), p. 1173521 (cit. on pp. 42, 52, 76, 100).

[170] Javier Rodríguez-Rodríguez, José Manuel Gordillo, and Carlos Martínez-Bazán. « Breakup time and morphology of drops and bubbles in a high-Reynolds-number flow ». *Journal of Fluid Mechanics* 548 (2006), pp. 69–86 (cit. on pp. 20, 21, 55).

[171] G. Rojas and M. R. Loewen. « Fiber-optic probe measurements of void fraction and bubble size distributions beneath breaking waves ». *Exp. in Fluids* 43 (2007), pp. 895–906 (cit. on pp. 113–115).

[172] Carlos Rosales and Charles Meneveau. « Linear forcing in numerical simulations of isotropic turbulence: Physical space implementations and convergence properties ». *Physics of fluids* 17.9 (2005) (cit. on pp. 25, 32, 33, 74, 117).

[173] Marco Edoardo Rosti, Arash Alizad Banaei, Luca Brandt, and Andrea Mazzino. « Flexible fiber reveals the two-point statistical properties of turbulence ». *Physical review letters* 121.4 (2018), p. 044501 (cit. on p. 49).

[174] Javier Ruiz-Rus, Patricia Ern, Véronique Roig, and C Martínez-Bazán. « Coalescence of bubbles in a high Reynolds number confined swarm ». *Journal of Fluid Mechanics* 944 (2022), A13 (cit. on p. 10).

[175] Daniel J. Ruth, Aditya K. Aiyer, Aliénor Rivière, Stéphane Perrard, and Luc Deike. « Experimental observations and modelling of sub-Hinze bubble production by turbulent bubble break-up ». *Journal of Fluid Mechanics* 951 (2022), A32 (cit. on pp. 103, 112, 115–117).

[176] Daniel J. Ruth, Wouter Mostert, Stéphane Perrard, and Luc Deike. « Bubble pinch-off in turbulence ». *Proceedings of the National Academy of Sciences* 116.51 (2019), pp. 25412–25417 (cit. on pp. 88, 124, 126, 145).

[177] Gregory Ryskin and L. Gary Leal. « Numerical solution of free-boundary problems in fluid mechanics. Part 3. Bubble deformation in an axisymmetric straining flow ». *Journal of Fluid Mechanics* 148 (1984), pp. 37–43 (cit. on pp. 55–57, 64).

[178] Ashwanth K.R. Salibindla, Ashik Ullah Mohammad Masuk, and Rui Ni. « Experimental investigation of the acceleration statistics and added-mass force of deformable bubbles in intense turbulence ». *Journal of Fluid Mechanics* 912 (2021), A50 (cit. on p. 85).

[179] Jörg Schumacher, Janet D Scheel, Dmitry Krasnov, Diego A Donzis, Victor Yakhot, and Katepalli R Sreenivasan. « Small-scale universality in fluid turbulence ». *Proceedings of the National Academy of Sciences* 111.30 (2014), pp. 10961–10965 (cit. on p. 7).

[180] M. Sevik and S. H. Park. « The Splitting of Drops and Bubbles by Turbulent Fluid Flow ». *Journal of Fluids Engineering* 95.1 (1973), pp. 53–60 (cit. on pp. 14, 74, 89, 90, 113).

[181] Jie Shen, Cheng Peng, Jianzhao Wu, Kai Leong Chong, Zhiming Lu, and Lian-Ping Wang. « Turbulence modulation by finite-size particles of different diameters and particle–fluid density ratios in homogeneous isotropic turbulence ». *Journal of Turbulence* 23.8 (2022), pp. 433–453 (cit. on p. 96).

[182] X.D. Shi, Michael P. Brenner, and Sidney R. Nagel. « A cascade of structure in a drop falling from a faucet ». *Science* 265.5169 (1994), pp. 219–222 (cit. on pp. 130, 136).

[183] Javier Sierra-Ausin, Paul Bonnefis, Antonia Tirri, David Fabre, and Jacques Magnaudet. « Dynamics of a gas bubble in a straining flow: Deformation, oscillations, self-propulsion ». *Phys. Rev. Fluids* 7 (11 2022), p. 113603 (cit. on pp. 55, 57, 59, 64, 72).

[184] Marian von Smoluchowski. « Drei vortrage uber diffusion, brownsche bewegung und koagulation von kolloidteilchen ». *Zeitschrift fur Physik* 17 (1916), pp. 557–585 (cit. on p. 8).

[185] E. D. Spiel and Gerrit De Leeuw. « Formation and production of sea spray aerosol ». *Journal of Aerosol Science* 27 (1996), S65–S66 (cit. on p. 113).

[186] Katepalli R Sreenivasan and Robert A Antonia. « The phenomenology of small-scale turbulence ». *Annual review of fluid mechanics* 29.1 (1997), pp. 435–472 (cit. on p. 7).

[187] Howard A. Stone, B.J. Bentley, and L. Gary Leal. « An experimental study of transient effects in the breakup of viscous drops ». *Journal of Fluid Mechanics* 173 (1986), pp. 131–158 (cit. on pp. 55, 57).

[188] Howard A. Stone and L. Gary Leal. « Relaxation and breakup of an initially extended drop in an otherwise quiescent fluid ». *Journal of Fluid Mechanics* 198 (1989), pp. 399–427 (cit. on pp. 55, 57).

[189] Henk Tennekes. « Eulerian and Lagrangian time microscales in isotropic turbulence ». *Journal of Fluid Mechanics* 67.3 (1975), pp. 561–567 (cit. on p. 92).

[190] Vinod Ashok Thale, Mostafa Abouelsoud, Hossain Chizari, and Marie-Jean Thoraval. « Impact force of an air-in-liquid compound drop ». *Physics of Fluids* 36.2 (2024) (cit. on p. 24).

[191] S.T. Thoroddsen, T.G. Etoh, and K. Takehara. « Experiments on bubble pinch-off ». *Physics of Fluids* 19.4 (2007) (cit. on pp. 130, 136, 140, 145, 146).

[192] Federico Toschi and Eberhard Bodenschatz. « Lagrangian properties of particles in turbulence ». *Annual review of fluid mechanics* 41 (2009), pp. 375–404 (cit. on p. 91).

[193] Adrien Toutant, E. Labourasse, O. Lebaigue, and Olivier Simonin. « DNS of the interaction between a deformable buoyant bubble and a spatially decaying turbulence: a priori tests for LES two-phase flow modelling ». *Computers & Fluids* 37.7 (2008), pp. 877–886 (cit. on p. 32).

[194] Arkady Tsinober. *An informal conceptual introduction to turbulence*. Springer, 2009 (cit. on p. 18).

[195] Arkady Tsinober, E. Kit, and T. Dracos. « Experimental investigation of the field of velocity gradients in turbulent flows ». *Journal of Fluid Mechanics* 242 (1992), pp. 169–192 (cit. on p. 16).

[196] C. Tsouris and L.L. Tavlarides. « Breakage and coalescence models for drops in turbulent dispersions ». *AIChE Journal* 40.3 (1994), pp. 395–406 (cit. on pp. 104, 110).

[197] J Antoon Van Hooft, Stéphane Popinet, Chiel C Van Heerwaarden, Steven JA Van der Linden, Stephan R De Roode, and Bas JH Van de Wiel. « Towards adaptive grids for atmospheric boundary-layer simulations ». *Boundary-layer meteorology* 167 (2018), pp. 421–443 (cit. on p. 24).

[198] Prakash Vedula and Pui-Kuen Yeung. « Similarity scaling of acceleration and pressure statistics in numerical simulations of isotropic turbulence ». *Physics of Fluids* 11.5 (1999), pp. 1208–1220 (cit. on pp. 91, 92).

[199] Jiří Vejražka, Mária Zedníková, and Petr Stanovskỳ. « Experiments on breakup of bubbles in a turbulent flow ». *AIChE Journal* 64.2 (2018), pp. 740–757 (cit. on pp. 8, 14, 104, 113, 118, 121).

[200] Alberto Vela-Martín and Marc Avila. « Deformation of drops by outer eddies in turbulence ». *Journal of Fluid Mechanics* 929 (2021), A38 (cit. on pp. 79, 81, 82, 91).

[201] Alberto Vela-Martín and Marc Avila. « Memoryless drop breakup in turbulence ». *Science Advances* 8.50 (2022), eabp9561 (cit. on pp. 100, 103).

[202] Gautier Verhille. « Deformability of discs in turbulence ». *Journal of Fluid Mechanics* 933 (2022), A3 (cit. on p. 49).

[203] P. Vieillefosse. « Local interaction between vorticity and shear in a perfect incompressible fluid ». *Journal de Physique* 43.6 (1982), pp. 837–842 (cit. on p. 18).

[204] P. Vieillefosse. « Internal motion of a small element of fluid in an inviscid flow ». *Physica A: Statistical Mechanics and its Applications* 125.1 (1984), pp. 150–162 (cit. on p. 18).

[205] Emmanuel Villermaux. « Fragmentation ». *Annu. Rev. Fluid Mech.* 39 (2007), pp. 419–446 (cit. on p. 145).

[206] Emmanuel Villermaux. « The formation of filamentary structures from molten silicates: Pele's hair, angel hair, and blown clinker ». *Comptes rendus. Mécanique* 340.8 (2012), pp. 555–564 (cit. on p. 138).

[207] Emmanuel Villermaux. « Fragmentation versus Cohesion ». *J. Fluid Mech.* 898 (2020) (cit. on pp. 4, 101, 119, 123, 127, 145).

[208] Emmanuel Villermaux, Ph Marmottant, and Jérome Duplat. « Ligament-mediated spray formation ». *Physical review letters* 92.7 (2004), p. 074501 (cit. on p. 145).

[209] Emmanuel Villermaux, Xiaofei Wang, and Luc Deike. « Bubbles spray aerosols: Certitudes and mysteries ». *PNAS nexus* 1.5 (2022), pgac261 (cit. on p. 4).

[210] Lionel Vincent, Laurent Duchemin, and Emmanuel Villermaux. « Remnants from fast liquid withdrawal ». *Physics of Fluids* 26.3 (2014) (cit. on p. 133).

[211] Romain Volk, Enrico Calzavarini, Emmanuel Lévêque, and Jean-François Pinton. « Dynamics of inertial particles in a turbulent von Kármán flow ». *Journal of Fluid Mechanics* 668 (2011), pp. 223–235 (cit. on pp. 83, 85).

[212] Romain Volk, Enrico Calzavarini, Gautier Verhille, Detlef Lohse, Nicolas Mordant, Jean-François Pinton, et al. « Acceleration of heavy and light particles in turbulence: comparison between experiments and direct numerical simulations ». *Physica D: Nonlinear Phenomena* 237.14-17 (2008), pp. 2084–2089 (cit. on pp. 82, 85, 86).

[213] Greg A. Voth, Arthur La Porta, Alice M. Crawford, Jim Alexander, and Eberhard Bodenschatz. « Measurement of particle accelerations in fully developed turbulence ». *Journal of Fluid Mechanics* 469 (2002), pp. 121–160 (cit. on pp. 83, 85, 86).

[214] Tiefeng Wang, Jinfu Wang, and Yong Jin. « A novel theoretical breakup kernel function for bubbles/droplets in a turbulent flow ». *Chemical Engineering Science* 58.20 (2003), pp. 4629–4637 (cit. on pp. 53, 74, 89, 104, 110, 119, 125).

[215] F.A. Williams. « Combustion theory addison-wesley ». *Redwood City* (1985) (cit. on p. 8).

[216] D.K. Woolf, I.S. Leifer, P.D. Nightingale, T.S. Rhee, P. Bowyer, Guillemette Caulliez, et al. « Modelling of bubble-mediated gas transfer: Fundamental principles and a laboratory test ». *Journal of Marine Systems* 66.1-4 (2007), pp. 71–91 (cit. on p. 4).

[217] Xiao Xiao, Jürgen Brillo, Jonghyun Lee, Robert W. Hyers, and Douglas M. Matson. « Impact of convection on the damping of an oscillating droplet during viscosity measurement using the ISS-EML facility ». *npj Microgravity* 7.1 (2021), p. 36 (cit. on p. 81).

[218] Hua-Dong Yao, Guo-Wei He, Meng Wang, and Xing Zhang. « Time correlations of pressure in isotropic turbulence ». *Physics of Fluids* 20.2 (2008) (cit. on p. 92).

[219] G.K. Youngren and Andreas Acrivos. « On the shape of a gas bubble in a viscous extensional flow ». *Journal of fluid mechanics* 76.3 (1976), pp. 433–442 (cit. on pp. 56, 64).

[220] Ben Yuan, Jiajia Li, and Pablo M. Carrica. « A turbulent bubble breakup model with application to LES ». *International Journal of Multiphase Flow* 148 (2022), p. 103966 (cit. on p. 104).

RÉSUMÉ

La présence de bulles dans des écoulements contribuent à augmenter le mélange, ainsi que les échanges de matière et de chaleur entre les deux phases. Leur présence est ainsi primordiale dans un grand nombre de procédés industriels ainsi que dans des contextes environnementaux, caractérisés par des écoulements inertiels voire turbulents. Pour quantifier l'impact des bulles, il faut d'abord comprendre et modéliser leur distribution de taille, et son évolution temporelle. Dans des environements dilués, où l'évolution de la distribution est contrôlée par la fragmentation, la distribution présente deux lois de puissance séparées par une taille critique.

Dans un premier temps, nous nous intéressons à l'origine de la taille critique. Celle-ci correspond à la limite entre les bulles stables et instables, appelée échelle de Kolmogorov-Hinze. Les écoulements turbulents étant intrinsèquement caractérisés par de larges fluctuations, à la fois de pression et de vitesse, cette taille critique reste mal définie. Ici, nous proposons une nouvelle définition, probabiliste, de cette limite, qui inclue le temps de résidence des bulles dans les zones turbulentes. Pour cela, nous étudions numériquement la déformation d'une bulle, d'abord dans une géométrie d'écoulement modèle puis dans un écoulement turbulent homogène isotrope. Dans les deux cas, nous montrons que la dynamique de déformation peut être reproduite par une dynamique 1D sur le mode de déformation oblate-prolate. En extrapolant la dynamique obtenue dans le cas turbulent à des bulles qui cassent, nous quantifions la probabilité de fracture en un temps donné et en déduisons l'évolution de la taille critique au cours du temps.

Dans un second temps, nous nous intéressons à la génération de bulles sous l'échelle de Kolmogorov-Hinze. En effet, s'il y a un consensus sur l'origine de la distribution des bulles plus grandes que la taille critique, l'origine de la distribution pour les petites bulles restait à déterminer. Grâce à des simulations numériques directes, nous identifions que ces bulles proviennent de la rupture de filaments gazeux produits lors de la déformation de bulles plus grandes que l'échelle critique. Nous caractérisons ensuite la production et la fragmentation de ces filaments dans une géométrie d'écoulement modèle. Nous découvrons que la fragmentation de ligaments sous contrainte d'étirement conduit à une distribution de taille de bulles en loi de puissance qui coïncide avec la distribution sous l'échelle critique en turbulence.

MOTS CLÉS

bulle, turbulence, fragmentation, déformation, simulations numériques, modélisation

ABSTRACT

Through their contributions to mixing, gas and heat transfers and aerosol production, bubbles play a central role in many industrial and environmental contexts, characterized by inertial flows, possibly turbulent. Understanding the physical processes controlling the bubble size distribution (BSD) and its temporal evolution, is key to quantify these exchanges. In dilute environments, in which breakup dominates, the BSD is characterized by two power laws separated by a critical size.

We first focus on the origin of this critical size. This size is known to be related to the Kolmogorov-Hinze scale, the size separating statistically stable, from unstable bubbles in turbulence. As a turbulent flow is characterized by large velocity and pressure fluctuations, this size is only defined in a statistical sense. We give here a new definition of this critical size, in terms of survival probability, which includes the residence time of bubbles within turbulent regions. To do so, we investigate numerically bubble deformations first in a model flow geometry and then in 3D homogeneous and isotropic turbulence (HIT). In both cases, we find that most of bubble deformation dynamics can be reproduced by a 1D model of the oblate-prolate mode. By extrapolating the deformation model obtained in turbulence to breaking bubbles, we deduce the probability of breaking and the evolution of the critical size in time.

We then investigate the generation of sub-Hinze bubbles. While there is a consensus for the origin of the power-law scaling for the super-Hinze BSD, the sub-Hinze BSD remained to be understood. By running DNS of bubbles in turbulence, we identify that sub-Hinze bubbles come from the fracture of gas filaments produced during the deformations of super-Hinze bubbles. We characterize filament production in a model flow configuration, as well as filament splitting. We find that filament breaking under stretching universally produces a power-law distribution, which coincides with the one obtained below breaking waves. This mechanism explains the origin of the sub-Hinze BSD.

KEYWORDS

bubble, turbulence, breakup, deformation, numerical simulations, modeling